IntechOpen

Wave Propagation Concepts for Near-Future Telecommunication Systems

Edited by Sandra Costanzo

WAVE PROPAGATION CONCEPTS FOR NEAR-FUTURE TELECOMMUNICATION SYSTEMS

Edited by **Sandra Costanzo**

Wave Propagation Concepts for Near-Future Telecommunication Systems
http://dx.doi.org/10.5772/61383
Edited by Sandra Costanzo

Contributors

Patricio Lautaro Robles, Francisco Pizarro, M Mainul Hoque, Norbert Jakowski, Jens Berdermann, Yiping Han, Shiyang Liu, Giuseppe Di Massa, Shulabh Gupta, Christophe Caloz, Lorenzo Luini, Roberto Nebuloni, Carlo Riva, Matteo Pastorino, Giovanni Leone, Sandra Costanzo

Notice

First published in Croatia, 2017 by INTECH d.o.o.
eBook (PDF) Published by IN TECH d.o.o.
Place and year of publication of eBook (PDF): Rijeka, 2019.
IntechOpen is the global imprint of IN TECH d.o.o.
Printed in Croatia

Legal deposit, Croatia: National and University Library in Zagreb

Additional hard and PDF copies can be obtained from orders@intechopen.com

Wave Propagation Concepts for Near-Future Telecommunication Systems
Edited by Sandra Costanzo

p. cm.

Print ISBN 978-953-51-3127-4

Online ISBN 978-953-51-3128-1

eBook (PDF) ISBN 978-953-51-4855-5

Meet the editor

Sandra Costanzo received her Laurea degree (summa cum laude) in Computer Engineering (Electronics and Telecommunication profile) from the University of Calabria in 1996 and her PhD degree in Electronic Engineering from the University of Reggio Calabria in 2000. Currently, she is an associate professor at University of Calabria, Italy, where she teaches the courses of electromagnetic wave propagation, radar and remote sensing and signal and waves in telecommunications. Her research interests are focused on near-field far-field techniques, antenna measurement techniques, antenna analysis and synthesis, numerical methods in electromagnetics, millimeter-wave antennas, reflectarrays, synthesis methods for microwave structures, electromagnetic characterization of materials and innovative antennas and technologies for radar applications. She serves as a reviewer for various international journals. She is an associate editor of *IEEE Antennas and Wireless Propagation Letters* and *IEEE Access and Radioengineering* journals, and she is a member of the Editorial Board for the *Electrical and Electronic Engineering* journal and Scientific and Academic Publishing. She is the lead editor of three Special Issues titled "Reflectarray Antennas: Analysis and Synthesis Techniques" (*International Journal of Antennas and Propagation*), "Advances in Radar Technologies" (*Journal of Electrical and Computer Engineering*), "Compressed Sensing: Applications in Radar and Communications" (*The Scientific World Journal*). She is the editor of the book *Microwave Materials Characterization* (ISBN 978-953-51-0848-1, InTech, 2012). She has coauthored more than 160 contributions in international journals, books and conferences.

Contents

Preface

The present book gives a collection of some recent studies on relevant challenges for the design of innovative telecommunication systems, with particular focus on the propagation aspects and radiating system design. The book is divided into two sections, both including original research contributions. Section 1 is devoted to the illustration of advanced results in terms of microwave propagation at high frequencies, while Section 2 is focused on new electromagnetic concepts and applications.

Section 1 consists of Chapters 1–5. Chapter 1 by S. Costanzo discusses the basic properties of nondiffracting Bessel beams, providing an overview of some potential applications.

In Chapter 2 the ionospheric propagation effects including higher order terms for microwave signals up to 100 GHz frequencies are analyzed by M. M. Hoque et al., with the aim to enhance the accuracy of precise positioning, navigation and frequency transfer.

Chapter 3 by L. Luini et al. deals with all aspects of characterizing the propagation of electromagnetic waves in the Ka, Q, V and W bands, spanning from the main impairments induced by the troposphere to how extreme atmospheric conditions can be handled making use of suitable fade mitigation techniques.

A conceptual frame for understanding the propagation of light through a dispersive medium is presented by P. Robles and F. Pizarro in Chapter 4, considering both the classical approach based on electromagnetic waves and a quantum description in terms of photons.

In Chapter 5, the problem of shaped beam scattering by typical particles with regular shapes is faced by Y. P. Han et al, and relevant results for some complex particles are discussed.

Section 2 consists of Chapters 6–10. G. Di Massa in Chapter 6 discusses some relevant applications of the interaction between slow electromagnetic waves and dielectric or corrugated media, to be helpful in the design of compact and easily integrable microwave devices and antennas.

In Chapter 7, the scattering response of non-planar frequency selective surfaces (FSS) and curved elements is numerically investigated by G. Leone et al, with the aim to provide a useful design tool for conformal FSS to be adopted in high-performance applications.

In Chapter 8, a real-time and low-cost system for precipitation detection from Satellite Digital Video Broadcasting (DVB-S) microwave signals is discussed by D. Caviglia et al.

In Chapter 9, real-time electromagnetic signal processing paradigm is presented by S. Gupta and C. Caloz, with the aim to control electromagnetic signals at low cost directly in the analog domain.

Chapter 10 by S. Liu et al. presents the design of zero-index materials with magnetic metamaterials based on multiple scattering theory and effective-medium theory.

I wish to thank all the book contributors for the original submitted results that came from their research activities. A special acknowledgement is due to the editorial assistants for their professional support during the book preparation.

Sandra Costanzo
University of Calabria
Italy

Section 1

Electromagnetic Propagation in Near-Future Telecommunication Systems

Chapter 1

Localized Bessel Beams: Basic Properties and Emerging Communication Applications

Sandra Costanzo

Additional information is available at the end of the chapter

http://dx.doi.org/10.5772/intechopen.68780

Abstract

Relevant properties of Bessel beams in terms of nondiffracting propagation over ideally infinite range, with unchanged transverse profile and self-healing capability, are revised and discussed in the present chapter. Promising applications in the framework of new-generation communication systems are also outlined.

Keywords: focused systems, nondiffracting fields, Bessel beam, propagation, slow waves

1. Introduction

Diffractive phenomena are strictly related to the wave nature of light: any field of wavelength λ, initially confined to a finite area having radius r, will be subjected to a diffractive spreading beyond a characteristic distance equal to $\frac{r^2}{\lambda}$, known as the Rayleigh range [1]. In the late 1980s, a class of diffraction-free mode solutions has been introduced [2] to describe well-defined nonspreading beams with extremely narrow central spot. They are called Bessel beams, due to the particular shape in the transverse plane, which is mathematically described by a Bessel function [3]. A qualitative comparison of Gaussian (diffractive) and ideal Bessel (localized) beams is illustrated in **Figures 1** and **2**: it is evident that Gaussian beam (**Figure 1**) soon diffracts for very short distance range, while the Bessel beam (**Figure 2**) ideally maintains a stationary transverse pattern along the propagation distance.

As deeply addressed in Section 2, Bessel beams are solutions to the Helmholtz equation in circular cylindrical coordinates, revealing many appealing features, namely

- they theoretically guarantee an indefinite extension along the axial (propagation) direction;

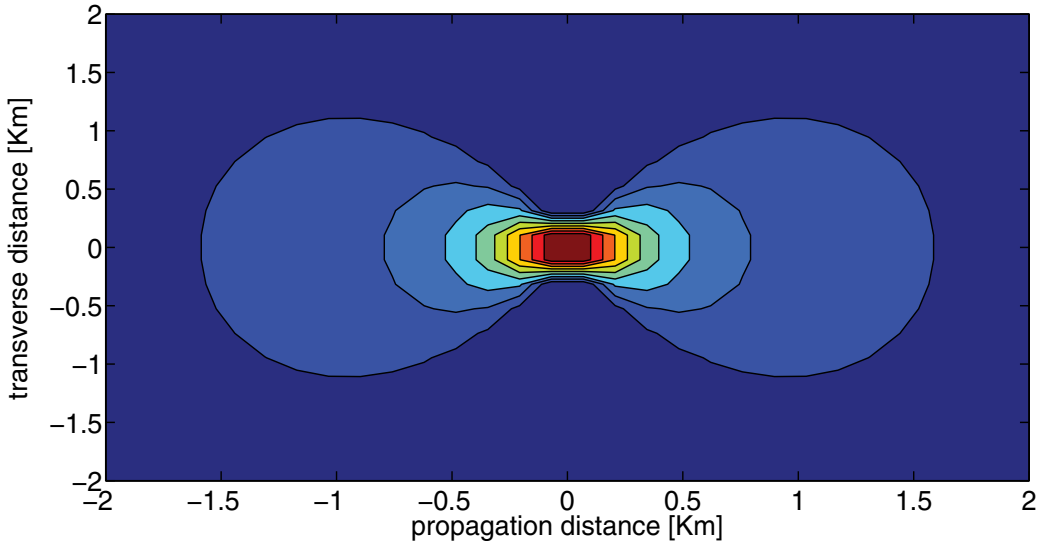

Figure 1. Gaussian beam propagating into a homogeneous medium.

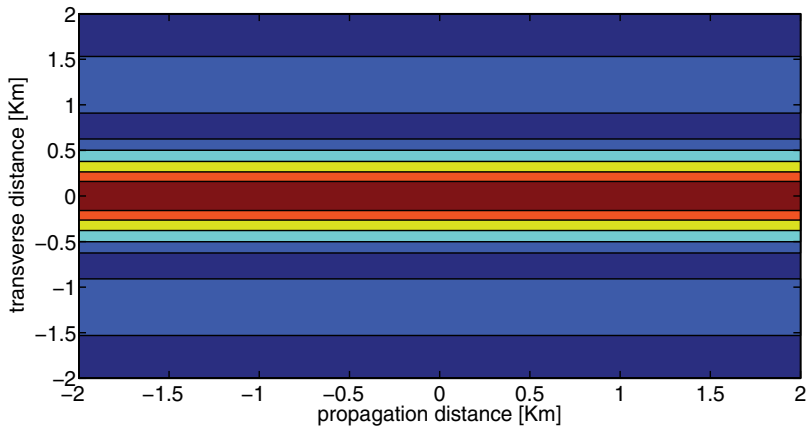

Figure 2. Bessel beam propagating into a homogeneous medium.

- they own the property of reconstruction after obstruction ("self-healing"), that is, if an obstacle occurs at the center of the beam, it will not block the rays, as they will interfere each other to reform the beam.

The ideal Bessel beam, having an infinite number of rings and covering an infinite distance, cannot physically exist, as it requires an infinite energy. Thus, physically meaningful beams are the apertured Bessel beams, possessing nearly diffracting properties within a limited axial distance. In this chapter, an overview of the basic properties of localized Bessel beams is provided, and some specific applications in the framework of emerging communication technologies are discussed. In particular, mathematical details on Bessel beams solutions are presented in Section 2, where the possibility to express the Bessel beam in terms of plane waves traveling on a

cone with the same phase velocity is demonstrated. In Section 3.1, a practical realization example of microwave Bessel beam source to be applied for focused high-penetration applications is described, while in Sections 3.2 and 3.3, a discussion about potential applications in the framework of high-performance communication systems is outlined.

2. Localized Bessel beam solutions

Let us consider the scalar wave equation:

$$\nabla^2\psi - \frac{1}{c^2}\frac{\partial^2\psi}{\partial t^2} = 0 \tag{1}$$

where c is the free-space velocity.

In any system of cylindrical coordinates (u_1, u_2, z), the wave equation (1) is satisfied by a solution of the form [4]:

$$\psi(\rho, z, t) = f(\rho)e^{j(k_z z - \omega t)} \tag{2}$$

where

$$\rho = \sqrt{u_1^2 + u_2^2} \tag{3}$$

is the transverse distance, and the radial function shape $f(\rho)$ is assumed to be preserved along the propagation axis z.

When replacing the solution (2) into Eq. (1), the following equation is obtained:

$$\rho^2\frac{d^2f(\rho)}{d\rho^2} + \rho\frac{df(\rho)}{d\rho} + \rho^2(k^2 - k_z^2)f(\rho) = 0 \tag{4}$$

where $k^2 = \omega^2/c^2$.

Eq. (4) satisfied by the radial function $f(\rho)$ can be easily recognized as Bessel's equation, namely

$$x^2\frac{d^2J_p(x)}{dx^2} + x\frac{J_p(x)}{d\rho} + (x^2 - p^2)J_p(x) = 0 \tag{5}$$

where $J_p(\ldots)$ is the cylindrical Bessel function of order p.

Thus, a solution of the wave equation (1) which maintains unchanged its radial shape can be written as

$$\psi(\rho, z, t) = J_o(k_\rho\rho)e^{j(k_z z - \omega t)} \tag{6}$$

where

$$k_\rho = k^2 - k_z^2$$

$$k^2 = \frac{\omega^2}{c^2} = k_1^2 + k_2^2 + k_z^2 = k_\rho^2 + k_z^2 \tag{7}$$

Recalling that

$$k_1 = k\sin\theta\cos\phi,\ k_2 = k\sin\theta\sin\phi,\ k_z = k\cos\theta \tag{8}$$

we have

$$k_\rho^2 = k_1^2 + k_2^2 = k^2\sin^2\theta \tag{9}$$

Replacing expression (9) into the solution (6), we can write

$$\psi(\rho, z, t) = J_o(\rho k\sin\theta)e^{j(kz\cos\theta - \omega t)} \tag{10}$$

In particular, for θ = 0°, the solution (10) reduces to a plane wave propagating along the z-direction.

Now, let us recall the Bessel function can be written as

$$J_o(\rho) = \frac{1}{2\pi}\int_0^{2\pi} e^{j\rho\cos\alpha}d\alpha \tag{11}$$

When imposing

$$\alpha = \phi - \phi',\ u_1 = \rho\cos\phi',\ u_2 = \rho\sin\phi' \tag{12}$$

Eq. (11) can be written as

$$J_o(\rho) = \frac{1}{2\pi}\int_0^{2\pi} e^{j(u_1\cos\phi + u_2\sin\phi)}d\phi \tag{13}$$

Then, if replacing expression (13) into solution (10), we have

$$\Psi(\rho, z, t) = \frac{1}{2\pi}\int_0^{2\pi} e^{jk(u_1\sin\theta\cos\phi + u_2\sin\theta\sin\phi + z\cos\theta)}e^{-j\omega t}d\phi = \frac{1}{2\pi}\int_0^{2\pi} e^{j(\underline{k}\cdot\underline{u} - \omega t)}d\phi \tag{14}$$

The latter equation demonstrates that a nondiffracting Bessel beam can be expressed in terms of plane waves, as it describes a cone of plane waves having the same inclination angle θ with respect to the propagation axis z.

Let us consider the solution expressed by Eq. (10). For $0 < k_\rho \le \frac{\omega}{c}$, it represents a nondiffracting beam whose intensity profile decays at a rate proportional to the product $k_\rho\rho$. The maximum value of the radial wavenumber k_ρ to have a nonevanescent field is given by $k_\rho = \frac{\omega}{c}$. From this condition, the spot width 2ρ of the Bessel beam can be easily derived to be equal to $\frac{3\lambda}{4}$ (**Figure 3**).

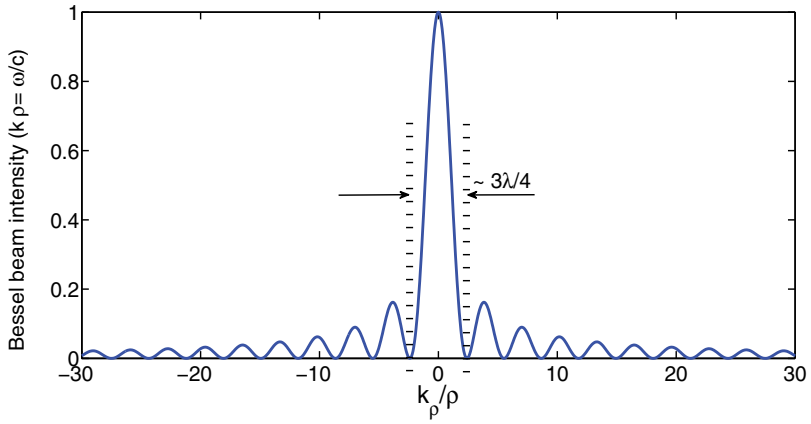

Figure 3. Spot width of Bessel beam.

As a matter of fact, the first null of the Bessel beam is equal to

$$k_\rho \rho = 2.325 \tag{15}$$

Thus, taking into account that $k_\rho = \frac{2\pi}{\lambda}$, it results

$$\rho = 0.37\lambda \tag{16}$$

As yet outlined in Section 1, the solution (10) describes an ideal Bessel beam, with extremely narrow intensity profile and infinite propagation distance. However, from simple energy argumentations, it can be demonstrated that such a Bessel beam is not physically realizable. The intensity field distribution given by Eq. (10) is described by the Bessel function J_o (…), which is not square integrable (it decays as $\frac{1}{\rho}$). This means that each ring contains the same amount of energy as the central spot. An infinite energy would be required to create the Bessel beam over the entire plane, due to the presence of an infinite number of rings. Thus, we should conclude that only an approximated Bessel beam can be practically realized over a finite area. It however maintains all appealing features of the ideal Bessel beam in terms of nondiffracting propagation over a finite distance z_{max}, as illustrated in **Figure 4**.

To derive the expression of the finite range z_{max}, let us consider the Bessel beam as given by the superimposition of plane waves, all having the same amplitude and traveling at the same angle θ relative to the propagation z-axis.

From Eq. (9), we have

$$\theta = \sin^{-1}\left(\frac{k_\rho \lambda}{2\pi}\right) \tag{17}$$

Then, applying geometrical optics considerations, the following expression can be derived:

$$z_{\max} = \frac{r}{tg\theta} = r\sqrt{\frac{1}{\sin^2\theta} - 1} = r\sqrt{(\frac{2\pi}{k_\rho \lambda})^2 - 1} \tag{18}$$

r being the aperture radius (**Figure 4**).

From Eq. (18) we can observe that, in order to produce a Bessel beam propagating on a long distance, either the radius r should be taken large, or the radial wavenumber k_ρ should be small, or alternately we should increase the operating frequency.

Let us consider the power P_r contained in a Bessel beam up to a radius r:

$$P_r = \int_0^{2\pi}\int_0^r |\psi(\rho)|^2 \rho d\rho d\phi = P_r = \int_0^{2\pi}\int_0^r |J_o(k_\rho \rho)|^2 \rho d\rho d\phi = r^2[J_o^2(k_\rho r) + J_1^2(k_\rho r)] \tag{19}$$

When imposing relation (15), we have

$$P_r = \pi r^2 J_1^2(2.325) \tag{20}$$

If comparing the above result with that relative to a Gaussian beam produced by the same aperture, an increased power delivery can be demonstrated.

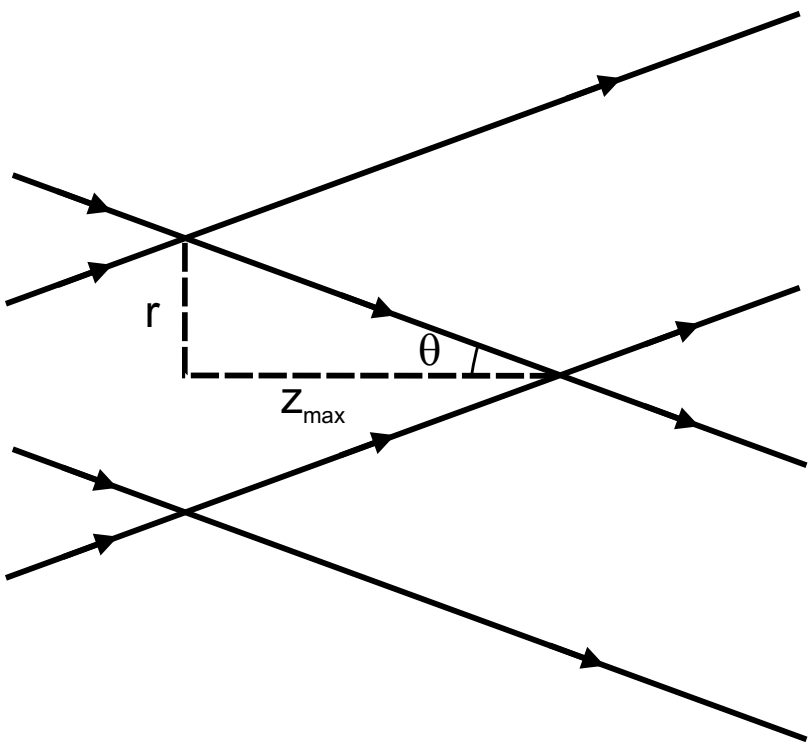

Figure 4. Finite propagation range of Bessel beam from finite aperture of radius r.

3. Potential applications of localized Bessel beams

The unique properties of Bessel beams in terms of self-reconstruction and profile stability over large distances make them ideal candidates in a variety of applications, requiring highly localized energy and/or diffraction mitigation. In this section, a few specific application examples to be adopted in the framework of new-generation telecommunication systems are reviewed. They include a microwave realization of Bessel beam launcher and the potential use of Bessel beams as an efficient transmission medium to increase data rate and overcome diffraction limits in long distance communications.

3.1. Waveguide-based microwave Bessel beam launcher

Most of existing works in the literature are mainly focused on the generation of Bessel beams in the optical regime, through the adoption of annular slit, axicons, or lasing devices [5–9], while much less results exist in the microwave regime.

In a recent ESA (European Space Agency) research study on "Microwave Drilling" [10], a practical X-band realization of Bessel beam launcher to be adopted as a focused near-field source has been performed. Following the theoretical approach outlined in [11], the microwave Bessel beam is generated as the aperture field at the open end of a metallic circular waveguide. In particular, a transverse electric (TE) representation is adopted for the zero-order Bessel beam, with an expansion in terms of a finite number of propagating TE_{0n} modes of the circular waveguide. These modes are produced by a set of elementary loop antennas, whose excitation coefficients are properly chosen to obtain the prescribed beam intensity and spot size. By imposing the Bessel beam to have n distinct annular sections, and choosing the radial wavenumber k_ρ to match the relative cutoff wavenumber χ_{cn} of the modes inside the circular waveguide [12], the Bessel beam can be fully represented by the single TE_{0n} mode.

The schematic configuration of X-band Bessel beam launcher developed in [10] is illustrated in **Figure 5**. A single-loop antenna is considered for the proper field generation inside the circular waveguide of radius $r = a$. The excitation antenna is located at a distance equal to $\frac{\lambda_o}{2}$ (at the central operating frequency f_o) from the short-circuited side of the circular waveguide, in order to match with the maximum value of the current, so to realize the maximum coupling with the magnetic field.

A Bessel beam with $n = 3$ distinct annular rings is chosen, so deriving the value of radius a from the relation [13]:

$$k_\rho a = \chi_{03} = 10.1735 \tag{21}$$

which gives $a \cong 1.5\lambda_o$.

The realized prototype, for a design frequency $f_o = 8.74\mathrm{GHz}$, is illustrated in **Figure 6**, where the microstrip loop antenna, designed on a standard substrate Arlon Diclad 880 ($\epsilon_r = 2.2$, thickness $t = 0.762$ mm) is also reported.

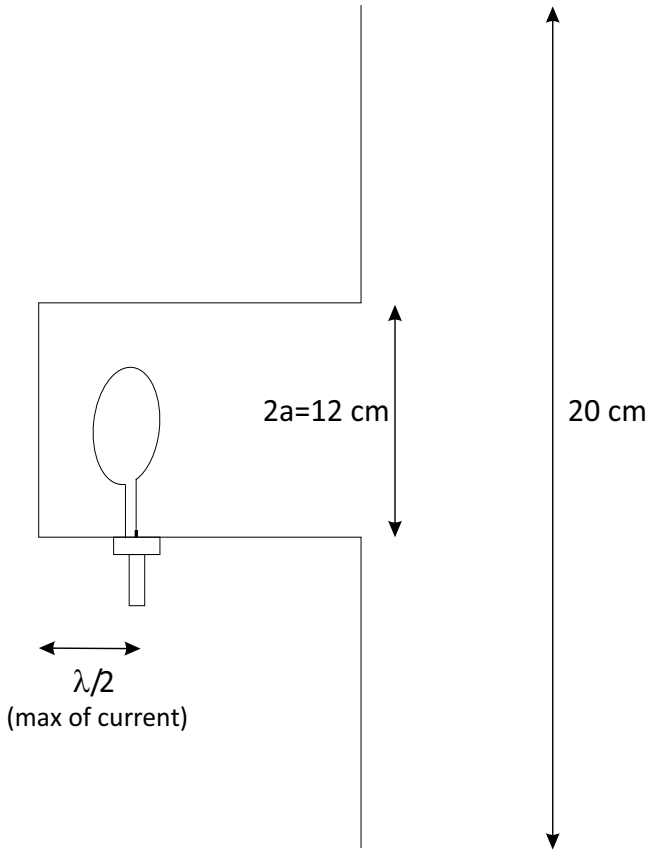

Figure 5. Schematic configuration of microwave Bessel beam launcher (taken from [10]).

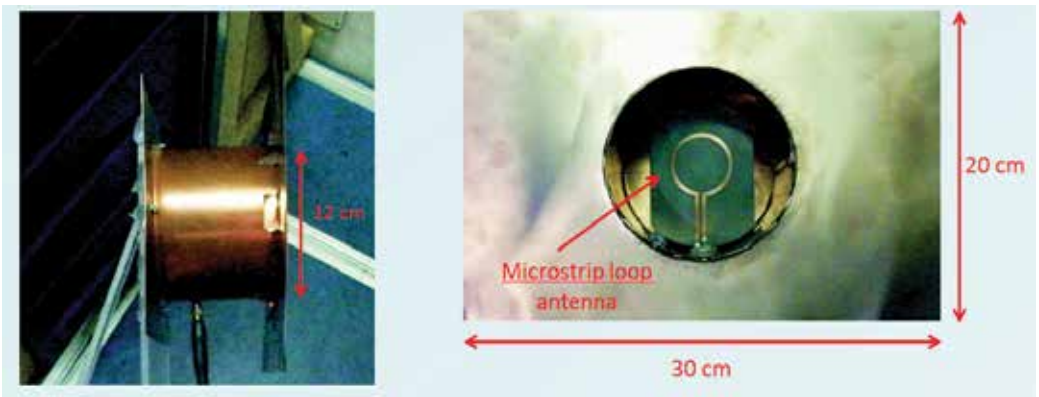

Figure 6. Photograph of realized microwave Bessel beam launcher (taken from [10]): (a) side view and (b) front view.

In order to verify the nondiffracting feature along the propagation range, near-field measurements are performed on various planes placed at different distances from the Bessel beam launcher. All near-field acquisitions are realized on a square grid of 43 × 43 points, with uniform spacing equal to $\frac{\lambda_0}{2}$, to satisfy the Shannon-Nyquist criterion. Near-field tests are executed into the anechoic chamber at the Microwave Laboratory of the University of Calabria, by adopting a standard X-band rectangular waveguide as a measuring probe. Contours profiles reported in **Figure 7**, referring to the acquisition planes at distances equal to 8 and 10 cm, respectively, reveal that Bessel beam produced by the designed microwave launcher properly maintains its shape on a long propagation distance.

3.2. Bessel beam as information carrier in telecommunication systems

The impressive property of unchanged shape over extended propagation distances makes Bessel beams appealing also in communication systems as information carriers. High-order Bessel beams expressed by

$$J_p(k_\rho \rho)e^{jp\phi} \tag{22}$$

have azimuthal index p which gives an additional degree of freedom to create custom fields [14–16] for carrying encoded information, by adopting the expansion:

$$\sum_p a_p(\rho)e^{jp\phi} \tag{23}$$

whose harmonics are independent of spatial scale and orthonormal over the azimuthal plane.

Researchers are currently looking at this interesting application of Bessel beam as a mean of transferring data, with a special focus on the development of efficient techniques to perform modal decomposition, but avoiding false detections due to cross-talk effects between neighboring modes.

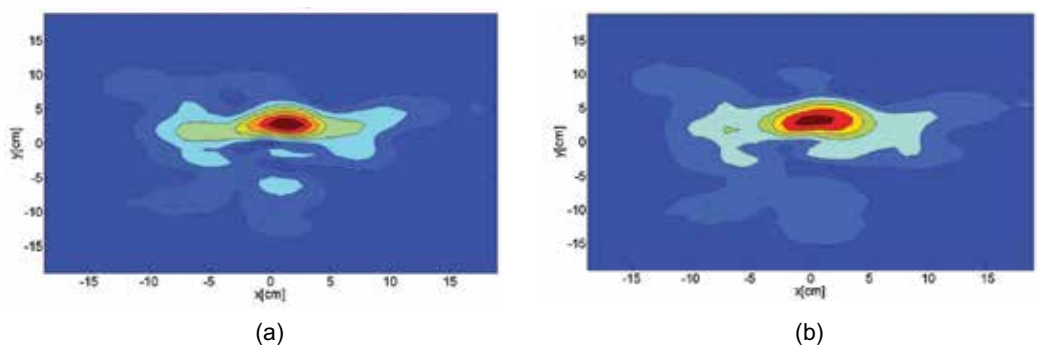

Figure 7. Intensity profile of measured Bessel beam at distances equal to (a) 8 cm and (b) 10 cm (taken from [13]): (a) side view and (b) front view.

3.3. Bessel beam application in free-space optical communication

Free-space optical (FSO) communication is a robust method to transmit information with high capacity, high speed, and security [17]. Gaussian beams are typically adopted to realize the propagation; however, they suffer from limitations caused by diffraction, leading to the spread of the beam's energy, thus lowering the signal-to-noise ratio (SNR) at the receiver and increasing the bit error rate (BER).

In order to investigate the above effects, nondiffracting Bessel beams can be successfully adopted as alternative to Gaussian beams. An efficient FSO communication system should have a transmission beam as small as possible, with high peak intensity and high power. As deeply discussed in [18], these criteria are fully satisfied by Bessel beams. First of all, thanks to relation (15), the aperture radius required for a Bessel beam to transmit the half power is smaller than that required by a Gaussian beam, with a reduction of about 25% [18]. Furthermore, when comparing Bessel and Gaussian beams generated with the same aperture, the peak intensity of Bessel beam results to be about 1.2 times greater than that of the Gaussian beam.

As a validation example, the intensity cross-sections for long range propagation at a distance of 22 km through atmosphere are simulated in **Figure 8** for Bessel beams (left hand) and Gaussian beams (right hand) and three different aperture radii. The presented results are taken from [18], vertical axis giving the radial distance in [m] and horizontal axis representing the propagation distance in [km]. The outperformances of Bessel beams are clearly visible.

The actual challenge to really achieve FSO communication systems with improved power delivery features for long propagation distances still remains the realizations of launchers less complex than standard axicons but able to produce Bessel beams efficiently.

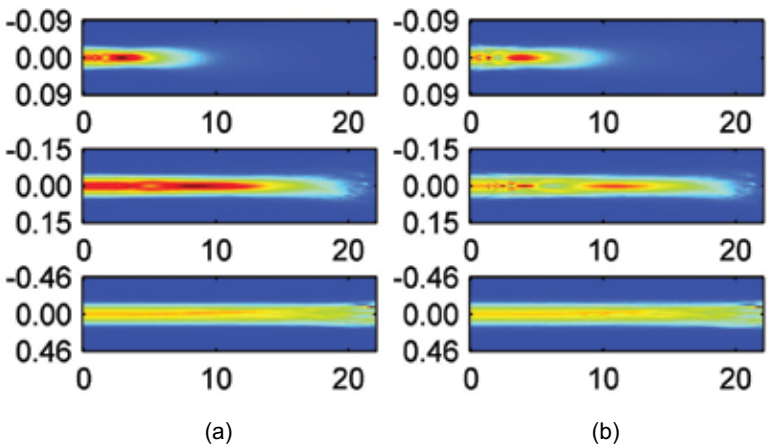

Figure 8. Intensity cross-sections for long-range propagation (taken from [18]): (a) Bessel beams and (b) Gaussian beams.

4. Conclusions

The basic features of nondiffracting Bessel beams have been reviewed in the present chapter, and mathematical discussions have been outlined to derive the relevant properties, such as the spot size, the maximum nondiffracting propagation range, and the delivered power. Assuming a waveguide-based structure as a beam launcher, it has been shown that three degrees of freedom exist to maximize the propagation distance of a Bessel beam without spreading, namely the radius of the aperture from which the beam is generated, the radial wavenumber (in turn depending on the launcher geometry and the dielectric medium properties), and the operating frequency (higher propagation ranges can be achieved when increasing frequency). Finally, potential applications of Bessel beam as an efficient information carrier for long range communication systems have been outlined.

Author details

Sandra Costanzo

Address all correspondence to: costanzo@deis.unical.it

University of Calabria, Italy

References

[1] Born M, Wolf E. Principles of Optics. Cambridge University Press; 1999.

[2] Durnin J, Miceli JJ Jr., Eberly JH. Diffraction-free beams, Physical Review Letters. 1987;**58** (15):1499–1501.

[3] Durnin J. Exact solutions for nondiffracting beams. I. The scalar theory. Journal of Optical Society of America A. 1987;**4(**4):651–654.

[4] Stratton JA. Electromagnetic Theory. McGraw-Hill; 1941.

[5] Lapointe M. Review of non-diffracting Bessel beam experiments. Optics & Laser Technology. 1992;**24**(6):315–321.

[6] Vasara A, Turunen J, Friberg AT. Realization of general nondiffracting beams with computer-generated holograms. Journal of Optical Society of America A. 1989;**6**:1748–1754.

[7] Scott G. Efficient generation of nearly diffraction-free beams using an axicon, Optical Engineering. 1992;**31**:2640–2646.

[8] Jabczynski JK. A diffraction-free resonator. Optics Communications. 1990;**77**:292–294.

[9] McGloin D, Garces-Chavez V, Dholakia K. Interfering Bessel beams for optical micromanipulation. Optics Letters. 2003;**28**:657–659.

[10] Costanzo S, Di Massa G, Borgia A, Raffo A, Versloot T. Ariadna study 'Microwave Drilling. Final Report, ESA Contract No 4000112047, 2015.

[11] Salem M, Kamel A, Niver E. Microwave Bessel beams generation using guided modes. IEEE Transaction on Antennas Propagation. 2011;**59**(6):2241–2247.

[12] Collin RE. Field Theory of Guided Waves. Wiley-IEEE Press; 1991.

[13] Costanzo S, Di Massa G, Borgia A, Raffo A, Versloot T, Summerer L. Microwave Bessel beam launcher for high penetration planetary drilling operations. In: 2016 10th European Conference on Antennas and Propagation, EuCAP 2016, Davos (Switzerland); April 11–15, 2016. doi: 10.1109/EuCAP.2016.7481513

[14] McGloin D, Dholakia K. Bessel beams: diffraction in a new light. Contemporary Physics. 2005;**46**(1):15–28.

[15] Dudley A, Lavery M, Padgett M, Forbes A. Unraveling Bessel beams. Optics and Photonics News, 24–29 June 2013.

[16] Dudley A, et al. Efficient sorting of Bessel beams. Optics Express. 2013;**21**(1):165–171.

[17] Zhu X, Kahn JM. Free-space optical communication through atmospheric turbulence channels. IEEE Transaction on Communication. 2002;**50**(6):1293–1300.

[18] Birch P, Ituen I, Young R, Chatwin C. Long distance Bessel beam propagation through Kolmogorov turbulence. Journal of Optical Society of America A, 2015.

Chapter 2

Transionospheric Microwave Propagation: Higher-Order Effects up to 100 GHz

Mohammed Mainul Hoque, Norbert Jakowski and Jens Berdermann

Additional information is available at the end of the chapter

http://dx.doi.org/10.5772/66659

Abstract

Ionospheric refraction is considered as one of the major accuracy limiting factors in microwave space-based geodetic techniques such as the Global Positioning System (GPS), Satellite Laser Ranging (SLR), very-long-baseline interferometry (VLBI), Doppler Orbitography and Radiopositioning Integrated by Satellite (DORIS), and satellite altimetry. Similarly, a high-performance ground-to-space and space-to-ground microwave link is considered to be very important for synchronizing clocks in global networks. Moreover, precise time and frequency transfer may lead to new applications in navigation, Earth observation, solar system science, and telecommunications. However, all transionospheric microwave signals are subject to ionospheric refraction and subsequent delays in the travel time. Since the ionosphere is a dispersive medium for radio signals, the first-order propagation effect can be removed by combining signals at two or more frequencies. Anyway, higher-order ionospheric effects remain uncorrected in such combinations. The residuals can significantly affect the accuracy of precise positioning, navigation, as well as the performance of time and frequency transfer. Here, we studied ionospheric propagation effects including higher-order terms for microwave signals up to 100 GHz frequencies. The possible combination between the L, S, C, X, Ku, and Ka band frequencies is studied for the first-order ionosphere-free solutions. We estimated the higher-order propagation effects such as the second- and third-order terms and ray-path bending effects in the dual-frequency group delay and phase advance computation. Moreover, the correction formulas originally developed for global navigation satellite systems (GNSS) L-band frequencies are tested for mitigating residual errors at higher frequencies up to 100 GHz.

Keywords: ionospheric group delay, phase advance, ray-path bending, correction model

1. Introduction

The propagation of a radio wave through the ionospheric plasma can be described by the refractive index of the ionosphere given by the Appleton-Hartree formula [1]. At very high frequencies (>100 MHz), the refractive index depends mainly on the electron density and on the strength and the direction of the geomagnetic field in relation to the ray path. It becomes evident that the spatial distribution of the electron density along the ray path and the corresponding geomagnetic field relationships determine the ionospheric impact on the electromagnetic wave.

Since the ionosphere is a dispersive medium, radio wave propagation is frequency dependent. Therefore, by combining two signals, more than 99% of the ionospheric propagation delay can be corrected. However, higher-order propagation effects such as the second- and third-order terms in the refractive index and ray-path bending errors remain uncorrected in dual-frequency ionosphere-free combination. The range (or travel time) computation using trans-ionospheric signal is affected up to several centimeters (or 1.e–9 s) due to higher-order ionospheric terms. Therefore, higher-order effects should not be neglected in precise time and positioning applications, especially during times of enhanced total electron content (TEC).

Early work was done by Brunner and Gu [2] in computing higher-order ionospheric effects and developing correction formulas for them. Since then higher-order ionospheric effects have been studied by different authors during the last two decades, e.g., Bassiri and Hajj [3], Jakowski et al. [4], Strangeways and Ioannides [5], Kedar et al. [6], Fritsche et al. [7], Hawarey et al. [8], Hoque and Jakowski [10–16], Hernandez-Pajares et al. [17], Datta-Barua et al. [18], Morton et al. [19], etc.

Brunner and Gu [2] considered the second-order term and the curvature correction term for the dual-frequency ionospheric correction of the Global Positioning System (GPS) observations. Similarly, Bassiri and Hajj [3] studied the second-order ionospheric term assuming an Earth-centered tilted dipole approximation for the geomagnetic field. Jakowski et al. [4] studied ionosphere induced ray-path bending effects in precise satellite positioning systems such as GPS (20,000 km altitude) and Navy Navigation Satellite System (NNSS) signals (1000 km altitude). Strangeways and Ioannides [5] considered the ratio of the curved path lengths and the geometric path length and the ratio of the TECs along GPS L1 and L2 ray paths for determining the geometric distance of the Earth-GPS path.

Hawarey et al. [8] investigated the second-order ionospheric term for very-long-baseline interferometry (VLBI) and found that further improvements can be achieved using a more realistic magnetic field model such as the International Geomagnetic Reference Field (IGRF) model. Fritsche et al. [7] found that Global Navigation Satellite Systems (GNSS) satellite positions can also be improved to the centimeter level by applying higher-order ionospheric corrections.

Datta-Barua et al. [18] estimated the higher-order ionospheric errors using data from the federal aviation administration's Wide Area Augmentation System (WAAS). They found that during ionospheric storms when slant range delays at GPS L1 can be as high as 100 m, the higher-order group errors in the GPS L1–L2 or L1–L5 dual-frequency combination can be tens

of centimeters. Morton et al. [19] studied the second-order error analysis based on an extensive collection of electron density profiles measured by the Arecibo incoherent scatter radar and geomagnetic field vectors generated using the IGFR model.

Hoque and Jakowski [10–12] derived different approximation formulas to correct the second- and third-order terms, errors due to excess path length in addition to the free space path length, and TEC difference at two GNSS frequencies for L-band signals. Petrie et al. [21] investigated the potential effects of the bending terms on global GPS network.

Recently, Hernandez-Pajares et al. [17, 20] made a comprehensive summary of the second-order effect in receiver position and clock, tropospheric delay, geocenter offset, and GNSS satellite position and clock. They considered all the relevant higher-order contributions such as the second- and third-order terms, geometric bending, and slant total electron content bending (i.e., the difference between the slant total electron content (STEC) for straight and bent paths).

In the present paper, we have investigated the ionospheric propagation effects including higher-order terms for microwave signals up to 100 GHz frequencies. The possible combination between the L, S, C, X, Ku, and Ka (1–2, 2–4, 4–8, 8–12, 12–18, 27–40 GHz, respectively) band frequencies is studied for the first-order ionosphere-free solutions. We estimated the remaining higher-order propagation effects such as the second- and third-order terms and ray-path bending effects in the dual-frequency group delay and phase advance computation.

In our previous work, we developed correction formulas for mitigating the second-order ionospheric term [10, 11], the third-order term, and errors due to ray-path bending [4, 12, 15, 16] in the dual-frequency ionosphere-free linear combination. The correction formulas are developed and validated mainly for precise (e.g., centimeter and millimeter level) GNSS positioning at L-band frequencies. In the present paper, we investigated the performance of these correction formulas for mitigating remaining errors at higher frequencies up to 100 GHz.

2. First-order ionospheric term

The travel time τ of the signal for traveling the geometric distance between the transmitting satellite S and the receiver R can be written in units of seconds as (by dividing the true range expression given in [15] by the speed of light):

$$\tau = \frac{L}{c} + \frac{1}{c}\int_S^R (1-n)ds - t_I^{len} \tag{1}$$

where the optical distance $L = \int_S^R nds$ is the line integral of the refractive index between the transmitting satellite and the receiver along the ray path, c is the velocity of light in a vacuum, $\frac{1}{c}\int_S^R (1-n)ds$ is the ionospheric time delay or advance, and t_I^{len} is the excess time delay due to

ionospheric ray-path bending in which ds is the ray-path element and n is either group or phase refractive index of the ionosphere. The Appleton-Hartree formula of the refractive index and its expansion for phase advance and group delay can be found in [3, 9, 15] and references therein. The ionospheric group delay t_{Igr} and phase advance t_I can be written in units of seconds as (by dividing ionospheric delay expressions given in [15] by the speed of light):

$$t_{Igr} = \frac{1}{c}\int_S^R \left(n_{gr} - 1\right)ds = \frac{p}{cf^2} \mp \frac{q}{cf^3} + \frac{u}{cf^4} \tag{2}$$

$$t_I = \frac{1}{c}\int_S^R (1 - n)ds = \frac{p}{cf^2} \mp \frac{q}{2cf^3} + \frac{u}{3cf^4} \tag{3}$$

where

$$p = 40.3\int n_e ds = 40.3{\cdot}TEC \tag{4}$$

$$q = 2.2566\times 10^{12}\int n_e B cos\Theta ds \tag{5}$$

$$u = 2437\int n_e^2 ds + 4.74\times 10^{22}\int n_e B^2\left(1 + cos^2\Theta\right)ds \tag{6}$$

The upper (−) and lower (+) signs in the expressions (2) and (3) are related to the ordinary and extraordinary waves, respectively. The group refractive index n_{gr} is greater than unity causing travel time greater than the speed of light, whereas the phase refractive index n is less than unity causing travel time less than the speed of light.

The quantity n_e is the electron density, B is magnetic induction, and Θ is the angle between the Earth's magnetic field vector and the propagation vector. The presence of the Earth's magnetic field makes the ionosphere anisotropic that means the refractive index as well as the signal propagation depends on the propagation direction. The integral $\int n_e ds$ along a signal path (i.e., curved path) is defined as the total electron content (TEC) and often measured in TEC units

Frequency [GHz]	Ionospheric delay [s]	Ionospheric delay [m]
2	3.3607e−10	0.1007
8	2.1004e−11	0.0063
15	5.9745e−12	0.0018
30	1.4936e−12	4.4778e−04
60	3.7341e−13	1.1194e−04
100	1.3443e−13	4.0300e−05

Table 1. Estimates of the first-order term at different frequencies for TEC = 1 TECU.

http://dx.doi.org/10.5772/66659

(1 TECU = 10^{16} electrons/m^2). The parameters p, q, and u given by Eqs. (4)–(6) together with signal frequency f determine the first-, second-, and third-order ionospheric refraction effects, respectively.

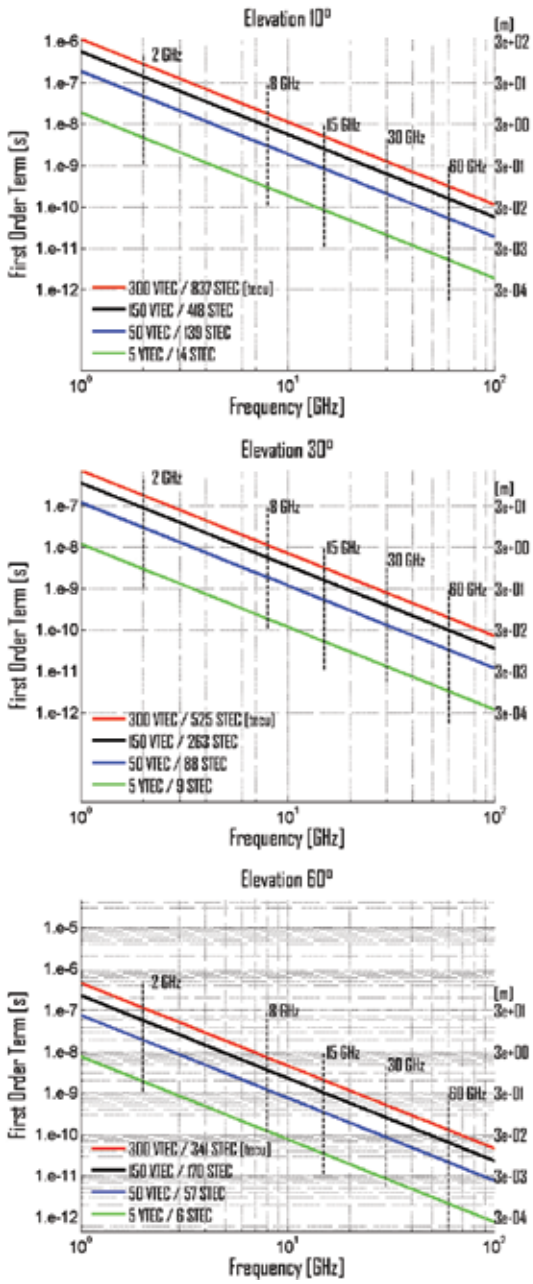

Figure 1. Frequency dependence of the first-order term at different levels of ionospheric ionization and elevation angles. Left and right scales correspond to the units of seconds and meters, respectively.

The first-order ionospheric effect (group delay or phase advance) contributes above 99% of the total ionospheric effect and can be written as

$$t_{Igr}^{(1)} = -t_I^{(1)} = \frac{40.3}{cf^2}\int n_e ds = \frac{40.3}{cf^2} TEC \tag{7}$$

in units of seconds where c is in m/s, TEC is in electrons/m^2, and f is in Hz. Eq. (7) indicates that the travel time caused by the first-order term is equal in magnitude but opposite in sign for group delay and phase advance.

The first-order term is directly proportional to the total number of electrons TEC, encountered by the signal during its travel through the ionosphere and inversely proportional to the square of the signal frequency. So, if frequency and link-related TEC are known, the first-order propagation effect can be derived by Eq. (7). The first-order ionospheric delay on different frequencies is determined for 1 TECU and given in **Table 1**.

The vertical TEC may vary between 1 TECU and 300 TECU depending on a number of factors such as local time, geographic/geomagnetic location, season, solar activity level, etc. The frequency dependence of the first-order ionospheric term up to 100 GHz frequency at different levels of ionospheric ionization characterized by the vertical total electron content (VTEC) = 300, 150, 50, and 5 TECU is plotted for elevations 10°, 30°, and 60° in **Figure 1**. The vertical total electron content of 300 and 150 TECU corresponds to VTEC during extreme space weather conditions, 50 TECU corresponds to midlatitude day time, and 5 TECU corresponds to mid-latitude night time VTEC. The following obliquity factor or mapping function is used to convert the vertical TEC to slant TEC [15]:

	VTEC [TECU]	
	300	**5**
	First term	
Frequency [GHz]	**[s]**	**[s]**
2	2.81e–07	4.69e–09
8	1.76e–08	2.93e–10
15	6.00e–09	8.33e–11
30	1.25e–09	2.08e–11
60	3.13e–10	5.21e–12
100	1.13e–10	1.88e–12

Table 2. Estimates of the first-order term at different frequencies for VTEC = 300 and 5 TEC units and elevation = 10°.

$$MF = \frac{STEC}{VTEC} = \frac{h_m + R_E}{\sqrt{(h_m + R_E)^2 - (R_h + R_E)^2 \cos^2\beta}} \tag{8}$$

where h_m is the maximum ionization height (e.g. 350 km), R_E is the Earth's mean radius (~6371 km), R_h (~0) is the receiver height from the Earth's surface, and β is the elevation angle.

Table 2 gives estimates of the first-order term at 2, 8, 15, 30, 60, and 100 GHz frequencies for 10° elevation angle and VTEC = 300 and 5 TEC units.

As **Figure 1** and **Table 2** demonstrate, the first-order ionospheric delay can reach up to the 1.e −09 and 1.e−10 s levels at 30 and 60 GHz frequencies, respectively.

3. Higher-order terms

Although higher-order effects are less than 1% of the total ionospheric effects, they cannot be ignored in precise time and position applications. In precise applications dual-frequency measurements are commonly used to eliminate the major part (first-order effect) of the ionospheric propagation effects. The remaining higher-order terms can be up to 30 cm at L-band frequencies (15, 18). However, they will be much less at C, X, Ku, and K band frequencies. When analyzing ionospheric effects on signal propagation, it is a common practice to consider the code pseudo-range and carrier-phase observation equations for group delay and phase advance computation. Considering extraordinary wave of propagation, the code pseudo-range and carrier-phase expressions can be written in terms of ionospheric effects as (by dividing pseudo-range and carrier-phase expressions given in [12] by the speed of light):

$$\Psi = \tau + t_{Igr} + t_I^{len} = \tau + \frac{p}{cf^2} + \frac{q}{cf^3} + \frac{u}{cf^4} + t_I^{len} \tag{9}$$

$$\Phi = \tau - t_I + t_I^{len} = \tau - \frac{p}{cf^2} - \frac{q}{2cf^3} - \frac{u}{cf^4} + t_I^{len} \tag{10}$$

where τ is the travel time in vacuum. Although the measured travel times Ψ and Φ are biased by satellite and receiver clock errors, instrumental biases and tropospheric effect, and multipath effects, we have ignored them for simplicity in Eqs. (9) and (10). Due to the dispersive nature of the ionosphere, the propagation effect is frequency dependent, and we can eliminate the first-order term by combining signals at two different frequencies (f_1, f_2). The remaining terms can be written in units of seconds as (e.g., [12])

$$\frac{f_1^2}{f_1^2 - f_2^2}\Psi_1 - \frac{f_2^2}{f_1^2 - f_2^2}\Psi_2 = \tau - \Delta t_{TEC} - \Delta t_2 - \Delta t_3 - \Delta t_{len} \tag{11}$$

$$\frac{f_1^2}{f_1^2 - f_2^2}\Phi_1 - \frac{f_2^2}{f_1^2 - f_2^2}\Phi_2 = \tau + \Delta t_{TEC} + \frac{\Delta t_2}{2} + \frac{\Delta t_3}{3} - \Delta t_{len} \tag{12}$$

$$\Delta t_{TEC} = \frac{40.3\times(TEC_2 - TEC_1)}{c\left(f_1^2 - f_2^2\right)} = \frac{40.3\times(\Delta TEC_{bend2} - \Delta TEC_{bend1})}{c\left(f_1^2 - f_2^2\right)} \tag{13}$$

$$TEC_{1,2} = \int n_e ds = (TEC_{LoS} + \Delta TEC_{band1,2}) \tag{14}$$

$$\Delta t_2 = \frac{2.2566\times10^{12}\int n_e B cos\Theta ds}{cf_1f_2\left(f_1 + f_2\right)} \tag{15}$$

$$\Delta t_3 = \frac{2437}{cf_1^2f_2^2}\int n_e^2 ds + \frac{4.74\times10^{22}}{cf_1^2f_2^2}\int n_e B^2\left(1 + cos^2\Theta\right)ds \tag{16}$$

$$\Delta t_{len} = \frac{t_2^{len}f_2^2 - t_1^{len}f_1^2}{c\left(f_1^2 - f_2^2\right)} \tag{17}$$

where Ψ_1 and Ψ_2 are the measured pseudoranges and Φ_1 and Φ_1 are the measured carrier phases on f_1 and f_2. The terms Δt_2 and Δt_3 are the dual-frequency second- and third-order ionospheric terms. Due to the dispersive nature of the ionosphere, the bending effects as well as the total electron content (TEC) along the f_1 path will be different from that along the f_2 path. Considering this, the additional terms Δt_{len} and Δt_{TEC} are introduced in Eqs. (11) and (12) referring the dual-frequency residual errors due to the excess path and TEC difference, respectively. The quantities ΔTEC_{bend1} and ΔTEC_{bend2} are the excess TEC due to bending in addition to the straight line of sight (LoS) TEC, and t_1^{len} and t_2^{len} are the excess path length in addition to the LoS path length for f_1 and f_2 signals, respectively.

In the following sub sections, we estimated various dual-frequency residual terms for signal combination at different frequency bands considering different levels of ionospheric ionization.

3.1. Dual-frequency second-order term

The imposed Earth's magnetic field causes an electron in the plasma to oscillate around the magnetic field line with the gyrofrequency fg = eB/(2πm) which is usually less than 1.4 MHz [22]. The value of B can be derived as ~5 × 10^{-5} Tesla for fg = 1.4 MHz and considered constant throughout the propagation. Therefore, assuming the worst case condition with B = 5 × 10^{-5} Tesla and Θ = 0, the maximum estimates of the dual-frequency second-order term (Eq. (15)) for group delay can be written as

$$\Delta t_2 = \frac{11.28\times10^7}{cf_1f_2\left(f_1 + f_2\right)}\int n_e ds = \frac{11.28\times10^7}{cf_1f_2\left(f_1 + f_2\right)}TEC \tag{18}$$

The elevation angle dependence of the Δt_2 at pair of frequencies (2, 15), (8, 30), and (8, 60) GHz for VTEC = 300 and 5 TECU is plotted in **Figure 2**.

http://dx.doi.org/10.5772/66659

Table 3 gives the maximum estimates of the second-order residual term at pair of frequencies (2, 15), (8, 30), and (8, 60) GHz for VTEC = 300 and 5 TECU and elevation = 10°, 30°, and 60°.

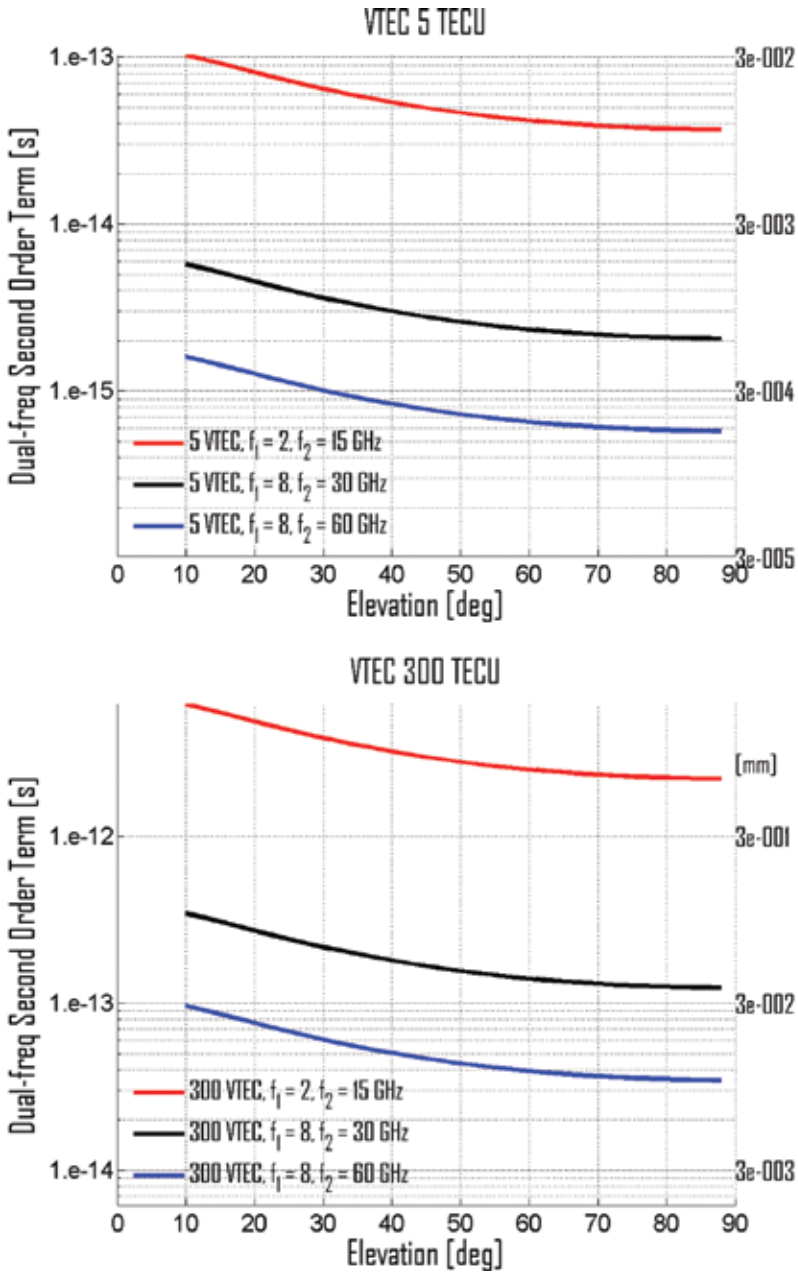

Figure 2. Elevation angle dependence of the Δt_2 at pair of frequencies (2, 15), (8, 30), and (8, 60) GHz for VTEC = 300 and 5 TECU. Left and right scales correspond to the units of seconds and millimeters, respectively.

	300 TECU			5 TECU		
	Elevation [deg]			Elevation [deg]		
Freq-comb. (code) [GHz]	10	30	60	10	30	60
2–15	6.17e–12	3.88e–12	2.51e–12	1.03e–13	6.46e–14	4.19e–14
8–30	3.45e–13	2.17e–13	1.41e–13	5.75e–15	3.61e–15	2.34e–15
8–60	9.65e–14	6.06e–14	3.93e–14	1.61e–15	1.01e–15	6.55e–16

Table 3. Maximum estimates of the second-order residual term in the dual-frequency group delay computation.

Figure 2 and **Table 3** show that the dual-frequency second-order residual term is bigger than the 1.e–14 and 1.e–15 s levels for frequency combinations (2–15) and (8–30) GHz, respectively, even at VTEC = 5 TECU. Therefore, the second-order residual term cannot be ignored if 1.e–16/ 1.e–17 s level accuracy is required in the time transfer.

3.2. Dual-frequency third-order term

Eq. (16) indicates that the third-order residual term is proportional to the square of the electron density as well as geomagnetic induction B and angle between the geomagnetic field vector and propagation direction. The dependency on n_e^2 can be simplified assuming that the ionosphere is composed of Chapman layer function [23]. In this case, the so-called shape parameter $\eta = \frac{\int n_e^2 ds}{N_m \times TEC}$ where Nm is the maximum ionization can be assumed to be 0.66 [2, 24], and thus the integral $\int n_e^2 ds$ in Eq. (16) can be written as 0.66NmTEC. Therefore, assuming the worst case condition with B = 5 × 10^{-5} Tesla and Θ = 0, Eq. (16) can be simplified as

$$\Delta t_3 = \frac{1608.4}{c f_1^2 f_2^2} N_m TEC + \frac{23.7 \times 10^{13}}{c f_1^2 f_2^2} TEC = \left(1608.4 N_m + 23.7 \times 10^{13}\right) \frac{TEC}{c f_1^2 f_2^2} \tag{19}$$

where Δt_3 is measured in seconds, c is in meters, TEC is in electrons/ m^2, f in Hz, and the maximum ionization Nm is measured in electrons/m^3. The maximum ionization Nm can be estimated for a Chapman profile using the expression given by [12]

$$VTEC = 4.13 H N_m \tag{20}$$

where VTEC is the TEC in vertical direction and H is the atmospheric scale height. The VTEC will be measured in electrons/m^2 when H is in meters and Nm is in electrons/m^3. The scale height H can be assumed as 70 km for a rough estimation of the third-order ionospheric term. The elevation angle dependence of the Δt_3 at pair of frequencies (2, 15), (8, 30), and (8, 60) GHz for VTEC = 300 and 5 TECU is plotted in **Figure 3**.

Table 4 gives the maximum estimates of the third-order residual term at pair of frequencies (2, 15), (8, 30), and (8, 60) GHz for VTEC = 300 and 5 TECU and elevation = 10°, 30°, and 60°.

http://dx.doi.org/10.5772/66659

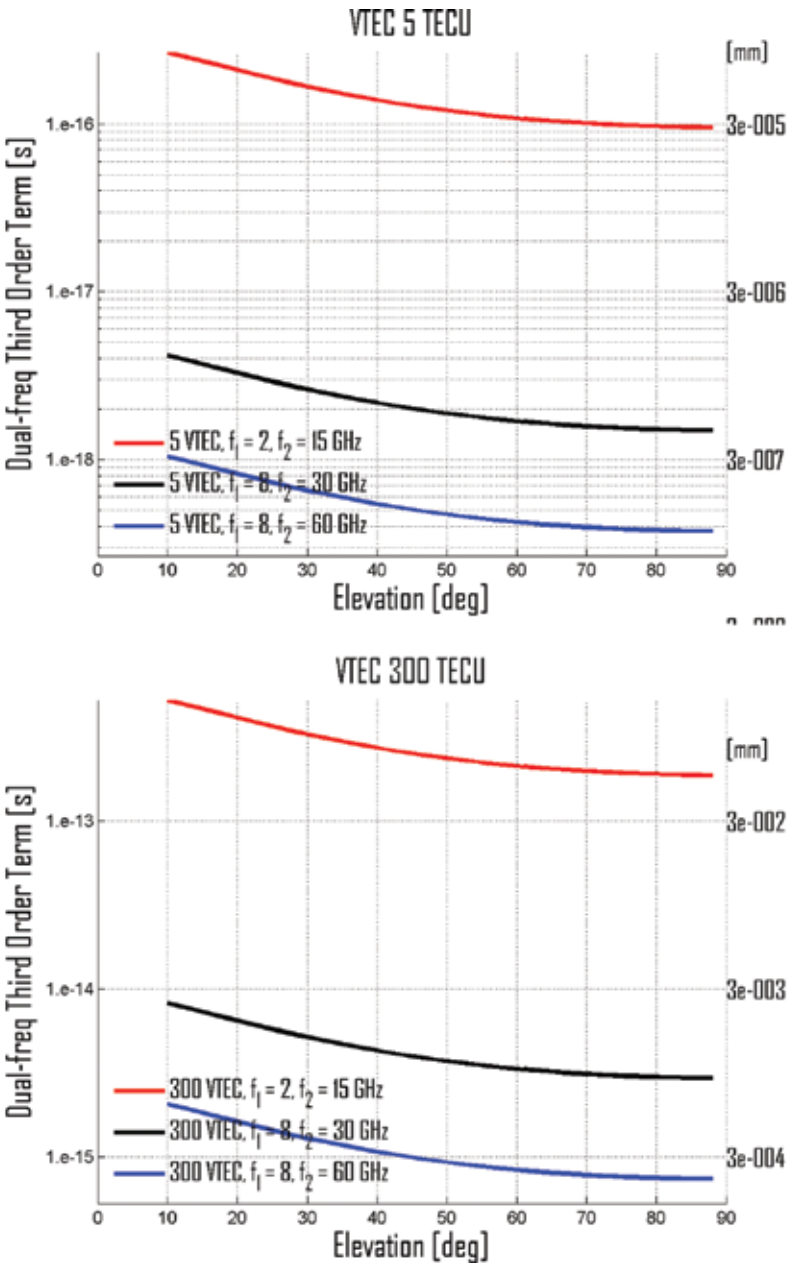

Figure 3. Elevation angle dependence of the Δt_3 at pair of frequencies (2, 15), (8, 30), and (8, 60) GHz for VTEC = 300 and 5 TECU. Left and right scales correspond to the units of seconds and millimeters, respectively.

Figure 3 and **Table 4** show that the dual-frequency third-order residual term can be bigger than the 1.e–13 and 1.e–15 s levels for frequency combinations (2–15) and (8–30) GHz, respectively, during times of high TEC such as VTEC = 300 TECU.

	300 TECU			5 TECU		
	Elevation [deg]			Elevation [deg]		
Freq-comb. (code) [GHz]	**10**	**30**	**60**	**10**	**30**	**60**
2–15	5.25e–13	3.30e–13	2.14e–13	2.66e–16	1.67e–16	1.08e–16
8–30	8.20e–15	5.15e–15	3.34e–15	4.16e–18	2.61e–18	1.69e–18
8–60	2.05e–15	1.29e–15	8.35e–16	1.04e–18	6.53e–19	4.24e–19

Table 4. Estimates of the third-order residual term in the dual-frequency group delay in units of seconds.

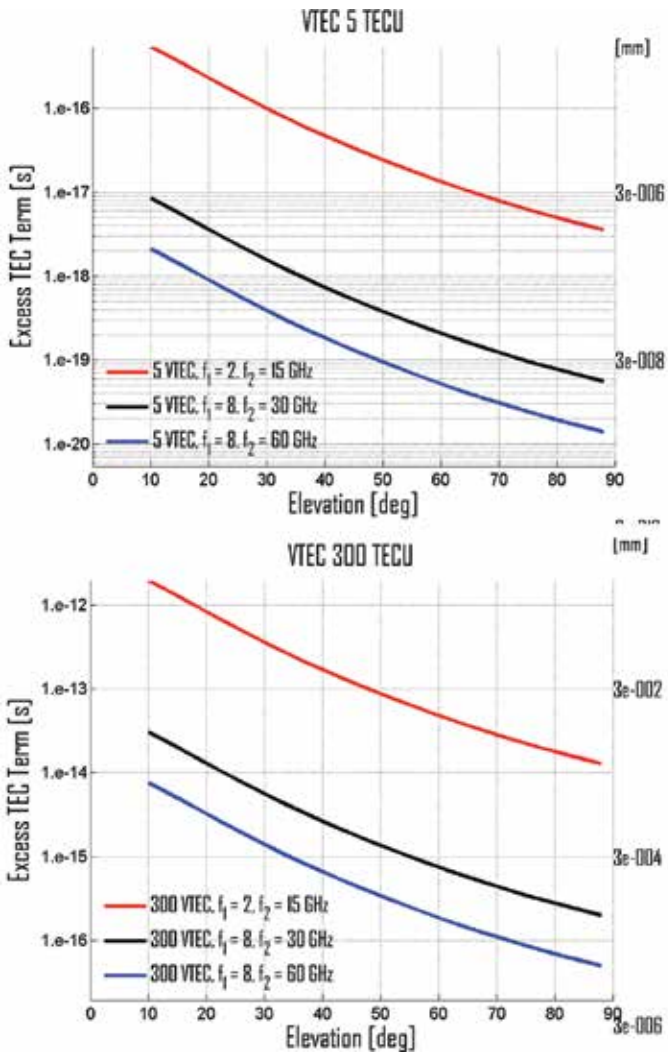

Figure 4. Elevation angle dependence of the Δt_{TEC} at pair of frequencies (2, 15), (8, 30), and (8, 60) GHz for VTEC = 300 and 5 TECU. Left and right scales correspond to the units of seconds and millimeters, respectively.

3.3. Dual-frequency excess TEC term

Due to ray-path bending or curvature effect, the estimate of electron density integrated over a curved path is slightly greater that that along the straight line of sight propagation (TEC_{LoS}). The excess TEC along a curved path in addition to the TEC_{LoS} can be written as [12]

$$\Delta TEC_{bend} = \frac{1.108\times10^{-3}\, exp\left(-2.1844\beta\right) TEC^2}{f^2 H h_m^{0.3}} \tag{21}$$

where ΔTEC_{bend} is measured in TECU, atmospheric scale height H is in km, the maximum ionization height h_m is in km, the signal frequency f is in GHz, TEC is in TECU, and elevation angle β is in radians. Typical values for the parameters H = 70 km and h_m = 350 km are used in the present studies. Thus, knowing ΔTEC_{bend} at two frequencies, we can calculate Δt_{TEC} by Eq. (21). The elevation angle dependence of the Δt_{TEC} at pair of frequencies (2, 15), (8, 30), and (8, 60) GHz for VTEC = 300, and 5 TECU is plotted in **Figure 4**.

Table 5 gives the maximum estimates of the residual excess TEC term at pair of frequencies (2, 15), (8, 30), and (8, 60) GHz for VTEC = 300 and 5 TECU and elevation = 10°, 30°, and 60°.

Figure 4 and **Table 5** show that the dual-frequency residual excess TEC term can be bigger than the 1.e−12 and 1.e−14 s levels for frequency combinations (2–15) and (8–30) GHz, respectively, at 10° elevation angle during times of high TEC such as VTEC = 300 TECU.

Eq. (21) requires the knowledge of the ionospheric parameters H and hmF2. If actual parameters are not known, the formula may not be used in practical cases. Considering this, Hoque and Jakowski [16] derived the following correction approach considering excess TEC dependency only on TEC and elevation angle.

$$\Delta TEC_{bend} = \frac{d_1}{f^2}\left(\frac{1}{\sqrt{1-d_2\cos^2\beta}}-1\right) TEC^2 \tag{22}$$

where d_1 = 1.4563 and d_2 = 0.8260. The coefficients are derived based on a nonlinear fit with ray-tracing results in least square senses. Although the correction given by the original approach Eq. (21) gives the best performance in comparison with the ray-tracing results, the correction results given by the new approach Eq. (22) is comparable.

	300 TECU			**5 TECU**		
	Elevation [deg]			**Elevation [deg]**		
Freq-comb.(code) [GHz]	**10**	**30**	**60**	**10**	**30**	**60**
2–15	1.95e−12	3.59e−13	4.81e−14	5.42e−16	9.96e−17	1.34e−17
8–30	3.05e−14	5.60e−15	7.51e−16	8.47e−18	1.56e−18	2.09e−19
8–60	7.62e−15	1.40e−15	1.88e−16	2.12e−18	3.89e−19	5.22e−20

Table 5. Estimates of the residual excess TEC term in the dual-frequency code combinations in units of seconds.

3.4. Dual-frequency excess path term

Again the estimate of the total path length along a curved path is slightly larger than the LoS path length, and their difference is defined as the excess path length and denoted by t_I^{len} in

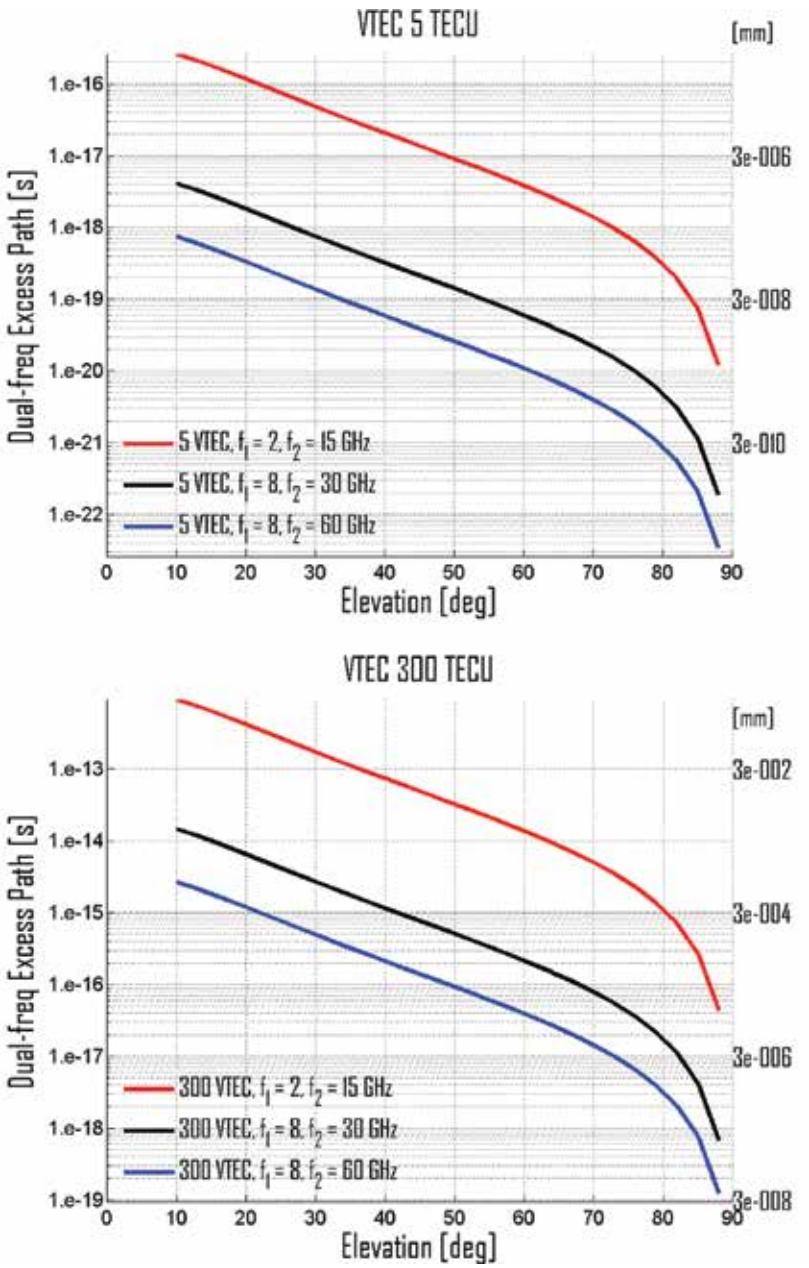

Figure 5. Elevation angle dependence of the Δt_{len} at pair of frequencies (2, 15), (8, 30), and (8, 60) GHz for VTEC = 300 and 5 TECU. Left and right scales correspond to the units of seconds and millimeters, respectively.

Eq. (17). To estimate the excess path length, we follow the estimates based on numerical ray-tracing computations given by [4]

$$t_I^{len} = \frac{b_1}{cf^4}\left(\frac{1}{\sqrt{(1 - b_2 \cos^2\beta)}} - 1\right) TEC^2 \tag{23}$$

where $b_1 = 2.495 \times 10^8$, $b_2 = 0.859$, and β is the elevation angle. The excess path length will be estimated in milliseconds when β is measured in radians, f is in MHz, TEC is in TECU, and c is in m/s. Now the dual-frequency residual excess path term Δt_{len} can be calculated by Eq. (17) in conjunction with Eq. (23). The elevation angle dependence of the Δt_{len} at pair of frequencies (2, 15), (8, 30), and (8, 60) GHz for VTEC = 300 and 5 TECU is plotted in **Figure 5**.

Figure 5 and **Table 6** show that the dual-frequency residual excess path term can be bigger than the 1.e−13 and 1.e−14 s levels for frequency combinations (2–15) and (8–30) GHz, respectively, at 10° elevation angle during times of high TEC such as VTEC = 300 TECU.

	300 TECU			**5 TECU**		
	Elevation [deg]			**Elevation [deg]**		
Freq-comb. (code) [GHz]	**10**	**30**	**60**	**10**	**30**	**60**
2–15	9.38e−13	1.73e−13	1.34e−14	2.61e−16	4.80e−17	3.83e−18
8–30	1.47e−14	2.70e−15	2.16e−16	4.07e−18	7.50e−19	5.99e−20
8–60	2.67e−15	4.92e−16	3.93e−17	7.42e−19	1.37e−19	1.09e−20

Table 6. Estimates of the residual excess path term in the dual-frequency group delay computation in units of seconds.

Table 6 gives the estimates of the residual excess path term at pair of frequencies (2, 15), (8, 30), and (8, 60) GHz for VTEC = 300 and 5 TECU and elevation = 10°, 30°, and 60°.

The estimation of excess path length can be improved if additional ionospheric parameters such as scale height H and peak density heights hmF2 are known. Such a formula is derived by [12].

$$d_I^{len} = \frac{7.5 \times 10^{-5}\, exp\left(-2.13\beta\right) TEC^2}{f^4 H (hmF_2)^{1/8}} \tag{24}$$

where the excess path is measured in meters, TEC in TEC units, frequency f in GHz, atmospheric scale height H and height of maximum ionization hmF_2 in kilometers, and elevation angle β in radians.

3.5. Total dual-frequency residuals in group delay and phase advance

In the previous sections, we estimated different dual-frequency-residual terms separately. It is worthy to estimate their combined effects on group delay and phase advance computation.

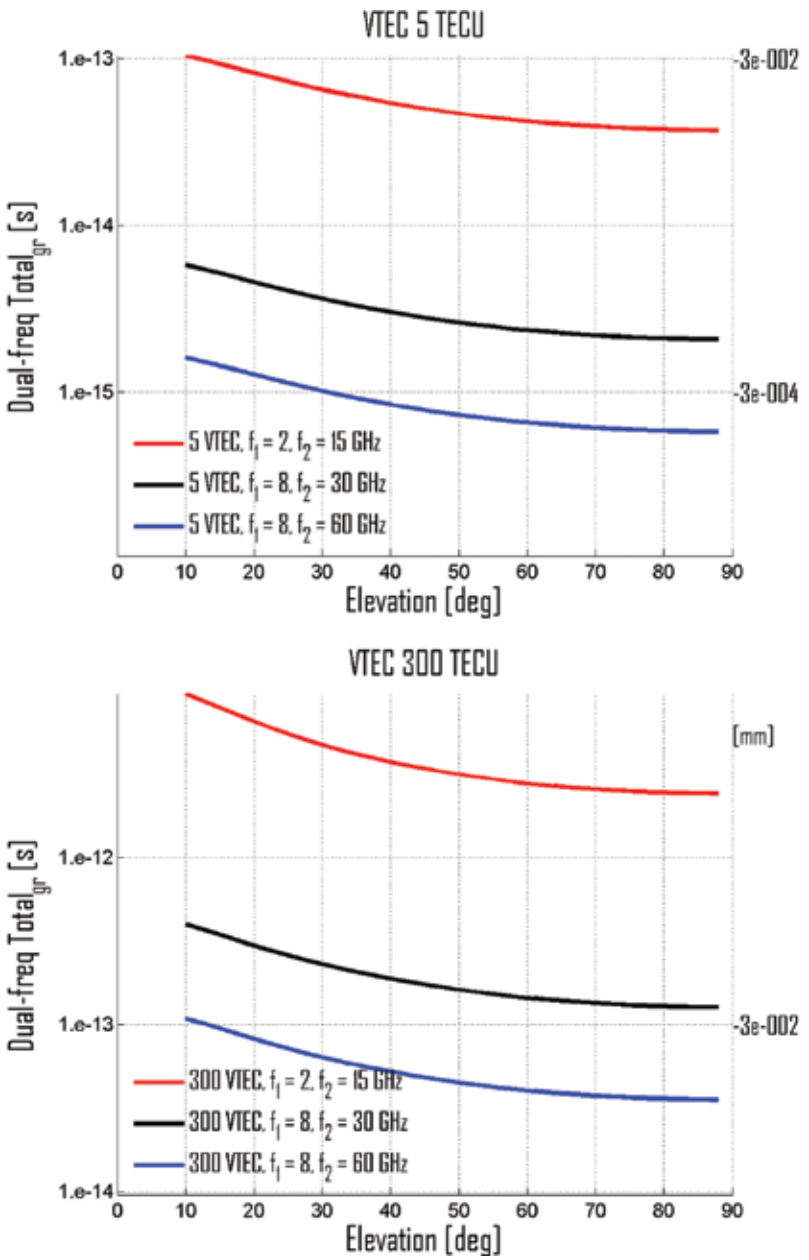

Figure 6. Elevation angle dependence of the total residuals (absolute values) in group delay computation at pair of frequencies (2, 15), (8, 30), and (8, 60) GHz for VTEC = 300 and 5 TECU. Left and right scales correspond to the units of seconds and millimeters, respectively.

http://dx.doi.org/10.5772/66659

	300 TECU			5 TECU		
	Elevation [deg]			Elevation [deg]		
Freq-comb.(code) [GHz]	**10**	**30**	**60**	**10**	**30**	**60**
2–15	−9.59e−12	−4.74e−12	−2.79e−12	−1.04e−13	−6.49e−14	−4.20e−14
8–30	−3.99e−13	−2.30e−13	−1.45e−13	−5.77e−15	−3.62e−15	−2.35e−15
8–60	−1.09e−13	−6.37e−14	−4.03e−14	−1.61e−15	−1.01e−15	−6.55e−16

Table 7. Estimates of the total residual error in the dual-frequency group delay in units of seconds.

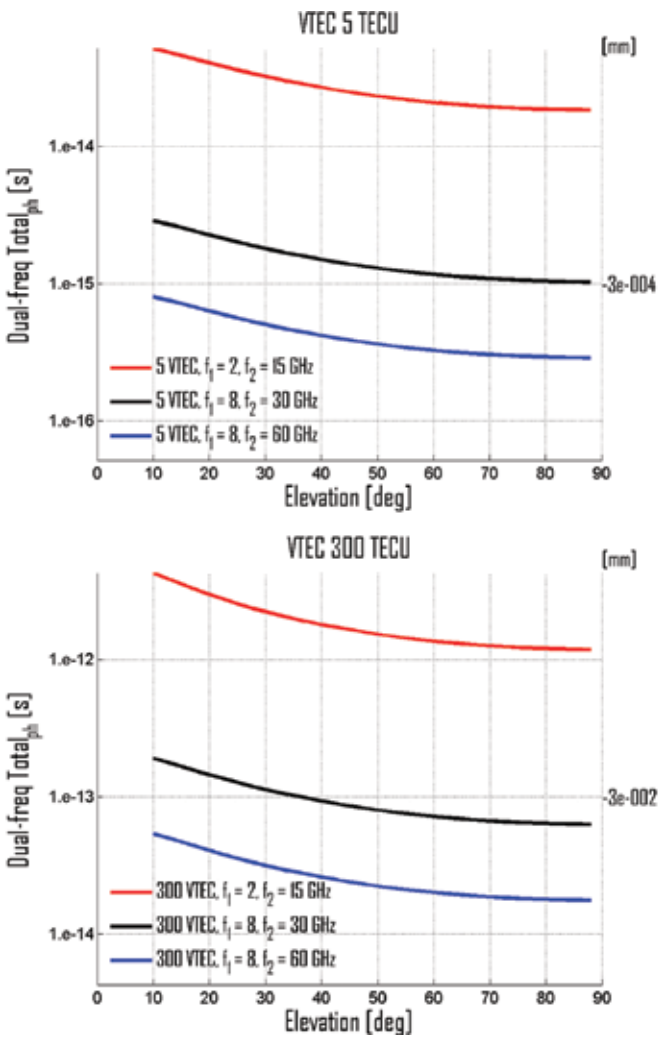

Figure 7. Elevation angle dependence of the total residuals in phase advance measurements at pair of frequencies (2, 15), (8, 30), and (8, 60) GHz for VTEC = 300 and 5 TECU. Left and right scales correspond to the units of seconds and millimeters, respectively.

	300 TECU			5 TECU		
	Elevation [deg]			Elevation [deg]		
Freq-comb. (code) [GHz]	10	30	60	10	30	60
2–15	4.27e−12	2.23e−12	1.36e−12	5.18e−14	3.24e−14	2.10e−14
8–30	1.91e−13	1.13e−13	7.19e−14	2.88e−15	1.81e−15	1.17e−15
8–60	5.39e−14	3.16e−14	2.01e−14	8.06e−16	5.05e−16	3.28e−16

Table 8. Estimates of the total residual term in the dual-frequency phase advance in units of seconds.

The elevation angle dependence in group delay ($\Delta t_{TEC} + \Delta t_2 + \Delta t_3 + \Delta t_{len}$, see Eq. 11) at pair of frequencies (2, 15), (8, 30), and (8, 60) GHz for VTEC = 300 and 5 TECU is plotted in **Figure 6**.

Table 7 gives the maximum estimates of the total dual-frequency residuals in the group delay at pair of frequencies (2, 15), (8, 30), and (8, 60) GHz for VTEC = 300 and 5 TECU and elevation = 10°, 30°, and 60°.

Similarly the elevation angle dependence of the total dual-frequency residuals in the phase advance ($\Delta t_{TEC} + \Delta t_2/2 + \Delta t_3/3 - \Delta t_{len}$, see Eq. (12)) at pair of frequencies (2, 15), (8, 30), and (8, 60) GHz for VTEC = 300 and 5 TECU is plotted in **Figure 7**.

Table 8 gives the maximum estimates of the total dual-frequency residuals in the phase advance at pair of frequencies (2, 15), (8, 30), and (8, 60) GHz for VTEC = 300 and 5 TECU and elevation = 10°, 30°, and 60°.

Figures 6 and **7** and **Tables 7** and **8** show that the residual error in the dual-frequency group delay and phase advance cannot be ignored if 1.e−16/1.e−17 s level accuracy is required in the time transfer.

4. Higher-order term correction

In the following sections, we have discussed the possibility of higher-order propagation effects correction at very high frequencies.

4.1. Possibilities of second-order term correction

For the second-order term correction, the following correction formula is proposed by [11] for the global navigation satellite systems (GNSS) users in Europe with geographic latitude 30–65° N and longitude 15° W–45° E. Although the formula gives the best performance for the L-band signals, the second-order term correction at S (2–4 GHz), C (4–8 GHz), X (8–12 GHz), Ku (12–18 GHz), K (18–27 GHz), and Ka (27–40 GHz) band signals is also possible by this formula.

Single frequency (deduced from Eqs. 2 and 5):

http://dx.doi.org/10.5772/66659

$$t_{lgr}^{(2)}q = \frac{2.2566\times10^{12}}{cf^3}\int n_e B\cos\Theta ds = \frac{2.2566\times10^{12}}{cf^3}\overline{B\cos\Theta}\times TEC \tag{25}$$

Dual frequency (deduced from Eq. 15):

$$\Delta t_2 = \frac{2.2566\times10^{12}\times\overline{B\cos\Theta}\times TEC}{cf_1f_2(f_1+f_2)} \tag{26}$$

In which

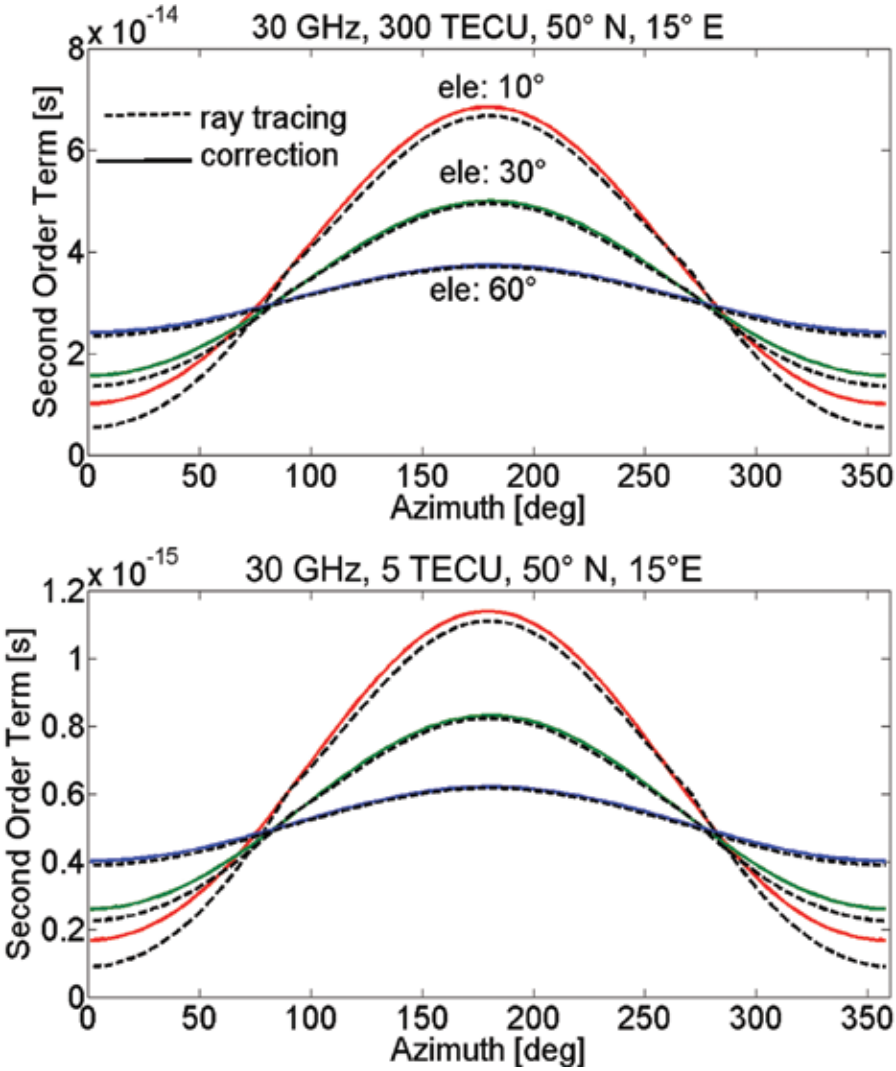

Figure 8. Estimates of second-order term by ray-tracing simulation and correction formula at 30 GHz for VTEC = 300 and 5 TECU (top and bottom plots, respectively) at elevation = 10°, 30°, and 60°.

$$\overline{BcosΘ} = -y_1 cos\alpha + \left|\sqrt{r_1^2 - y_1^2 sin^2\alpha}\right| - 2r_2 \cos \acute{\alpha} \tag{27}$$

where $\overline{BcosΘ}$ is the average value of the longitudinal component of the Earth's magnetic field along the ray path. The parameters r_1, r_2, and y_1 are the functions of the receiver-to-satellite elevation angle β, geographic latitude φ, and longitude λ at the receiver position. The quantity α is the receiver-to-satellite azimuth angle and α' is the modified azimuth angle. For details of formulation, we refer to [11].

To check the performance of the correction formula at very high frequency, e.g., 30 GHz, we estimated the second-order term by a 2D ray-tracing tool [12] and also by the correction formula Eqs. (25) and (27). The effect of the Earth's magnetic field on the radio wave propagation is taken into account by considering the international geomagnetic field (IGRF) model in the ray-tracing tool. **Figure 8** gives their comparisons.

We found that during times of high TEC such as VTEC = 300 TECU, the differences between the ray-tracing and correction results are in the level of 1.e−15 s.

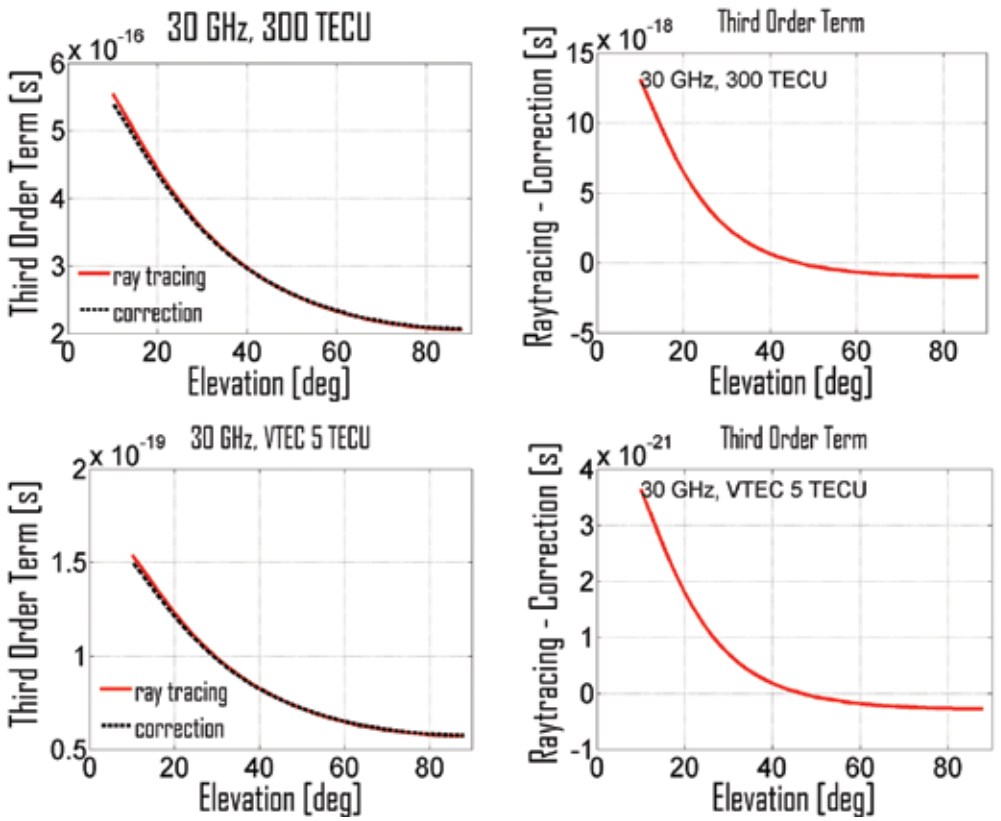

Figure 9. Estimates of the third-order term by ray-tracing simulation and correction formula at 30 GHz for VTEC = 300 and 5 TECU as a function of the elevation.

4.2. Possibilities of third-order term correction

To correct the third-order ionospheric term, we proposed a correction formula based on analytical integration of the Chapman layer [12].

Single frequency (deduced from Eqs. 2 and 6):

$$t_{Igr}^{(3)} = \frac{2487}{cf^4}\int n_e^2 ds = \frac{1608}{cf^4} N_m TEC \tag{28}$$

Dual frequency (deduced from Eqs. 15 and 36):

$$\Delta t_3 = \frac{1608}{cf_1^2 f_2^2} N_m TEC \tag{29}$$

The third-order term Δt_3 will be measured in meters when f is measured in Hertz and the maximum ionization N_m and TEC in electrons/m^3 and electrons/m^2, respectively.

The above correction formula was validated for the GNSS L-band signals in former studies. Therefore, to check the performance of the correction formula at very high frequency, e.g., 30 GHz, we have estimated the third-order term by a 2D ray-tracing tool [12] and also by the correction formula Eq. (28). **Figure 9** gives their comparisons.

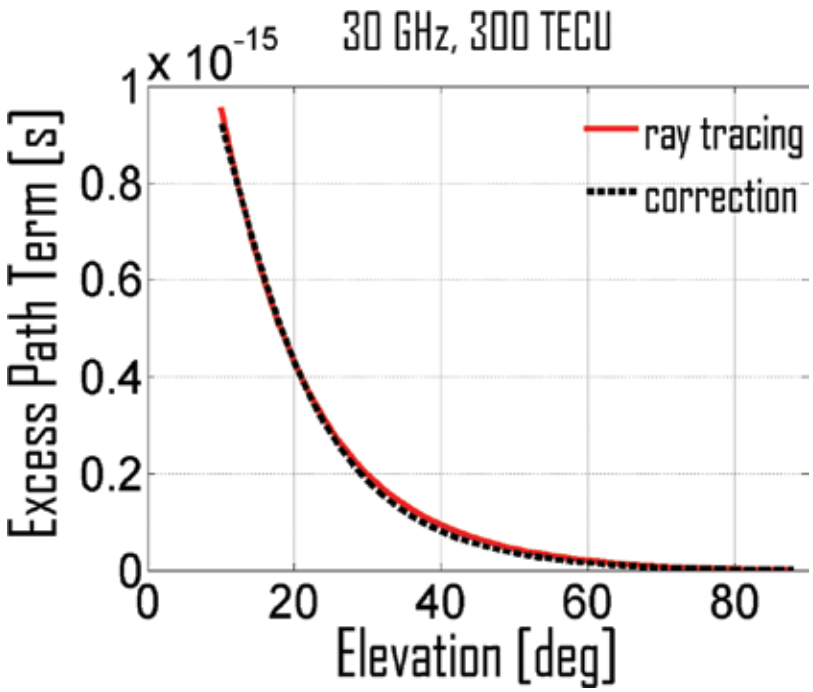

Figure 10. Estimates of the excess path term by ray-tracing simulation and correction formula at 30 GHz for VTEC = 300 TECU as a function of the elevation.

We see that during times of high TEC such as VTEC = 300 TECU, the differences between the ray-tracing and correction results are in the level of 1.e−18 s.

4.3. Possibilities of excess path term correction

To correct the excess path length, Jakowski et al. [4] proposed a correction formula based on simulation studies of the Chapman layers. The formula is already given by Eq. (23) for single frequency applications.

The correction formula was mainly derived for the GNSS L-band signals. Therefore, to check the performance of the correction formula at very high frequency, e.g., 30 GHz, we estimated the excess path length by the 2D ray-tracing tool [12] and also by the correction formula Eq. (23). **Figure 10** gives their comparisons.

We found that during times of high TEC such as VTEC = 300 TECU, the differences between the ray-tracing and correction results are in the level of 1.e−17 s.

5. Conclusions

From our simulation studies, we have found that the time delay due to the first-order ionospheric term is in the range of 1.e−9–5.e−12 s depending on the ionospheric ionization and elevation angles at 30–60 GHz frequencies. The corresponding second- and third-order terms are in the ranges of 1.e−13–2.e−16 s and, respectively. The corresponding excess path length error due to bending is in the range of 1.e−15–2.e−20 s.

We found that for the second-order ionospheric term, the differences between the ray-tracing and correction results are in the order of 1.e−15 s for a microwave link at 30 GHz when assuming high vertical total electron content (VTEC) such as VTEC = 300 TECU. The corresponding differences are at the level of 1.e−18 and 1.e−17 s for the third-order and ray-path bending terms, respectively.

European Space Agency (ESA) Atomic Clock Ensemble in Space (ACES) mission on board International Space Station (2014–2016) is aimed to transfer clock signals from low earth orbiting (LEO) satellites to the Earth using a time and frequency transfer link in the microwave domain supporting the clock performance at the level of 10^{-16} s [25]. High-performance frequency comparison of optical clocks between space and ground is essential for supporting future missions in the field of fundamental physics. Such a metrology link must provide frequency and time comparison and dissemination with an uncertainty level of 10^{-18} and beyond. Our investigation shows that for achieving such an accuracy level in the time and frequency transfer using trans-ionospheric microwave links, the higher-order ionospheric propagation effects must be corrected for.

Author details

Mohammed Mainul Hoque*, Norbert Jakowski and Jens Berdermann

*Address all correspondence to: mainul.hoque@dlr.de

German Aerospace Center (DLR), Neustrelitz, Germany

References

[1] Appleton EV. Wireless studies of the ionosphere. J Inst Elect Eng 1932;**71**

[2] Brunner FK, Gu M. An improved model for the dual frequency ionospheric correction of A GPS observations. Manuscrip Geodaet. 1991;**16**(3), pp. 205–214

[3] Bassiri S, Hajj GA. Higher-order ionospheric effects on the global positioning system observables and means of modeling them. Manuscrip Geodaet. 1993;**18**(6), pp. 280–289

[4] Jakowski N, Porsch F, Mayer G. Ionosphere-induced-ray-path bending effects in precise satellite positioning systems. Zeitschrift für Satellitengestützte Positionierung. 1994;**SPN 1/94**

[5] Strangeways HJ, Ioannides RT. Rigorous calculation of ionospheric effects on GPS Earth-Satellite paths using a precise path determination method. Acta Geod Geoph Hung. 2002;**37**(2–3), pp. 281–292

[6] Kedar S, Hajj G, Wilson B, Heflin M. The effect of the second order GPS ionospheric correction on receiver positions. Geophys Res Lett. 2003;**30**(16). DOI: 10.1029/2003 GL017639

[7] Fritsche M, Dietrich R, Knöfel C, Rülke A, Vey S, Rothacher M, Steigenberger P. Impact of higher-order ionospheric terms on GPS estimates. Geophys Res Lett. 2005;**32**(23). DOI: 10.1029/2005GL024342

[8] Hawarey M, Hobiger T, Schuh H. Effects of the 2nd order ionospheric terms on VLBI measurements. Geophys Res Lett. 2005;**32**(11). DOI: 10.1029/2005GL022729

[9] Budden KG (1985) The Propagation of Radio Waves: the theory of radio waves of low power in the ionosphere and magnetosphere. Cambridge University Press, Cambridge, ISBN 0 521 25461 2

[10] Hoque MM, Jakowski N. Higher-order ionospheric effects in precise GNSS positioning. J Geod. 2006;**81**(4):259-268. DOI: 10.1007/s00190-006-0106-0

[11] Hoque MM, Jakowski N. Mitigation of higher order ionospheric effects on GNSS users in Europe. GPS Solut. 2007;**12**(2). DOI: 10.1007/s10291-007-0069-5

[12] Hoque MM, Jakowski N. Estimate of higher order ionospheric errors in GNSS positioning. Radio Sci 2008;**43**:RS5008. DOI: 10.1029/2007RS003817

[13] Hoque MM, Jakowski N. Higher order ionospheric propagation effects on GPS radio occultation signals. J Adv Space Res. 2010. DOI: 10.1016/j.asr.2010.02.013 **46**(2), 15 July 2010, 162–173

[14] Hoque MM, Jakowski N. Ionospheric bending correction for GNSS radio occultation signals. Radio Sci. 2011. DOI: 10.1029/2010RS004583 **46**(6), Version of Record online: 6 JUL 2011

[15] Hoque MM, Jakowski N. Ionospheric propagation effects on GNSS signals and new correction approaches. In: Shuanggen J, editor. Global Navigation Satellite Systems: Signal, Theory and Applications. InTech; 2012. DOI: 10.5772/1134

[16] Hoque MM, Jakowski N. New correction approaches for mitigating ionospheric higher order effects in GNSS applications. In: ION GNSS 2012; September 17-21; Nashville, Tennessee. 2012.

[17] Hernández-Pajares, H, JM Juan, Sanz J and Orús R. Second-order ionospheric term in GPS: Implementation and impact on geodetic estimates. J Geophys Res. 2007;**112**:B08417. DOI: 10.1029/2006JB004707

[18] Datta-Barua, S, Walter, T, Blanch, J, Enge, P. Bounding higher-order ionosphere errors for the dual-frequency GPS user. Radio Sci. 2008;**43**:RS5010. DOI: 10.1029/2007RS003772

[19] Morton, YT, Zhou, Q, van Graas, F. Assessment of second-order ionosphere error in GPS range observables using Arecibo incoherent scatter radar measurements. Radio Sci. 2009;**44**:RS1002. DOI: 10.1029/2008RS003888

[20] Hernández-Pajares, M, Aragón-Ángel, À, Defraigne, P, Bergeot, N, Prieto-Cerdeira, R and Garc´ea-Rigo A. Distribution and mitigation of higher-order ionospheric effects on precise GNSS processing. J Geophys Res Solid Earth. 2014;**119**:3823–3837. DOI: 10.1002/2013JB010568

[21] Petrie, EJ, Matt AK, Philip M, and David AL. A first look at the effects of ionospheric signal bending on a globally processed GPS network. J Geod . 2010;**84**:491–499. DOI: 10.1007/s00190-010-0386-2

[22] Kelso JM. Radio Ray Propagation in the Ionosphere. New York: McGraw-Hill; 1975. ISBN 111434172X

[23] Rishbeth H, Garriott OK, editors. Introduction to Ionospheric Physics. New York: Academic Press; 1969.

[24] Hartmann GK, Leitinger R. Range errors due to ionospheric and tropospheric effects for signal frequencies above 100 MHz. Bull Geod. 1984;**58**(2):109-136.

[25] Cacciapuoti L and Salomon C. Space clocks and fundamental tests: The ACES experiment. Eur Phys J Spec Topics. 2009;**172**(1). DOI: 10.1140/epjst/e2009-01041-7.

Chapter 3

Ka-to-W Band EM Wave Propagation: Tropospheric Effects and Countermeasures

Lorenzo Luini, Roberto Nebuloni and Carlo Riva

Additional information is available at the end of the chapter

http://dx.doi.org/10.5772/66660

Abstract

Near future satellite and terrestrial telecommunication (TLC) systems are expected to benefit from the use of operational frequencies spanning the Ka, Q, V and W bands, the main advantages being the availability of larger bandwidths and the smaller antenna size for a given gain. Moreover, the possibility of using on-board antennas with enhanced directivity is attractive for satellite systems whose coverage area is subdivided into spot beams for frequency reallocation or regional services. For example, the W band is attractive for fixed satellite services (FSS), especially for geostationary high-throughput systems (HTSs), in which the use of such frequencies for the feeder link (i.e. large available bandwidth) could reduce significantly the number of gateways with respect to Ka and Q/V bands. As for deep space missions, the main driver for the interest in using frequencies in the Ka to W bands is the possible increase in the on-board antenna gain with respect to the values at X band considered for current or planned missions. The drawback of using electromagnetic waves at frequencies in Ka, Q, V and W bands is the definite impact of the impairments caused by the troposphere. As a consequence, the design of TLC systems at such frequencies, and in particular satellite-based ones, cannot rely on the classical approach of simply assigning an extra power margin to counteract atmospheric fades. The extensive use of fade mitigation techniques (FMTs), such as link power control (LPC), site diversity or on-board adaptive power allocation, from the propagation side, adaptive coding and modulation (ACM) and data rate adaptation (DRA), from the telecommunication side, is mandatory. A reduction of the quality of service (QoS) should also be considered. This chapter deals with all these aspects characterizing the propagation of electromagnetic waves in the Ka, Q, V and W bands, spanning from the main impairments induced by the troposphere (and how they change as the frequency increases), to how extreme atmospheric conditions can be handled making use of suitable FMTs.

Keywords: electromagnetic wave propagation, atmospheric effects, satellite communications, fade mitigation techniques

1. Tropospheric effects at Ka band and above

Satellite and terrestrial telecommunication (TLC) using very high frequency bands (Ka band and above) benefit from the available larger bandwidths and the smaller antenna size for a fixed gain or the larger gain for a fixed antenna size. Unfortunately, radiowaves at Ka band and above are more severely affected by impairments due to tropospheric elements [1–4] and, in particular, gases, clouds, rain and turbulence.

Oxygen and water vapour are the relevant gaseous components for radio wave propagation in the 20–300 GHz frequency range. Oxygen attenuation is weakly dependent on temperature and atmospheric pressure and its space and time variations are quite limited. The dependence on frequency is much larger with a resonant absorption band at 60 GHz (with specific attenuation that can exceed 10 dB/km) and smaller absorption (less than 0.1 dB/km) below 40–50 GHz and above 70–80 GHz. The water vapour absorption strongly depends on temperature, pressure and humidity, exhibiting marked daily, seasonal and geographical variations. Water vapour-specific attenuation is characterized by a broadened peak around the H_2O absorption line at 22.2 GHz (up to about 0.2 dB/km in reference conditions[1]) and monotonically increases in the 40–100 GHz band (up to about 1 dB/km in reference conditions). As shown in **Figure 1** [5], the specific gas (oxygen and water vapour) attenuation in reference conditions is around 0.1 dB/km (with a peak of 0.2 dB/km at 22.2 GHz) in Ka band, while it increases with frequency from 0.1 to 0.4 dB/km in Q/V band. Due to the opposite

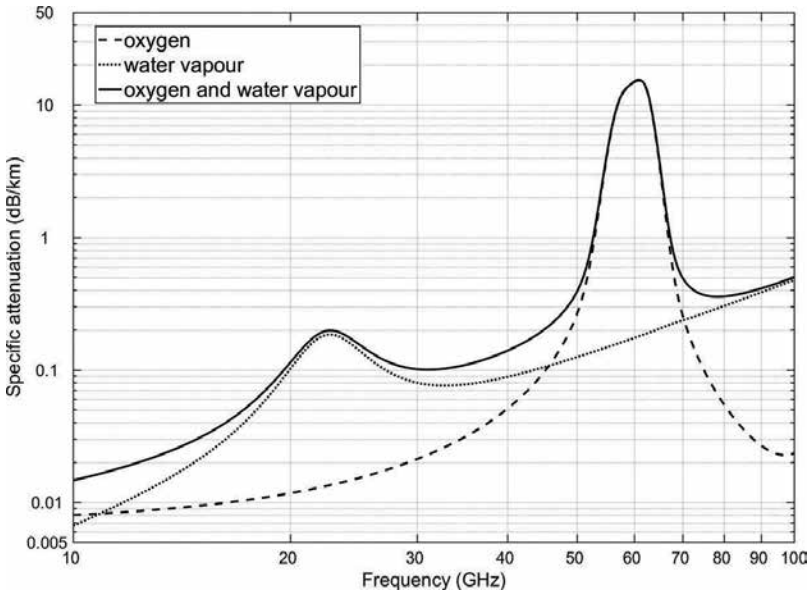

Figure 1. Oxygen (dashed line), water vapour (dotted line) and total gas (solid line) specific attenuation at reference conditions (water vapour density 7.5 g/m3, temperature 15°C, atmospheric pressure 1013 hPa).

[1]Temperature 15°C, pressure 1013 hPa, water vapour density 7.5 g/m3 [5].

http://dx.doi.org/10.5772/66660

dependence of oxygen and water vapour attenuation on frequency, the specific gas attenuation in the W band is included in the interval between 0.36 and 0.5 dB/km, being higher at the bandwidth edges (70 and 95 GHz) and lower in the centre. The total gas attenuation along a slant path depends on the atmospheric profile of temperature, relative humidity and pressure. The models currently recommended by the International Telecommunication Union-Radiocommunication (ITU-R) sector for the prediction of the slant path gas attenuation [5] rely on solid physical bases and are expected to be quite accurate at least up to 100 GHz. Such models introduce simplifications relying on the description of vertical profiles of oxygen and water vapour concentrations by using effective parameters, like the oxygen effective height (analytical function of frequency and pressure) and the water vapour total content (global maps of this parameter are available in Ref. [6]). The mean yearly distribution of oxygen and water vapour attenuation at the zenith is calculated by multiplying their specific attenuation (in reference conditions) by the effective parameters and the slant path attenuation is then obtained through the cosecant law, reasonably assuming the local homogeneity of the atmosphere. As an example, the predicted zenith gas attenuation exceeding 1% of the average yearly time at 20 (Ka band), 50 (V band) and 80 (W band) GHz ranges almost all over the globe in the intervals 0.1–1, 1-2.5 and 1–3 dB, respectively.

In non-precipitating atmosphere, the attenuation due to clouds must be also considered. Since in the 10–100 GHz band the size of suspended water droplets in clouds is smaller than the wavelength, the extinction cross sections can be calculated by using the Rayleigh approximation, according to which the cloud attenuation turns out to depend only on the liquid water content, on the droplets temperature and on frequency. Cloud attenuation changes with climate and reveals a large temporal variability, depending on the presence of clouds along the link and on their liquid water content. It is monotonically increasing with frequency in the 10–100 GHz band. In ITU-R recommendation P.840-6 [7], cloud attenuation is calculated through the reduced liquid water total content (kg/m^2) or (mm), an effective parameter that depends on frequency and is available through global maps (presently calculated for the 20–50 GHz band) [7]. Cloud attenuation depends also on the water permittivity, the frequency and the elevation angle. The predicted zenith cloud attenuation exceeding 1% of the average yearly time at 20 GHz does not exceed 2 dB all over the globe, while it can exceed 10 dB in equatorial and tropical regions at 80 GHz, as shown in **Figure 2**. It is then clear that, even in absence of rain, cloud attenuation only limits availability in the W band.

As for precipitating atmosphere, the wavelength above 10 GHz becomes comparable to the size of hydrometeors (few millimetres), causing absorption and scattering, and consequently attenuation, of the incident wave. The rain attenuation along a slant path can be calculated by integrating the specific attenuation, which statistically depends on rain intensity, R (mm/h), as follows:

$$\gamma = kR^{\alpha} \tag{1}$$

In Eq. (1), k and α are coefficients (provided, for instance, in recommendation ITU-R P.838-3 [8]), which depend on frequency, elevation angle, drop temperature, wave polarization (as raindrops are not spherical), drop size distribution (DSD) and shape. DSD and shape can vary during a single event or from one event to the other, leading to significant differences in specific rain attenuation. In the W band, the effect of the DSD is more evident than in the

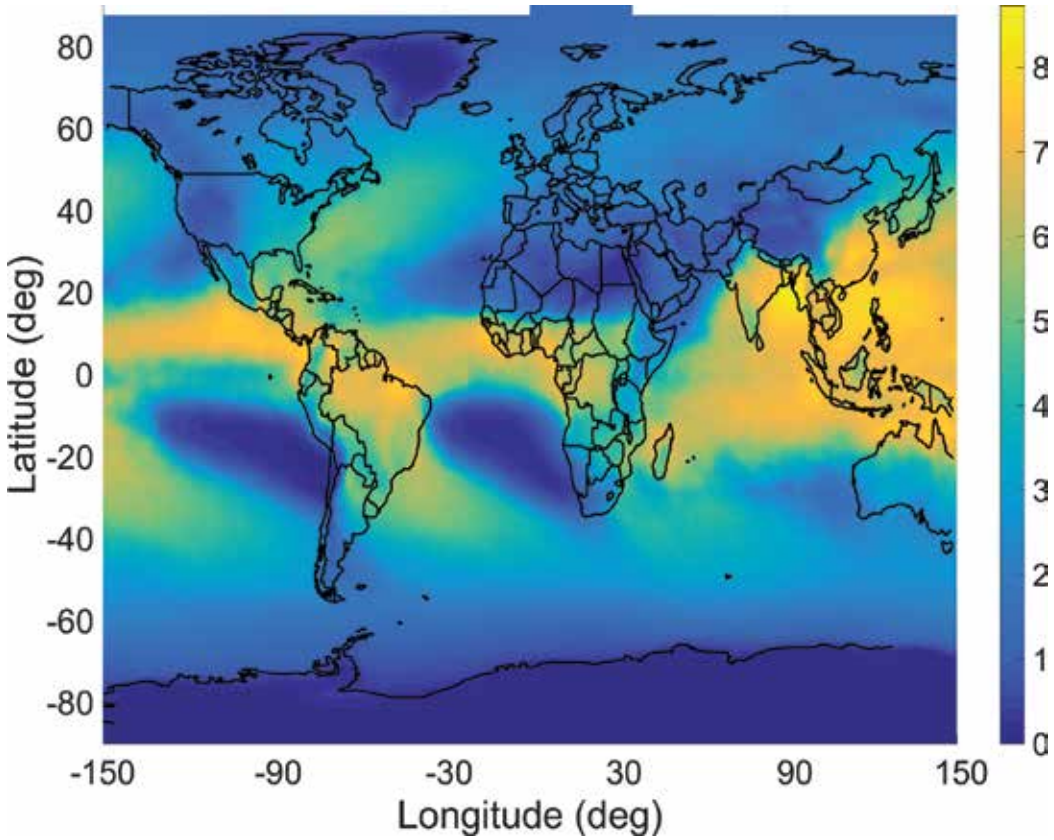

Figure 2. Zenith cloud attenuation (dB) at 80 GHz exceeded for 1%, prediction according to recommendation ITU-R P.840-6 [7].

lower bands, with a marked dependence on rain intensity: for example, at 10 mm/h, the peak to peak relative variation of the specific attenuation for various DSD is about 40% (for both polarizations). The difference between specific attenuation in vertical and horizontal polarization is well below 5%. As for the prediction of rain attenuation in the 10–100 GHz band, the k and α coefficients in Ref. [8] can be used, though they originate from a best-fitting procedure up to V band, and their accuracy in W band is still to be verified.

The rain attenuation exceeded for a certain time percentage in a year is related to the local rain rate exceeded for the same percentage, which may vary significantly across the globe; as an example, **Figure 3** shows the global map [9] of the rain rate (mm/h) exceeded for 0.01% of the average year (which corresponds approximately to 1 h in a year). The probability to have rain, P_0, is very close to the probability to have rain attenuation, P_A; typically, for temperate climate, $P_0 \approx 4$–8% [9], and $P_A \approx 6$–10%, depending on the link elevation angle.

Several models have been developed in the last decades to predict rain attenuation statistics from the local rain rate statistics. Their accuracy in the 10–50 GHz range [10] is generally satisfactory. Since experimental statistics from earth-to-satellite links are not available for prediction models testing above 50 GHz, in this frequency range, physically based methods should

http://dx.doi.org/10.5772/66660

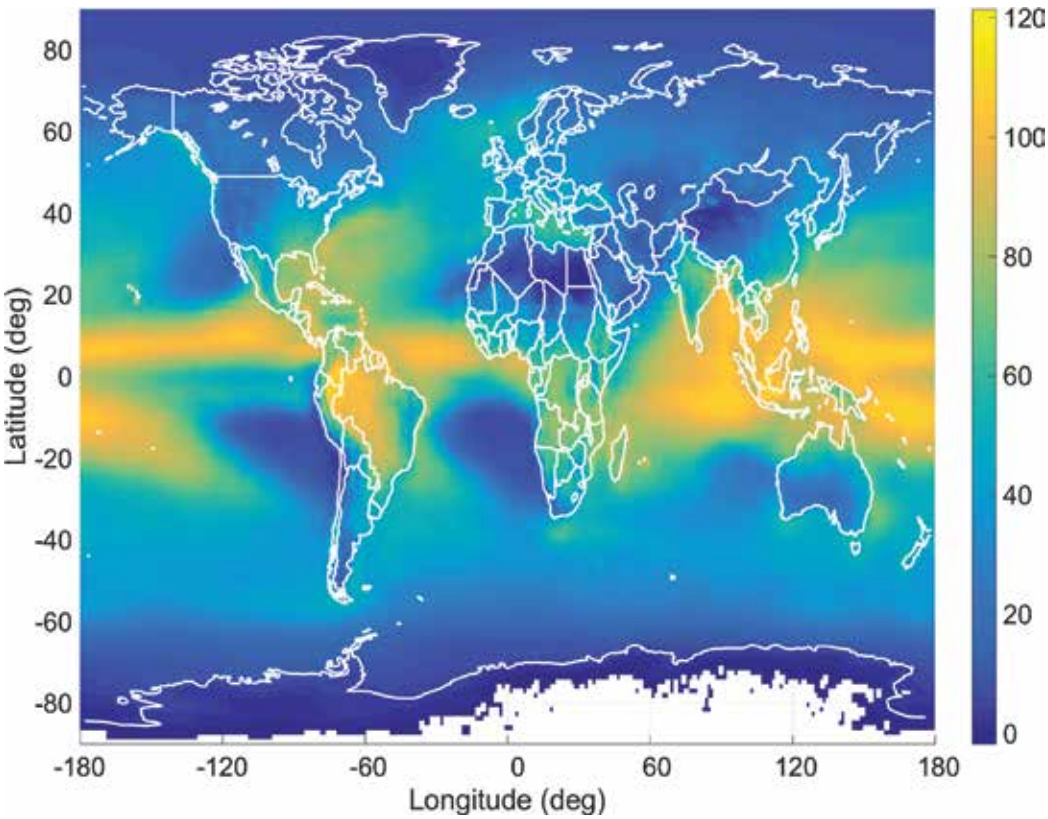

Figure 3. Global map of rain rate (mm/h) exceeded for 0.01% of the average year.

be privileged, as their accuracy is not expected to depend significantly on the frequency. The SC EXCELL (Stratiform Convective EXponential CELL) model [11, 12], for example, describes the precipitation through a set of synthetic isolated rain cells with exponential rain rate profile; moreover, SC EXCELL takes separately into account stratiform and convective rain contributions, using different rain heights for the two types of precipitation. Finally, the contribution due to melting layer (the layer, lying just on the top of rain, where snow and ice particles gradually melt during their fall to the ground) is added only to stratiform rain through an equivalent rain slab whose height depends on frequency. **Figure 4** shows an example of rain attenuation statistics (specifically, the complementary cumulative distribution function [CCDF]) predicted by SC EXCELL for a satellite slant path (elevation angle 35°) at 20, 50 and 80 GHz (vertical polarization). It is evident from the figure that, due to rain effects only, a system availability of 99.99% (outage of 0.01%) is realistic only in Ka band (20 GHz), with a propagation power margin of about 20 dB. In V (50 GHz) and W (80 GHz) band, a maximum availability of 99% is probably feasible, if no adequate fade mitigation techniques (FMTs) are implemented.

In case of dual polarization systems, another effect induced by rain must be taken into account: depolarization (specifically, cross polarization discrimination, XPD), which is introduced by non-spherical drops. It is worthwhile observing that anisotropic ice crystals also produce the

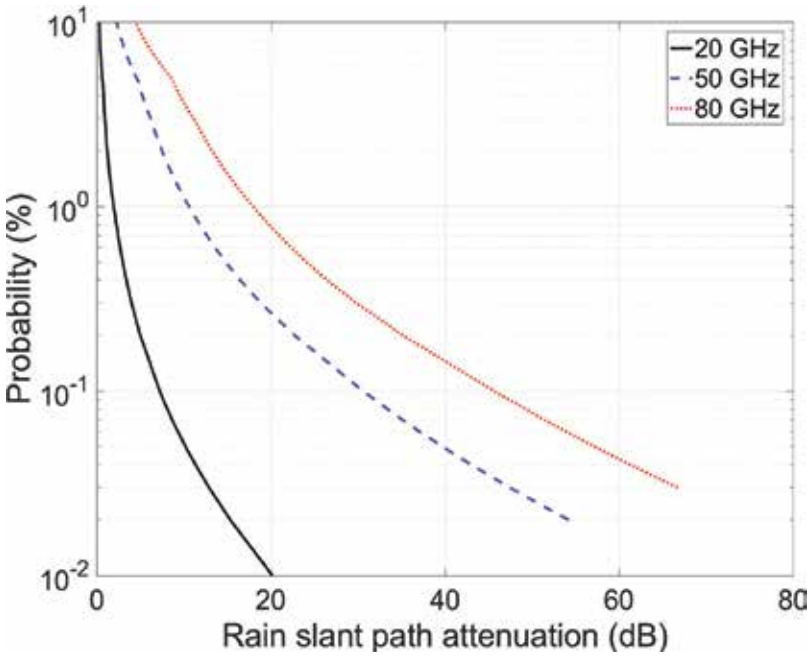

Figure 4. CCDF of rain attenuation (predicted by the SC EXCELL model [11]) for a satellite slant path (elevation angle 35°) from a ground station located in Milano (lat. 45.5°N, long. 9.2°E, alt. 120 m a.m.s.l.) at 20 GHz (black solid line), 50 GHz (blue dashed line) and 80 GHz (red dotted line) with vertical polarization.

same effect in presence or absence of rain. The physical parameters that cause XPD are the anisotropy (i.e. the polarization dependent forward scattering of the particles, both for hydrometeors and ice crystals) and the angle of the symmetry axes of the particles with respect to the polarization plane, named canting angle. Like rain attenuation, also XPD increases dramatically with the frequency; by scaling anisotropies, it is possible to scale depolarization with frequency [13]. The hydrometeor axes, however, are not equi-aligned, and the dispersion of these orientations generally reduces the XPD. This aspect and the co-presence of water and ice particles along the path makes the depolarization phenomenon complex and difficult to describe. Ice XPD is the critical issue for low margin systems at high frequencies (above Ka band) since, during rainy periods, the system is probably already in outage. On the other hand, the XPD due to rain can have an impact when attenuation is close to the fade margin of gateway systems with high availabilities.

Finally, turbulence effect must be mentioned. Turbulent eddies in the troposphere cause small-scale inhomogeneity of the atmospheric refractive index along the propagation path, which produces signal scintillation, that is, rapid fluctuations of the received signal amplitude, above about 10 GHz. Scintillation, when expressed in decibels, is characterized by a Gaussian distribution with a stationary standard deviation over few minutes. In turn, scintillation standard deviation depends on the turbulence structure index; it increases with the frequency (but much less than rain attenuation) [14] and with the path length, and it decreases with the increasing antenna size, due to the aperture averaging effect. Scintillation can also

be due to the variation of the arrival angle of the main ray; in this case, it increases with the decreasing beamwidth as a result of the effect of the antenna radiation pattern [14]. The impact of scintillation, typically quite smaller than that of attenuation, can be important for low elevation angles and low margin systems. Moreover, scintillation can interfere with tracking systems or fade mitigation techniques. Scintillation can also occur during rain events and, in this case, the signal variations are mixed with the fast fluctuations induced by rain itself.

2. Fade mitigation in the Q/V feeder link channel

The actual generation of fixed satellite services (FSS) for TLC applications (e.g. Eutelsat KA-SAT and Hughes EchoStar XVII) achieve throughputs of the order of 100 Gbit/s by exploiting full Ka-band operation, multibeam architectures with frequency reuse on the user link side, and a number of high-capacity gateway (GW) links on the feeder link side. A further increase in the capacity of future HTS by an order of magnitude up to the Terabit/s is now under investigation as it would be supported by the growing market demand for broadband access [15]. However, it involves several technological challenges as well. Designing the general architecture of an HTS is a complex task and it is beyond the scope of this chapter. Here the focus is on the impact of the propagation channel on the design of the feeder link, that is, the connection between the GW station and the satellite. To this aim, a reference scenario for a future HTS is sketched and the most suitable FMTs to counteract atmospheric attenuation are reviewed.

2.1. Number of beams

A simple calculation of the required number of GW beams and user beams to achieve Terabit/s capacity can be carried out once the available bandwidth, the frequency reuse scheme and the modulation scheme are given. An important assumption is that the traffic is uniform, that is, the system capacity is shared in equal parts among the user beams as well as among the GW beams. If the same MODCOD (MODulation and CODing) is transmitted, the relationship between total satellite capacity C_{tot} (one-way) and number of user beams N_{UB} is given as:

$$C_{tot} = N_{UB} \frac{N_p}{F} B \times SE \tag{2}$$

where N_p is the number of polarizations, F is the frequency reuse factor, B is the bandwidth per beam, and SE is the spectral efficiency of the MODCOD. For instance, assuming B = 0.5 GHz/beam, that is, the entire exclusive bandwidth available for FSS across the European Community [16], SE = 3.433 (corresponding to the 32 APSK 5/6), N_p = 2 and F = 4, we obtain

$$N_{UB} = C_{tot} \frac{F}{N_p} \frac{1}{B \times SE} = 500 \frac{4}{2} \frac{1}{0.5 \times 3.433} = 583 \tag{3}$$

being the 1 Terabit/s shared between uplink and downlink. Furthermore, the capacity on the user link side must equal the one of the feeder link, that is

$$C_{GW} N_{GW} = C_{UB} N_{UB} \tag{4}$$

In the Q-V band, a much larger bandwidth (4–5 GHz) would be available even though in Europe there are no exclusive bandwidths for FSS [16]. Assuming that each GW has the entire Q-V bandwidth at its disposal, that is, $B = 4$ GHz, and $SE = 3.433$, $N_p = 1$ and $F = 1$, the required number of GW beams would approximately be equal to

$$N_{GW} = 500 \frac{1}{4 \times 3.433} = 36 \quad (5)$$

Hence, each GW would serve 4×2/0.5 = 16 user beams.

In the design practice, other factors contribute to find the optimum number of spots, such as available on-board power, complexity of the on-board antenna system, interference issues, etc.

2.2. Space diversity

The drawback of higher frequencies, specifically Q/V-band, is the increased vulnerability to the propagation impairments. Rain fades at Q/V-band are much larger than the dynamic range of receiver systems with typical feeder link availability targets (99.9%), even when uplink power control is featured. To this aim, a well-known FMT is single site diversity (SSD), where a GW is backed up by an idle GW located within the same feeder beam (**Figure 5**).

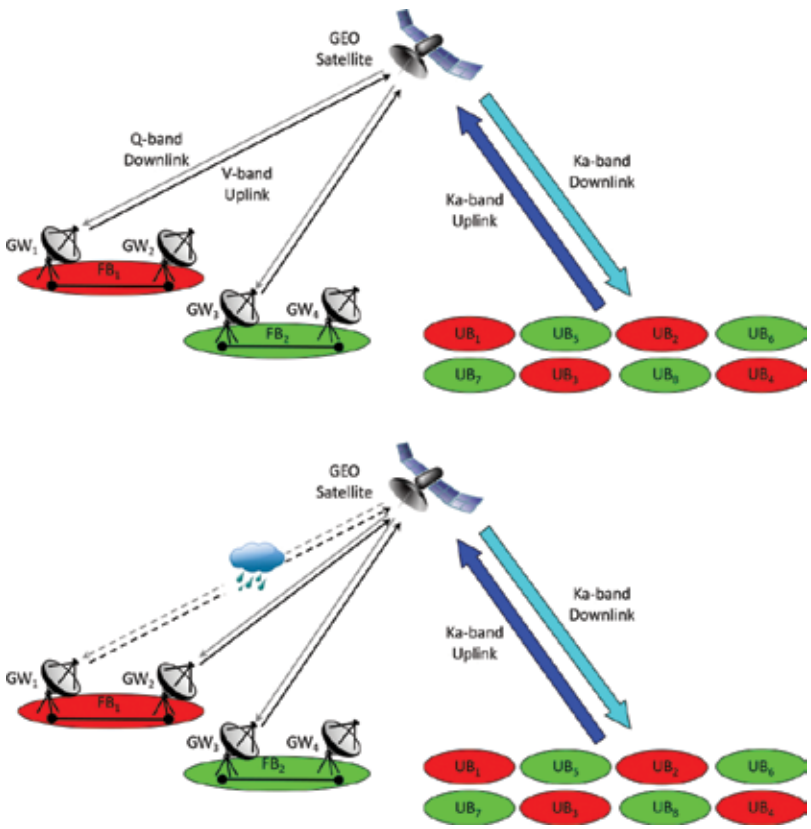

Figure 5. Single site diversity across the feeder link of an FSS.

http://dx.doi.org/10.5772/66660

When GW_1 is faded, the traffic is switched to GW_2 which transmits the same set of carriers as GW_1. The payload is therefore transparent to the process of allocating users from the GW in outage to the idle GW (switchover). The higher the distance between GW_1 and GW_2 the lower the probability that both are faded.

Conventional SSD, relying on the availability of an idle GW to back up a faded GW, is not a cost-effective solution when many GWs are required to convey the user beams traffic, as it basically doubles the cost of the ground segment. On the other side, the diversity scheme in **Figure 6** achieves the required availability target while minimizing the number of redundant GWs with respect to SSD. There are N operational GWs and $P < N$ redundant GWs ($N = 2$ and $P = 1$ in the figure, for the purpose of illustration), each located within its own feeder beam. The redundant capacity provided by the P back-up GWs is shared among the user beams: when one of the operational GWs (GW_1 or GW_2) is faded, it is replaced by GW_3. The above "$N + P$" scheme tolerates up to P GWs in outage with no loss of capacity. As a drawback, $N + P$ implies a higher degree of complexity both on the ground segment and on-board. In fact, the GWs must be interconnected by high-speed fibre optic links to form a smart-gateway network (SGN). For instance, in **Figure 6**, the GWs nodes form a star topology where the central node, namely the

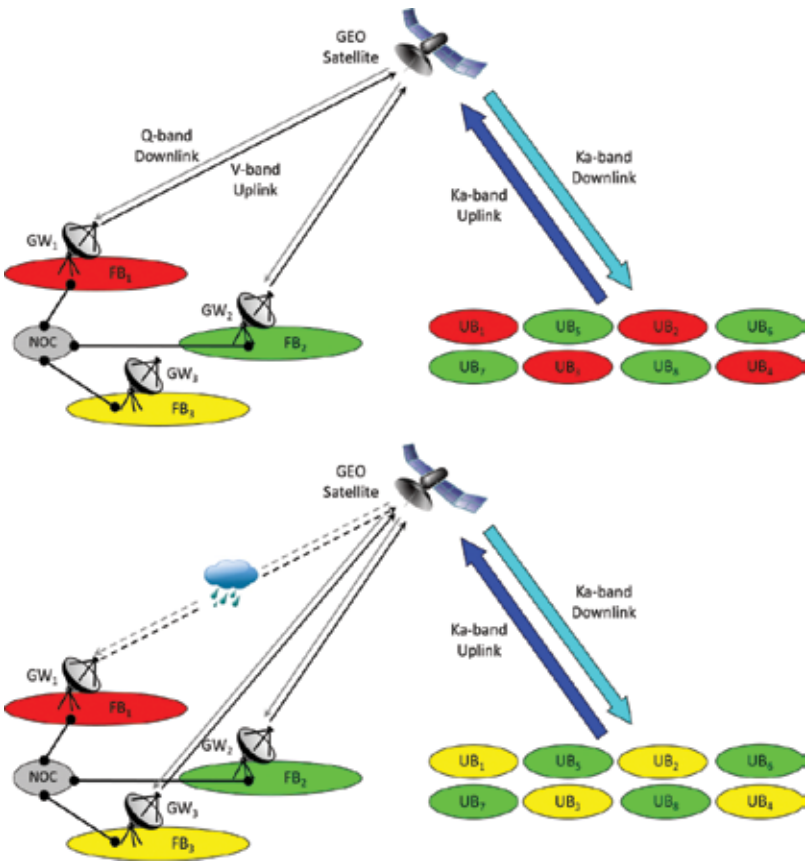

Figure 6. $N + P$ diversity scheme across the feeder link of an FSS.

network operation centre (NOC), carries out resource management and controls traffic switchover. Moreover, the payload should host $N + P$ (instead of N) receiver-transmitter front-end chains and should provide rerouting capability from every user beam to any of the back-up GWs. In general, a trade-off between flexibility in managing system resources and complexity (both ground segment and payload) must be addressed.

With SSD and N + P diversity, a user beam is served by a single GW at a time. More complex diversity schemes have been proposed as well, where a single user-beam is connected to several GWs at a time through frequency division multiple access (FDMA) [17]. When a GW is in outage, the user beam traffic conveyed by its carriers is switched to a different GW serving the same set of beams as the faded GW. If the system does have some redundancy (i.e. unused carriers in ideal conditions), an outage event does not imply a loss of capacity. These solutions are more challenging than $N + P$ as they envisage a number of complex tasks including evaluation and distribution of the available resources, signalling and synchronization to the new carrier and assignment of the user terminals among the new set of carriers.

2.3. $N + P$ performance

Let us now assess the effectiveness of $N + P$ in mitigating the impact of the atmospheric channel on the Q-V band feeder link for the reference scenario described above. The following figures of merit are considered:

- The propagation margin, that is, the extra decibel margin to be included in the link budget equation to guarantee a targeted feeder link availability.
- The duration and the rate of fades, which, in turn, have an impact on the algorithms controlling the switchover process.

The propagation margin can be calculated from the CCDF of rain attenuation at each GW site and basic statistical theory, provided that the rain process is assumed to occur independently over different GW links. On the other side, a full characterization of the propagation channel can be carried out only by models able to generate realistic time series of attenuation in every GW site, possibly taking into account the correlation of the rain process in time and space. Here, we have used the multisite time series synthesizer (MTS) proposed in Ref. [18] to simulate the rainy atmospheric channel for a V-band (50 GHz) feeder link (we consider here uplink only). The MTS generates synthetic time series of rain attenuation across an arbitrary ensemble of slant paths up to the V-band by combining series of measured data carried out during the ITALSAT propagation campaign. First-order statistics are reproduced and the spatial correlation of rain is duly taken into account. The contribution of non-rainy components, that is, clear-sky attenuation, is obviously non-negligible at V-band, as shown in the first part of this chapter. However, clear-sky attenuation is on the order of few decibels and though time variant, its fluctuations can be managed by FMTs such as uplink power control. On the other side, the peaked and fast fades produced by rain prompt for an approach based on space diversity.

Without loss of generality, let us consider a system of 10 GWs operating in a 9 + 1 diversity scheme. In fact, the 36-GW system necessary to achieve the Terabit/s capacity could be divided into four independent clusters of 9 + 1 GWs each. Indeed, this architecture would

result in a decrease in the number of high-speed connections among the GWs, with respect to, for example, a 36 + 4 diversity scheme. The 10 selected GW sites are reported in **Table 1**, assuming a GEO satellite providing continental coverage across Europe, alongside the climatologic probability of rain and the slant-path rain attenuation exceeded for 0.1 and 0.01% of time, respectively. The distance between the stations that should be maximized in the design process ranges from less than 500 km to about 3200 km.

Id	Site	Lat. (°)	Lon. (°)	Alt. (m)	P_0 (%)	0.1%	0.01%
1	Helsinki	60.1697	24.9383	5	3.55	19.1	49.8
2	Berlin	52.5192	13.4058	48	3.43	17.0	45.7
3	Cork	51.8967	−8.4861	20	7.85	22.3	51.9
4	Trieste	45.6494	13.7778	28	6.51	28.9	68.0
5	Athens	37.9836	23.7292	75	3.85	17.5	46.6
6	Cyprus	35.1264	33.4297	122	1.47	24.7	68.5
7	Turin	45.0628	7.6783	235	5.98	25.5	61.6
8	Paris	48.8564	2.3522	48	4.68	18.0	45.6
9	Madrid	40.4167	−3.7036	655	2.98	13.1	37.1
10	Cagliari	39.2236	9.1217	46	1.94	14.7	45.8

GEO satellite located at 9°E.

Table 1. Coordinates, altitude, probability of rain and 50-GHz slant-path rain attenuation (in dB) in 10 sites throughout Europe.

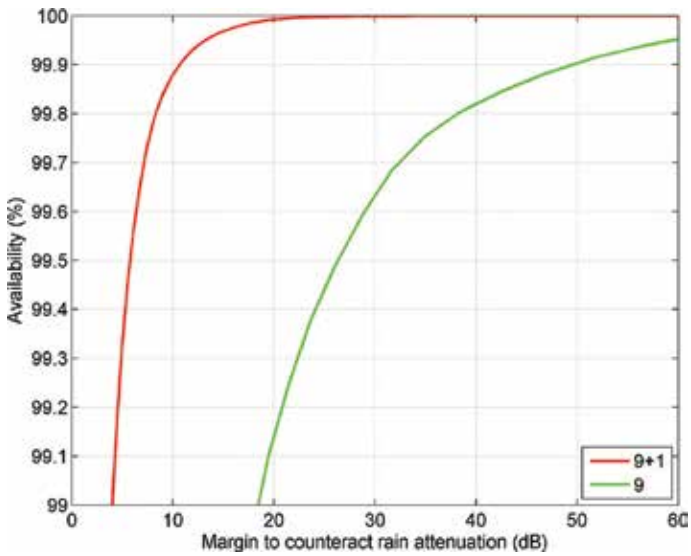

Figure 7. Performance of the 9 + 1 diversity scheme at V-band.

Figure 7 shows the benefits of 9 + 1 diversity with respect to a 9 + 0 system, used here only as a benchmark, in terms of the reduction of the required margin against rain fades that must be included in the link budget. For a typical feeder link availability of 99.9%, a 9 + 1 system requires a 10.7 dB margin against an unfeasible 50 dB, if the 9 + 0 system was operational for 99.9% of time. The 9 + 1 curve has been obtained as follows: (a) generate the time series of rain attenuation taking (in every sampling time) the second-worst value of attenuation among the ten GW links and (b) build the CCDF of the resulting time series. The underlying assumption is that instantaneous switchover is feasible.

The characteristics of fades are crucial for implementing the algorithms that control traffic switchover from a GW in outage to another. The operation involves higher layer network operations; hence, it is a good practice to design the diversity scheme in order to minimize the switching rate. Moreover, switching algorithms must be robust to short and intense signal fades that are more likely to occur at such high frequencies. Thresholding methods based on hysteresis are a simple solution that prevents from switching triggered by false alarms. The switchover will be carried out when signal attenuation across an operational link exceeds a certain value, namely a certain fade depth D. The statistics of events exceeding D can be calculated in several different ways. Here the distribution of the number of fades longer than D is calculated over an average year as generated by the MTS.

If we target a 99.9% availability, from **Figure 7**, the system margin against rain fades is 10.7 dB at V-band, which means that a fade depth equal to (or greater than) 10.7 dB occurring at the same time across two links produces system outage. **Figure 8** shows the distribution of fade durations corresponding to a fade depth equal to 10.7 dB. A fade occurring across a

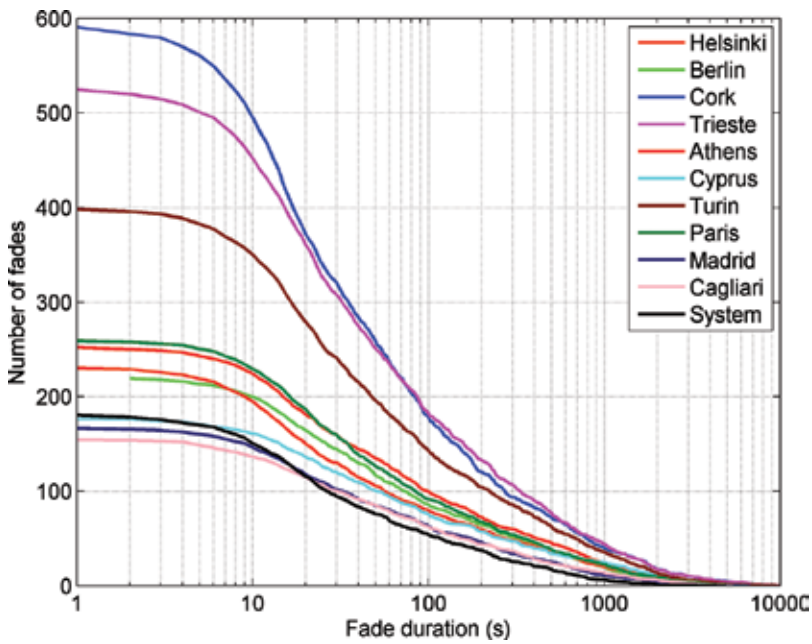

Figure 8. Number of fades exceeding a 10.7 dB depth (corresponding to 99.9% availability) in a 9 + 1 diversity scheme at V-band.

http://dx.doi.org/10.5772/66660

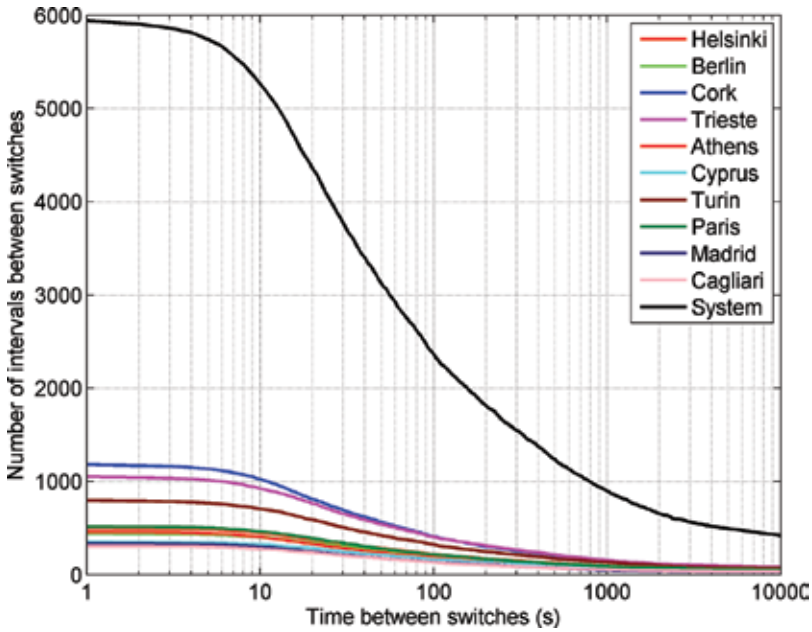

Figure 9. Number of intervals between switchovers in a 9 + 1 diversity scheme at V-band. Availability: 99.9%.

certain link is counted only if it does not produce system outage. The curves of the individual links are similar to the ones obtained as if they were operating independently of each other (not shown here). If the curves were normalized to the total number of fades, they would be packed together. Indeed, it is known that the relative occurrence of fades of different duration is rather site independent, whereas the number of fades of a given duration obviously is not.

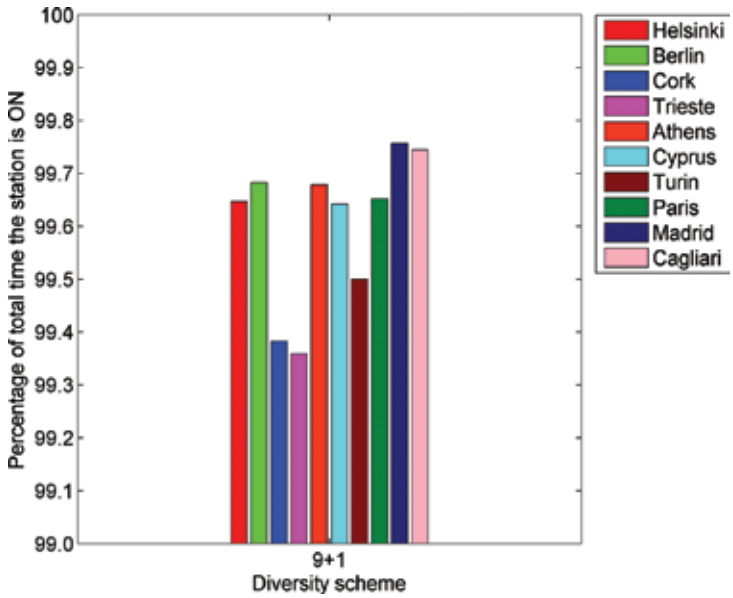

Figure 10. In-service time of each GW in a 9 + 1 diversity scheme at V-band. System availability: 99.9%.

Finally, the curve labelled "system" refers to the fades detected in the time series of attenuation built-up considering the best nine links (assuming instantaneous switching).

Figure 9 shows the distribution of the time intervals between consecutive switches for each GW in the 9 + 1 diversity scheme. In the average year, the system is expected to operate about 6000 switchovers, that is, approximately, once every 1.5 h. However, a non-negligible percentage of switchovers must be carried out in few seconds.

Finally, **Figure 10** shows the ratio of the time during which each link is operational normalized to the time when the system is operational. Note that operation time (hence the resources) is rather uniformly shared among the stations. Lower operation times correspond to the stations that exhibit worse CCDFs of rain attenuation.

3. Fade mitigation in the Ka band user link channel

As discussed above, the $N + P$ diversity scheme is much more cost-effective than SSD, which, on the contrary, represents a viable solution to significantly improve the system performance on the user link side (typically operating in the Ka band [16]), especially when such a user requires a reliable broadband service (e.g. emergency applications). Indeed, a two-site diversity system for the user link with stations at a distance ranging between 20 and 50 km typically allows a considerable increase in the link availability (reduced outage time) and/or performance (increased data rates) [19], mainly associated to the strongly uneven spatial distribution of precipitation.

In order to properly estimate the advantage achievable with such a kind of system, reliable and accurate propagation models are required, especially when limited propagation data are available to test their accuracy. To this aim, a combination of physically based models can be used: MultiEXCELL (Multi EXponential CELL) to synthesize rain rate fields [20], SMOC (Stochastic MOdel of Clouds) to reproduce cloud fields [21] and SMOV (Stochastic MOdel of water Vapour) to generate water vapour fields [22]. As preliminary shown in Ref. [23], these diversified synthetic fields can be combined (including the constant attenuation due to oxygen, whose variability in time and space is extremely low) so as to maintain the local first-order (i.e. CCDF) and second-order (i.e. spatial correlation) statistics of the single atmospheric elements, as well as to preserve their mutual correlation (e.g. clouds covering areas affected by precipitation and higher water vapour content where clouds lie). This is exemplified in **Figure 11**, which depicts a sample cloud field (vertical integrated liquid water content) and the associated water vapour field (vertical integrated water vapour content), as well as in **Figure 12**, which shows that the synthetic fields generated by MultiEXCELL, SMOC and SMOV also take into account the vertical development of rain rate, clouds and water vapour to allow a more realistic simulation of the interaction between electromagnetic waves and the atmosphere. This not only means a direct combination of the impairments due to the various constituents in the atmosphere (in contrast to the statistical approach proposed in recommendation ITU-R P.618-12 [24] to combine the attenuation due to clouds, rain and gases), which is expected to increase the prediction accuracy, but also provides a high flexibility of the model,

http://dx.doi.org/10.5772/66660

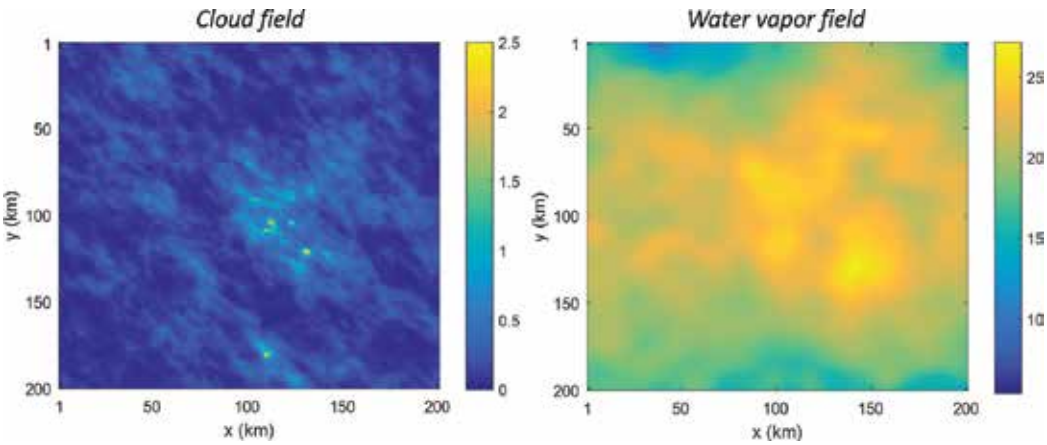

Figure 11. A sample water vapour field generated by SMOV associated to a cloud field synthesized by SMOC.

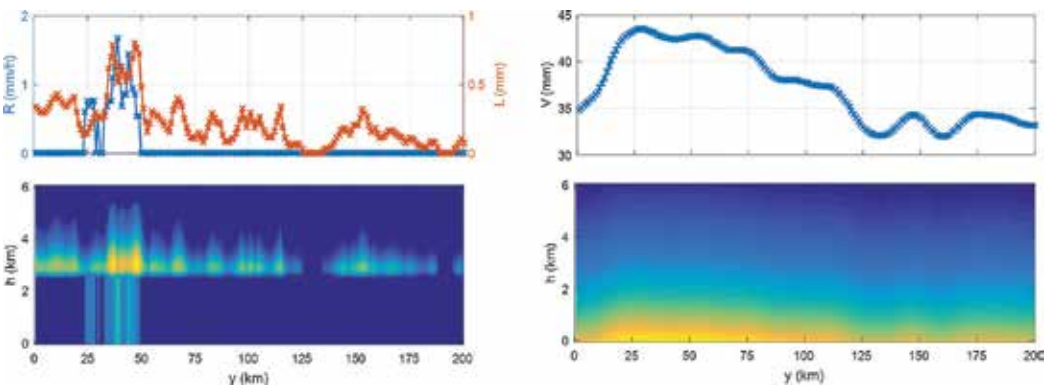

Figure 12. Trend of the rain rate *R*, the integrated liquid water *L* and integrated water vapour *V* along a horizontal line crossing the fields, for a sample of coupled rain rate, cloud and water vapour fields (top part), together with the vertical development of precipitation, clouds and water vapour content (bottom part).

which can indeed be applied to estimate the interaction between electromagnetic waves and the atmosphere in diversified scenarios, including those involving complex system distributed in space, taking advantage of the site diversity concept.

As an example, let us consider a user link operating at 19.7 GHz [16], whose ground station lies close to Milan (latitude 45.4°N, longitude 9.5°E, altitude 84 m a.m.s.l.) and consists of two stations separated by *D* kilometres. The system points to a GEO satellite with orbital positon at 9°E (as the Ka-SAT by Eutelsat) with an elevation angle of 37.8°.

Figure 13 shows the statistics of total attenuation (i.e. including the effects induced by rain, clouds, water vapour and oxygen) estimated by simulating the interaction between the whole set of synthetic maps generated by the physically based models mentioned above and the

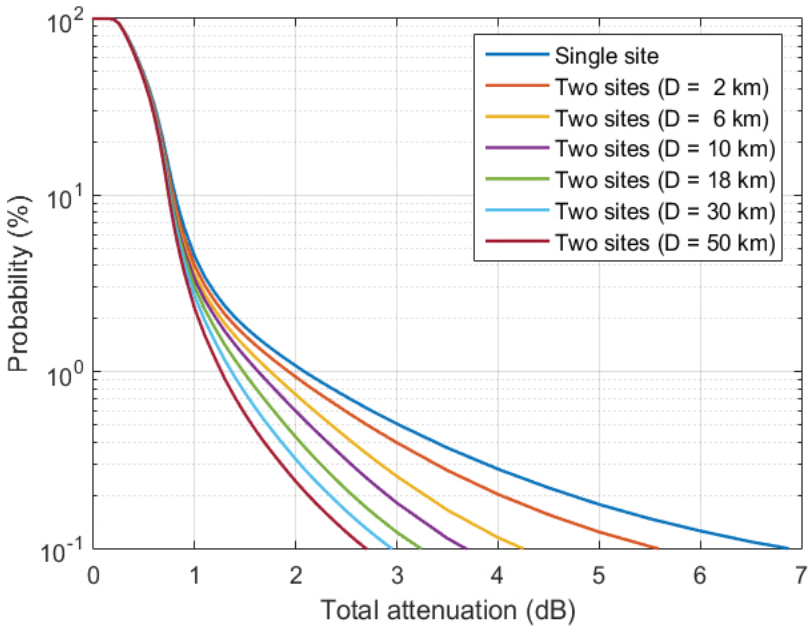

Figure 13. Statistics of total attenuation: two-site diversity system, for different values of separation distance *D*.

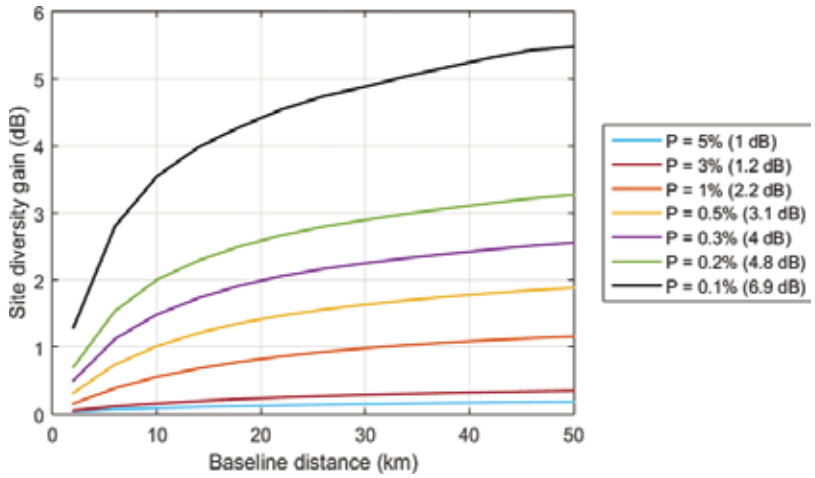

Figure 14. Trend of the site diversity gain *G* as a function of the separation distance *D* and for different outage probabilities of the single-link scenario *P*.

two-site system, for different values of separation distance *D*. The assumption underpinning these results is that the lowest attenuation affecting the two stations is always selected on instantaneous basis (perfect switching). The comparison with the reference single-link case (no site diversity) allows to point out the advantage originating from using two stations: as an

example, the margin needed to cope with the attenuation exceeded for 0.1% of the yearly time varies from approximately 7 to 2.7 dB when employing two stations at 50 km of distance. This is even clearer in **Figure 14**, which depicts the trend of the site diversity gain G as a function of D and for different outage probabilities of the single-link scenario P. G is defined as

$$G(D, P) = A_S(P) - A_J(D, P) \tag{6}$$

where A_S and A_J are the attenuation values of the CCDFs (both for the same probability P), respectively, relative to the single site and to the two-site diversity scheme. As expected, G increases as P decreases (higher probability of intense rainy events) and as the stations are more and more apart (lower degree of correlation). As it turns out, for 99.9% of the time and for distances larger than 30 km, the margin needed to counteract the atmospheric attenuation is lower than roughly 70% of the one required in the single-link scenario. On the other hand, assigning the single-link power margin to the system, the use of two stations leads to a significant increase in the overall data rate, as a higher signal-to-noise ratio allows the use of much more efficient MODCODs [16].

Author details

Lorenzo Luini[1, 2]*, Roberto Nebuloni[2] and Carlo Riva[1, 2]

*Address all correspondence to: lorenzo.luini@polimi.it

1 Department of Electronics, Information and Bioengineering, Politecnico di Milano, Milano, Italy

2 Institute of Electronics, Computer and Telecommunication Engineering, National Research Council of Italy, Milano, Italy

References

[1] P. Mikkonen. Modern 60 GHz radio link. In: Microwave Conference, 1999; Oct. 1999; Munich, Germany. IEEE; 1999. pp. 83–86. DOI: 10.1109/EUMA.1999.338533

[2] M. Grabner, V. Kvicera, G. Timms. 60 GHz Band propagation experiments on terrestrial paths in Sydney and Praha. Radioengineering. 2005;**14**(4):27–32.

[3] M. Ueba, A. Miura, S. Kitazawa, S. Saito, T. Ohira. Feasibility study on millimetre wave multi-gigabit wireless LAN system. In: 2007 European Microwave Conference; Oct. 2007; Munich, Germany. 2007. pp. 688–691. DOI: 10.1109/EUMC.2007.4405285

[4] C. Riva, C. Capsoni, L. Luini, M. Luccini, R. Nebuloni, A. Martellucci. The challenge of using the W band in satellite communication. International Journal of Satellite Communications and Networking. 2013;**32**(3):187–200. DOI: 10.1002/sat.1050

[5] International Telecommunication Union – Radiocommunication Sector. Recommendation ITU-R P.676-10, Attenuation by atmospheric gases [Internet]. 09/2013. Available from: https://www.itu.int/dms_pubrec/itu-r/rec/p/R-REC-P.676-10-201309-I!!PDF-E.pdf [Accessed: May 2016]

[6] International Telecommunication Union – Radiocommunication Sector. Recommendation ITU-R P.836-5, Water vapour: surface density and total columnar content [Internet]. 09/2013. Available from: http://www.itu.int/dms_pubrec/itu-r/rec/p/R-REC-P.836-5-201309-I!!PDF-E.pdf [Accessed: May 2016]

[7] International Telecommunication Union – Radiocommunication Sector. Recommendation ITU-R P.840-6, Attenuation due to clouds and fog [Internet]. 09/2013. Available from: http://www.itu.int/dms_pubrec/itu-r/rec/p/R-REC-P.840-6-201309-I!!PDF-E.pdf [Accessed: May 2016]

[8] International Telecommunication Union – Radiocommunication Sector. Recommendation ITU-R P.838-3, Specific attenuation model for rain for use in prediction methods [Internet]. 03/2005. Available from: http://www.itu.int/rec/R-REC-P.838/en [Accessed: May 2016]

[9] International Telecommunication Union – Radiocommunication Sector. Recommendation ITU-R P.837-6, Characteristics of precipitation for propagation modelling [Internet]. 02/2012. Available from: http://www.itu.int/dms_pubrec/itu-r/rec/p/R-REC-P.837-6-201202-I!!PDF-E.pdf [Accessed: May 2016]

[10] C. Capsoni, M. D'Amico, L. Luini, E. Matricciani, A. Paraboni, C. Riva (Editor), L. Castanet, T. Deloues, V. Fabbro, L. Feral, F. Lacoste, J. Lemorton, E. Kubista, T. Prechtl, M. Schönhuber, "Characterisation and Modelling of Propagation Effects in 20-50 GHz Band", Final report for the European Space Agency under ESTEC Contract No. 17760/03/NL/JA, 2006.

[11] C. Capsoni, L. Luini, A. Paraboni, C. Riva, A. Martellucci. A new prediction model of rain attenuation that separately accounts. IEEE Transactions on Antennas and Propagation. 2009;**57**(1):196–204. DOI: 10.1109/TAP.2008.2009698

[12] L. Luini, C. Capsoni. The SC EXCELL model for the prediction of rain attenuation on terrestrial radio links. Electronics Letters. 2013;**49**(4):307–308. DOI: 10.1049/el.2012.3835

[13] A. Paraboni, A. Martellucci, C. Capsoni, C. Riva. The physical basis of atmospheric depolarization in slant paths in the V band: theory, Italsat experiment and models. IEEE Transactions on Antennas Propagation. 2011;**59**(11):4301–4314. DOI: 10.1109/TAP.2011.2164207

[14] M.M.J.L. Van de Kamp, C. Riva, J.K. Tervonen, E.T. Salonen. Frequency dependence of amplitude scintillation. IEEE Transactions on Antennas and Propagation. 1999;**47**(1):77–85.

[15] B. Evans, P. Thompson, L. Castanet, M. Bousquet and T. Mathiopoulos. Concepts and Technologies for a Terabit/s Satellite. In: SPACOMM; April 2011; Budapest (Hungary).

[16] B. Evans and P. Thompson. Key issues and technologies for a Terabit/s satellite. In: 28th AIAA International Communications Satellite Systems Conference (ICSSC-2010); 30 Aug–2 Sep 2010; Anaheim (California).

[17] P. Angeletti, R. De Gaudenzi, and E. Re. Smart gateways concepts for high-capacity multi-beam networks. In: Proceedings of the 18th Ka and Broadband Communications, Navigation and Earth Observation Conference; 2012; Ottawa (Canada).

[18] R. Nebuloni, C. Capsoni and M. Luccini. Advanced time series synthesizer for simulation of joint rain attenuation conditions. Radio Science. 2014;**49**(9):699–708.

[19] L. Luini, C. Capsoni. A rain cell model for the simulation and performance evaluation of site diversity schemes. IEEE Antennas and Wireless Propagation Letters. 2013; **12**(1):1327–1330.

[20] L. Luini, C. Capsoni. MultiEXCELL: a new rain field model for propagation applications. IEEE Transactions on Antennas and Propagation. 2011;**59**(11):4286–4300.

[21] L. Luini, C. Capsoni. Modeling high resolution 3-D cloud fields for earth-space communication systems. IEEE Transactions on Antennas and Propagation. 2014;**62**(10):5190–5199.

[22] L. Luini, "Modeling and Synthesis of 3-D Water Vapor Fields for EM Wave Propagation Applications", IEEE Transactions on Antennas and Propagation, vol. 64, no. 9, Page(s): 3972 –3980, September 2016.

[23] L. Luini, C. Capsoni. Joint effects of clouds and rain on Ka-band earth observation data downlink systems. European Conference on Antennas and Propagation (EuCAP) 2015, pp. 1–5, 12–17 April 2015; Lisbon, Portugal.

[24] International Telecommunication Union - Radiocommunication Sector. Recommendation ITU-R P.618-12, Propagation data and prediction methods required for the design of earth-space telecommunication systems [Internet]. 07/2015. Available from: https://www.itu.int/rec/R-REC-P.618-12-201507-I/en [Accessed: May 2016]

Chapter 4

Photon Propagation Through Dispersive Media

Patricio Robles and Francisco Pizarro

Additional information is available at the end of the chapter

http://dx.doi.org/10.5772/66673

Abstract

In the present chapter, we study the propagation of photons through dispersive media, starting from a description of the dynamics of free photons using a Dirac-like equation with an analysis of the energy solutions arising from this equation. A comparison with the case of a free electron is made. We present an analysis of the interaction between photons with the medium considering both a classical and a quantum treatment of light, and also we analyse the propagation of photons along a waveguide where they behave as if they did have a finite mass. As a technological application of the theoretical frame here presented, we consider the use of the properties of metamaterials to control the propagation of waves through waveguides filled with this kind of materials.

Keywords: photon, Hamiltonian, wave function, antiparticle, dielectrics, coherence, metamaterials

1. Introduction

Up to now, the photon is understood as the quantum of electromagnetic radiation. In 1905, Einstein proposed that energy quantization was a property of electromagnetic radiation itself. Accepting the validity of Maxwell's theory, he pointed out that several experiments with results unpredictable by the classical electrodynamics theory could be explained if the energy of a light wave was localized into point-like quanta moving independently of one another. A very simple and intuitive interpretation at the level of undergraduate teaching of quantum physics is that photons are the fundamental particles of light having the property that they behave both as a particle and a wave (wave-particle duality). They also have characteristics, which make them different from other particles. One of these characteristics is that, as theorized up to now, when freely propagating, they behave as massless particles not interacting between them and carrying linear and intrinsic angular momentum.

In modern terms, a photon is considered as an elementary excitation of the quantized electromagnetic field, and it can be treated as a (quasi-) particle, roughly analogous to an electron.

It has unique properties, arising from its zero rest mass and its spin-one nature. In particular, since the early days of quantum mechanics, it has been argued that there is no position operator for a photon, leading someone to conclude that there can be no properly defined wave function, in the Schrödinger sense, which allows to know the probability of finding the particle in a given spatial region. Nevertheless, photon position operators have been postulated whose eigenvectors form bases of localized states, as in Ref. [1].

The aim of this chapter is study the propagation of photons through dispersive media. This chapter is organized as follows. In Section 2, a semiclassical description of the dynamics of free photons is presented using a Dirac-like equation. In Section 3, the positive and negative energy solutions arising from these equations are analysed. A comparison with the case of a free electron is made. Section 4 presents an analysis of the interaction of photons with the medium considering both a classical as a quantum treatment of light. Section 5 includes an analysis of the propagation of photons along a waveguide where they behave as if they did have a finite mass. In Section 6, some technological applications of the theoretical frame here presented are shown, such as the use of the properties of metamaterials to control the propagation of waves through waveguides filled with this kind of materials.

2. A Dirac-like equation for the photon

Maxwell's equations can be considered as a classical field theory for a single photon that can be field (or "second") quantized to obtain a quantum field theory of many photons.

In Ref. [2], it has been shown that in a region without sources Maxwell's equations can be written in the form of a Schrödinger-like equation for a single photon adding a transversality condition. Although in quantum mechanics Schrödinger's equation is valid for describing the dynamics of a nonrelativistic particle, its application for the case of a photon must be considered only within the context of classical electrodynamics and taking into account that we are dealing with an equation which has the form of Schrödinger's equation and that it is equivalent to Maxwell's equations.

Considering that one important requirement of a quantum theory for describing the dynamics of photons is Lorentz invariance, in this section, we study the application of a Dirac-like equation. In Refs. [3, 4] it has been shown that Maxwell's equations without sources can be written in a form analogous to that of Dirac's equation for a free electron. These last works also show that optical spin and light orbital angular momentum can be obtained from this Dirac-like equation. As an extension of these works we give arguments for obtaining this equation in a similar form to those used for the deduction of Dirac's equation for an electron, starting from the relativistic expression for the energy. For example, see Ref. [5]. We also study the positive and negative energy states obtained from the corresponding Hamiltonian and the form that this equation takes for the propagation of a photon in a magnetodielectric medium.

As in Ref. [6], we begin with a derivation of a Dirac-like equation for a photon starting from Dirac equation for a massless particle in free motion, so that we postulate an equation of the form:

http://dx.doi.org/10.5772/66673

$$i\hbar\frac{\partial}{\partial t}\psi = \hat{H}\psi \tag{1}$$

Since Eq. (1) is linear in the time derivative, it seems natural to construct a Hamiltonian operator also linear in the spatial derivatives. This is compatible with the energy-momentum relation for the photon $E = c|\vec{p}|$ for the photon. Therefore, we postulate a Hamiltonian of the form:

$$\hat{H} = c\vec{\alpha}\cdot\vec{p} \tag{2}$$

where $\vec{p} = -i\hbar\nabla$ is the momentum operator and $\hat{H}$ is the Hamiltonian operator.

As in Ref. [7], a possible election for $\vec{\alpha}$ is a vector operator of the form

$$\vec{\alpha} = \begin{pmatrix} 0 & \vec{\tau} \\ \vec{\tau} & 0 \end{pmatrix} \tag{3}$$

where $\vec{\tau}$ is a vector matrix whose components are the spin-1 matrices

$$\tau_x = \begin{pmatrix} 0 & 0 & 0 \\ 0 & 0 & -i \\ 0 & i & 0 \end{pmatrix}; \tau_y = \begin{pmatrix} 0 & 0 & i \\ 0 & 0 & 0 \\ -i & 0 & 0 \end{pmatrix}; \tau_z = \begin{pmatrix} 0 & -i & 0 \\ i & 0 & 0 \\ 0 & 0 & 0 \end{pmatrix} \tag{4}$$

In Section 3, it is shown that the above equations lead to the relation $E = c|\vec{p}|$ for a free photon propagating in an unbounded medium, so that the Dirac-like equation given by Eq. (1) gives a solution analogous to the energy of a free fermion obtained from Dirac's equation in the limit of zero mass. Nevertheless, this must be considered only as a formal analogy since photons have spin 1 and Dirac's equation is applicable for particles of spin ½.

There exist a variety of Dirac-like formulations of Maxwell's equations and alternative ways for choosing the wave function ψ. Considering that photons have only energy and no other scalar quantities such as mass or charge, it is convenient to choose ψ so that its modulus squared correspond to energy density not of probability density for localization as is the case of a particle with mass like the electron. Therefore, we choose as wave function the following column vector of dimension $6x1$

$$\psi = \begin{pmatrix} k_1\vec{E} \\ ik_2\vec{B} \end{pmatrix} \tag{5}$$

In this last equation, the components of $\vec{E}$ and $\vec{B}$ are written as column vectors $3x1$ and taking $k_1 = \sqrt{\epsilon_0/2}$ and $k_2 = 1/\sqrt{2\mu_0}$ we obtain

$$\psi^{+}\psi = \frac{1}{2}\epsilon_0\vec{E}^2 + \frac{\vec{B}^2}{2\mu_0} = w_{\text{em}} \tag{6}$$

This last expression corresponds to the density of energy in the electromagnetic field.

For an electromagnetic wave propagating in a linear magnetodielectric and nonconducting medium, there is an induced polarization and magnetization classically represented by the polarization and magnetization vectors $\vec{P}$ and $\vec{M}$, respectively. These vectors are related with the electric and magnetic fields as $\vec{D} = \epsilon_0 \vec{E} + \vec{P}$ and $\vec{B} = \mu_0(\vec{H} + \vec{M})$. Using these relations, Maxwell's equation corresponding to Ampere's law may be rewritten as

$$\nabla \times \vec{H} = \frac{\partial \vec{D}}{\partial t} + \vec{J}_{\text{ind}} \tag{7}$$

where $\vec{J}_{\text{ind}} = \frac{\partial \vec{P}}{\partial t} + \nabla \times \vec{M}$ is an equivalent current density associated to the polarization and magnetization of the medium. In this case, the Dirac-like equation becomes

$$i\hbar \frac{\partial}{\partial t}\psi = c\vec{\alpha} \cdot \vec{p}\ \psi - \frac{i\hbar}{2k_1}\tilde{J} \tag{8}$$

where $\tilde{J} = \begin{pmatrix} \vec{J}_{\text{ind}} \\ 0 \end{pmatrix}$ is a column matrix of dimension 6x1.

From Eq. (8), a continuity equation for the wave function ψ may be derived taking the scalar product with ψ^+ on both sides, obtaining

$$\frac{1}{2}\frac{\partial}{\partial t}|\psi^2| = -c\psi^+ \vec{\alpha} \cdot \nabla\psi - \frac{i\hbar}{2k_1}\psi^+ \cdot \tilde{J} \tag{9}$$

Using Eqs. (6)–(9) and the definition of the column matrix $\tilde{J}$ given previously, one obtains the classical equation for conservation of electromagnetic energy

$$\frac{\partial}{\partial t}\left\{\epsilon_0 \vec{E}^2 + \mu_0 \vec{H}^2\right\} + \vec{E} \cdot \vec{J}_{\text{ind}} = -\nabla \cdot (\vec{E} \times \vec{H}) \tag{10}$$

3. Positive and negative energy states for a photon

The energy eigenvalues are obtained by looking for stationary state solutions of the Dirac-like equation. A plane wave solution of this equation has the form

$$\psi_k(\vec{r}, t) = A_k \exp\left[\frac{i}{\hbar}(\vec{p} \cdot \vec{r} - \hbar\omega t)\right] \tag{11}$$

for $k = 1$ to 6, where $\vec{p}$ is the momentum vector and ω is the angular frequency. Considering a momentum vector with components along two directions, for example, parallel to x and y

http://dx.doi.org/10.5772/66673

axes, from Eqs. (2) and (3), it can be shown that the values of the energy for a photon can be obtained from the eigenvalues of the 3x3 matrix $(c\vec{\tau}\cdot\vec{p})^2$ for this case given by:

$$(c\vec{\tau}\cdot\vec{p})^2 = c^2\begin{bmatrix} p_y^2 & -p_x p_y & 0 \\ -p_x p_y & p_x^2 & 0 \\ 0 & 0 & p_x^2+p_y^2 \end{bmatrix} \tag{12}$$

The corresponding solutions for the energy are $E=+cp$, $E=-cp$ and $E=0$ where $p=|\vec{p}|$. The negative energy solution may be interpreted using Feynman concept of antiparticles associating to photon states going backward in time and postulating that the photon is its own antiparticle. For example, see Refs. [8, 9]. The solution $E=0$ has no physical meaning since it would imply that a photon in vacuum could be at rest (zero momentum) and from the point of view of classical electrodynamics, it would result in an electromagnetic wave propagating in an unbounded medium with a field component parallel to the direction of propagation, what is not compatible with Maxwell's equations. That can be seen if one considers, for example, motion along the z direction with momentum $p_z=p$. In that case, the calculation of the eigenvalues and eigenvectors of the Hamiltonian given by Eq. (2) shows that the positive and negative energy solutions are valid because they are compatible with an electromagnetic wave propagating in vacuum and satisfying the condition that the electric and magnetic field vectors must have only transversal components (that is perpendicular to the z axis in this case). On the other hand, the solutions with zero energy are not valid since they imply that the electric or magnetic field have longitudinal components (parallel to the direction of propagation).

It is important to consider that Dirac's equation for a particle like an electron only gives positive and negative energy solutions.

4. Interaction between photons and the medium

4.1. Introduction

When light passes through a material, there is an electromagnetic interaction with the particles of the medium. This interaction is macroscopically manifested by two main effects: absorption of energy from the incident beam and scattering.

Considering that every particle has electric charge that acquires a motion due to the electric field associated to the incident electromagnetic wave, the absorption of energy may be understood using a phenomenological model of electric dipoles with negative charges whose positions oscillate with respect to the centre of positive charges, with a frequency corresponding to that of the incident light. This oscillatory motion has a damping associated to the dielectric losses.

The scattering of light may be thought of as the redirection that takes place when an electromagnetic wave encounters an obstacle or non-homogeneity. The accelerated motion of the

charges gives rise to radiation of electromagnetic energy in all directions producing secondary waves, process known as scattering.

4.2. Classical model for the interaction between light and matter

A classical model for representing the optical response of a polarizable medium through which travels a monochromatic electromagnetic wave of frequency ω is the Drude model where it is imagined that due to the electric field vector associated to this wave, each electron bound to the nucleus of an atom performs harmonic oscillations. Therefore, oscillating electric dipoles are formed, and considering that the electric dipolar moment is related to the electric field through the atomic polarizability $\alpha(\omega)$, we get

$$\alpha(\omega) = \frac{e^2/m}{\omega_{oe}^2 - \omega^2 - i\Gamma_d} \tag{13}$$

In this last equation, $\omega_{oe} = \sqrt{k/m}$ is the natural frequency of oscillation, $\Gamma_d = \gamma/m$ is the absorption parameter and m is the mass of the electron.

At a macroscopic scale, the formation of electric dipoles in a dielectric material subjected to an applied electric field is described by means of the polarization vector $\vec{P}$ defined as the electric dipolar moment per unit of volume and related with the electric field and displacement vectors as

$$\vec{D} = \epsilon_0 \vec{E} + \vec{P} = \epsilon_0 \vec{E} + \chi \epsilon_0 \vec{E} = \epsilon \epsilon_0 \vec{E} \tag{14}$$

In this last equation, χ is the dielectric susceptibility and $\epsilon = 1 + \chi$ is the dielectric function which in general depends on the frequency ω.

If n is the volumetric density of molecules dipoles each one with Ze electrons, the polarization vector is rewritten as

$$\vec{P} = \frac{nZ_e^2/m}{\omega_{oe}^2 - \omega^2 - i\Gamma_d} \vec{E} \tag{15}$$

Therefore, we obtain the Drude model for the dielectric function:

$$\epsilon(\omega) = 1 + \frac{\omega_{pe}^2}{\omega_{oe}^2 - \omega^2 - i\Gamma_d} \tag{16}$$

where ω_{pe} is the plasma frequency given by $\omega_{pe}^2 = nZ_e^2/m\epsilon_0$.

From Eq. (16), it can be seen that a lossy dielectric medium has a complex refraction index $n_r = \sqrt{\epsilon(\omega)}$ whose imaginary part is associated to the attenuation of the intensity of an electromagnetic wave propagating in this medium due to absorption of energy.

For the magnetic permeability, as in Ref. [10], a Drude-Lorentz model similar to that given by Eq. (16) can be used:

http://dx.doi.org/10.5772/66673

$$\mu(\omega) = 1 + \frac{\omega_{\mathrm{pm}}^2}{\omega_{\mathrm{Te}}^2 - \omega^2 - i\Gamma_{\mathrm{dm}}} \tag{17}$$

where ω_{pm} is the magnetic coupling strength, ω_{Te} is the transverse resonance frequency, and Γ_{dm} is the absorption parameter. The real part of $\epsilon(\omega)$ and $\mu(\omega)$ are negative for the following frequency ranges:

$$\omega_{\mathrm{oe}}^2 < \omega^2 < \omega_{\mathrm{oe}}^2 + \omega_{\mathrm{pe}}^2 \text{ for } Re[\epsilon(\omega)] < 0$$

$$\omega_{\mathrm{Tm}}^2 < \omega^2 < \omega_{\mathrm{Tm}}^2 + \omega_{\mathrm{pm}}^2 \text{ for } Re[\mu(\omega)] < 0$$

When both $\epsilon(\omega)$ and $\mu(\omega)$ have negative real parts, the real part of the index of refraction is also negative and the medium has the behaviour of a left-handed material (also known as a double-negative material) with the Poynting vector and the wave vector having opposite directions. For example, see Ref. [11].

4.3. Quantum treatment

When an incident pulse enters into a dielectric medium, it undergoes modifications due to dispersion and absorption and in the case of a dielectric slab due to reflections from its surfaces. These modifications give rise to a distortion of the transmitted pulse in comparison with the incident pulse. Furthermore, the transmission of the pulse may be affected by thermal emission from the slab at elevated temperatures.

In classical electrodynamics, the interaction of light with matter is performed in two stages. First, an explicit model of the medium is assumed and its response to an electromagnetic field is calculated. The interaction is represented by the dielectric function, which embodies the optical properties of the material. In the second stage, this dielectric function is used for studying the propagation of the electromagnetic wave through the medium, determining effects as energy absorption and velocity of propagation. Nevertheless, for a finite number of photons, there are effects that cannot be described by a classical approach such as zero average electric field between two conducting plates and electric force between the plates even if the number of photons is zero (the so-called vacuum fluctuation and Casimir forces, respectively). In addition, for a nonclassical pulse propagating in an absorbing and dispersive medium, there are modifications in the correlation properties that can only be described by a quantum theory of the photon.

As in Refs. [12, 13], the formalism for electromagnetic field quantization in a dispersive and absorbing dielectric, in general, includes the following steps:

1. Express Maxwell's equations in terms of transverse electric and magnetic vector operators obtained from a vector potential operator.
2. Express the above vector potential operator as a function of the complex refraction index and of a current operator associated with noise sources coupled with the electromagnetic field in presence of lossy dielectrics.

3. Incorporate boson-type operators and commutation relations between the electromagnetic field operators.

In what follows, we illustrate the application of this procedure for the case of light propagating in the x direction in a dielectric homogeneous medium with index of refraction $n_r = \eta(\omega) + iK(\omega)$, focusing our analysis in the determination of the first-order correlation of the electromagnetic field in two separate points at the same instant.

As shown in Ref. [12] for a state with N photons, the quantum field-field correlations between two points placed over the x axis at positions x_1 and x_2 are

$$\langle E(x_1,\omega)E(x_2,\omega)\rangle = \frac{N^2\hbar\omega \exp[-K\omega|x_2-x_1|/c]}{\epsilon_0 cS(\eta^2+K^2)}\left\{\eta\cos\left(\frac{\eta\omega|x_2-x_1|}{c}\right)+K\sin\left(\frac{\eta\omega|x_2-x_1|}{c}\right)\right\}. \tag{18}$$

$$\langle E(x_1,\omega)E(x_1,\omega)\rangle = \frac{N^2\hbar\omega}{\epsilon_0 cS(\eta^2+K^2)}\eta \tag{19}$$

We consider the following definition of the spatial first-order coherence function for two points placed over the x axis and separated by a distance s (e.g., see Refs. [14, 15])

$$g^{(1)} = \left|\frac{\langle E(x,\omega)E(x+s,\omega)\rangle}{E(x,\omega)E(x,\omega)}\right| \tag{20}$$

Therefore, from Eqs. (18–20), we obtain

$$g^{(1)} = \frac{\exp[-K\omega|x_2-x_1|/c]}{\eta}\left\{\eta\cos\left(\frac{\eta\omega|x_2-x_1|}{c}\right)+K\sin\left(\frac{\eta\omega|x_2-x_1|}{c}\right)\right\} \tag{21}$$

As an example, we make a comparison of this last result with that obtained calculating the classical coherence function. For that purpose, we consider a beam of light produced by excitation of two linearly polarized waves with frequencies ω_1 and ω_2 propagating in the x direction in a medium with refraction index $n_r(\omega)$ so that the resulting electric field is

$$\vec{E}\,(x,t) = \hat{y}E_1\exp\left[i\frac{\omega_1}{c}\left(n_r(\omega_1)x-ct\right)\right] + \hat{y}E_2\exp\left[i\frac{\omega_2}{c}\left(n_r(\omega_2)x-ct\right)\right] \tag{22}$$

The Fourier transform of this field is

$$\vec{E}\,(x,\omega) = \hat{y}E_1\exp\left[i\frac{n_r(\omega_1)\omega_1}{c}x\right]\delta(\omega-\omega_1) + \hat{y}E_2\exp\left[i\frac{n_r(\omega_2)\omega_2}{c}x\right]\delta(\omega-\omega_2) \tag{23}$$

From the definition of the classical spatial coherence function:

$$\langle E(x,\omega)E(x+s,\omega)\rangle = \frac{1}{L}\int_0^L \mathrm{d}x[E(x,\omega)]^*[E(x+s,\omega)] \tag{24}$$

http://dx.doi.org/10.5772/66673

we obtain that the classical spatial first order coherence function calculated for this case is

$$g_{cl}^{(1)}(\omega) = \exp\left[\frac{-K(\omega)\omega s}{c}\right] \tag{25}$$

Due to the exponential factor of this last equation, the classical coherence function for the considered case has a value lower than 1 meaning that measurements of the electric field at two separated points are partially correlated in a medium with absorption and for $s \to \infty$ the correlation goes to zero.

Comparing Eqs. (21) and (25), it can be seen that if absorption is neglected the classical model predicts total coherence, while the quantum treatment in this case gives an oscillatory behaviour of the spatial coherence function with respect to the distance between the points considered, with null partial coherence for some values of this distance. It is worth to note that this result is also valid for a left-handed medium if absorption may be neglected.

5. Propagation of photons through a waveguide

When the propagation of an electromagnetic wave of a given frequency ω is restricted to a region bounded by conducting walls, as is the case of a waveguide, the photon appears to acquire an effective mass. For example, see Ref. [16]. For flow along the waveguide axis, the action of confinement may be viewed as yielding longitudinal photons propagating with a mass proportional to the cut-off frequency of the corresponding electromagnetic mode.

This is illustrated considering the propagation of a transverse electric (TE) mode in a rectangular waveguide with transversal section having dimensions a and b in the plane xy. We consider propagation along the z direction taken parallel to the axis of the waveguide. As known, the magnetic field in the TE mode of order nl in a rectangular waveguide has a component parallel to the direction of propagation of the guided light (axial component), while the electric field has only transverse components. As shown in Ref. [17], each component of the electromagnetic field satisfies a Klein-Gordon-like equation:

$$\left[\frac{1}{c^2}\frac{\partial}{\partial t^2} - \frac{\partial^2}{\partial z^2} + \frac{m_\gamma^2 c^2}{\hbar^2}\right]\psi_j = 0 \tag{26}$$

where $m_\gamma = \hbar k_c/c = \hbar\pi\sqrt{(n/a)^2 + (l/a)^2}/c$ is the effective mass acquired by the photon.

For a relativistic fermion of mass m, Klein-Gordon's equation can be obtained from Dirac's equation. For example, see Ref. [18]. This makes natural to wonder what is the form that the Dirac-like equation takes for a photon moving along a waveguide. This can be determined writing the Dirac-like equation in the following form:

$$i\hbar\alpha^{\mu}\partial_{\mu}\psi = 0 \tag{27}$$

with $\alpha^{\mu} = (\alpha^0, -\vec{\alpha})$, $\partial_{\mu} = \partial/\partial x^{\mu}$, $x^{\mu} = (t, -\vec{r})$, $\partial_0 = \partial/\partial(ct)$ and

$$\alpha^0 = \begin{pmatrix} I_{3\times3} & 0 \\ 0 & -I_{3\times3} \end{pmatrix} \tag{28}$$

For a photon moving along the waveguide, let us write the wave functions as

$$\psi(t, \vec{r}) = \varphi(t, z)\exp[-i(k_x x + k_y y)] \tag{29}$$

From Eqs. (27) and (29), we get

$$\frac{i\hbar}{c}\alpha^{o}\frac{\partial\varphi}{\partial t} + i\hbar\alpha_z\frac{\partial\varphi}{\partial z} + (\hbar k_x\alpha_x + \hbar k_y\alpha_y)\varphi = 0 \tag{30}$$

This last equation may be recast as

$$i\hbar\alpha^{\mu}\left(\partial_{L\mu} - i\frac{p_{T\mu}}{\hbar}\right)\varphi = 0 \tag{31}$$

For propagation along the z direction, as it is considered in this case:

$$\partial_{L\mu} = \left(\frac{\partial}{c\partial t}, \frac{\partial}{\partial z}, 0, 0\right); p_{T\mu} = (0, p_x, p_y, 0)$$

Equation (31) is the Dirac-like equation for photons moving along the waveguide and it can be shown that leads to the Klein-Gordon equation applying the operator ∂_L^{μ} by the left and considering that $p_{T\mu}p^{T\mu} = -(m_\gamma c)^2$.

6. Some technological applications

On the last years, several articles about the properties of a special kind of materials, known as metamaterials, have been published. These materials can exhibit negative values on their permittivity or permeability. They are also named "left handed materials" and can have negative refraction index, which leads to interesting phenomena for the wave propagation. The effect of negative refraction was predicted in 1968 by Veselago in Ref. [19], principle that has led to many technological applications. For example, see Ref. [20]. Nowadays is possible to build artificial metamaterials with different geometries. These arrays can achieve negative values of permittivity or permeability, achieving either single negative material (SNG), where ϵ or μ are negative, or double negative material (DNG), where both ϵ and μ are negative. On the other hand, natural medias, such as plasmas, can behave as an SNG media, depending on its physical characteristics.

http://dx.doi.org/10.5772/66673

Metamaterials constructed by circuit arrays are based on a group of elements organized periodically, and designed in order to respond to an impinging electromagnetic field. The size and spacing of each element of the array must be much lower than the wavelength of the wave interacting with the array. This will allows that the impinging wave interacts with the artificial material as a homogeneous material with certain ϵ and μ characteristics.

There are different type of structures to obtain negative permittivity and permeability. To obtain a negative permittivity, periodic structures based on wire arrays that are based on the Drude-Lorentz model for dielectric constant are used. For example, see Refs. [21–23]. On the other hand, to obtain negative permeability values, split ring resonators (SRR) and the induced current on wire structures are used, as can be seen in Refs. [21, 24, 25]. Currently, we can find two kind of artificial metamaterials that can exhibit negative refraction: photonic crystals, as shown in Refs. [26, 27], and composite materials as shown in Ref. [28]. Composite materials exhibit simultaneously negative permittivity and permeability within a certain frequency range. This immediately leads to a negative index of refraction. Dielectric photonic crystals are composed of materials with positive ϵ' and μ' but exhibit negative refraction because of peculiarities of dispersion characteristics at some frequencies, as shown in Ref. [29].

The possibility of having SNG or DNG metamaterials opens a huge number of new applications that these physical characteristics can offer. Some examples of these applications are invisible materials or cloaking, as shown in Refs. [30, 31], phase control of propagating modes on waveguides, as shown in Refs. [32, 33], antenna miniaturization as shown in Refs. [34, 35], and superlens, as shown in Refs. [36, 37].

For each application, the design parameters of the metamaterials are an important issue. If the parameters that determine the permittivity and permeability of the material are known beforehand, it is possible to predict the behaviour of the electromagnetic wave that propagates on the media. The following study is intended to analyse the possible variations of the wavenumber of metamaterials, depending on their design parameters.

6.1. Wavenumber on SNG media depending on metamaterial parameters

The first analysis to be developed is the variation of the wavenumber in terms of the material properties. The complex relative permittivity and permeability of the metamaterials (either real or artificial) can be modelled by adopting a simplified Drude's model, which uses the following expressions based in Ref. [38]:

$$\epsilon_r(\omega) = 1 - \frac{{\omega_{\mathrm{pe}}}^2}{\omega(\omega - i\Gamma_{\mathrm{e}})} \tag{32}$$

$$\mu_{\mathrm{r}}(\omega) = 1 - \frac{{\omega_{\mathrm{pm}}}^2}{\omega(\omega - i\Gamma_{\mathrm{m}})} \tag{33}$$

where ω_{pe} and ω_{pm} correspond to the plasma frequency, Γ_{e} and Γ_{m} correspond to the damping frequencies, and ω is the angular frequency of the impinging wave on the metamaterial. On the design of metamaterials, it is important to know the behaviour of these parameters in order to

characterize the impinging wave on the media. In the analysis of artificial metamaterials, the damping frequencies are not considered or neglected, which implies that are considered as lossless metamaterials. In other materials, such as cold plasmas, we cannot ignore this parameter because implies that we are ignoring the plasma collision frequency, which is fundamental for the plasma generation, and depends on the gas parameters of the plasma. Nevertheless, it is important to consider the losses in the design of any metamaterial in order to have a better estimation of the behaviour of the impinging wave on the metamaterial, and knowing beforehand for which frequencies the metamaterial will behave as a SNG or DNG material.

One way to describe the behaviour of the wave is to describe the permittivity o the permeability as function of a parameter ratio, and use this relation on the wavenumber k. Let us take for example the permittivity described in Eq. (48) and express it on terms of ω_{pe}/ω and Γ_e/ω in the form:

$$\epsilon_r = 1 - \frac{\left(\frac{\omega_{pe}}{\omega}\right)^2}{1+\left(\frac{\Gamma_e}{\omega}\right)^2} - i\frac{\left(\frac{\omega_{pe}}{\omega}\right)^2\left(\frac{\Gamma_e}{\omega}\right)}{1+\left(\frac{\Gamma_e}{\omega}\right)^2} \tag{34}$$

Figure 1 shows the real and imaginary part of the relative permittivity as function of ω_{pe}/ω and Γ_e/ω.

From **Figure 1(a)** and **(b)**, we can notice the necessary ratios of ω_{pe}/ω and Γ/ω for achieving a negative permittivity on a lossy media. Considering those ratios also, we can estimate the losses due to the increment of the imaginary part of the relative permittivity of the SNG media. For example, if we want a negative permittivity of $\varepsilon_r = -10$, is possible to obtain it only within the ratios $\omega_{pe}/\omega > 3$ and $\Gamma/\omega < 3$. By knowing these ratios, it is possible to see where the imaginary part of the permittivity will be lower, and so, the losses. Therefore, it is possible to extend this analysis on a media with negative permeability instead of negative permittivity.

After the analysis of the permittivity or permeability on a media than can achieve SNG characteristics, we can express the complex wavenumber k of a wave propagating on an infinite media where its permittivity can have negative values, normalized by the wavenumber on free space k_0 (**Figure 2**). By knowing the complex wavenumber of the wave

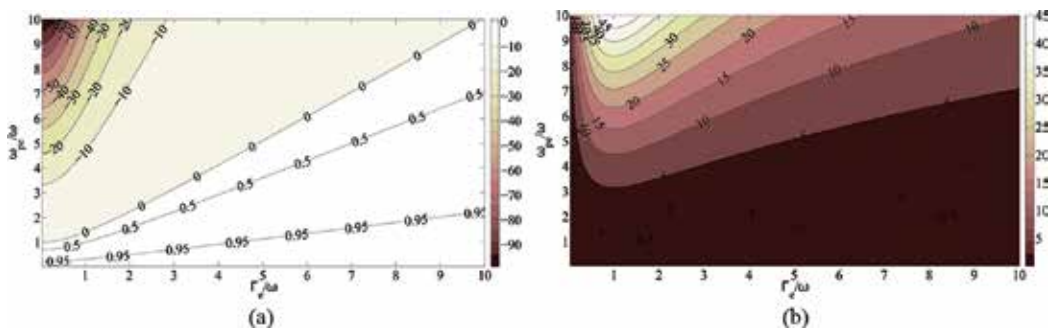

Figure 1. Complex relative permittivity of a media depending on the ω_{pe}/ω and Γ/ω ratios. (a) Real part of the relative permittivity. (b) Imaginary part of the relative permittivity.

http://dx.doi.org/10.5772/66673

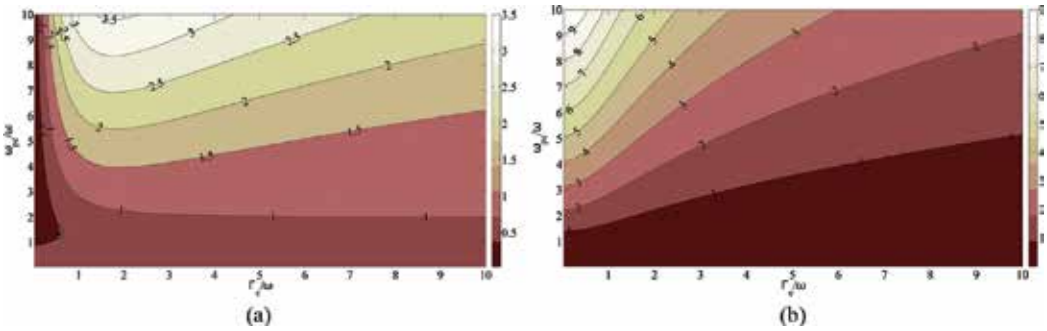

Figure 2. Variation of the wavenumber k in a lossy media with complex permittivity depending on the ω_{pe}/ω and Γ/ω ratios. (a) Real part of k normalized by k_0 (rad/m). (b) Imaginary part k normalized by k_0 (Np/m).

propagating on a media, we can determine for example the cut-off frequency of a waveguide filled with the material.

If we consider the wavenumber $k = \omega\sqrt{\epsilon\mu}$, where only ϵ or μ can be negative and the other parameter remains positive (SNG media), there are two interesting cases. If we consider a lossless media ($\Gamma_e = 0$), the wavenumber expression becomes:

$$k = k_0\sqrt{1-\frac{\omega_{pe}^2}{\omega^2}} \tag{35}$$

When $\omega \ll \omega_{pe}$, and considering a lossless media, the wavenumber becomes purely imaginary and there is no propagation on the media ($k \approx ik_0\,\omega_{pe}/\omega$). On the other hand, when $\omega \gg \omega_{pe}$, the waves propagates on the media with a wavenumber with a value near k_0. When the media presents losses, there is always propagation on the media, even if $\omega \ll \omega_{pe}$. The propagation in this case will occur with an attenuation, that depending of the values of Γ_e, can be important.

Equation (35) may be related with the description in terms of massive photons propagating in a plasma: As shown in Ref. [16], the presence of the plasma decreases the rate of electromagnetic energy flow, reaching a zero speed when $\hbar\omega = \hbar\omega_p = m_\gamma c^2$, a photon energy below which the propagation is not possible.

6.2. Wavenumber on DNG media depending on metamaterial parameters

It is possible to do a further analysis considering now a variation of the permittivity and permeability where both takes negatives values (DNG media). In this case, we will consider a material with its permittivity an permeability following the Drude's model expressed in Eqs. (20) and (21), and its parameters changes equally in terms of the ratios ω_p/ω and Γ/ω ratios ($\omega_{pe}/\omega = \omega_{pm}/\omega$ and $\Gamma_e/\omega = \Gamma_m/\omega$). **Figure 3** shows the real and complex values of the wavenumber k of the described material. Using this last figure we can relate the values of the wavenumber and the ratios ω_p/ω, Γ/ω when both permittivity an permeability are negative. For these calculations, some values of k'' can result on negative values (remember that here

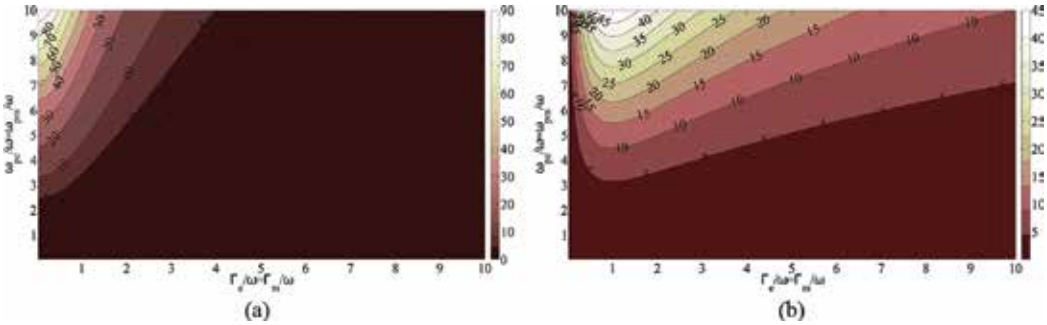

Figure 3. Variation of the wavenumber k in a lossy media where ϵ and μ can be negative (DNG) depending on the $\omega_{pe}/\omega = \omega_{pm}/\omega$ and $\Gamma_e/\omega = \Gamma_m/\omega$ ratios. (a) Real part of k normalized by k_0 (rad/m). (b) Imaginary part k normalized by k_0 (Np/m).

both permittivity and permeability can be negative). As this is not possible, because the imaginary part must be positive due to the conservation of energy, as shown in Ref. [39], there is a change of sign for those values. For these calculations, some values of k'' can result on negative values (remember that here both permittivity and permeability can be negative).

In a more practical way, both ratios are not necessarily modified in the same way. Normally, the periodical structures can present with different parameters of design its negative permittivity or permeability. This means that ω_{pe}/ω ratio does not change in the same way that ω_{pm}/ω and Γ_e/ω do not change in the same way that Γ_m/ω. For solving this problem, we can rewrite Eqs. (32) and (33) in terms of other parameters as follows, so we can relate the different changes of permittivity and permeability.

$$\epsilon_r = 1 - \frac{\left(\frac{\omega_{pe}}{\Gamma_e}\right)^2}{1 + \left(\frac{\omega}{\Gamma_e}\right)^2} - i\frac{\left(\frac{\omega_{pe}}{\Gamma_e}\right)^2}{\left(1 + \left(\frac{\omega}{\Gamma_e}\right)^2\right)\left(\frac{\omega}{\Gamma_e}\right)} \tag{36}$$

$$\mu_r = 1 - \frac{\left(\frac{\omega_{pm}}{\Gamma_m}\right)^2}{1 + \left(\frac{\omega}{\Gamma_m}\right)^2} - i\frac{\left(\frac{\omega_{pm}}{\Gamma_m}\right)^2}{\left(1 + \left(\frac{\omega}{\Gamma_m}\right)^2\right)\left(\frac{\omega}{\Gamma_m}\right)} \tag{37}$$

Expressing the complex permittivity and complex permeability in terms of ω_{pe}/Γ_e, ω_{pm}/Γ_m, ω/Γ_e and ω/Γ_e allows to describe in a more independent way the effects of the material parameters on the design of the metamaterial and the resultant permittivity or permeability. Other important thing to consider is that in practice, the angular frequency of the impinging wave on the media is higher that the damping frequencies ($\omega \gg \Gamma$) due to the applications involved on the use of metamaterials. If we fix a ratio of ω/Γ_e and ω/Γ_m, we can analyse the variation of the permittivity and permeability, and so the wavenumber, depending on the ω_{pe}/Γ_e and ω_{pm}/Γ_m ratios. **Figure 4** shows the real and imaginary part of the relative permittivity as function of ω_{pe}/Γ_e with a ω/Γ_e ratio equals to 5 and ω/Γ_e ratio equals to 10.

http://dx.doi.org/10.5772/66673

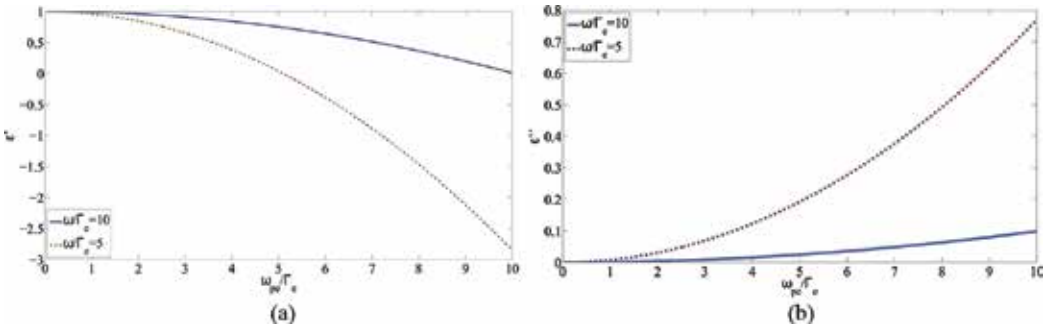

Figure 4. Complex relative permittivity of a media depending on the ω_{pe}/Γ_e. (a) Real part of the relative permittivity. (b) Imaginary part of the relative permittivity.

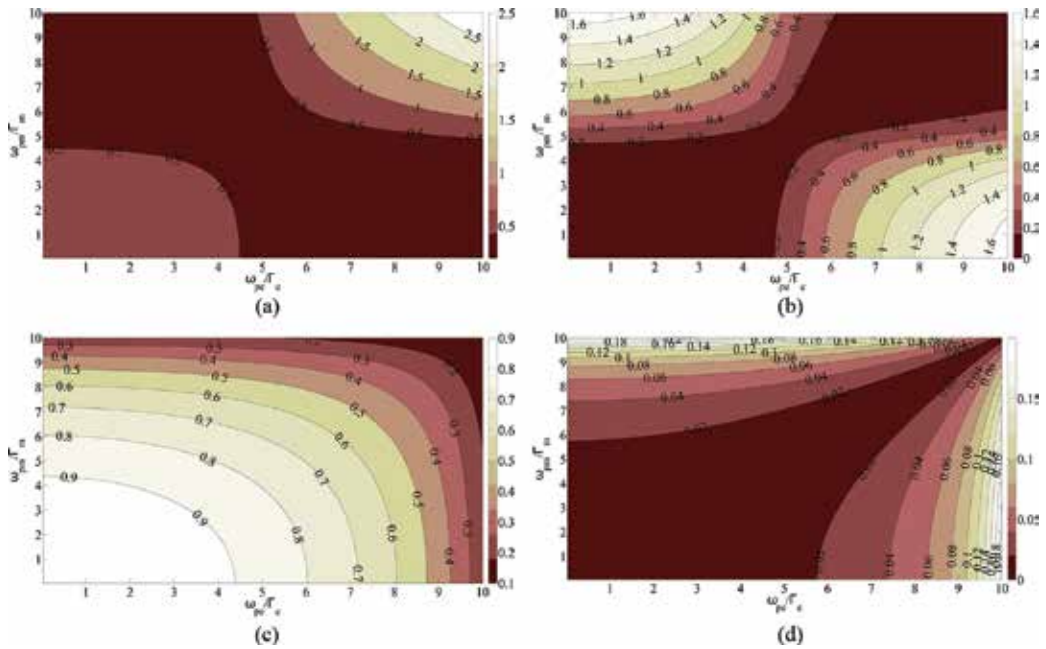

Figure 5. Variation of the wavenumber k in a lossy media where ϵ and μ can be negative (DNG) depending on the ω_{pe}/Γ_e and ω_{pm}/Γ_m ratios, having a fixed ω/Γ ratio ($\omega/\Gamma_e = \omega/\Gamma_m$= 5 and $\omega/\Gamma_e = \omega/\Gamma_m$= 10). (a) Real part of k normalized by k_0 (rad/m) when $\omega/\Gamma_e = \omega/\Gamma_m = 5$. (b) Imaginary part k normalized by k_0 (Np/m) when $\omega/\Gamma_e = \omega/\Gamma_m = 5$. (c) Real part of k normalized by k_0 (rad/m) when $\omega/\Gamma_e = \omega/\Gamma_m = 10$. (d) Imaginary part k normalized by k_0 (Np/m), when $\omega/\Gamma_e = \omega/\Gamma_m = 10$.

From **Figure 4**, we can observe when the material have negative or positive values of ϵ. Extending this analysis to μ_r, we can determine the ratios of ω_p/Γ, where the material will exhibit a DNG behaviour. Having this information, as shown in **Figure 5**, we can trace the wavenumber in function of the different variations of ω_{pe}/Γ_e and ω_{pm}/Γ_m having a fixed ω/Γ ratio ($\omega/\Gamma_e = \omega/\Gamma_m$= 5 and $\omega/\Gamma_e = \omega/\Gamma_m$= 10).

From this analysis, we can notice that the values of the attenuation and of the phase constant will vary depending of the design parameters of ω_{pe}/Γ_e and ω_{pm}/Γ_m. However, it is important to consider the ratio between ω/Γ_m, in terms that depending of this value, we can achieve or not the DNG behaviour of the material.

In conclusion, for the design of metamaterials, it is important to know how the parameters that are described on the Drude's model vary, in order to predict the behaviour of the wave that propagates on the media.

7. Discussion

From the point of view of unification of electromagnetic fields and relativistic quantum theory, it is useful to study the dynamics of a photon in a form comparable with the case of a particle like an electron. As a first stage towards this unification, an important result is that the Dirac-like equation allows to write Maxwell's equations in a compact form and that for light propagating in an homogeneous medium this equation has energy solutions similar to those obtained by Dirac's equation for fermions in the limit of zero mass, except that in this case there is no a solution with zero energy. Nevertheless, this must be considered only as a formal analogy since photons have spin 1 and Dirac's equation is applicable for particles of spin ½.

Among other issues related with the behaviour of photons that have been a matter of discussion in several publications, it is worth to mention those concerned with localizability, Zitterbewegung and its relation with spin.

The localizability of massless photons was first examined in Ref. [40] by Newton and Wigner and later by Wightman in Ref. [41], showing that there is no position operator for a massless particle with spin higher than ½ leading many authors to conclude that it is not possible to define a wave function for a photon, which has zero mass and spin (or helicity) 1. Wightman has proved that the only localizable massless elementary system has spin zero and that a free photon is not localizable.

However, Bialynicki-Birula in Refs. [42, 43] and, independently, Sipe in Ref. [44] introduced a function of the position and time coordinates that completely describes the quantum state of a photon. Such function may be referred to as the photon wave function. The wave equation for this function can be derived from the Einstein kinematics for a particle with spin 1 and zero mass in the same way that the Dirac equation is obtained for a massive particle with spin ½. For example, see Refs. [45, 46]. A strong argument in favour of this photon wave function formulation is that the corresponding wave equation is completely equivalent to the Maxwell equations in vacuum. In addition in Ref. [1], a position operator has been postulated whose eigenvectors form bases of localized states.

The concept of spin of a photon and its relation with Zitterbewegung is still a matter of discussion and deserves further research. In Ref. [47], it has been postulated that the spin of the photon can be considered as a consequence of the orbital angular momentum due to the photon's Zitterbewegung. This postulate is based on a Schrödinger-like equation, having a

velocity operator that undergoes oscillations in a direction orthogonal to its momentum, effect known as Zitterbewegung, with a spatial amplitude equal to the classical wavelength. The spin of the photon would be the orbital angular momentum due to the Zitterbewegung. Nevertheless, up to now, this is a theoretical postulate which results from an equation of the form of Schrödinger's equation which is known, was formulated for a nonrelativistic particle. In this context it seems formally more suitable to use a Dirac-like equation.

8. Conclusion

We have presented a conceptual frame for understanding the propagation of light through a dispersive and absorptive medium, considering both the classical description based on electromagnetic waves and a quantum description considering photons as elementary excitations of the quantized electromagnetic field.

A semiclassical description of the dynamics of a photon propagating freely in an unbounded medium has been presented using a Dirac-like equation, discussing the solutions for the energy and comparing with those corresponding to a free electron as given by the Dirac's equation.

The interaction of light with the medium of propagation has been analysed using both a classical and a quantum treatment. In particular and as a specific example, the first-order field-field spatial correlation for a beam of light produced by the excitation of two linearly polarized waves has been calculated, comparing results between the classical and quantum model. For this specific case, it is concluded that in absence of absorption, the classical model predicts total coherence at all points, while the quantum treatment predicts that for some distances between the considered points there is null coherence.

The propagation of light along a rectangular waveguide has been studied showing how the Dirac-like equation previously studied is modified due to the bounding conditions in the propagation imposed by the conducting walls verifying the result obtained in several publications that in this condition photons appear to acquire an effective mass.

As an application to communication engineering, we have analysed conditions for which the dielectric permittivity and magnetic permeability of a medium filled with plasma behaves as a metamaterial.

Author details

Patricio Robles* and Francisco Pizarro

*Address all correspondence to: probles@ucv.cl

Escuela de Ingeniería Eléctrica, Pontificia Universidad Católica de Valparaíso, Chile

References

[1] Hawton M. Photon wave mechanics and position eigenvectors. Phys. Rev. A. 2007; **75**: 062107–062120. DOI: 10.1103/PhysRevA.75.062107

[2] Kobe D.H. A relativistic Schrödinger-like equation for a photon and its second quantization. Found. Phys. 1999; **29**: 1203–1231. DOI: 10.1023/A:1018855630724

[3] Barnett S.M. Optical Dirac equation. New J. Phys. 2014; **16**: 093008-1–093008-25. DOI: 10.1088/1367-2630/16/9/093008

[4] Mohr P. Solutions of the Maxwell equations and photon wave functions. Ann. Phys. 2010; **325:** 607–663. DOI: 10.1016/j.aop.2009.11.007

[5] Robles P. An introduction to relativistic quantum mechanics: a round trip between Schrödinger and Dirac equations. Int. J. Eng. Tech. Res. (IJETR). 2016; **4**: 125–132. ISSN: 2321-0869 (P)

[6] Thaller B. The Dirac Equation. 1st ed. Berlin, Heidelberg, New York: Springer-Verlag, 2000

[7] Zhi-Yong W., Cai-Dong X., Bing H.E. Quantum mechanical description of waveguides. Chin. Phys. B. 2008; **17**: 3985–3997. DOI: 10.1088/1674-1056/17/11/008

[8] Feynman R.P. Quantum Electrodynamics. New York: Benjamin, 1962, pp. 66–70.

[9] Feynman R.P. The theory of positrons. Phys. Rev. 1949; **76**: 749–759. DOI: 10.1103/PhysRev.76.749

[10] Ruppin R. Electromagnetic energy density in a dispersive and absorptive material. Phys. Lett. A. 2002; **299**: 309–312. DOI: 10.1016/S0375-9601(01)00838-6

[11] Dung Ho T., Buhmann S.Y., Knöll L., Welsh D.G., Scheel S. Electromagnetic-field quantization and spontaneous decay in left-handed material. Phys. Rev. A. 2003; **68**: 043816–043832. DOI: 10.1103/PhysRevA.68.043816

[12] Matloob R., Loudon R., Barnett S.M., Jeffers J. Electromagnetic field quantization in absorbing dielectrics. Phys. Rev. A 1995; **52**:4823–4838. DOI: 10.1103/PhysRevA.52.4823

[13] Huttner B., Barnett S.M. Quantization of the electromagnetic field in dielectrics.Phys. Rev. A 1992; **46**: 4306–4322. DOI: 10.1103/PhysRevA.46.4306

[14] Loudon R. The Quantum Theory of Light. 3rd. Ed. Oxford, UK: Oxford University Press, 2000.

[15] Gerry C.G., Knight P.L. Introductory Quantum Optics. Cambridge UK: Cambridge University Press, 2005.

[16] Robles P., Claro F. Can there be massive photons? A pedagogical glance at the origin of mass. Eur. J. Physics. 2012; **33**: 1217–1226. DOI: 10.1088/0143-0807/33/5/1217

[17] Rojas R., Robles P. Teaching on the common aspects in mechanical, electromagnetic and quantum waves at interfaces and waveguides. Eur. J. Phys. 2011; **32**: 1–11. DOI: 10.1088/0143-0807/32/6/019

[18] Greiner W. Relativistic Quantum Mechanics Wave Equations. 3rd. Ed. Berlin, Heidelberg, New York: Springer-Verlag, 2000.

[19] Veselago V. The electrodynamics of substances with simultaneously negative values of ε and μ. Soviet Physics Uspekhi. 1968; **10**: 509–514. DOI: 10.1070/PU1968v010n04ABEH003699

[20] Hippler R., Kersten H., Schmidt M., Schoenbach K.H. Low Temperature Plasmas: Fundamentals, Technologies and Techniques, Wiley, 2nd Ed., 2010, Germany, ISBN: 978-3-527-40673-9.

[21] Pendry J.B., Smith D.R. Reversing light with negative refraction. Phys. Today. 2004; **57**(6): 37–43. DOI: 10.1063/1.1784272

[22] Hrabar S., Bonefacic D., Muha D. Application of wire-based metamaterials for antenna miniaturization. 2009 3rd European Conference on Antennas and Propagation, Berlin, 2009, pp. 620–623. DOI: 10.1109/LMWC.2003.822563

[23] Dutta Gupta S. Subliminal to superluminal propagation in a left-handed medium. Phys. Rev. B. 2004; **69**(11): 113104. DOI: 10.1103/PhysRevE.91.033206

[24] Smith D.R., Padilla W.J., Vier D.C., Nemat-Nasser S.C., Schultz S. Composite medium with simultaneously negative permeability and permittivity. Phys. Rev. Lett. 2000; **84**(18): 4184–4187. DOI: 10.1103/PhysRevLett.84.4184

[25] Shelby R.A., Smith D.R., Schultz S. Experimental verification of a negative index of refraction. Science. 2001; **292**(5514): 77–79. DOI: 10.1103/PhysRevLett.90.107401

[26] Grigorenko A.N., Geim A.K., Gleeson H.F., Zhang Y., Khrushchev I.Y., Petrovic J. Nanofabricated media with negative permeability at visible frequencies. Nature. 2005; **438**: 335–338. DOI: 10.1038/nature04242

[27] Di Gennaro E., Parimi P.V., Lu W.T., Sridhar S., Derov J.S., Turchinetz B. Slow microwaves in left-handed materials. Phys. Rev. B. 2005; **72**(3): 033110. DOI: 10.1103/PhysRevB.72.033110

[28] Podolskiy V.A., Narimanov E.E. Strongly anisotropic waveguide as a nonmagnetic lefthanded system. Phys. Rev. B. 2005; **71**(20): 201101. DOI: 10.1103/PhysRevB.71.201101

[29] Veselago V., Braginsky L., Shklover V., Hafner C. Negative refractive index materials. J. Comput. Theor. Nanosci. 2006; **3**: 1–30.

[30] Zhang X., Yao J., Liu Z., Liu Y., Wang Y., Sun C., Bartal G., Stacy A.M. Optical negative refraction in bulk metamaterials of nanowires. Science. 2008; **321**(5891): 930. DOI: 10.1126/science.1157566

[31] Zhang X., Valentine J., Zentgraf T., Ulin-Avila E., Genov D.A., Bartal G. Three dimensional optical metamaterial with a negative refractive index. Nature. 2008; **455**(7211): 376. DOI: 10.1063/1.3656286

[32] Alù A., Engheta N. Guided modes in a waveguide filled with a pair of single-negative (SNG), double-negative (DNG), and/or double-positive (DPS) layers. IEEE Trans. Microwave Theory Tech. 2004; **MTT-52**: 199–210. DOI: 10.1109/TMTT.2003.821274

[33] Alù A., Engheta N. Pairing an epsilon-negative slab with a Mu-negative slab: anomalous tunneling and transparency. IEEE Trans. Antennas Propag. 2003; **AP-51**: 2558–2570. DOI: 10.1109/TAP.2003.817553

[34] Ziolkowski R.W., Kipple A. Application of double negative metamaterials to increase the power radiated by electrically small antennas. IEEE Trans. Antennas Propag. 2003; **AP-51**: 2626–2640. DOI: 10.1109/TAP.2003.817561

[35] Ziolkowski R.W., Kipple A.D. Reciprocity between the effects of resonant scattering and enhanced radiated power by electrically small antennas in the presence of nested metamaterial shells. Phys. Rev. E. 2005; **72**: 036602. DOI: 10.1103/PhysRevE.72.036602

[36] Iyer A.K., Eleftheriades G.V. Free-space imaging beyond the diffraction limit using a Veselago-Pendry transmission-line metamaterial superlens. IEEE Trans. Antennas Propag. 2009; **57**(6): 1720–1727. DOI: 10.1109/TAP.2009.2019890

[37] Fang N., Zhang X. Imaging properties of a metamaterial superlens, Nanotechnology, 2002. IEEE-NANO 2002. In: Proc. 2002 2nd IEEE Conference on, 2002, pp. 225–228. DOI: 10.1063/1.1536712

[38] Engheta N., Ziolkowsky R. (Ed.). Metamaterials: Physics and Engineering Explorations. Wiley, IEEE Press, 2006, United States

[39] Lee D.H., Park W.S. A new material classification of lossy metamaterials. Microw. Opt. Technol. Lett. 2011; pp. 445–447, **53**(2).

[40] Newton T.D., Wigner E.P. Localized states for elementary systems. Rev. Mod. Phys. 1949; **21**: 400–406. DOI: 10.1103/RevModPhys.21.400

[41] Wightman A.S. On the localizability of quantum mechanical systems. Rev. Mod. Phys. 1962; **34**: 845–872. DOI: 10.1103/RevModPhys.34.845

[42] Bialynicki-Birula I. On the wave function of the photon. Acta Phys. Pol. A. 1994; **86**: 97–116. DOI: 10.12693/APhysPolA.86.97

[43] Bialynicki-Birula I. Photon wave function. Progr. Optics. 1996; **XXXVI**: 245–294. arXiv: quant-ph/0508202

[44] Sipe J.E. Photon wave functions. Phys. Rev. A. 1995; **52**: 1875–1883. DOI: 10.1103/PhysRevA.52.1875

[45] Raymer M.G., Smith B.J. The Maxwell wave function of the photon. In: Proc. SPIE 5866, The Nature of Light: What Is a Photon? August 04, 2005, pp. 293–297. DOI: 10.1117/12.619359

[46] Smith B.J., Raymer M.G. Photon wave functions, wave-packet quantization of light, and coherence theory. New J. Phys. 2007; **9**: 1–37. DOI: 10.1088/1367-2630/9/11/414

[47] Kobe D.H. Zitterbewegung of a photon. Phys. Lett. A. 1999; **253**: 7–11. DOI: 10.1016/S0375-9601(99)00011-0

Chapter 5

Light Wave Propagation and Scattering Through Particles

Yi Ping Han, Zhi Wei Cui and Jia Jie Wang

Additional information is available at the end of the chapter

http://dx.doi.org/10.5772/66662

Abstract

The study of light propagating and scattering for various particles has always been important in many practical applications, such as optical diagnostics for combustion, monitoring of atmospheric pollution, analysis of the structure and pathological changes of the biological cell, laser Doppler technology, and so on. This chapter discusses propagation and scattering through particles. The description of the solution methods, numerical results, and potential application of the light scattering by typical particles is introduced. The generalized Lorenz-Mie theory (GLMT) for solving the problem of Gaussian laser beam scattering by typical particles with regular shapes, including spherical particles, spheroidal particles, and cylindrical particles, is described. The numerical methods for the scattering of Gaussian laser beam by complex particles with arbitrarily shape and structure, as well as random discrete particles are introduced. The essential formulations of numerical methods are outlined, and the numerical results for some complex particles are also presented.

Keywords: light scattering, small particles, Gaussian laser beam, generalized Loren-Mie theory, numerical method

1. Introduction

The investigation of light propagation and scattering by various complex particles is of great importance in a wide range of scientific fields, and it has lots of practical applications, such as detection of atmospheric pollution, optical diagnostics for aerosols, remote sensing of disasters [1–3]. Over the past few decades, some theories and numerical methods have been developed to study the light wave propagation and scattering through various particles. For the particles with special shape, such as spheres, spheroids, and cylinders, the generalized Lorenz-Mie theory (GLMT) [4–15] can obtain an analytic solution in terms of a limited linear system of equations using the method of separation of variables to solve the Helmholtz

equation in the corresponding coordinate system. For the complex particles of arbitrary shapes and structure, some numerical methods, such as the discrete dipole approximation (DDA), the method of moments (MOM), the finite element method (FEM), and the finite-difference time-domain (FDTD), have been utilized. For random media composed of many discrete particles, the T-matrix method, the sparse-matrix canonical-grid (SMCG) method, and the characteristic basis function method (CBFM) can be applied to obtain simulation results.

This chapter discusses the light propagation and scattering through particles. Without loss of generality, the incident light is assumed to be Gaussian laser beam, which can be reduced to conventional plane wave. The detailed description of the solution methods, numerical results, and potential application of the light scattering by systems of particles is introduced.

2. Light scattering by regular particles

2.1. Light scattering by a homogeneous sphere

The geometry of light scattering of a Gaussian beam by a homogeneous sphere is illustrated in **Figure 1**. As shown in **Figure 1**, two Cartesian coordinates $Oxyz$ and O_buvw are used. The $Oxyz$ is attached to the particle whose center is located at O, and the O_buvw is attached to the shaped beam. Due to the spherical symmetry of the homogeneous sphere, it is common to assume that the axes O_bu, O_bv, and O_bw are parallel to the axes Ox, Oy, and Oz, respectively. The shaped

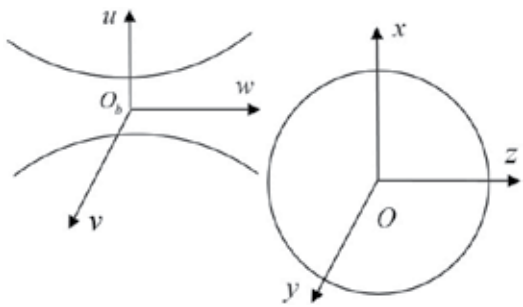

Figure 1. Geometry of the scattering of a Gaussian beam by a homogeneous sphere.

beam is assumed to be propagating along the positive w-axis of the beam system, with its electric field polarized along the u-axis. The time-dependent part of the electromagnetic fields is $\exp(-i\omega t)$, which will be omitted throughout this section.

Within the framework of the GLMT, the electromagnetic field components of the illuminating beam are described by partial wave expansions over a set of basic functions, e.g., vector spherical wave functions in spherical coordinates, vector spheroidal wave functions in spheroidal coordinates, and vector cylindrical wave functions in cylindrical coordinates. The expansion coefficients or sub-coefficients are named as beam-shape coefficients (BSCs) are denoted as $g_{n,X}^{m}$

http://dx.doi.org/10.5772/66662

(X is TE, transverse electric, or TM, transverse magnetic, with n from 1 to ∞, m from $-n$ to n). Considering the scattering of a spherical particle, the incident Gaussian beam can be expanded in terms of vector spherical wave functions in the particle coordinate system $Oxyz$ as

$$\mathbf{E}^i = E_0 \sum_{n=1}^{\infty} \sum_{m=-n}^{n} C_{nm} \left[i g_{n,TE}^m \mathbf{m}_{mn}^{(1)}(kR,\theta,\varphi) + g_{n,TM}^m \mathbf{n}_{mn}^{(1)}(kR,\theta,\varphi) \right] \tag{1}$$

$$\mathbf{H}^i = E_0 \frac{k}{\omega\mu} \sum_{n=1}^{\infty} \sum_{m=-n}^{n} C_{nm} \left[g_{n,TE}^m \mathbf{n}_{mn}^{(1)}(kR,\theta,\varphi) - i g_{n,TM}^m \mathbf{m}_{mn}^{(1)}(kR,\theta,\varphi) \right] \tag{2}$$

where the superscript "i" indicates "incident". The C_{nm} is a constant with explicit expression

$$C_{nm} = (-1)^{(m-|m|)/2} \frac{(n-m)!}{(n-|m|)!} i^{n-1} \frac{2n+1}{n(n+1)}. \tag{3}$$

The $\mathbf{m}_{mn}^{(j)} = \mathbf{m}_{emn}^{(j)} + i\mathbf{m}_{omn}^{(j)}$ and $\mathbf{n}_{mn}^{(j)} = \mathbf{n}_{emn}^{(j)} + i\mathbf{n}_{omn}^{(j)}$ are the vector spherical wave functions with detailed expressions

$$\begin{bmatrix} \mathbf{m}_{emn}^{(j)} \\ \mathbf{m}_{omn}^{(j)} \end{bmatrix} = m\pi_n^m(\cos\theta)\, z_n^{(j)}(kR) \begin{bmatrix} -\sin m\varphi \\ \cos m\varphi \end{bmatrix} \mathbf{e}_\theta - z_n^{(j)}(kR)\tau_n^m(\cos\theta) \begin{bmatrix} \cos m\varphi \\ \sin m\varphi \end{bmatrix} \mathbf{e}_\varphi \tag{4}$$

$$\begin{bmatrix} \mathbf{n}_{emn}^{(j)} \\ \mathbf{n}_{omn}^{(j)} \end{bmatrix} = \left\{ z_n^{(j)}(kR) n(n+1) P_n^m(\cos\theta) \begin{bmatrix} \cos m\varphi \\ \sin m\varphi \end{bmatrix} \mathbf{e}_R + \frac{d\left[kR z_n^{(j)}(kR)\right]}{d(kR)} \tau_n^m(\cos\theta) \begin{bmatrix} \cos m\varphi \\ \sin m\varphi \end{bmatrix} \mathbf{e}_\theta \right.$$
$$\left. + \frac{d[kR z_n^{(j)}(kR)]}{d(kR)} m\pi_n^m(\cos\theta) \begin{bmatrix} -\sin m\varphi \\ \cos m\varphi \end{bmatrix} \mathbf{e}_\varphi \right\} \cdot \frac{1}{kR} \tag{5}$$

the index corresponds to the spherical Bessel functions of the first, second, third, or fourth kind ($j = 1, 2, 3, 4$). The angular functions $\pi_n^m(cos\theta)$ and $\tau_n^m(cos\theta)$ are defined as

$$\pi_n^m(cos\theta) = \frac{P_n^m(cos\theta)}{\sin\theta}, \tau_n^m(cos\theta) = \frac{d}{d\theta} P_n^m(cos\theta). \tag{6}$$

The electric component of the internal field and the scattered field can be expanded in terms of vector spherical wave functions in the particle coordinate system $Oxyz$, respectively, as

$$\mathbf{E}^{int} = E_0 \sum_{n=1}^{\infty} \sum_{m=-n}^{n} \left[f_{mn} \mathbf{m}_{mn}^{(1)}(kR,\theta,\varphi) + g_{mn} \mathbf{n}_{mn}^{(1)}(kR,\theta,\varphi) \right] \tag{7}$$

$$\mathbf{E}^{sca} = E_0 \sum_{n=1}^{\infty} \sum_{m=-n}^{n} \left[a_{mn} \mathbf{m}_{mn}^{(3)}(kR,\theta,\varphi) + b_{mn} \mathbf{n}_{mn}^{(3)}(kR,\theta,\varphi) \right]. \tag{8}$$

To solve the scattering problem, light scattering, the scattering coefficients a_{mn} and b_{mn} are then determined by applying the tangential continuity of the electric and magnetic fields at the surface of the sphere

$$a_{mn} = a_n \cdot g^m_{n,TM}, b_{mn} = b_n \cdot g^m_{n,TM} \tag{9}$$

where a_n, b_n are the classical scattering coefficients of the Lorenz-Mie theory as

$$a_n = \frac{\psi_n(x)\psi'_n(Mx) - M\psi'_n(x)\psi_n(Mx)}{\xi^{(1)}_n(x)\psi'_n(Mx) - M\xi'^{(1)}_n(x)\psi_n(Mx)} \tag{10}$$

$$b_n = \frac{M\psi_n(x)\psi'_n(Mx) - \psi_n(Mx)\psi'_n(x)}{M\xi^{(1)}_n(x)\psi'_n(Mx) - \xi'^{(1)}_n(x)\psi_n(Mx)} \tag{11}$$

where $M = k/k_0$. Once the obtained scattering coefficients are determined, the far-zone scattered field E^{sca}_{far} can be obtained, and the differential scattering cross section (DSCS) of particles can be calculated by

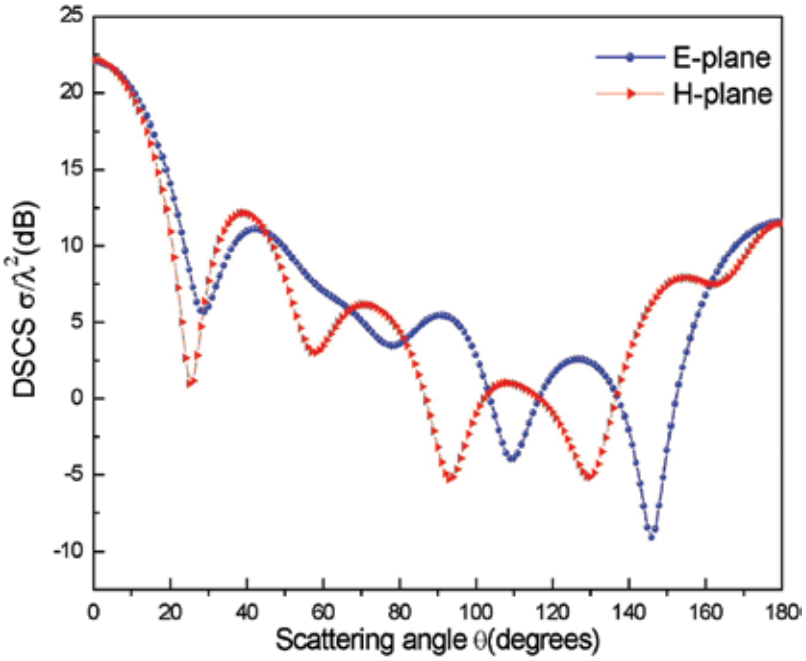

Figure 2. DSCS for a homogeneous spherical dielectric particle illuminated by a Gaussian beam.

$$\sigma(\theta, \varphi) = \lim_{r \to \infty} 4\pi r^2 |E^{sca}_{far}/E_0|^2. \tag{12}$$

Figure 2 presents the normalized DSCS for the scattering of a Gaussian beam by a homogeneous spherical dielectric particle. The radius of the spherical particle is $r = 1.0\lambda$, and the

refractive index of the particle is $m = 2.0$. The beam center is located at the origin of the particle system with beam waist radius of $\omega_0 = 2\lambda$, and the angle set of the beam is $\alpha = \beta = \gamma = 0^o$.

2.2. Light scattering by a spheroidal particle

Light scattering by a spheroid has been of great interest to many researchers in the past several decades since it provides an appropriate model in many practical situations. For example, during the atomization processes, the shape of fuel droplets departs from sphere to spheroid when it impinges on the wall and breaks. Due to the inertial force, the raindrop also departs from the spherical particle to the near-spheroidal one. A rigorous solution to the scattering problem concerning a homogeneous spheroid illuminated by a plane wave was first derived by Asano and Yamamoto [16]. It was extended later to the cases of shaped beam illumination [17], a layered spheroid [18], and a spheroid with an embedded source [19]. Nevertheless, only parallel incident of the shaped beam, including on-axis and off-axis Gaussian beam scattered by a spheroid was studied, that is to say, the propagation direction of the incident beam is assumed to be parallel to the symmetry axis of the spheroid. An extension of shaped beam scattering with arbitrary incidence was developed within the framework of GLMT by Han et al. [20–22] and Xu et al. [23, 24].

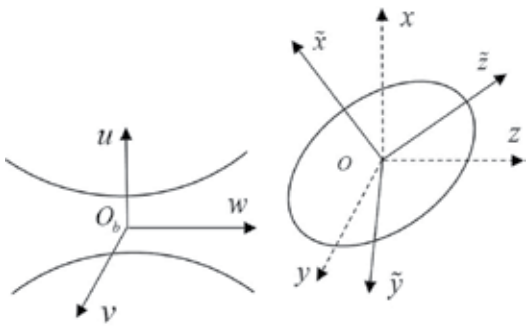

Figure 3. Geometry of a prolate spheroid illuminated by a shaped beam.

To deal with the shaped beam scattering of a spheroidal particle within the framework of GLMT, the incident Gaussian beam is required to be expanded in terms of the vector spheroidal wave functions in spheroidal coordinates, which can be achieved using the relationship between the vector spherical wave functions and the spherical wave functions. The geometry of shaped beam scattering by a prolate spheroid is illustrated in **Figure 3**. According to the expansion of shaped beam in unrotated spherical coordinates in Eq. (1), we can rewrite it as

$$\begin{aligned}\mathbf{E}^{inc} = E_0 \sum_{n=1}^{\infty} \sum_{m=0}^{n} [&\overline{g_{n,TE}^{m}} \mathbf{m}_{emn}^{r(1)}(kR,\theta,\varphi) + \overline{g'^{m}_{n,TE}} \mathbf{m}_{omn}^{r(1)}(kR,\theta,\varphi) \\ &+ i\overline{g'^{m}_{n,TM}} \mathbf{n}_{emn}^{r(1)}(kR,\theta,\varphi) + i\overline{g_{n,TM}^{m}} \mathbf{n}_{omn}^{r(1)}(kR,\theta,\varphi)]\end{aligned} \tag{13}$$

where we have

$$\begin{pmatrix} \overline{g^{m}_{n,TE}} \\ \overline{g'^{m}_{n,TE}} \\ \overline{g^{m}_{n,TM}} \\ \overline{g'^{m}_{n,TM}} \end{pmatrix} = i^{n} \frac{2n+1}{n(n+1)} \frac{1}{(1+\delta_{0m})} \begin{pmatrix} 1 \\ i \\ -i \\ -1 \end{pmatrix} \begin{pmatrix} (g^{m}_{n,TE} + g^{-m}_{n,TE}) \\ (g^{m}_{n,TE} - g^{-m}_{n,TE}) \\ (g^{m}_{n,TM} - g^{-m}_{n,TM}) \\ (g^{m}_{n,TM} + g^{-m}_{n,TM}) \end{pmatrix} \tag{14}$$

where δ_{0m} is the Kronecker delta functions.

Considering the vector spheroidal wave functions in the spheroidal coordinates, whose explicit expressions are the same as the ones used in Refs. [14, 25], the relationship between the vector spherical wave functions and vector spheroidal wave functions is given as:

$$(\mathbf{m},\mathbf{n})^{r(1)}_{\substack{e \\ o}\ mn}(kR,\theta,\varphi) = \sum_{l=m,m+1}^{\infty}{}' \frac{2(n+m)!}{(2n+1)(n-m)!} \cdot \frac{i^{l-n}}{N_{ml}} d^{ml}_{n-m}(c)(\mathbf{M},\mathbf{N})^{r(1)}_{\substack{e \\ o}\ ml}(c,\zeta,\eta,\varphi). \tag{15}$$

From Eq. (15), we can obtain the expansion of Gaussian beam in spheroidal coordinates. Accordingly, the electric component of the internal field and the scattered field can be expanded in terms of vector spheroidal wave functions. The unknown scattered coefficients can be determined by applying the boundary conditions of continuity of the tangential electromagnetic fields over the surface of the particle. Thus, the solution of scattering for Gaussian beam by a spheroidal particle can be obtained.

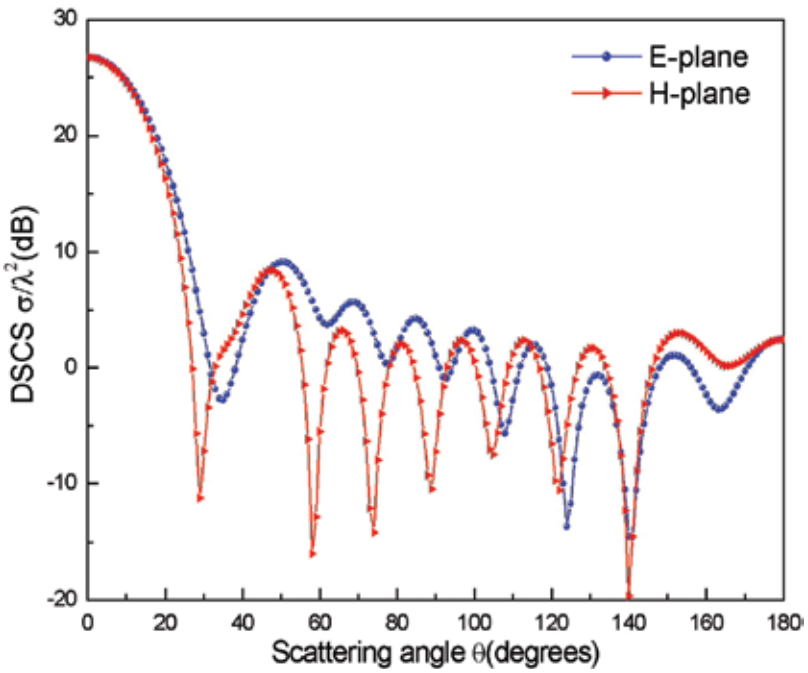

Figure 4. DSCS for incidence of a Gaussian beam on a dielectric spheroidal particle.

http://dx.doi.org/10.5772/66662

For the purpose of demonstration, **Figure 4** shows angular distributions of the DSCS for a spheroid with a semimajor axis and a semiminor axis being $a = 2.0\lambda$ and $b = 1.0\lambda$, respectively, and refractive index $m = 1.55$. The beam center is located at the origin of the particle system with beam waist radius of $\omega_0 = 2\lambda$, and the angle set of the beam is $\alpha = \beta = \gamma = 0^o$.

2.3. Light scattering by a circular cylindrical particle

The geometry of shaped beam scattering by a circular cylinder is illustrated in **Figure 5**. Similarly to a spheroidal particle, due to the lack of spherical symmetry, the arbitrary orientation is also compulsory in the case of GLMTs for cylinders. The expansion of the case of an arbitrary-shaped beam propagating in an arbitrary direction, based on which an approach to expand the shaped beam in terms of cylindrical vector wave functions natural to an infinite cylinder of arbitrary orientation is given below.

The vector cylindrical wave functions in the cylindrical coordinates (r, ϕ, z) are defined as

$$\begin{aligned}\mathbf{m}_{n\lambda}^{(j)}(kr,\phi,z) &= e^{ihz}e^{im\phi}[i\frac{m}{r}J_m(\lambda r)\mathbf{i}_r - \frac{\partial}{\partial r}J_m(\lambda r)\mathbf{i}_\varphi] \\ \mathbf{n}_{n\lambda}(kr,\phi,z) &= e^{ik_z z}e^{im\phi}\left[\frac{ih}{k}\frac{\partial}{\partial r}J_m(\lambda r)\mathbf{i}_r - \frac{hm}{kr}J_m(\lambda r)\mathbf{i}_\varphi + \frac{\lambda^2}{k}J_m(\lambda r)\mathbf{i}_z\right]\end{aligned} \tag{16}$$

where $(\mathbf{m}_{n\lambda}^{(j)}, \mathbf{n}_{n\lambda}^{(j)}) = (\mathbf{m}_{en\lambda}^{(j)}, \mathbf{n}_{en\lambda}^{(j)}) + i(\mathbf{m}_{on\lambda}^{(j)}, \mathbf{n}_{on\lambda}^{(j)})$ are the cylindrical vector wave functions of the first kind in the cylindrical coordinates (r, ϕ, z), and $(\mathbf{m}_{en\lambda}^{(j)}, \mathbf{n}_{en\lambda}^{(j)}), (\mathbf{m}_{on\lambda}^{(j)}, \mathbf{n}_{on\lambda}^{(j)})$ are the same as $(\mathbf{m}_{en\lambda}^{(j)}, \mathbf{n}_{en\lambda}^{(j)})e^{ihz}, (\mathbf{m}_{on\lambda}^{(j)}, \mathbf{n}_{on\lambda}^{(j)})e^{ihz}$ in defined by Stratton. The subscript "e" refers to even ϕ dependence while "o" refers to odd ϕ dependence, and we have $\lambda^2 + h^2 = k^2$, $h = k\cos\zeta$, $\lambda = k\sin\zeta$.

The relationship between the vector spherical wave functions and the vector cylindrical wave functions is defined as

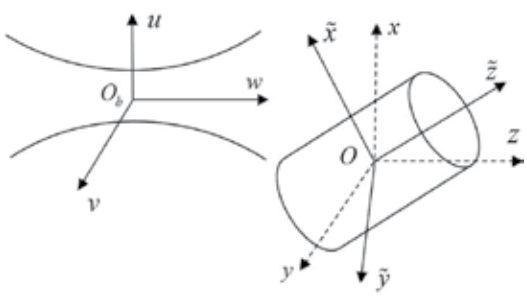

Figure 5. Geometry of a circular cylinder illuminated by a shaped beam.

$$\begin{aligned}\mathbf{m}_{mn}^{r(1)}(kR,\theta,\varphi) &= \int_0^{\pi}\left[c_{mn}(\zeta)\mathbf{m}_{m\lambda}^{(1)} + a_{mn}(\zeta)\mathbf{n}_{m\lambda}^{(1)}\right]e^{ihz}\sin\zeta d\zeta \\ \mathbf{n}_{mn}^{r(1)}(kR,\theta,\varphi) &= \int_0^{\pi}\left[c_{mn}(\zeta)\mathbf{n}_{m\lambda}^{(1)} + a_{mn}(\zeta)\mathbf{m}_{m\lambda}^{(1)}\right]e^{ihz}\sin\zeta d\zeta\end{aligned} \tag{17}$$

where

$$c_{mn}(\zeta) = \frac{i^{m-n+1}}{2k}\frac{dP_n^m(\cos\zeta)}{d(\cos\zeta)}, a_{mn}(\zeta) = \frac{mk}{\lambda^2}\frac{i^{m-n-1}}{2}P_n^m(\cos\zeta) \tag{18}$$

Based on Eqs. (17) and (1), we can obtain the expansion of the incident shaped beam in terms of the cylindrical vector wave functions in cylindrical coordinates as

$$\mathbf{E}^i = E_0\sum_{m=-\infty}^{\infty}\int_0^{\pi}[I_{m,TE}(\zeta)\mathbf{m}_{n\lambda} + I_{m,TM}(\zeta)\mathbf{n}_{n\lambda}]\sin\zeta d\zeta \tag{19}$$

where $I_{m,TE}(\zeta)$ and $I_{m,TM}(\zeta)$ are the BSCs in cylindrical coordinates, with explicit expressions

$$\begin{aligned}I_{m,TE}(\zeta) &= \sum_{n=|m|}^{\infty}[ig_{n,TE}^m c_{mn}(\zeta) + g_{n,TM}^m a_{mn}(\zeta)]. \\ I_{m,TM}(\zeta) &= \sum_{n=|m|}^{\infty}[ig_{n,TE}^m a_{mn}(\zeta) + g_{n,TM}^m c_{mn}(\zeta)]\end{aligned} \tag{20}$$

Accordingly, the electric component of the internal field and the scattered field can be expanded in terms of cylindrical vector wave functions. The unknown scattered coefficients can be determined by applying the boundary conditions of continuity of the tangential electromagnetic fields over the surface of the particle. Thus, the solution of scattering for Gaussian beam by a cylindrical particle can be obtained.

3. Light scattering by complex particles of arbitrary shapes and structure

3.1. Surface integral equation method

Many particles encountered in nature or produced in industrial processes, such as raindrops, ice crystals, biological cells, dust grains, daily cosmetics, and aerosols in the atmosphere, not only have irregular shapes but also have complex structures. The study of light scattering by these complex particles is essential in a wide range of scientific fields with many practical applications, including optical manipulation, particle detection and discrimination, design of new optics devices, etc. Here, we introduce the surface integral equation method (SIEM) [26–28] to simulate the light scattering by arbitrarily shaped particles with multiple internal dielectric inclusions of arbitrary shape, which can be reduced to the case of arbitrarily shaped homogeneous dielectric particles. For SIEM, the incident Gaussian beam can be described

http://dx.doi.org/10.5772/66662

using the method of combing Davis-Barton fifth-order approximation [29] in combination with rotation Euler angles [30].

Now, let us consider the problem of Gaussian beam scattering by an arbitrarily shaped particle with multiple dielectric inclusions of arbitrary shape. As illustrated in **Figure 6**, let S_h represent the surface of the host particle and S_i represent the surface of the $ith(i = 1, 2, \cdots, N)$ inclusion, with N being the total number of the internal inclusions. Let ε_h, μ_h and ε_i, μ_i represent the permittivity and permeability of the host particle and the *ith* dielectric inclusion, respectively. The surrounding medium is also considered to be free space with parameters ε_0 and μ_0. Let Ω_0, Ω_i and Ω_h, respectively, denote the free space region, the region occupied by the *ith* internal inclusion and the region occupied by the host particle except those occupied by all the inclusions. Introducing equivalent electromagnetic currents $\mathbf{J}_h$, M_h on S_h and $\mathbf{J}_i$, M_i on $S_i(i = 1, 2, \cdots, N)$. On the bases of the surface equivalence principle, the fields in each region can be expressed in terms of the equivalent electric and magnetic currents. Specifically, the scattered fields $\mathbf{E}_0^{sca}$ and $\mathbf{H}_0^{sca}$ in the region Ω_0, due to the equivalent electromagnetic currents $\mathbf{J}_h$ and M_h on S_h, can be expressed as Eqs. (21) and (22)

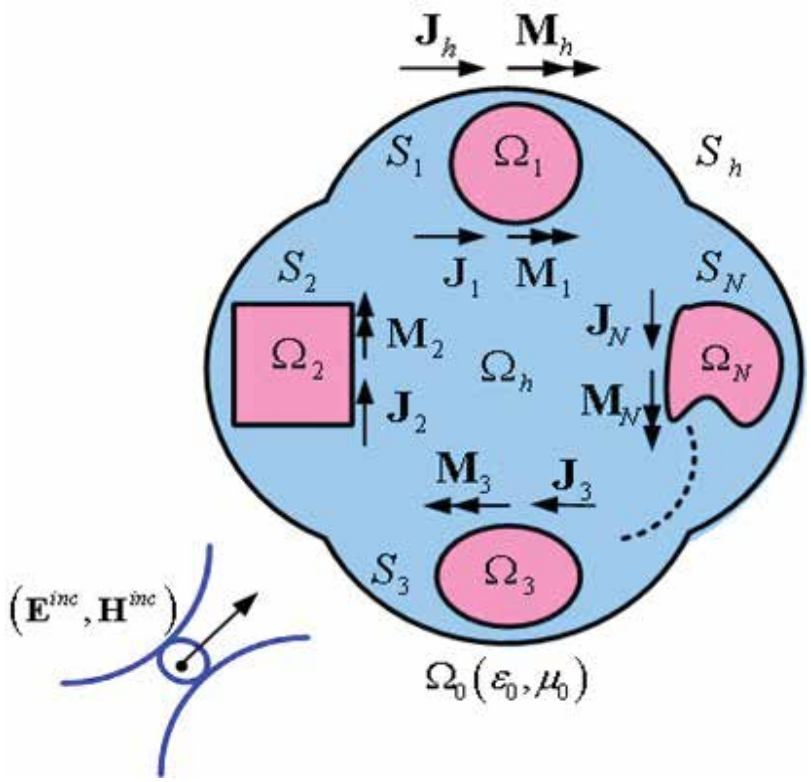

Figure 6. Configuration of an arbitrarily shaped particle with multiple internal inclusions of arbitrary shape.

$$\mathbf{E}_0^{sca} = Z_0 \mathbf{L}_0^{S_h}(\mathbf{J}_h) - \mathbf{K}_0^{S_h}(\mathbf{M}_h) \tag{21}$$

$$\mathbf{H}_0^{sca} = \mathbf{K}_0^{S_h}(\mathbf{J}_h) + \frac{1}{Z_0}\mathbf{L}_0^{S_h}(\mathbf{M}_h) \tag{22}$$

where the integral operators $\mathbf{L}_0^S$ and $\mathbf{K}_0^S$ are defined as

$$\mathbf{L}_0^S(\mathbf{X}) = -ik_0 \iint_S \left[\mathbf{X}(\mathbf{r}') + \frac{1}{k_0^2}\nabla\nabla' \cdot \mathbf{X}(\mathbf{r}')\right] G_0(\mathbf{r}, \mathbf{r}') dS' \tag{23}$$

$$\mathbf{K}_0^S(\mathbf{X}) = -\iint_S \mathbf{X}(\mathbf{r}') \times G_0(\mathbf{r}, \mathbf{r}') dS' \tag{24}$$

in which the subscript "0" represents the medium in which the scattered fields are computed and the superscript "S" represents the surface on which the integration is performed, $G_0(\mathbf{r}, \mathbf{r}')$ is the Green's function in region Ω_0. The fields in region Ω_h are produced by the equivalent electromagnetic currents $-\mathbf{J}_h$, $-M_h$ on S_h and $\mathbf{J}_i$, M_i on $S_i (i = 1, 2, \ldots, N)$ and can be expressed as

$$\mathbf{E}_h = \left[Z_h \mathbf{L}_h^{S_h}(-\mathbf{J}_h) - \mathbf{K}_h^{S_h}(-\mathbf{M}_h)\right] + \sum_{i=1}^{N}\left[Z_h \mathbf{L}_h^{S_i}(\mathbf{J}_i) - \mathbf{K}_h^{S_i}(\mathbf{M}_i)\right] \tag{25}$$

$$\mathbf{H}_h = \left[\mathbf{K}_h^{S_h}(-\mathbf{J}_h) + \frac{1}{Z_h}\mathbf{L}_h^{S_h}(-\mathbf{M}_h)\right] + \sum_{i=1}^{N}\left[\mathbf{K}_h^{S_i}(\mathbf{J}_i) + \frac{1}{Z_h}\mathbf{L}_h^{S_i}(\mathbf{M}_i)\right]. \tag{26}$$

Also based on the surface equivalence principle, the fields $\mathbf{E}_i$ and $\mathbf{H}_i$ in region $\Omega_i (i = 1, 2, \cdots, N)$ can be expressed in terms of the equivalent electric and magnetic currents $-\mathbf{J}_i$ and $-M_i$ as

$$\mathbf{E}_i = Z_i \mathbf{L}_i^{S_i}(-\mathbf{J}_i) - \mathbf{K}_i^{S_i}(-\mathbf{M}_i) \tag{27}$$

$$\mathbf{H}_i = \mathbf{K}_i^{S_i}(-\mathbf{J}_i) + \frac{1}{Z_i}\mathbf{L}_i^{S_i}(-\mathbf{M}_i) \tag{28}$$

where $Z_i = \sqrt{\mu_i/\varepsilon_i}$ and the operators $\mathbf{L}_i^S$ and $\mathbf{K}_i^S$ are also defined similarly to $\mathbf{L}_0^S$ and $\mathbf{K}_0^S$, provided that all the subscripts are changed from "0" to "i".

By enforcing the continuity of the tangential electromagnetic fields across each surface, the following integral equations may be established

http://dx.doi.org/10.5772/66662

$$|Z_0\mathbf{L}_0^{S_h}(\mathbf{J}_h)-\mathbf{K}_0^{S_h}(\mathbf{M}_h)+Z_h\mathbf{L}_h^{S_h}(\mathbf{J}_h)-\mathbf{K}_h^{S_h}(\mathbf{M}_h) -\sum_{i=1}^{N}[Z_h\mathbf{L}_h^{S_i}(\mathbf{J}_i)-\mathbf{K}_h^{S_i}(\mathbf{M}_i)]=-\mathbf{E}^{inc}|_{\tan(S_h)} \tag{29}$$

$$|\mathbf{K}_0^{S_h}(\mathbf{J}_h)+\frac{1}{Z_0}\mathbf{L}_0^{S_h}(\mathbf{M}_h)+\mathbf{K}_h^{S_h}(\mathbf{J}_h)+\frac{1}{Z_h}\mathbf{L}_h^{S_h}(\mathbf{M}_h) -\sum_{i=1}^{N}\left[\mathbf{K}_h^{S_i}(\mathbf{J}_i)+\frac{1}{Z_h}\mathbf{L}_h^{S_i}(\mathbf{M}_i)\right]=-\mathbf{H}^{inc}|_{\tan(S_h)} \tag{30}$$

$$|Z_h\mathbf{L}_h^{S_h}(\mathbf{J}_h)-\mathbf{K}_h^{S_h}(\mathbf{M}_h)-Z_i\mathbf{L}_i^{S_i}(\mathbf{J}_i)+\mathbf{K}_i^{S_i}(\mathbf{M}_i)-Z_h\mathbf{L}_h^{S_i}(\mathbf{J}_i) +\mathbf{K}_h^{S_i}(\mathbf{M}_i)-\sum_{j=1,j\neq i}^{N}[Z_h\mathbf{L}_h^{S_j}(\mathbf{J}_j)-\mathbf{K}_h^{S_j}(\mathbf{M}_j)]=0|_{\tan(S_i)} \tag{31}$$

$$|\mathbf{K}_h^{S_h}(\mathbf{J}_h)+\frac{1}{Z_h}\mathbf{L}_h^{S_h}(\mathbf{M}_h)-\mathbf{K}_i^{S_i}(\mathbf{J}_i)-\frac{1}{Z_i}\mathbf{L}_i^{S_i}(\mathbf{M}_i)-\mathbf{K}_h^{S_i}(\mathbf{J}_i) -\frac{1}{Z_h}\mathbf{L}_h^{S_i}(\mathbf{M}_i)-\sum_{j=1,j\neq i}^{N}\left[\mathbf{K}_h^{S_j}(\mathbf{J}_j)+\frac{1}{Z_h}\mathbf{L}_h^{S_j}(\mathbf{M}_j)\right]=0|_{\tan(S_i)} \tag{32}$$

where the subscripts "$\tan(S_p)$" and "$\tan(S_i)$" stand for tangential components of the fields on S_h and $S_i(i=1,2,\cdots,N)$, respectively. Applying the method of moments (MOMs) with RWG basis functions to the above established integral equations yields a linear system of equations as follows:

$$\begin{bmatrix} Z_{J_hJ_h} & Z_{J_hM_h} & Z_{J_hJ_1} & \cdots & Z_{J_hJ_N} & Z_{J_hM_1} & \cdots & Z_{J_hM_N} \\ Z_{M_hJ_h} & Z_{M_hM_h} & Z_{M_hJ_1} & \cdots & Z_{M_hJ_N} & Z_{M_hM_1} & \cdots & Z_{M_hM_N} \\ Z_{J_1J_h} & Z_{J_1M_h} & Z_{J_1J_1} & \cdots & Z_{J_1J_N} & Z_{J_1M_1} & \cdots & Z_{J_1M_N} \\ \vdots & \vdots & \vdots & \vdots & \vdots & \vdots & \vdots & \vdots \\ Z_{J_NJ_h} & Z_{J_NM_h} & Z_{J_NJ_1} & \cdots & Z_{J_NJ_N} & Z_{J_NM_1} & \cdots & Z_{J_NM_N} \\ Z_{M_1J_h} & Z_{M_1M_h} & Z_{M_1J_1} & \cdots & Z_{M_1J_N} & Z_{M_1M_1} & \cdots & Z_{M_1M_N} \\ \vdots & \vdots & \vdots & \vdots & \vdots & \vdots & \vdots & \vdots \\ Z_{M_NJ_h} & Z_{M_NM_h} & Z_{M_NJ_1} & \cdots & Z_{M_NJ_N} & Z_{M_NM_1} & \cdots & Z_{M_NM_N} \end{bmatrix} \begin{Bmatrix} J_h \\ M_h \\ J_1 \\ \vdots \\ J_N \\ M_1 \\ \vdots \\ M_N \end{Bmatrix} = \begin{Bmatrix} b_E \\ b_H \\ 0 \\ \vdots \\ 0 \\ 0 \\ \vdots \\ 0 \end{Bmatrix}. \tag{33}$$

The resultant matrix Eq. (33) can also be solved iteratively by employing the multilevel fast multipole algorithm (MLFMA). Once obtained the unknown equivalent electromagnetic currents, the far-zone scattered fields and DSCS can be calculated.

3.2. Numerical results

First, we consider the reduced case of arbitrarily shaped homogeneous dielectric particles. To illustrate the validity of the proposed method, the scattering of a focused Gaussian beam by a

homogeneous spherical dielectric particle is considered. The radius of the spherical particle is $r = 1.0\lambda$, and the refractive index of the particle is $m = 2.0$. The beam center is located at the origin of the particle system with beam waist radius of $\omega_0 = 2\lambda$, and the angle set of the beam is $\alpha = \beta = \gamma = 0^o$. **Figure 7** shows the computed DSCS as a function of the scattering angle in the E-plane. For comparison, the results obtained using the GLMT are given in the same figure. Excellent agreements are observed between them.

To illustrate the validity of the proposed method for composite particles with inclusions, we consider the scattering a Gaussian beam by a spheroidal particle with a spherical inclusion at the center, as shown in **Figure 8**. The semimajor axis and the semiminor axis of the host spheroid are $a = 2.0\lambda$ and $b = 1.0\lambda$, respectively. The radius of the spherical inclusion is $r_i = 0.5\lambda$. The host spheroid is characterized by refractive index $m = 2.0$. For the case of dielectric inclusion, the refractive index is $m_1 = 1.414$. The particle is illuminated by an on-axis normally incident Gaussian beam with $\omega_0 = 2.0\lambda$ and $x_0 = y_0 = z_0 = 0.0$. The computed DSCSs as a function of the scattering angle in the E-plane and the H-plane are shown in **Figure 9**. For comparison, the result obtained using the analytical theory GLMT is given in the same figure. Excellent agreements are observed between them.

Finally, the scattering of an obliquely incident Gaussian beam by a cubic particle containing 27 randomly distributed spherical inclusions is considered to illustrate the capabilities of the proposed method. The center of the host cube is located at the origin of the particle system and the side length of the cube is $l = 3.0\lambda$. All the spherical inclusions are assumed to be uniform, and the positions are generated using the Monte Carlo method described in Ref. [31] with fractional volume $f = 6.0\%$, as shown in **Figure 10**. The host cube is characterized by

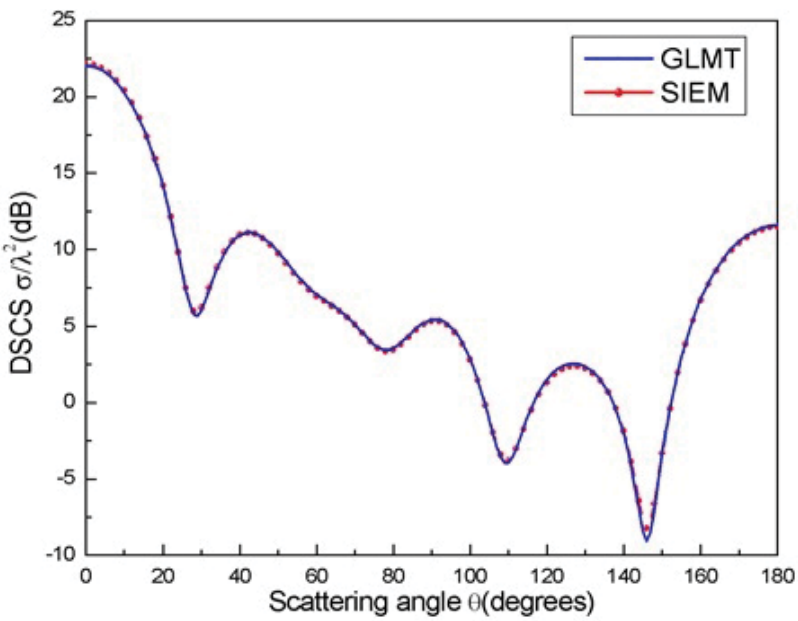

Figure 7. Comparison of the DSCS for a spherical dielectric particle obtained from the SIEM and the GLMT.

http://dx.doi.org/10.5772/66662

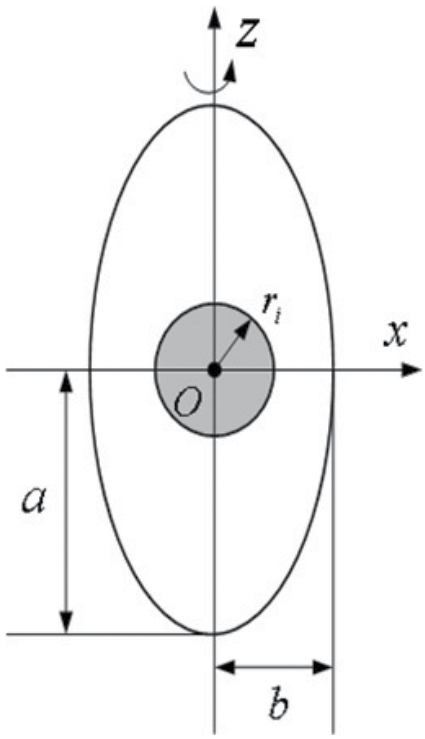

Figure 8. Geometry of a spheroidal particle with a spherical inclusion at the center.

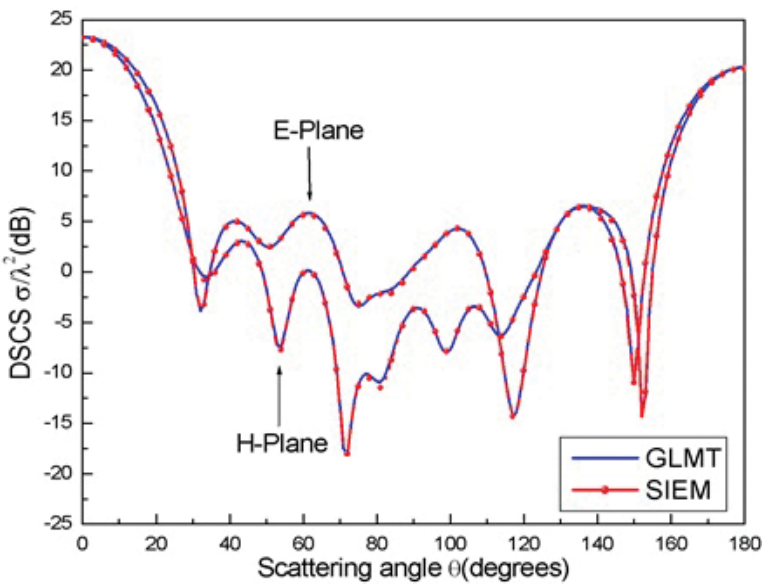

Figure 9. Comparison of the DSCSs for a spheroidal particle with a spherical inclusion at the center obtained from the SIEM and that from the GLMT.

refractive index $m = 1.2{-}i0.2$. For the case of dielectric inclusion, the complex refractive index is $m = 1.5{-}i0.1$. The beam waist is centered at $x_0 = y_0 = z_0 = 0.0$ with a beam waist radius of $\omega_0 = 2.0\lambda$. The rotation Euler angles are $\alpha = 0^o, \beta = 45^o$ and $\gamma = 0^o$. **Figure 11** presents the simulated DSCSs as a function of the scattering angle in both the E-plane and the H-plane.

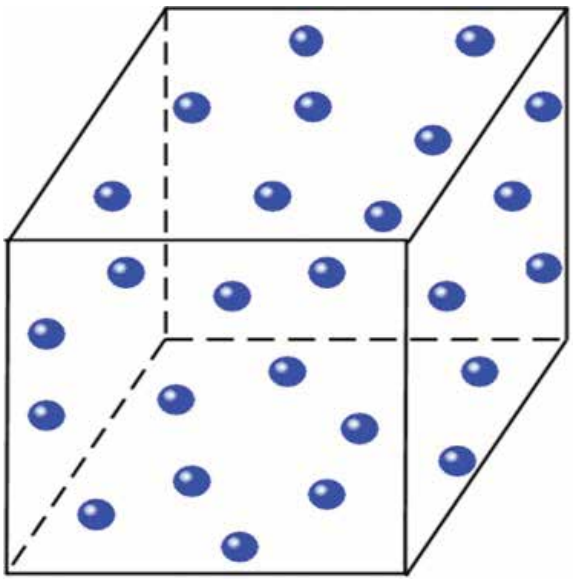

Figure 10. Illustration of a cubic particle containing 27 randomly distributed spherical inclusions.

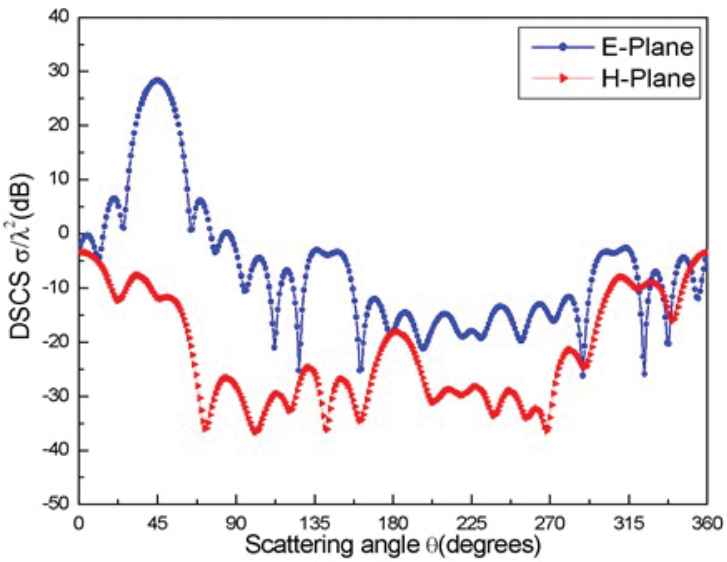

Figure 11. The DSCSs for a cubic particle with 27 randomly distributed spherical inclusions.

http://dx.doi.org/10.5772/66662

4. Light scattering by random discrete particles

Due to the wide range of possible applications in academic research and industry, the problem of light scattering by random media composed of many discrete particles is a subject of broad interest. Over the past few decades, some theories and numerical methods have been developed to study the light scattering by random discrete particles [32–48]. In this section, we introduce a hybrid finite element-boundary integral-characteristic basis function method (FE-BI-CBFM) to simulate the light scattering by random discrete particles [49]. In this hybrid technique, the finite element method (FEM) is used to obtain the solution of the vector wave equation inside each particle and the boundary integral equation (BIE) is applied on the surfaces of all the particles as a global boundary condition. To reduce computational burdens, the characteristic basis function method (CBFM) is introduced to solve the resultant FE-BI matrix equation. The incident light is assumed to be Gaussian laser beam.

4.1. FE-BI-CBFM for random discrete particles

Now, let us consider the scattering of an arbitrarily incident focused Gaussian beam by multiple discrete particles with a random distribution, as depicted in **Figure 12**. For simplicity, the background region, which is considered to be free space, is denoted as Ω_0, the region

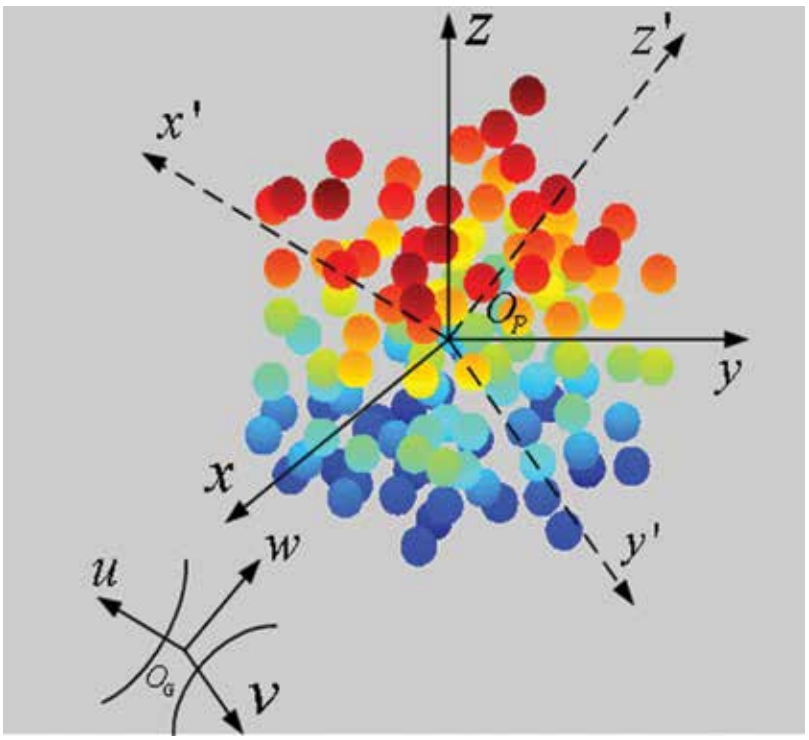

Figure 12. Illustration of an arbitrarily incident Gaussian beam impinges on multiple discrete particles with a random distribution.

occupied by the *ith* particle is denoted as $\Omega_i (i = 1, 2, \ldots, M)$, and the corresponding volume and boundary surface are denoted as V_i and S_i, respectively. In accordance with the variational principle [50], the solution to the field in region Ω_i can be obtained by solving an equivalent variational problem with the functional given by

$$F(\mathbf{E}_i) = \frac{1}{2}\iiint_{V_i}\left[\frac{1}{\mu_r}(\nabla\times\mathbf{E}_i)\cdot(\nabla\times\mathbf{E}_i) - k_0^2\varepsilon_r\mathbf{E}_i\cdot\mathbf{E}_i\right]dV + ik_0Z_0\iint_{S_i}(\mathbf{E}_i\times\mathbf{H}_i)\cdot\hat{n}_i dS. \tag{34}$$

where $\hat{n}_i$ denotes the outward unit vector normal to S_i, ε_r, and μ_r are the relative permittivity and permeability of the particles. Using the FEM with Whitney vector basis functions defined on tetrahedral elements [50], the functional F can be converted into a sparse matrix equation

$$\begin{bmatrix} K_i^{II} & K_i^{IS} & 0 \\ K_i^{SI} & K_i^{SS} & B_i \end{bmatrix}\begin{Bmatrix} E_i^I \\ E_i^S \\ H_i^S \end{Bmatrix} = \begin{Bmatrix} 0 \\ 0 \end{Bmatrix} \tag{35}$$

where $[K_i^{II}]$, $[K_i^{IS}]$, $[K_i^{SI}]$ and $[K_i^{SS}]$ are contributed by the volume integral in Eq. (34), whereas $[B_i]$ is contributed by the surface integral. Also, $\{E_i^I\}$ is a vector containing the discrete electric fields inside V_i, and $\{E_i^S\}$ and $\{H_i^S\}$ are the vectors containing the discrete electric and magnetic fields on S_i, respectively.

Since Eq. (35) is independent of the excitation, we can remove the interior unknowns to derive a matrix equation that only includes the unknowns on S_i, as follows:

$$\left[\tilde{K}_i^{SS}\right]\{E_i^S\} + [B_i]\{H_i^S\} = \{0\} \tag{36}$$

where

$$\left[\tilde{K}_i^{SS}\right] = \left[K_i^{SS}\right] - \left[K_i^{SI}\right]\left[K_i^{II}\right]^{-1}\left[K_i^{IS}\right]. \tag{37}$$

For the convenience of description, we write the relation between $\{E_i^S\}$ and $\{H_i^S\}$ as

$$\{E_i^S\} = [S_i]\{H_i^S\} \tag{38}$$

where

$$[S_i] = -\left[\tilde{K}_i^{SS}\right]^{-1}[B_i]. \tag{39}$$

It is worth to notice that the calculations of Eqs. (37) and (39) in each particle are independent and can be completely parallelized. Furthermore, since the particles are uniform, the coefficient matrices are the same for each particle. This implies that only one particle needs to be dealt

http://dx.doi.org/10.5772/66662

with to obtain all the matrices $[S_i], (i = 1, 2, \ldots, M)$. For simplicity, let $[S_1] = [S_2] = \cdots [S_M] = [S]$. As a result, the relation between the electric and magnetic fields on all the surfaces can be written as

$$\begin{Bmatrix} E_1^S \\ E_2^S \\ \vdots \\ E_M^S \end{Bmatrix} = \begin{bmatrix} S & & & \\ & S & & \\ & & \ddots & \\ & & & S \end{bmatrix} \begin{Bmatrix} H_1^S \\ H_2^S \\ \\ H_M^S \end{Bmatrix}. \tag{40}$$

To formulate the field in region Ω_0, we introduce the equivalent electric and magnetic currents $\mathbf{J}_i$ and M_i on $S_i (i = 1, 2, \ldots, M)$. By invoking Huygens's principle, the scattered fields in region Ω_0, due to the equivalent currents $\mathbf{J}_i$ and M_i on $S_i (i = 1, 2, \ldots, M)$, can be represented as

$$\mathbf{E}_0^{sca} = \sum_{i=1}^{M} [Z_0 \mathbf{L}_i(\mathbf{J}_i) - \mathbf{K}_i(\mathbf{M}_i)] \tag{41}$$

$$\mathbf{H}_0^{sca} = \sum_{i=1}^{M} \left[\frac{1}{Z_0} \mathbf{L}_i(\mathbf{M}_i) + \mathbf{K}_i(\mathbf{J}_i) \right]. \tag{42}$$

Enforcing boundary condition on S_i yields an electric field integral equation (EFIE)

$$\left| -\hat{n}_i \times \mathbf{M}_i + \sum_{j=1}^{M} [Z_0 \mathbf{L}_j(\mathbf{J}_j) - \mathbf{K}_j(\mathbf{M}_j)] = -\mathbf{E}^{inc} \right|_{\tan(S_i)} \tag{43}$$

and a magnetic field integral equation (MFIE)

$$\left| -\mathbf{J}_i \times \hat{n}_i + \sum_{j=1}^{M} \left[\frac{1}{Z_0} \mathbf{L}_j(\mathbf{M}_j) + \mathbf{K}_j(J_j) \right] = -\mathbf{H}^{inc} \right|_{\tan(S_i)} \tag{44}$$

where the subscript "$\tan(S_i)$" stands for tangential components of the fields on S_i. To remove the interior resonance, we employ the CFIE, which combines the EFIE and MFIE in the following form

$$\mathrm{CFIE}_i = \mathrm{EFIE}_i + \hat{n}_i \times Z_0 \mathrm{MFIE}_i \tag{45}$$

where the subscript i denotes the integral equation is established by enforcing boundary condition on S_i. Using the MOM with RWG vector basis functions, which are completely compatible with the Whitney vector basis functions [50], the CFIE can be converted into a full matrix equation

$$\begin{bmatrix} P_{11} & P_{12} & \cdots & P_{1M} \\ P_{21} & P_{22} & \cdots & P_{2M} \\ \vdots & \vdots & \ddots & \vdots \\ P_{M1} & P_{M2} & \cdots & P_{MM} \end{bmatrix} \begin{Bmatrix} E_1^S \\ E_2^S \\ \vdots \\ E_M^S \end{Bmatrix} + \begin{bmatrix} Q_{11} & Q_{12} & \cdots & Q_{1M} \\ Q_{21} & Q_{22} & \cdots & Q_{2M} \\ \vdots & \vdots & \ddots & \vdots \\ Q_{M1} & Q_{M2} & \cdots & Q_{MM} \end{bmatrix} \begin{Bmatrix} H_1^S \\ H_2^S \\ \vdots \\ H_M^S \end{Bmatrix} = \begin{Bmatrix} b_1 \\ b_2 \\ \vdots \\ b_M \end{Bmatrix}. \tag{46}$$

The expressions of the elements for matrices $[P_{ij}]$ and $[Q_{ij}]$ and vectors $\{b_i\}, (i,j=1,2,\cdots,M)$ can be found in Ref. [49]. Substituting Eq. (40) into Eq. (46), we obtain the final FE-BI matrix equation

$$\left(\begin{bmatrix} P_{11} & P_{12} & \cdots & P_{1M} \\ P_{21} & P_{22} & \cdots & P_{2M} \\ \vdots & \vdots & \ddots & \vdots \\ P_{M1} & P_{M2} & \cdots & P_{MM} \end{bmatrix} \begin{bmatrix} S & & & \\ & S & & \\ & & \ddots & \\ & & & S \end{bmatrix} + \begin{bmatrix} Q_{11} & Q_{12} & \cdots & Q_{1M} \\ Q_{21} & Q_{22} & \cdots & Q_{2M} \\ \vdots & \vdots & \ddots & \vdots \\ Q_{M1} & Q_{M2} & \cdots & Q_{MM} \end{bmatrix}\right) \begin{Bmatrix} H_1^S \\ H_2^S \\ \\ H_M^S \end{Bmatrix} = \begin{Bmatrix} b_1 \\ b_2 \\ \vdots \\ b_M \end{Bmatrix}. \tag{47}$$

The above equation can be written in a more compact form as

$$\begin{bmatrix} \mathbf{Z}_{11} & \mathbf{Z}_{12} & \cdots & \mathbf{Z}_{1M} \\ \mathbf{Z}_{21} & \mathbf{Z}_{22} & \cdots & \mathbf{Z}_{2M} \\ \vdots & \vdots & \ddots & \vdots \\ \mathbf{Z}_{M1} & \mathbf{Z}_{M2} & \cdots & \mathbf{Z}_{MM} \end{bmatrix} \begin{bmatrix} \mathbf{J}_1 \\ \mathbf{J}_2 \\ \vdots \\ \mathbf{J}_M \end{bmatrix} = \begin{bmatrix} \mathbf{V}_1 \\ \mathbf{V}_2 \\ \vdots \\ \mathbf{V}_M \end{bmatrix} \tag{48}$$

where $\mathbf{Z}_{ij} = [P_{ij}][S] + [Q_{ij}]$ are $N \times N$ matrices, $\mathbf{J}_i = \{H_i^S\}$ and $\mathbf{V}_i = \{b_i\}(i,j=1,2,\cdots,M)$ are column vectors of length N, with N being the number of unknowns for magnetic field on the surface of each particle. The solution to Eq. (51) can be obtained by the CBFM described in Ref. [47]. It is based on the use of a set of high-level basis functions, called the characteristic basis functions (CBFs) that are constructed according to the Foldy-Lax multiple scattering equations. These CBFs are comprised of primary CBFs arising from the self-interactions from within the particles, and secondary CBFs that account for the mutual coupling effects from the rest of the particles. Based on the Foldy-Lax equations, the primary CBF for each particle is constructed by exciting that particular particle with the incident field and ignoring the scattered fields of all other particles. By replacing the incident field with the scattered fields, the first secondary CBF for a given particle can be constructed. This is because the primary CBFs induced on all particles except from itself. In this way, additional secondary CBFs can be constructed similarly. A significant reduction in the number of unknowns is realized due to the use of these basis functions, which gives a substantial size reduction in the resultant matrix. Consequently, it enables us to handle the reduced matrix using a direct solver instead of iteration method. Furthermore, the computational burden can be significantly relieved since this method only requires the solution of small-size matrix equations associated with isolated particles. The detailed description of CBFM can be found in Ref. [49].

4.2. Numerical results and discussion

In what follows, some numerical results are presented. First, we consider the scattering of Gaussian beam by 125 randomly distributed conducting spherical particles with a radius of

http://dx.doi.org/10.5772/66662

$r = 0.25\lambda$, as shown in **Figure 12**. The particle positions are generated randomly in a cubic box with which the fractional volume is 10%. The incident Gaussian beam center is centered at $x_0 = y_0 = z_0 = 0.0$, and the angle set of the beam is $\alpha = \beta = \gamma = 0^o$. Results of DSCS are displayed in **Figure 13** as a function of the scattering angle in the E-plane. As can be seen from the figure, the DSCS for Gaussian beams is smaller than that for a plane wave. In addition, for a Gaussian beam incidence with a relatively large waist radius of $\omega_0 = 20\lambda$, the results are in excellent agreement with the results in the case of plane wave illumination.

We then consider the multiple scattering of an obliquely incident Gaussian beam by 512 randomly distributed inhomogeneous spherical particles with which the fractional volume is 10%. Each primary particle consists of a conducting sphere with radius $r = 0.1\lambda$ covered by a dielectric coating with a thickness $t = 0.1\lambda$. The complex refractive index of the coating layer is $m = 1.6–i0.2$. The beam waist is centered at $(x_0, y_0, z_0) = (-1.0, -1.0, -1.0)\lambda$ with a beam waist radius of $\omega_0 = 2.5\lambda$, and the rotation Euler angles are specified as $\alpha = 45, \beta = 45$ and $\gamma = 0$. **Figure 14** presents the simulated DSCSs as a function of the scattering angle.

Finally, we use the present numerical method to simulate the multiple scattering of Gaussian beam by 1000 randomly distributed homogeneous dielectric spherical particles with which the fractional volume is 10%. The radius and the refractive index of the primary particles are assumed as $r = 50$ nm and $m = 1.6–i0.6$, respectively. The wavelength of the incident Gaussian beam is assumed to be $\lambda = 532$ nm. The location of the beam waist center is $x_0 = y_0 = z_0 = 0.0$, and the beam waist radius equals to $\omega_0 = 2.0\lambda$. The Euler angles are $\alpha = 45, \beta = 45$ and $\gamma = 0$. The DSCS is displayed in **Figure 15**. Furthermore, the DSCS of the ensembles of randomly distributed particles for the independent scattering is also calculated. Specifically, an

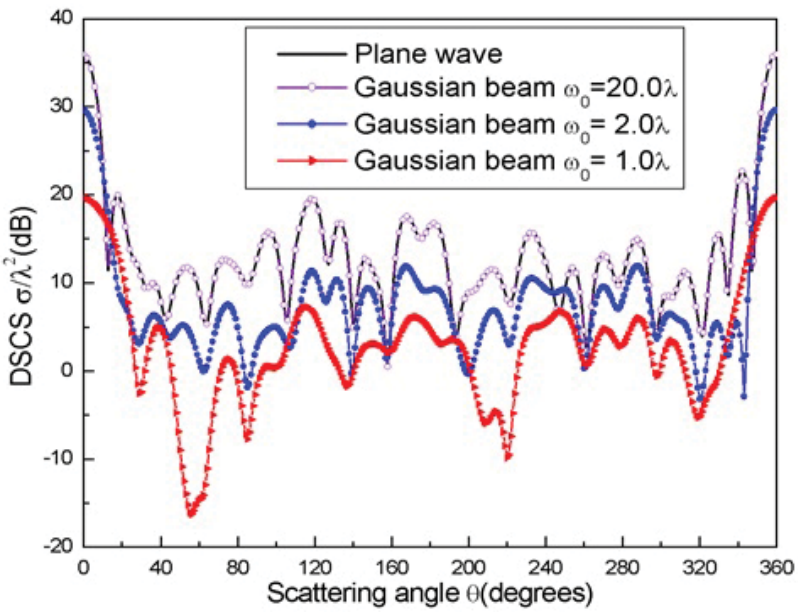

Figure 13. DSCS for 125 randomly distributed conducting spherical particles.

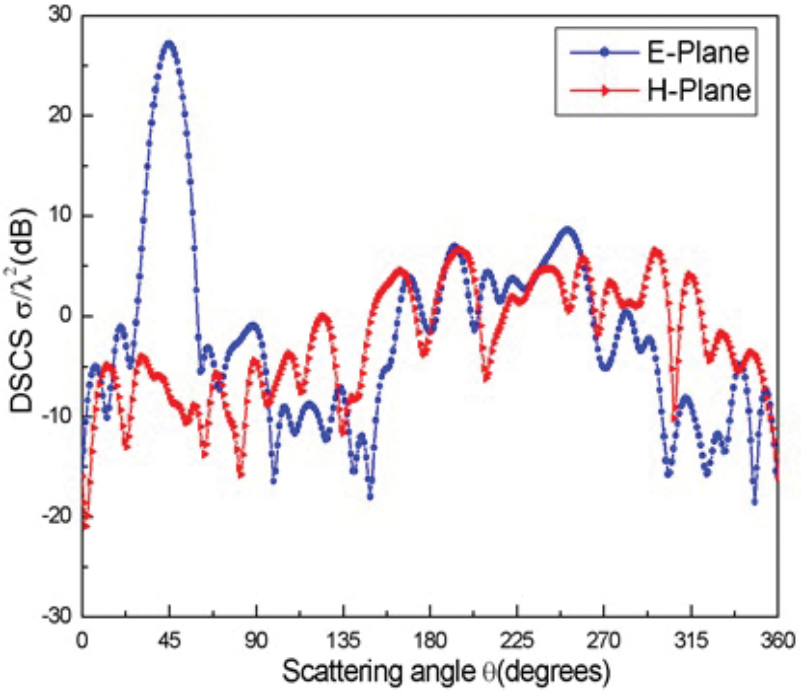

Figure 14. DSCS for 512 randomly distributed inhomogeneous spherical particles.

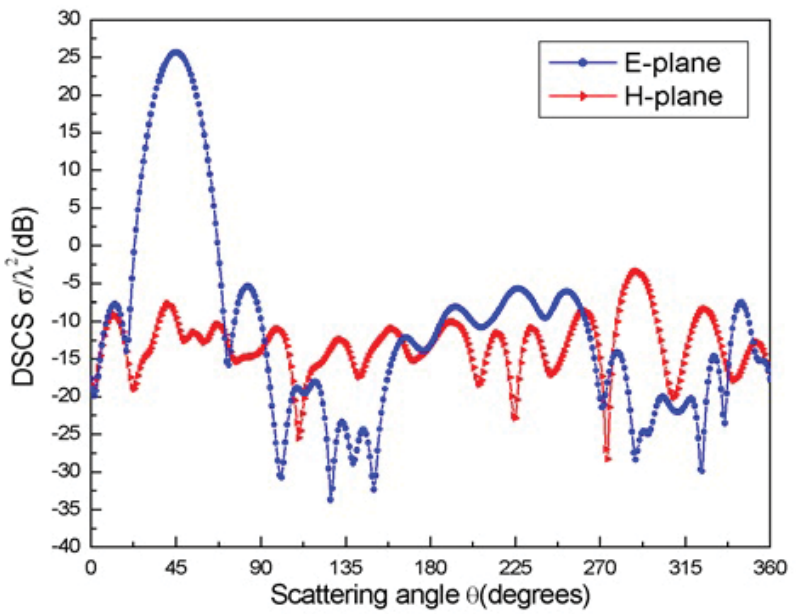

Figure 15. DSCS for 1000 randomly distributed homogeneous dielectric spherical particles.

http://dx.doi.org/10.5772/66662

individual particle is assumed to scatter light without interactions with other particle in the ensemble. The computed DSCS for the independent scattering is displayed in **Figures 16** and **17**. Comparisons between independent scattering and the multiple scattering are made. The

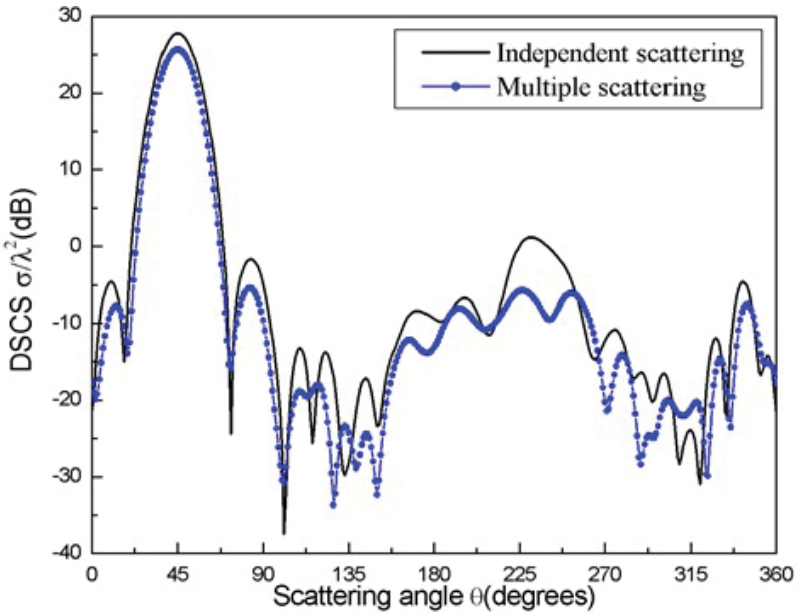

Figure 16. Comparison of the DSCS for the independent scattering and the multiple scattering: E-plane.

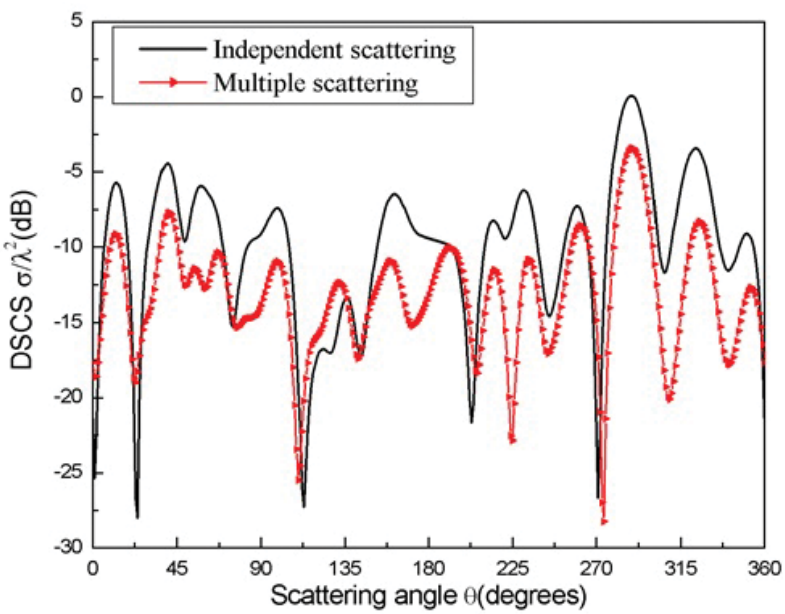

Figure 17. Comparison of the DSCS for the independent scattering and the multiple scattering: H-plane.

results show that the interactions of the particles lead to a reduction in the scattering intensities, which are identical to the general idea of scattering theory.

Author details

Yi Ping Han*, Zhi Wei Cui and Jia Jie Wang

*Address all correspondence to: yphan@xidian.edu.cn

School of Physics and Optoelectronic Engineering, Xidian University, China

References

[1] Gouesbet G and Onofri FRA. Preface: laser-light and interactions with particles (LIP), 2014. Journal of Quantitative Spectroscopy & Radiative Transfer. 2015;162:1–7.

[2] Mishechenko MI, Travis LD, and Lacis AA. Scattering, absorption, and emission of light by small particles. 2002, Cambridge: Cambridge University Press.

[3] Doicu A, Wriedt T, and Eremin YA. Light scattering by systems of particles null-field method with discrete sources: theory and programs. 2006, Berlin: Springer-Verlag.

[4] Gouesbet G and Gréhan G. Generalized Lorenz-Mie theories. 2011, Berlin: Springer.

[5] Lock JA and Gouesbet G. Rigorous justification of the localized approximation to the beam-shape coefficients in generalized Lorenz-Mie theory. I. On-axis beams. The Journal of the Optical Society of America A. 1994;11(9):2503–2515.

[6] Gouesbet G and Lock JA. Rigorous justification of the localized approximation to the beam-shape coefficients in generalized Lorenz-Mie theory. II. Off-axis beams. The Journal of the Optical Society of America A. 1994;11(9):2516–2525.

[7] Gouesbet G, Maheu B, and Grehan G. Light scattering from a sphere arbitrarily located in a Gaussian beam, using a Bromwich formulation. The Journal of the Optical Society of America A., 1988;5:1427–1443.

[8] Wang JJ, Gouesbet G, Han YP, and Grehan G. Study of scattering from a sphere with an eccentrically located spherical inclusion by generalized Lorenz-Mie theory: internal and external field distribution. The Journal of the Optical Society of America A. 2011;28:24–39.

[9] Han L, Han YP, Wang JJ, and Cui ZW. Internal and near-surface electromagnetic fields for a dielectric spheroid illuminated by a zero-order Bessel beam. Journal of the Optical Society of America a-Optics Image Science and Vision. 2014;31(9):1946–1955.

[10] Onofri F, Grehan G, and Gouesbet G. Electromagnetic scattering from a multilayered sphere located in an arbitrary beam. Applied Optics. 1995;30:7113–7124.

[11] Gouesbet G, Wang JJ, and Han YP. Transformations of spherical beam shape coefficients in generalized Lorenz-Mie theories through rotations of coordinate systems. I. General formulation. Optics Communication. 2010;283:3218–3225.

[12] Wang JJ, Gouesbet G, and Han YP. Transformations of spherical beam shape coefficients in generalized Lorenz-Mie theories through rotations of coordinate systems. II. Axisymmetric beams. Optics Communication. 2010;283:3226–3234.

[13] Gouesbet G, Lock JA, Wang JJ, and Grehan G. Transformations of spherical beam shape coefficients in generalized Lorenz-Mie theories through rotations of coordinate systems. V. Localized beam models. Optics Communication. 2011;284:411–417.

[14] Han YP, Zhang Y, Zhang HY, and Han GX. Scattering of typical particles by beam shape in oblique illumination. Journal of Quantitative Spectroscopy & Radiative Transfer. 2009;110:1375–1381.

[15] Edmonds AR. Angular momentum in quantum mechanics. 1957, Princeton: Princeton University Press.

[16] Asano S and Yamamoto G. Light scattering by a spheroid particle. Applied Optics. 1975;14:29–49.

[17] Barton JP. Internal and near-surface electromagnetic fields for a spheroidal particle with arbitrary illumination. Applied Optics. 1995;34:5542–5551.

[18] Barton JP. Internal, near-surface, and scattered electromagnetic fields for a layered spheroid with arbitrary illumination. Applied Optics. 2001;40(21):3598–3607.

[19] Barton JP. Electromagnetic fields for a spheroidal particle with an arbitrary embedded sources. The Journal of the Optical Society of America A. 2000;17:458–464.

[20] Yiping H and Zhensen W. The expansion coefficients of a spheroidal particle illuminated by Gaussian beam. IEEE Transactions on Antennas and Propagation. 2001;49(4): 615–620.

[21] Han YP, Grehan G, and Gouesbet G. Generalized Lorenz-Mie theory for a spheroidal particle with off-axis Gaussian-beam illumination. Applied Optics. 2003;42:6621–6629.

[22] Han YP, Mees L, Ren KF, Grehan G, Wu ZS, and Gouesbet G. Far scattered field from a spheroid under a femtosecond pulsed illumination in a generalized Lorenz-Mie theory framework. Optics Communication. 2004;231:71–77.

[23] Xu F, Ren KF, Gouesbet G, Grehan, and Cai X. Generalized Lorenz-Mie theory for an arbitrary oriented, located, and shaped beam scattered by homogeneous spheroid. The Journal of the Optical Society of America A. 2007;24:119–131.

[24] Xu F, Ren K, and Cai X. Expansion of an arbitrarily oriented, located, and shaped beam in spheroidal coordinates. The Journal of the Optical Society of America A. 2007;24 (1):109–118.

[25] Flammer C. Spheroidal wave functions. 1957, California: Stanford U.P.

[26] Cui ZW, Han YP, and Zhang HY. Scattering of an arbitrarily incident focused Gaussian beam by arbitrarily shaped dielectric particles. The Journal of the Optical Society of America B. 2011;28:2625–2632.

[27] Han YP, Cui ZW, and Gouesbet G. Numerical simulation of Gaussian beam scattering by complex particles of arbitrary shape and structure. Journal of Quantitative Spectroscopy & Radiative Transfer. 2012;113:1719–1727.

[28] Han YP, Cui ZW, and Zhao WJ. Scattering of Gaussian beam by arbitrarily shaped particles with multiple internal inclusions. Optics Express. 2012;20:718–731.

[29] Barton JP and Alexander DR. Fifth-order corrected electromagnetic fields components for a fundamental Gaussian beam. Journal of Applied Physics. 1989;66:2800–2802.

[30] Edmonds AR. Angular momentum in quantum mechanics. 1957, Princeton: Princeton University Press.

[31] Tsang L, Kong JA, Ding KH, and Ao CO. Scattering of electromagnetic waves, numerical simulations. 2001, New York: Wiley.

[32] Ishimaru A. Wave propagation and scattering in random media. 1978, New York: Academic.

[33] Foldy LL. The multiple scattering of waves. I. General theory of isotropic scattering by randomly distributed scatterers. Physical Review Letters. 1945;67:107–119.

[34] Lax M. Multiple scattering of waves. Reviews of Modern Physics. 1951;23:287–310.

[35] Varadan VV and Varadan VK. Multiple scattering of electromagnetic waves by randomly distributed and oriented dielectric scatters. Physical Review. 1980;21:388–394.

[36] Varadan VK, Bringi VN, Varadan VV, and Ishimaru A. Multiple scattering theory for waves in discrete random media and comparison with experiments. Radio Science. 1983;18:321–327.

[37] Furutsu K. Multiple scattering of waves in a medium of randomly distributed particles and derivation of the transport equation. Radio Science. 1975;10:29–44.

[38] Tsang L, Kong JA, and Ding KH. Scattering of electromagnetic waves, theories and applications. 2000, New York : Wiley.

[39] Tishkovets VP and Jockers K. Multiple scattering of light by densely packed random media of spherical particles: dense media vector radiative transfer equation. Journal of Quantitative Spectroscopy & Radiative Transfer. 2006;101:54–72.

[40] Lu CC, Chew WC, and Tsang L. The application of recursive aggregate T-matrix algorithm in the Monte Carlo simulations of the extinction rate of random distribution of particles. Radio Science. 1995;30:25–28.

[41] Chew WC, Lin JH, and Yang XG. An FFT T-matrix method for 3D microwave scattering solution from random discrete scatterers. Microwave and Optical Technology Letters. 1995;9:194–196.

[42] Siqueira PR and Sarabandi K. T-matrix determination of effective permittivity for three-dimensional dense random media. IEEE Transactions on Antennas and Propagation. 2000;48:317–327.

[43] Mishchenko MI, Liu L, Mackowski DW, Cairns B, and Videen G. Multiple scattering by random particulate media: exact 3D results. Optics Express. 2007;15:2822–2836.

[44] Chart CH and Tsang L. A sparse-matrix canonical-grid method for scattering by many scatterers. Microwave and Optical Technology Letters. 1995;8:114–118.

[45] Barrowes BE, Ao CO, Teixeira FL, and Kong JA. Sparse matrix/canonical grid method applied to 3-D dense medium simulations. IEEE Transactions on Antennas and Propagation. 2003;51:48–58.

[46] Cui ZW, Han YP, and Xu Q. Numerical simulation of multiple scattering by random discrete particles illuminated by Gaussian beams. The Journal of the Optical Society of America A. 2011;28:2200–2208.

[47] Sun YF, Chan CH, Mittra R, and Tsang L. Characteristic basis function method for solving large problem arising in dense medium scattering. IEEE Antennas and Propagation Society International Symposium. 2003;2:1068–1071.

[48] Mackowski DW and Mishchenko MI. Direct simulation of multiple scattering by discrete random media illuminated by Gaussian beams. Physical Review Letters A. 2011;83:013804.

[49] Cui ZW, Han YP, and Li CY. Simulation of electromagnetic scattering by random discrete particles using a hybrid FE-BI-CBFM technique. Waves Random Complex Media. 2012;22:207–221.

[50] Jin JM. The finite element method in electromagnetics. 2002, New York: Wiley.

Section 2

Advanced Electromagnetic Concepts and Applications

Chapter 6

Slow Electromagnetic Waves: Theory and New Applications

Giuseppe Di Massa

Additional information is available at the end of the chapter

http://dx.doi.org/10.5772/66672

Abstract

In this chapter, the usage of slow electromagnetic waves in several application domains is deeply discussed. Starting from an outline of the classical Cerenkov effect, various related topics are presented in detail, namely the generation of electromagnetic waves by the Cerenkov effect, the Cerenkov free-electron laser, pickup and kickers in accelerators, pulse compression in radar and linac, and compact components and waveguides in the microwave region.

Keywords: slow electromagnetic waves, propagation, pulse compression, electron beam pickup and kicker

1. Introduction

The pioneering work of Pavel Alekseyevich Cerenkov [1] reports the existence of a visible radiation from pure liquids and solids when electrons go through the medium with a velocity greater than that of light. The radiation, not observed until then, had characteristics that the physical processes responsible for its production were not any of the usual ones associated with atomic or molecular changes. During his studies Cerenkov showed that the radiation was not fluorescent, and that it was polarized with the electric vector parallel to the direction of the electron beam. In a later work [2], he showed that the radiation depended uniquely on the refractive index of the medium and had the unusual property of being emitted asymmetrically.

In [3], a theoretical explanation has been given on this phenomenon which is entirely classical, but in agreement with the qualitative observations of Cerenkov. A striking feature of this theory is that it describes a new process for the production of radiation.

In recent years, the research interest in Cherenkov radiation has arisen due to progress in its new applications such as biomedical imaging, photonic structures, metamaterials, and beam

physics. These new applications require Cherenkov radiation theory of short bunches to be extended to rather more complicated media and structures.

The effect of Cerenkov electromagnetic radiation is similar to that of a sonic boom when an object moves faster than the speed of sound; in this case, the radiation is a shock wave set up in the electromagnetic field.

In this chapter, we report techniques for the excitation of slow waves in guiding structures highlighting classic and new applications, namely:

- Generation of electromagnetic waves by the Cerenkov effect;
- Cerenkov free-electron laser;
- Pickup and kickers in accelerators;
- Pulse compression in radar and linac;
- Compact components and waveguides in microwave region.

2. Outline of Cerenkov radiation

We consider a charged particle traveling at a uniform velocity in a dielectric medium and the electromagnetic field close to the particle that polarizes the medium along its track.

In this process, the atoms are not excited by the charged particle and neither are they removed from their bound states (ionization). It is true that there is in addition ionization, when the impacts are sufficiently close, but the process with which we are concerned here arises from only very small displacements by a very large number of electrons.

Now, when the particle is slow, less than the velocity of light in the considered medium, the radiation from these displaced electrons is not observed, owing to destructive interference. If, however, the velocity of the particle in the medium is faster than the phase velocity of light in the medium, the waves are in phase with one another on a wavefront inclined to the direction of the track, and a coherent electromagnetic radiation is then observed.

If a particle travels a distance AB (**Figure 1**) inside a dielectric medium [4], at a high velocity βc, where c is the velocity of light in a vacuum, and we denote, as sources of spherical waves, the points P_1,P_2,P_3, then the resulting wave front will lie along the line BC, and the direction of emission of the radiation will be along the line AC, at right angles to BC. The distance the particles travels, in a time Δt, will be $AB = \beta c \Delta r$; at the same time, the waves will have traveled a distance $AC = (c/n)\Delta t$ where n is the refractive index of the medium. From these relations, we obtain

$$\cos\theta = \frac{1}{\beta n} \tag{1}$$

Eq. (1) is a fundamental relation between the velocity of the particle, the refractive index of the medium, and the angle at which the light is emitted. This relation is known as the Cerenkov relation.

http://dx.doi.org/10.5772/66672

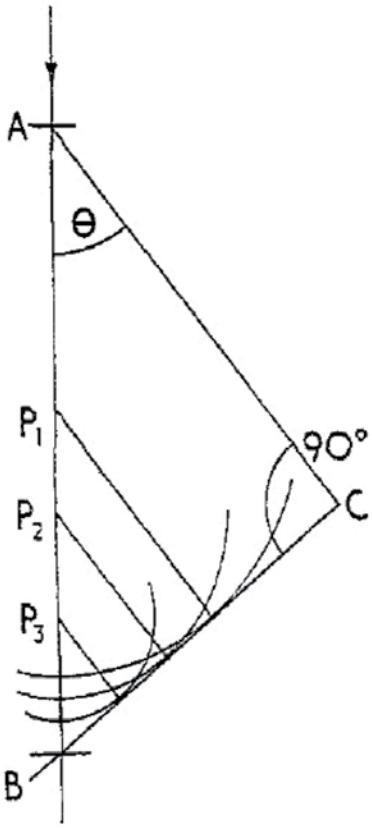

Figure 1. The coherent nature of Cerenkov radiation.

The quantity β is related to the kinetic energy E of the particle, and to its rest mass m, by the equation:

$$E = mc^2\left[\frac{1}{\sqrt{1-\beta^2}} - 1\right] \tag{2}$$

Two special conditions are included in Eq. (1) for limiting cases. First, there is a threshold condition, namely when $\beta = l/n$ and $\theta = 0$. This implies a kinetic energy for the particle below which no radiation takes place. Second, there is a maximum angle at which the light may be emitted, when the particle is traveling at ultrarelativistic velocities. This arises when $\beta - > 1$, in which case $\theta_{\max} - > \cos^{-1}(1/n)$.

The situation depicted in **Figure 1** has been drawn in one plane. In practice, the light is emitted over a conical surface, the axis of which coincides with that of the particle, and the semiapex angle of which is the angle θ, which is shown in **Figure 2**. The polarization of the electric vector E is always at right angles to the direction of propagation of the light, and the magnetic vector H is always tangential to the surface of the cone, as shown in **Figure 2**.

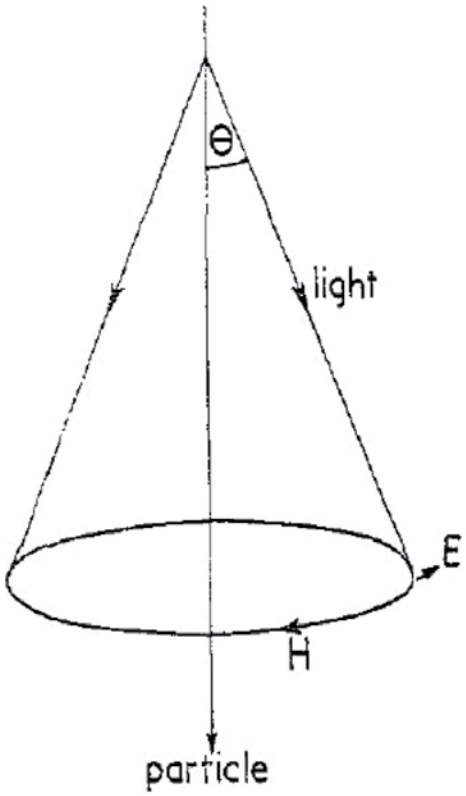

Figure 2. Cerenkov cone of radiation.

3. Cerenkov radiation in the microwave region

A charged particle of velocity v is a potential source of electromagnetic waves which has an infinite and uniform spectrum [5]. It is well know that if it is traveling in an infinite dielectric medium of index of refraction $n(f)$, function of frequency f, we get an electromagnetic radiation for all frequencies satisfying the following equation:

$$n(f)v > 1 \tag{3}$$

So we have conical waves at which have an angle ϑ with respect to the axis of motion for which Eq. (1) holds.

We wonder now what would be the behavior of the electromagnetic radiation in the case when the dielectric has a cylindrical indefinite hole of radiation d parallel to the motion. This hole is necessary for the passage of intense beams. As first guess, if the hole is sufficiently small, it is an irrelevant perturbation for the Cerenkov radiation. Now, we must refine the concept of small or large hole. The particle sees the dielectric by means of its harmonic contents for those wavelengths such that

http://dx.doi.org/10.5772/66672

$$\lambda \geq d \tag{4}$$

So that Cherenkov radiation occurs only below certain frequencies (low pass filter behavior). So that, if the radius d is of the order of centimeter, we expect this will occur at frequencies of the order of GHz.

We understand also that radiation in the optical range is possible only if the dimensions of the hole are of the order of microns.

If in addition, the dielectric is limited and surrounded by an infinite metallic cylinder (**Figure 3**), becoming a partially loaded waveguide, we get a cutoff frequency, so the whole system behaves as passband filter.

A quantitative analysis can be conducted by using the mode expansion of the electromagnetic field in the waveguide matched to the Fourier expansion of the source current [6].

The configuration of this device gives an additional phenomenon, which can be exploited in the microwave range in order to enhance the intensity of radiation. In fact, the Cherenkov wave is trapped in the dielectric and therefore it is possible to pump power in it.

We can understand this trapping by considering the wave number in the dielectric and in the vacuo. They must satisfy the following triangular relations:

$$k_x^2 + k_y^2 + k_z^2 = k_0^2 \tag{5}$$

$$(k_x^d)^2 + k_y^2 + k_z^2 = n^2 k_0^2 \tag{6}$$

From Eqs. (5) and (6), taking into account that $k_x^d = nk_0 \sin\theta$, we have

$$k_x^2 = (1 - n^2 \cos^2\theta) k_0^2 \tag{7}$$

If relation (3) holds, k_x is pure imaginary. The wave is evanescent toward the vacuum. There is no power flux in the transverse direction because the wave in the dielectric is in condition of total reflection. The wave is trapped, because of the multiple reflections on the metallic walls and the interface between the dielectric and the vacuum. Accordingly, there is the possibility to increase the power flux with waves with an adequate phase relation among them when the particle beam has a sinusoidal density modulation.

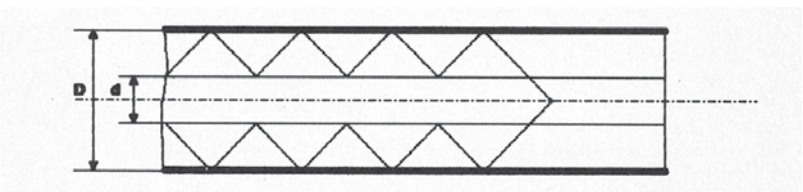

Figure 3. Cherenkov radiation in partially filled waveguide.

4. Cerenkov free-electron laser

Laboratories around the world have realized free-electron laser (FEL) sources, emitting in spectral regions where conventional laser sources are not easily available (e.g., UV, FIR, and millimeter-wave). FEL facilities have been realized in the United States, Japan, China, and Europe. The European FEL sources emit in complementary spectral regions and, altogether, cover a wide spectral range from the UV to the millimeter wave region. The region between 150 and 1 mm is particularly attractive, when continuous tunability and high brightness at the same time are allowed, because conventional laser sources usually do not satisfy these requirements. Small size, moderate cost FEL can be built at such wavelengths. There are a variety of phenomena that can be studied in this region in a solid-state and biological samples with

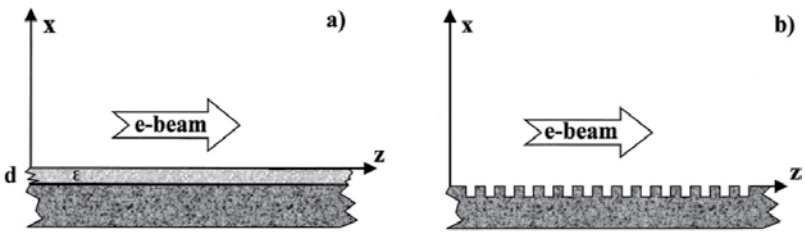

Figure 4. Coupling scheme for the C-FEL (a) and the G-FEL (b). The e-beam passes above the surface of a dielectric film, or of a metal grating, respectively, exciting TM-like surface waves.

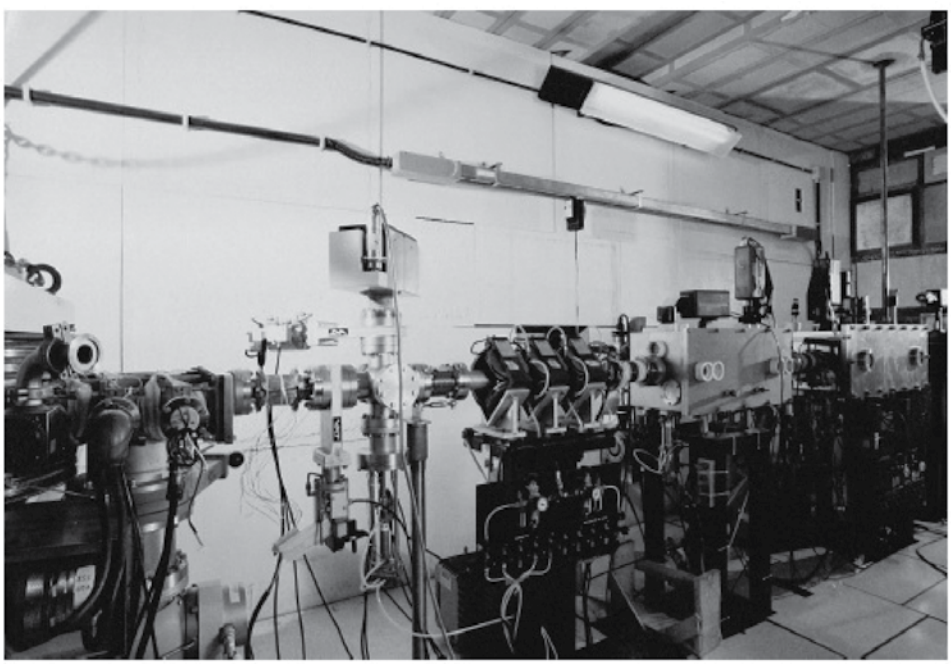

Figure 5. FEL facility developed at the ENEA Research Center in Frascati.

particular respect to their nonlinear response. Moreover, a FEL utilizing as a driver, a radio-frequency (RF) accelerator (**Figure 4**) is a unique source capable of providing picosecond pulses of coherent radiation at such wavelengths (**Figure 5**).

It is known [7] that the rate of energy exchange between flowing charges and a wave, **Figure 4**, is given by the integration of the product **J**·**E** over the volume of the region of space where the interaction occurs (Section 6).

The energy exchange will only occur between corresponding components of the electron current density and the wave electric field. In general, the longitudinal component of the current density due to the drift motion of the electrons will not couple to an electromagnetic wave propagating in the free space, since the latter one has zero longitudinal electric field component. However, in a waveguide or in a suitable loaded structure like the traveling wave tube (TWT) TM modes can be excited, which have a longitudinal component of the electric field. Cerenkov free-electron lasers and orotrons or grating rely on this type of coupling scheme [7].

In Section 6, a general theory is proposed to study the coupling between an electron beam and a hybrid waveguide.

5. Cherenkoscopy imaging

When charged particles travel through dielectric media, such as biological tissue, faster than the speed of light, Cherenkov radiation exists.

Detection of this radiation can allow a new approach to superficial dose estimation, functional imaging, and quality assurance for radiation therapy dosimetry. The first *in vivo* Cherenkov images of a real-time Cherenkoscopy have been recently presented [8]. The imaging system consisted of a time-gated intensified charge coupled device (ICCD) coupled with a commercial lens. The ICCD was synchronized to the linear accelerator to detect Cherenkov photons only during the 3.25μs radiation bursts. Images of a tissue phantom under irradiation show that the intensity of Cherenkov emission is directly proportional to radiation dose.

Cherenkoscopy was obtained from the superficial regions of a canine oral tumor during planned, Institutional Animal Care and Use Committee approved, conventional (therapeutically appropriate) irradiation. Coregistration between photography and Cherenkoscopy validated that Cherenkov photons were detected from the planned treatment region. Real-time images correctly monitored the beam field changes corresponding to the planned dynamic wedge movement, with accurate extent of overall beam field, and expected cold and hot regions.

The experimental configuration is shown in **Figure 6**. The external beam irradiator was a Varian Clinic 2100CD linear accelerator (LINAC, Varian Medical Systems, Palo Alto, CA). A time-gated intensified charge coupled device (ICCD) camera was set up on a tripod to image the entrance region of the treatment beam on tissue phantoms or tissue. The LINAC delivers radiation in a pulsed mode and the ICCD camera was synchronized to the 3.25μs radiation bursts, detecting Cherenkov emission effectively and rejecting most of the ambient light. This

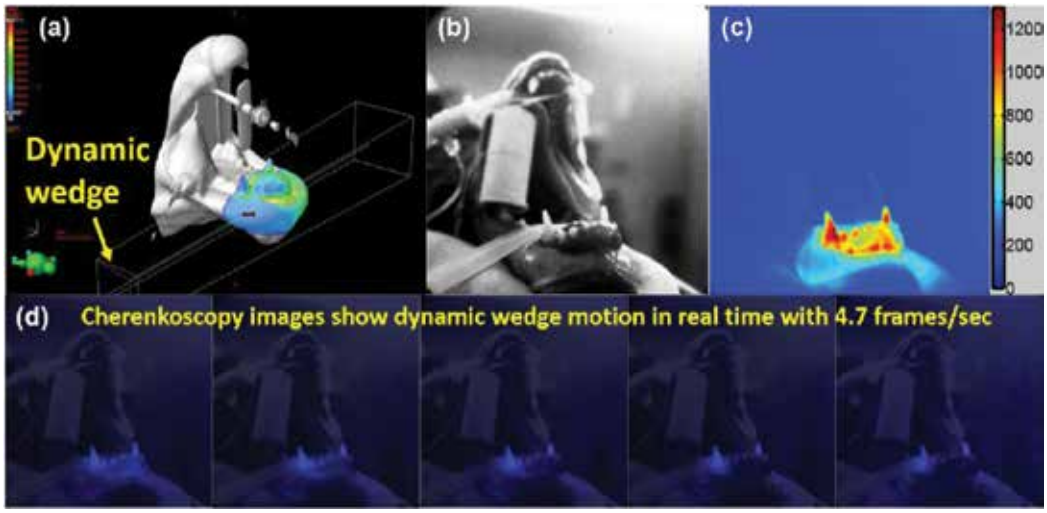

Figure 6. (a) The treatment plan shows incident of the beam and dynamic wedge. (b) Field view of the treatment region. (c) Cherenkoscopy of the treatment region while irradiation progresses. (d) Cherenkoscopy overlaid on the white-light images of the treatment field and sequence of Cherenkoscopy showing the beam field changing while a wedge is moved into the beam. From Ref. [8].

imaging system was first tested by imaging Cherenkov emission from a slab 30304 cm^3 phantom made of opaque water equivalent plastic while irradiating it with a 6 MV square 1010 cm^2 2 photon beam at a dose rate of 600 monitor units per minute. Cherenkov images for different delivered doses at d_{max} were acquired [8].

6. General pickup theory

The extension of stochastic cooling to SPS accelerator of CERN needs high sensitivity pickup (PU) and kickers. To achieve this goal the author, during a period spent a CERN, introduced a new class of pickup and kickers [9]: synchronous PU. The main concept is to use the synchronism between the beam and a slow wave propagating in a structure in which the phase velocity of the wave coincides with the beam velocity. In a metallic rectangular waveguide, the phase velocity is always larger than the velocity of light. However, if we change the *surface impedance* of two opposite walls of the guide slow waves (waves with a phase velocity lower than the velocity of light) propagate in the inhomogeneous waveguide. We have several possibilities to change the surface impedance. The following two solutions will be examined: dielectric slabs and metallic corrugation.

The modes propagating within an inhomogeneous waveguide are a combination of TE and TM modes (hybrid modes). They are classified [10] as LSE (longitudinal section electric) and LSM (longitudinal section magnetic). The component of the fields can be derived from scalar Hertzian potential: the electric type Π_E for LSM modes and the magnetic type Π_H for LSE modes.

http://dx.doi.org/10.5772/66672

The solution of the equation for the potential Π_E or Π_H is a superposition of an even and odd solution with respect to the transverse dimension. The odd solution for Π involves an even dependence of $E_{z(mn)}$ and suggests the use as a longitudinal pickup because the hybrid mode is excited by the beam placed in the center of the structure. On the other hand, the even solution for Π (odd for $E_{z(mn)}$) is excited when the beam is off-center in the waveguide and this suggests to use this solution for a transverse pickup.

6.1. The reciprocity theorem

To establish the fundamental relations between the input-output, we use a simple representation of the pickup, or kicker (**Figure 7**): a black box connected to the vacuum chamber where the beam circulates along the *z*-axis having an output port terminated by a matched load. For a given beam current traveling through the pickup, we want to calculate the complex voltage on the output termination.

The PU is divided into two parts:

- Synchronous part AA′-BB′ where the phase velocity of the EM field is approximately the same as that of the particles.
- A transition part BB′-CC′ where the EM field excited in AA′-BB′ is transformed into a wave propagation in the output waveguide.

We assume that there is a perfect coupling that is all power flowing in the part AA′-BB′ is transformed into power flowing into the output part. This means that no field propagates along the beam pipe. The coupling between the beam and the transition region where there is no synchronism is also neglected.

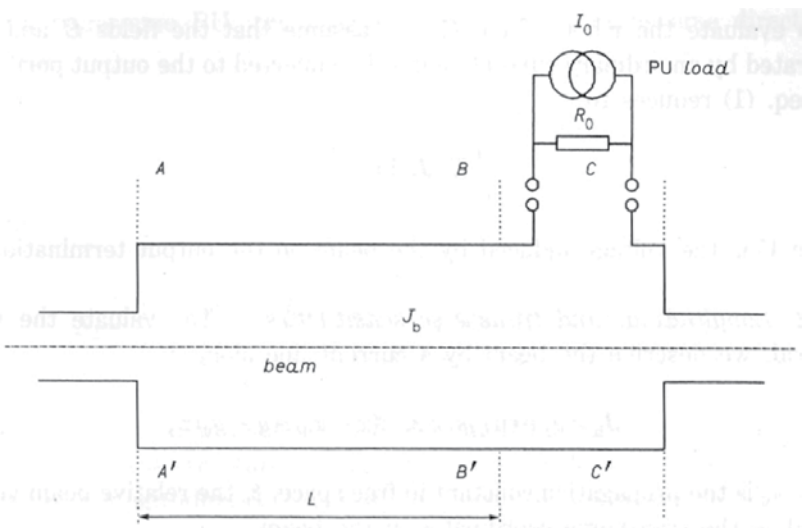

Figure 7. Pickup structure.

In order to apply the reciprocity theorem, we consider the electromagnetic fields $\mathbf{E_b}$ and $\mathbf{H_b}$ generated by the beam with a current density $\mathbf{J_b}$, and the fields $\mathbf{E}$ and $\mathbf{H}$ in the PU structure produced by another current source having a current density $\mathbf{J}$.

The Lorentz reciprocity theorem states

$$\oiint_S (\mathbf{E}_b \times \mathbf{H} - \mathbf{E} \times \mathbf{H}_b) \cdot \hat{\mathbf{n}} ds = \iiint_V [\mathbf{E} \cdot \mathbf{J}_b - \mathbf{E}_b \cdot \mathbf{J}] \, dv \tag{8}$$

In Eq. (8), V is the volume enclosed by the surface S, where there is interaction between the beam and the slow wave structure, $\hat{\boldsymbol{n}}$ is the unity vector normal to S.

To evaluate the r.h.s. of Eq. (8) we assume that the fields $\mathbf{E}$ and $\mathbf{H}$ are generated by an ordinary current source I_0 connected to the output port. In this case, Eq. (8) reduces to

$$\iiint_V \mathbf{E} \cdot \mathbf{J}_b dv = I_0 V \tag{9}$$

where V is the voltage induced by the beam on the output termination R_0.

6.1.1. Longitudinal and transverse sensitivities

To evaluate the volume integral, we describe the beam by a current line along z:

$$\mathbf{J}_b = J_b e^{\left[j\frac{k_0}{\beta_p} z\right]} \delta(x - x_0)\delta(y - y_0)\hat{z} \tag{10}$$

Where k_0 is the propagation constant in free space, β_p is the relative beam velocity, x_0 and y_0 are the transverse coordinates of the beam.

Assuming that the wave excited by I_0 in the structure is a pure traveling wave, of the form

$$E_z(x,y,z) = E_z(x,y) e^{\left[j\frac{k_0}{\beta_w} z\right]} \tag{11}$$

β_w being its phase velocity, Eq. (9) transforms into

$$\frac{V}{I_b} = \frac{E_z(xo,yo)}{I_b} L \left| \operatorname{sinc} \left\{ k_0 \frac{L}{2} \left(\frac{1}{\beta_p} - \frac{1}{\beta_w} \right) \right\} \right| \tag{12}$$

where L is the pickup length, I_b is the Fourier component of the beam current and sinc the sin x/x function.

This wave carries the power P_T given by

$$P_T = \frac{1}{2} \iint_\Sigma \mathbf{E} \mathbf{x} \mathbf{H}^* \hat{n} d\Sigma \tag{13}$$

The current source I_0, which generates P_T, is split in two equal parts: $I_0/2$ flows into the PU load Ro and $I_0/2$ in the PU itself. It follows:

$$P_T = \frac{1}{2} R_0 \left(\frac{I_0}{2} \right)^2 \tag{14}$$

In the longitudinal case, the PU sensitivity (or transfer impedance) defined as $S = V/I_b$ is obtained simply by combining Eqs. (12) and (13).

$$S = \frac{1}{2} \sqrt{\frac{R_0}{2P_T}} E_z(x_0, y_0) L \left| \operatorname{sinc} \left\{ k_0 \frac{L}{2} \left(\frac{1}{\beta_p} - \frac{1}{\beta_w} \right) \right\} \right| \tag{15}$$

For a transverse PU, the sensitivity S_Δ, for the transverse direction x, is defined as

$$S_\Delta = \frac{1}{I_b} \frac{\partial V}{\partial x} \bigg|_{x=x_0} \tag{16}$$

leads to

$$S_\Delta = \frac{1}{2} \sqrt{\frac{R_0}{2P_T}} \left[\frac{\partial E_z(x, y_0)}{\partial x} \right]_{x=x_0} L \left| \operatorname{sinc} \left\{ k_0 \frac{L}{2} \left(\frac{1}{\beta_p} - \frac{1}{\beta_w} \right) \right\} \right| \tag{17}$$

We have to evaluate P_T, using Eq. (14), for a given field supported by the structure. We consider an even mode, for E_z, in the case of a longitudinal PU and an odd mode for a transverse PU.

6.2. Kicker transfer functions

The force on a charge q, moving with the velocity $v = v\hat{z}$, in an electromagnetic field (**E**, **H**)

$$\frac{d\mathbf{p}}{dt} = q\mathbf{E}(t) q\mu_0 v \left(\hat{y} H_x(t) - \hat{x} H_y(t) \right) \tag{18}$$

Integrating along the kicker length L one obtains, in frequency domain,

$$\Delta\mathbf{p} = \frac{q}{v} \int_0^L [(\mathbf{E} + \mu_0 v(H_x \hat{y} - H_y \hat{x})] e^{j\frac{k_0}{\beta_p} z} dz \tag{19}$$

The projection of Eq. 19 along the z-axis

$$\Delta p_z = \frac{q}{V} \int_0^L E_z e^{j\frac{k_0}{\beta_p} z} dz \tag{20}$$

gives the kicker transfer function in the longitudinal case.

To obtain the transverse sensitivity, the projection of Eq. (20) along the x-axis is considered

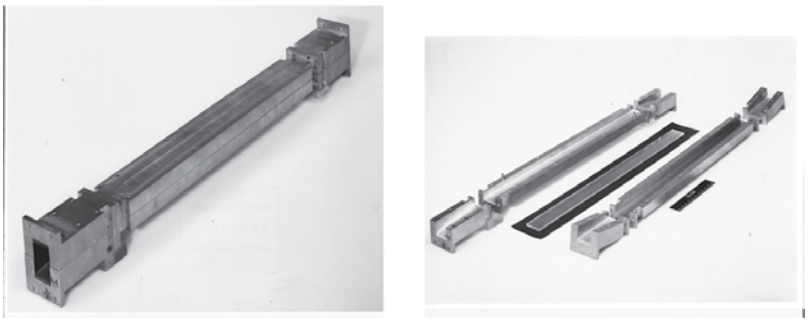

Figure 8. Dielectric pickup.

$$\Delta p_x = \frac{q}{v}\int_0^L \left[E_x - \frac{v}{j\omega}\left(\frac{\partial E_z}{\partial x} - \frac{\partial E_x}{\partial z}\right)\right] e^{j\frac{k_0}{\beta_p}z} dz \tag{21}$$

For a wave propagating along z, of the form $exp\left[j\frac{k_0}{\beta_p}z\right]$, Eq. (20) gives

$$\Delta p_x = \frac{q}{v}\int_0^L \left[E_x\left(1 - \frac{\beta_p}{\beta_w}\right) + j\frac{\beta_p}{k_0}\frac{\partial E_z}{\partial x}\right] e^{j\frac{k_0}{\beta_p}z} dz \tag{22}$$

When $\beta_p = \beta_w$, i.e., at synchronism, the first term in the integral vanishes. Eqs. (22) and (17) are then essentially the same as well as Eqs. (13) and (8) for the longitudinal case. In conclusion, PU sensitivity and kicker transfer function are basically the same quantities, for a given geometry or, in other words as we can expect that kickers are essentially pickup structures working in reverse.

In **Figure 8** is presented a dielectric pickup developed a CERN from the author for the stochastic cooling of bunched beams in the SPS accelerator.

7. Corrugated waveguide

As example of waveguide supporting slow waves, we consider the corrugated waveguide depicted in **Figure 9**.

The electromagnetic field inside the waveguide, when we consider the hybrid longitudinal section electric (LSE) mode, can be described by the Hertzian potential

$$\mathbf{\Pi}^H = \hat{\mathbf{x}} P(x,y) e^{\gamma_n z} \tag{23}$$

$$\mathbf{E} = -j\omega\mu_0 \nabla \times \nabla \times \mathbf{\Pi}^H \tag{24}$$

$$\mathbf{H} = \nabla \times \mathbf{\Pi}^H \tag{25}$$

The solution of Eqs. (23)–(25) gives the field components:

http://dx.doi.org/10.5772/66672

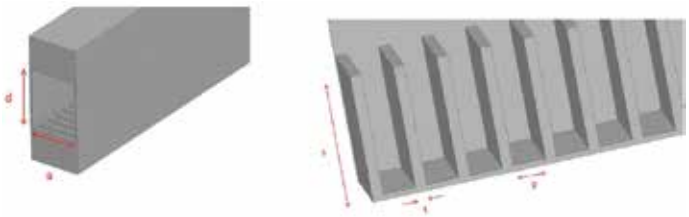

Figure 9. Geometry of corrugated waveguide.

$$e_x = 0 \tag{26}$$

$$e_y = -\omega\mu_0\gamma_n P(x,y) \tag{27}$$

$$e_z = -j\omega\mu_0 \frac{\partial}{\partial y} P(x,y) \tag{28}$$

$$h_x = -\left(\frac{\partial^2}{\partial y^2} + \frac{\partial^2}{\partial z^2}\right) P(x,y) \tag{29}$$

$$h_y = \frac{\partial^2}{\partial x \partial y} P(x,y) \tag{30}$$

$$h_z = -j\gamma_n \frac{\partial}{\partial x} P(x,y) \tag{31}$$

$$k_0^2 = \gamma_n^2 + k_x^2 + \alpha^2 \tag{32}$$

Inside the corrugation, we have

$$E_z = -j\omega\mu_0 B \sin\beta\left(\frac{d}{2} + s - y\right) \cos\frac{\pi}{a}x \tag{33}$$

$$H_y = \frac{\pi}{a} B \sin\beta\left(\frac{d}{2} + s - y\right) \sin\frac{\pi}{a}x \tag{34}$$

$$H_x = -\beta B \cos\beta\left(\frac{d}{2} + s - y\right) \cos\frac{\pi}{a}x \tag{35}$$

The dispersion equation inside the corrugation gives

$$k_0^2 = \beta^2 + k_x^2 \tag{36}$$

Eqs. (32) and (36) give

$$\beta^2 = \gamma_n^2 + \alpha^2 \tag{37}$$

Expression (37) for slow waves ($\alpha = jq$) becomes

$$\beta^2 = \gamma_n^2 - q^2 \tag{38}$$

The general solution of the potential equation is a superposition of an even and an odd solution, with respect to ($y = 0$). For the even solution, we have

$$P(x,y) = A\cos\left(\frac{n\pi}{a}x\right)\cosh(qy) \tag{39}$$

Imposing the boundary condition for the field (Eq. (24)) on the air-corrugation interface:

$$e_z\left(\frac{d}{2},x\right) = E_z\left(\frac{d}{2},x\right) \tag{40}$$

$$h_x\left(\frac{d}{2},x\right) = H_x\left(\frac{d}{2},x\right) \tag{41}$$

the following transcendental equation is obtained

$$\frac{1}{\alpha}\tan\alpha\frac{d}{2} = \frac{1}{\beta}\cot\beta s \tag{42}$$

In the slow wave case ($\alpha = jq$), we have

$$\tanh q\frac{d}{2} = \frac{q}{\beta}\cot\beta s \tag{43}$$

The solution of Eqs. (42) and (38) gives the dispersion equation of waveguide.

8. Waveguide pulse compression

Pulsed radars can achieve high-resolution range using pulses with a very short duration. The maximum range for the system requires a fixed pulse repetition rate that represents a reduction of mean power unless there is an increment of the peak power. A limit to the peak power is imposed by transmitter components, so an attractive alternative consists in the use of f.m. pulse-compression techniques.

Passive compressors for pulse consist of a passive circuit with frequency dispersion with a phase-modulated input pulse.

As dispersive circuit, one can use a section of metallic waveguide in which group velocities depend on the frequency. Thus, if the input microwave pulse is frequency modulated, each component of the pulse travels with its velocity. With a linear growing frequency, one can obtain a situation such that all parts of the pulse simultaneously arrive at the waveguide output.

Standard metallic waveguides are strongly dispersive near the cutoff frequency which limits the use to low power levels with short input pulse durations. More sophisticated waveguide

can be used for better performance. The corrugated waveguide, where it is possible to excite a slow wave, is a good candidate.

9. Slow wave compressor

From Eq. (38), the propagation constant in the corrugated waveguide is found as

$$\gamma_n^2 = \beta^2 + \frac{12}{d^2} - \frac{24}{\beta d^3}\cot\beta s \tag{44}$$

From Eq. (44), it is possible to find the group velocity

$$v_g = \frac{\partial\omega}{\partial\gamma_n} \tag{45}$$

We use modulated pulse with a linear swept frequency that monotonically increasing group velocity propagating through the waveguide. This results in pulse shortening and growth in power amplitude if the losses are small. The maximum compression ratio is obtained at the exit of the waveguide where all the frequency components of the pulse arrive at the same time. The compression ratio is derived from the electromagnetic wave propagating along an isotropic dispersive medium

$$K = \Delta FL\left(\frac{1}{v_{g1}} - \frac{1}{v_{g2}}\right)e^{-\delta L} \tag{46}$$

Where v_{g1} and v_{g2} are the group velocity of the beginning and the end frequencies of the microwave pulse, L is the length of waveguide, ΔF is the frequency band, and δ is the loss factor.

Dispersion relation, group velocity, and compression ratio of a typical slow wave waveguide are reported in **Figures 10–12**.

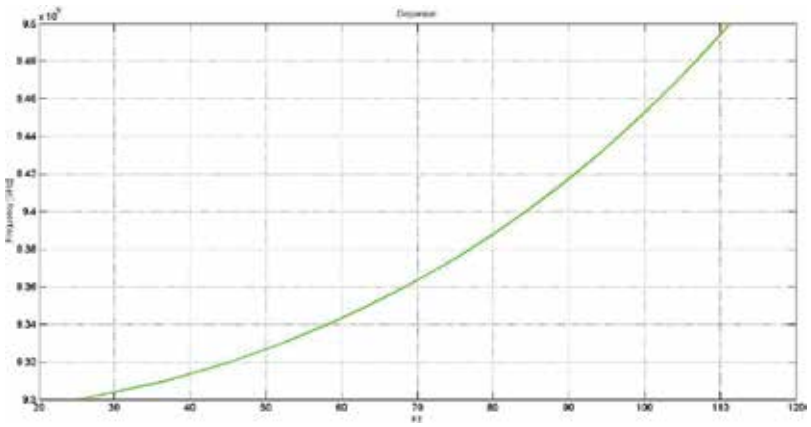

Figure 10. Dispersion of corrugated waveguide.

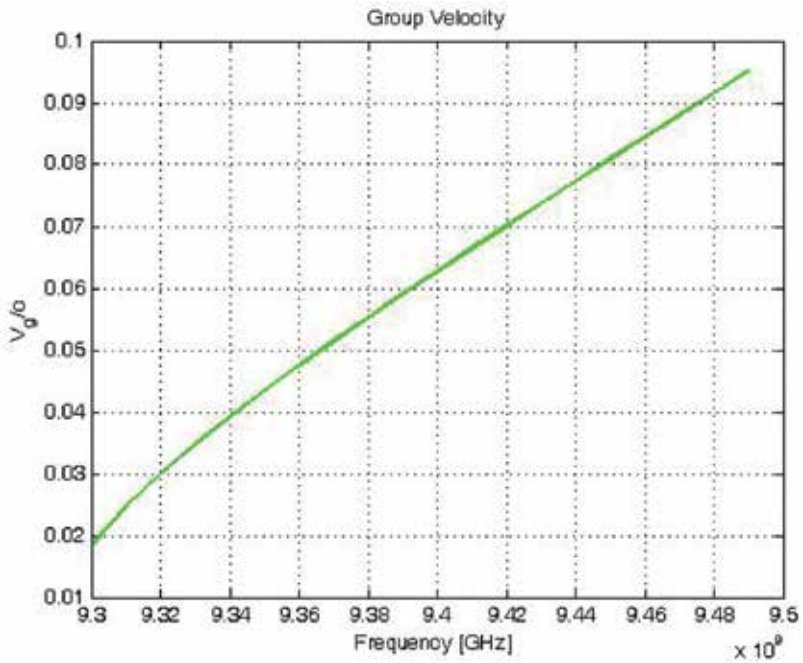

Figure 11. Group velocity of corrugated waveguide.

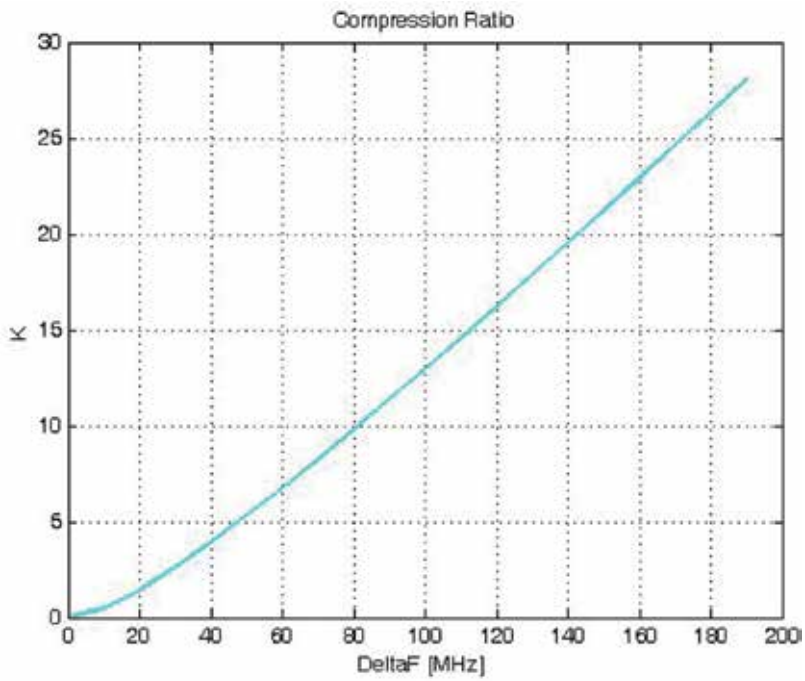

Figure 12. Compression ratio of corrugated waveguide.

10. Compact components and waveguide in microwave region

A slow-wave coplanar waveguide transmission lines, combining the advantages of both coplanar transmission lines and microstrip lines, is reported [11] to create high-performance passive components for millimeter wave integrating circuits. To achieve a slow wave, periodical slot-type floating shields are used to enable a reduction in a chip area while still maintaining high performance. Slot-type floating shields also enhance the immunity of slow-wave CPW transmission lines from ac noise (**Figure 13**).

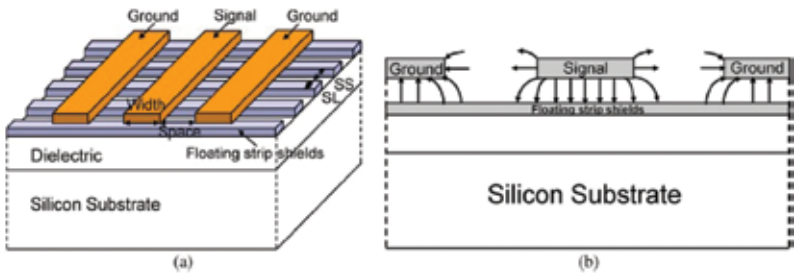

Figure 13. Slow-wave coplanar waveguide transmission line with slot-type floating shields. (a) Schematic view and (b) electric field distribution from 3-D EM simulation. From Ref. [11].

If the length of the periodical structure is short compared to the wavelength, each segment of signal line can be modeled by an inductance and capacitance lumped-element equivalent circuit, where L and C are the series inductance and the shunt capacitance per unit length, respectively. The density R of the slot-type floating shields is defined as

$$R = \frac{SL}{SL + SS} \tag{47}$$

Consequently, the phase velocity V_p with the slow-wave effect can be expressed as

$$V_p = \frac{1}{\sqrt{LC(nR)}} \tag{48}$$

where n represents the increased ratio in capacitance as a result of coupling to the slot-type shields. The slow-wave phenomenon can be explained in Eq. (48), which shows that the phase velocity is decelerated by a factor of $\sqrt{nR}$.

11. Conclusions

The chapter reports some applications of the interaction of slow electromagnetic waves with dielectric or corrugated media. The thread through the chapter is the possibility of generating electromagnetic waves from traveling particles in the considered medium or, vice versa, the

possibility to influence the motion of particles. An extension of this approach is the possibility of compressing the fields for applications in radars and linacs or to think about microwave devices and antennas of reduced dimensions for integration in the active circuits.

Author details

Giuseppe Di Massa

Address all correspondence to: dimassa@deis.unical.it

University of Calabria, Italy

References

[1] P. A. Cerenkov, Visible emission of clean liquids by action of γ radiation C. R. Acad. Sci. USSR, **8**, 451,1934.

[2] Cerenkov P A, Visible radiation produced by electrons moving in a medium with velocities exceeding that of light, Phys. Rev. 52, 378, 1937.

[3] I. Frank, I. Tamm, Coherent visible radiation from fast electrons passing through matter, C. R. Acad. Sci. USSR, **14**, No. 3, 1937.

[4] J. V. Jelley, *Cerenkov radiation and its applications*, Br. J. Appl. Phys., **6**, 227, 1955.

[5] G. Di Massa, V. G. Vaccaro, *Cherenkov Pick-up in the Microwave Band*, Hadronic Physic at Intermediate Energy, Elsevier Science Publishers, North Holland, Amsterdam, pp. 455–463, 1986.

[6] H. L. Andrews, C. A. Brau, *Three-Dimensional Theory of the Cerenkov Free-Electron Laser*, Proc. of FEL 2007, Novosibisk, Russia.

[7] G. P. Gallerano, A. Doria, E. Giovenale, A. Renieri, Compact free electron lasers: From Cerenkov to waveguide free electron lasers, Infrared Phys. Technol., **40**, 1999.

[8] R. Zhang, D. J. Gladstone, L. A. Jarvis, R. R. Strawbridge, P. J. Hoopes, O. D. Friedman, A. K. Glaser, B. W. Pogue, *Real-time in vivo Cherenkoscopy imaging during external beam radiation therapy*, J. Biomed. Opt., **11**, 2013.

[9] G. Di Massa, *High frequency slow wave pick-ups for stochastic cooling of bunched beams*, Il Nuovo Cimento, **100**, 1988.

[10] R. E. Collin, *Field Theory of Guided Waves, McGraw Hill, N. Y., 1960*, IEEE Trans. Plasma Sci., **30**, No. 3, 755–786, 2002.

[11] Hsiu-Ying Cho, Tzu-Jin Yeh, Sally Liu, and Chung-Yu Wu, *High-performance slow-wave transmission lines with optimized slot-type floating shields*, IEEE Trans. Electron Dev., **56**, 2009.

Chapter 7

Numerical Investigation about Frequency Behaviour of Conformal FSS

Giovanni Leone, Francesco Mattiello and
Rocco Pierri

Additional information is available at the end of the chapter

http://dx.doi.org/10.5772/66661

Abstract

Frequency selective surfaces (FSSs) are spatial filters widely employed in high-performance applications like hybrid radomes for radars and antennas. While planar geometries are widely studied, less attention has been devoted to conformal ones, where we must consider the influence of both the lattice geometry and the shape and size of the individual elements. In the planar case, periodicity first impacts on the general reflecting properties of the surface, while the shape and the size of the individual element affect its detailed both spatial and frequency filtering behaviour. In particular, the frequency response is dictated mainly by the scattering by the individual element and attains its maximum at resonance conditions. We mean to numerically investigate whether the same also occurs for non-planar surfaces and curved elements, for both cylindrical and conical surfaces. We compare the results of the general frequency behaviour of FSS both made of strips in free space and slots cut in a perfectly conducting material. The effect of the lattice geometrical parameters is also appreciated. The main conclusions are that also for curved elements a frequency selective behaviour can be appreciated and the interaction with the single elements plays an important role, when mutual coupling is not strong.

Keywords: electromagnetic scattering, FSS, conformal surfaces, thin strips, slots, mutual coupling

1. Introduction

Frequency selective surfaces (FSSs) have been studied for the last five decades, and comprehensive books have been also published [1, 2]. They have evolved from simple canonical forms to the complex geometries known today [3]. Moreover, since FSSs are a part of the broad family of artificial materials [4], new research efforts have been dedicated to this topic.

The FSS can be fabricated as planar two-dimensional periodic arrays of metallic elements with special geometric shapes or may be created by periodic openings in a metal screen. The transmission and reflection properties of these surfaces are dependent on the operating frequency and may also depend on the polarization and the incidence angle of the electromagnetic wave impinging the material. While the frequency behaviour of the surface is dictated both by the elements spacing and the shape of the basic element, hereafter we are interested to consider the effect of the latter one. In this chapter, we consider a comparison between the planar and the cylindrical case, in order to verify if the frequency behaviour remains similar when the surface is conformal. In addition, results of the scattering by a conical surface are presented.

While several numerical approaches are available for planar FSS [5] and for complicated structures [6], conformal (or curved) FSSs are more difficult to be analysed since the periodicity and the infinite extent of the surface are lost and a unit cell cannot be recognized. For instance, for a conformal surface made of thin loops, an approach based on the numerical solution of the relevant integral equation by the method of moments is introduced in Ref. [7] leading to the observation that each elements is excited in a different way by an impinging plane wave. In Ref. [8], a spectral domain approach is introduced to try to alleviate the computation burden for the scattering by a spherical FSS.

In Ref. [9], frequency-selective behaviour has been observed for the field scattered by a periodically slotted cylinder compared to a solid cylinder. In Ref. [10], an electromagnetic model for their scattering is introduced, but the numerical analysis cannot provide definitive results.

Therefore, the interest arises to conduct further investigation, by a purely numerical approach, about their frequency behaviour. In particular we focus our attention on the curvature and periodicity effects, due to the conformal geometry (cylinder or cone), to which less interest has been paid in the literature. We start out our analysis by considering first, in Section 2, a surface made of thin perfectly electrical conducting (PEC) periodic strips in free space. For the sake of comparison, first a planar arrangement is reported and next the scattering of a plane wave by a cylindrical one is evaluated. The strips are both aligned along the axis of the cylinder and oriented along its cross section. The longitudinal and transverse (with respect to the cylinder axis) periods are varied. Finally, an example for strips arranged on a finite conical surface is reported.

In Section 3, we move to examine the scattering by slotted PEC surfaces. While for slotted planar geometries, it is possible to use the Babinet's principle so that the results obtained for the strips (complementary structure) can be used to predict its frequency behaviour, for conformal structures the Babinet's principle is not applicable, and it is necessary to use a numerical analysis of the entire structure in order to evaluate the frequency behaviour. In this chapter, we analyse a conformal cylindrical structure, made by a PEC circular cylinder in which thin slots are cut. For the purpose of the numerical simulation, the scattering from a finite slotted strip of the cylinder is used with the appropriate periodic boundary conditions to simulate an infinite cylinder. Again different periods between the slot elements are considered and a comparison with the results of planar structures is performed. At the end of the section, again, an example of a slotted finite cone is reported.

All results are computed by numerical simulation of the electromagnetic scattering by PEC objects through a commercial software based on the Finite Difference Time Domain method,

http://dx.doi.org/10.5772/66661

which is the common choice for broad-band analysis. Since we are not interested in the angular filtering properties of the structures but only in exploring possible frequency filtering about their scattered field, we choose to report the total scattered power vs. frequency.

2. Strip geometry

2.1. Planar strips

In the first scenario, an infinite planar passive FSS, made by metallic straight strips is simulated to verify the frequency behaviour. In particular, we focus our attention on the scattered field vs. frequency, and we run simulations changing the spatial period (horizontal and vertical) to verify the modification of the frequency behaviour. **Figure 1** shows a top view of the geometry where TD and VD denote the transverse and vertical spacings between the elements, respectively.

The strip is 15 mm long and 1 mm wide, and the excitation is provided by a *y*-polarized incident plane wave, propagating along the *z* direction (**Figure 1**). **Figure 2** shows the scattered power for different spatial (vertically and transverse with respect to the alignment of the strip) periods.

As expected, when the strips are far away, the maximum interactions occur when their lengths are around $\lambda/2$, that is, at resonance with the isolated strip. On the contrary due to the increased mutual coupling effect, for lower spacings, resonance moves to higher frequencies. In addition, transverse displacement affects more mutual coupling and so also the scattered power.

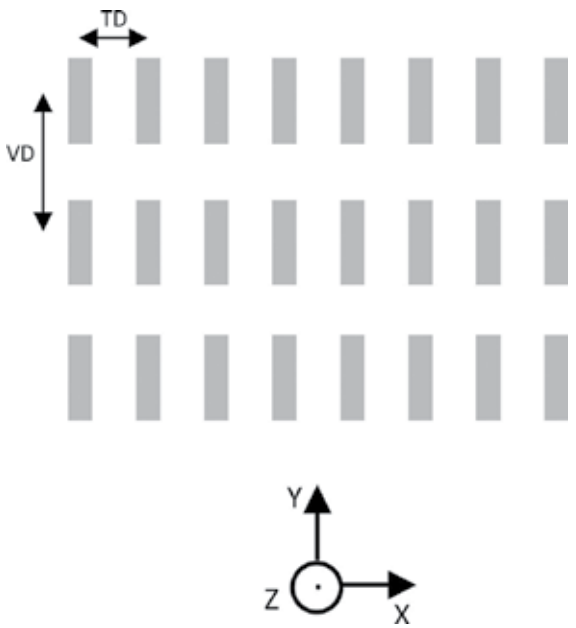

Figure 1. Geometry of a planar passive FSS composed of metallic strips.

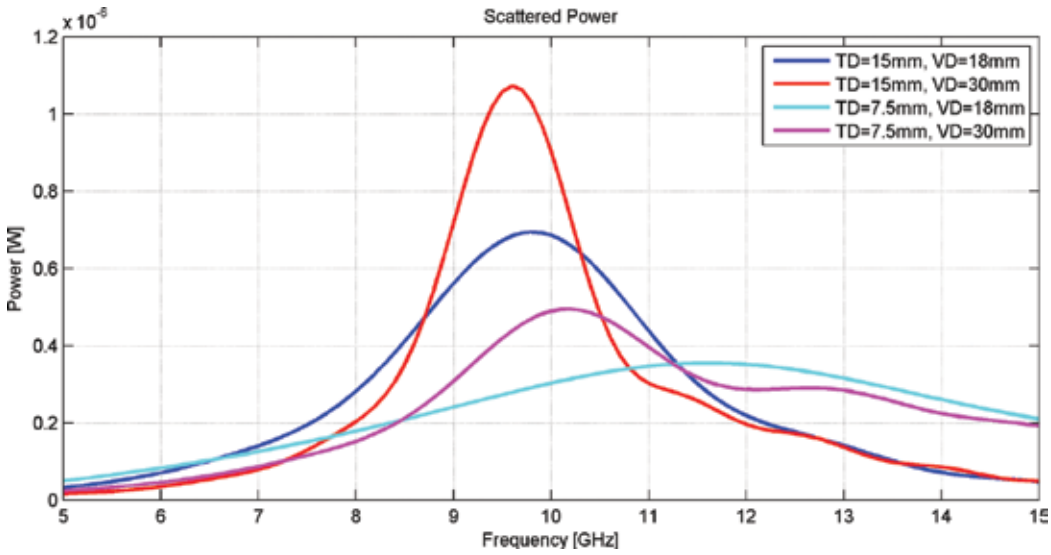

Figure 2. The power scattered by a planar FSS made of strips, for various transverse (TD) and vertical (VD) spacings.

2.2. Planar thin loop

In this scenario, an infinite planar passive FSS is considered, made by circular 1 mm large loop strips with 30 mm circumference (**Figure 3**). The same plane wave excitation as above is assumed.

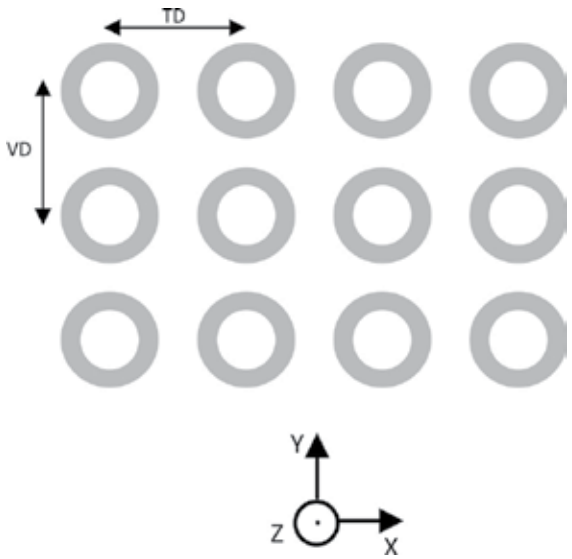

Figure 3. Geometry of planar passive FSS composed of metallic strip loops.

http://dx.doi.org/10.5772/66661

Figure 4 shows the scattered power by an infinite planar FSS made by circular loop strips, for different (equal) spacings between the loops.

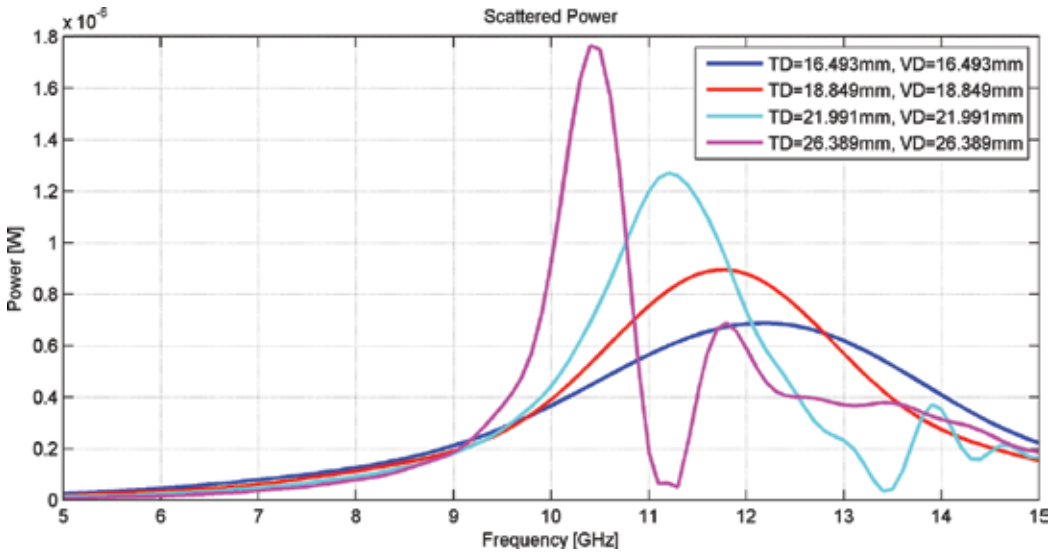

Figure 4. The power scattered by a planar FSS made of loop strips, for various transverse (TD) and vertical (VD) spacings.

As expected, when the loops are far away, the maximum interactions occur when their length is around λ, that is, at resonance with the isolated loop. On the contrary due to the increased mutual coupling effect, for lower spacings, resonance moves to higher frequencies.

2.3. Straight strips on a cylinder

In this scenario, the strips are placed on a conformal cylindrical surface with a radius of 42 mm (**Figure 5**). An infinite structure is considered by imposing periodic boundary conditions in the numerical simulations along the *z*-axis at various VD spacings. Again, we show the results obtained by changing the transverse spatial period, so implying different number of strips. Again the strips have the same dimensions as in the previous case. The impinging plane wave is polarized along the *z*-axis and propagates along a direction normal to the cylinder.

From **Figure 6**, a frequency-selective behaviour, though for a rather broad band, can be still appreciated for the non-planar surface case mainly for the largest transverse spacing. Instead, the mutual coupling badly affects this behaviour in a similar way as observed for the planar structures.

2.4. Curved strips on a cylinder

In this scenario, we consider curved, 15 mm long and 1 mm wide strips arranged on a conformal cylindrical surface with a radius of 42 mm (**Figure 7**). In this way, two curvature effects are considered, that is, of both the single scattering element and the surface. An infinite struc-

ture along the z-axis is simulated by resorting to periodic boundary conditions. The incident plane wave is y-polarized and propagates normally to the cylinder.

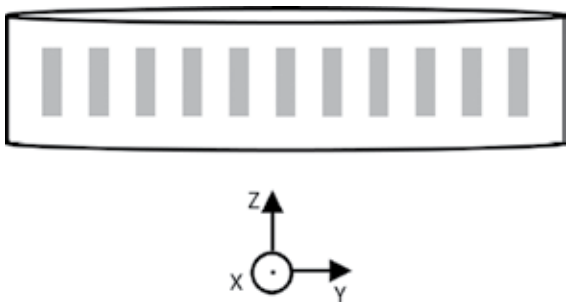

Figure 5. Relevant to the geometry of a conformal cylindrical FSS composed of straight metallic strips.

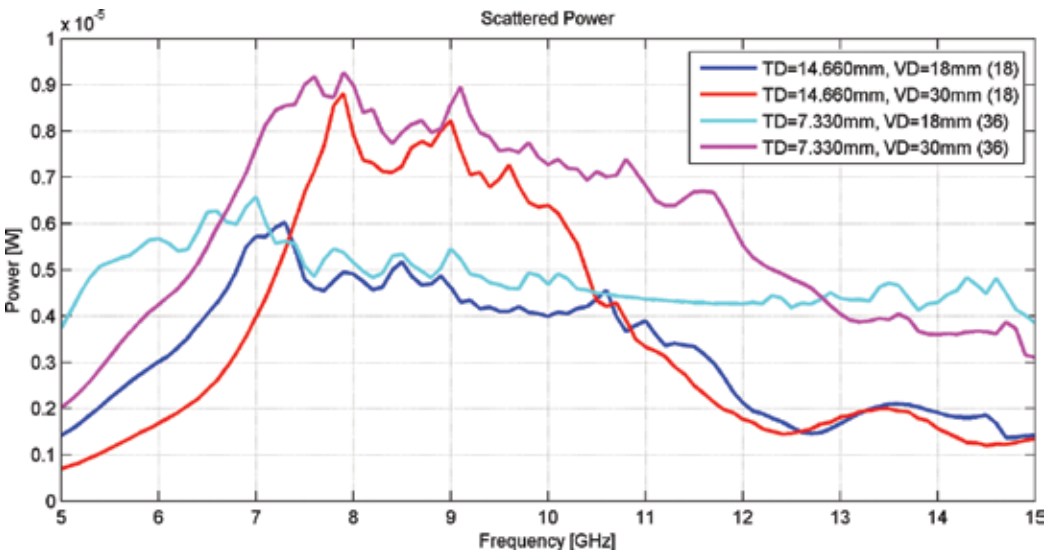

Figure 6. The power scattered by a cylindrical FSS made of straight strips, for various transverse (TD) and vertical (VD) spacings (in brackets, the number of strips is reported).

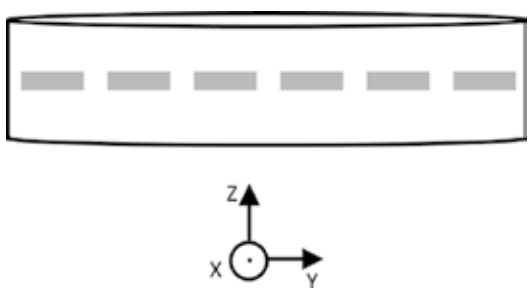

Figure 7. Relevant to the geometry of a conformal cylindrical FSS composed of curved metallic strips.

http://dx.doi.org/10.5772/66661

From **Figure 8**, a frequency-selective behaviour, though for a rather broad band, can be still appreciated for the non-planar surface case and curved strips mainly for the largest transverse spacing. Again, the mutual coupling affects badly this behaviour in a similar way as observed for the planar structures. In fact, as well known, the radiation of wire structures is more affected by similar wire objects when they are approaching each other along the transverse direction, where the induced current is stronger, than along the vertical direction, where the current vanishes.

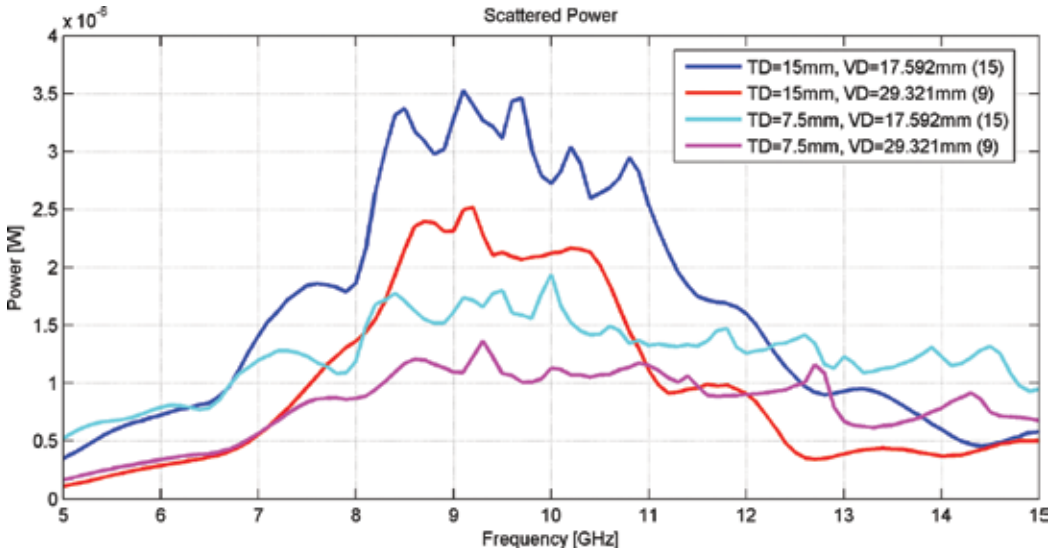

Figure 8. The power scattered by a cylindrical FSS made of curved strips, for various transverse (TD) and vertical (VD) spacings (in brackets, the number of strips is reported).

2.5. Curved loops on a cylinder

Finally, we consider a circular crown, made of curved loop strips, arranged on the same cylindrical surface as above (**Figure 9**). The transverse and vertical spacings are varied for the same amount for different simulations. The incident plane wave is z-polarized and propagates normally to the cylinder.

From the results of **Figure 10**, a frequency-selective behaviour of the scattered power is observed around the same frequency as it occurs in the planar case, that is, when the loop length is about λ. However, when the loops are approaching each other the mutual coupling affects the selectiveness by slightly reducing it.

2.6. Straight strips on a cone

In this scenario, the strips are placed on a conformal conical surface with 30° aperture angle. The cone height (along z) is 268.9 mm and eight rows of strips are distributed along its surface as given in **Figure 11**; the height of the row closest to the vertex is 5.85 mm. The vertical spacing

between the rows is 30 mm, while for all rows, the transverse one is about 15 mm along the arc. Again, the strips have the same dimensions as in the previous cases. The impinging plane waves are linearly polarized.

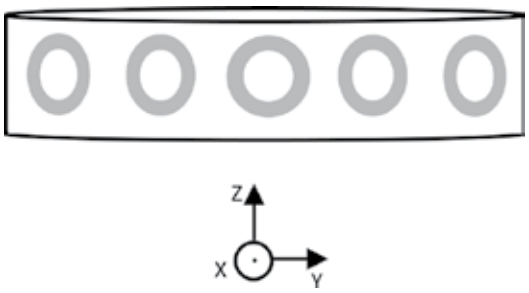

Figure 9. Relevant to the geometry of a conformal cylindrical FSS composed of metallic loop strips.

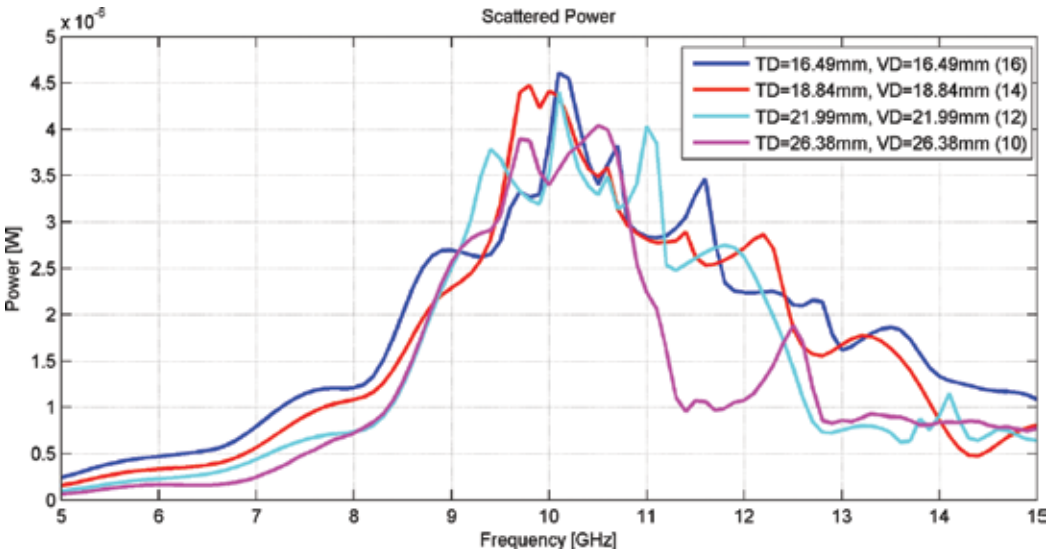

Figure 10. The power scattered by a cylindrical FSS made of curved loops, for various transverse (TD) and vertical (VD) spacings (in brackets, the number of loops is reported).

From **Figure 12**, a frequency-selective behaviour can be appreciated, similar to the planar and cylindrical case of previous sections.

2.7. Curved strips on a cone

In this scenario, the strips are placed on a conformal conical surface with 30° aperture angle. The cone height (along *z*) is 149.4 mm, and eight rows of strips are distributed along its surface as given in **Figure 13**; the height of the row closest to the vertex is 39 mm. The transverse spacing between the rows is 15 mm, while for all rows, the vertical one is about 30 mm along the arc. Again, the strips have the same dimensions as in the previous cases. The impinging plane waves are linearly polarized.

http://dx.doi.org/10.5772/66661

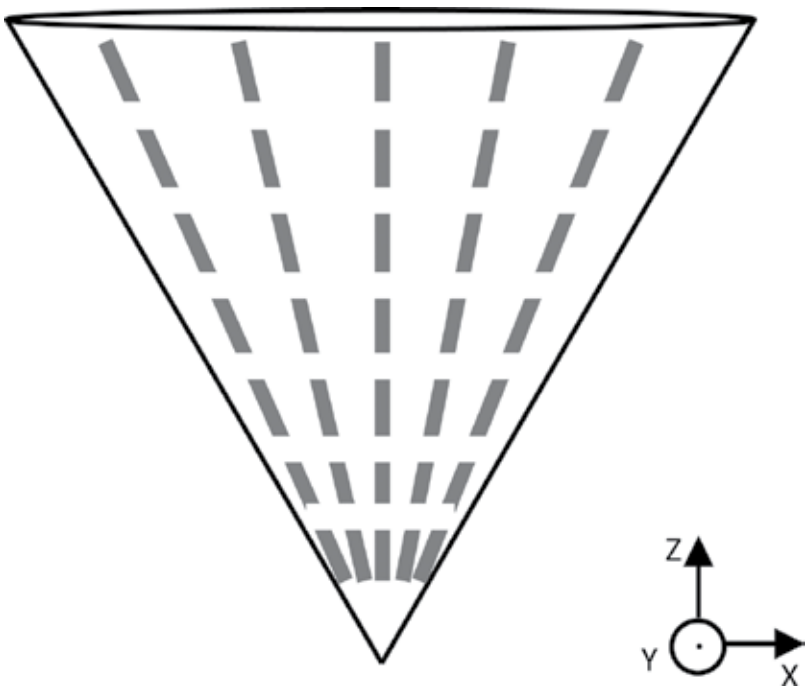

Figure 11. Geometry of a conformal conical FSS composed of straight metallic strips.

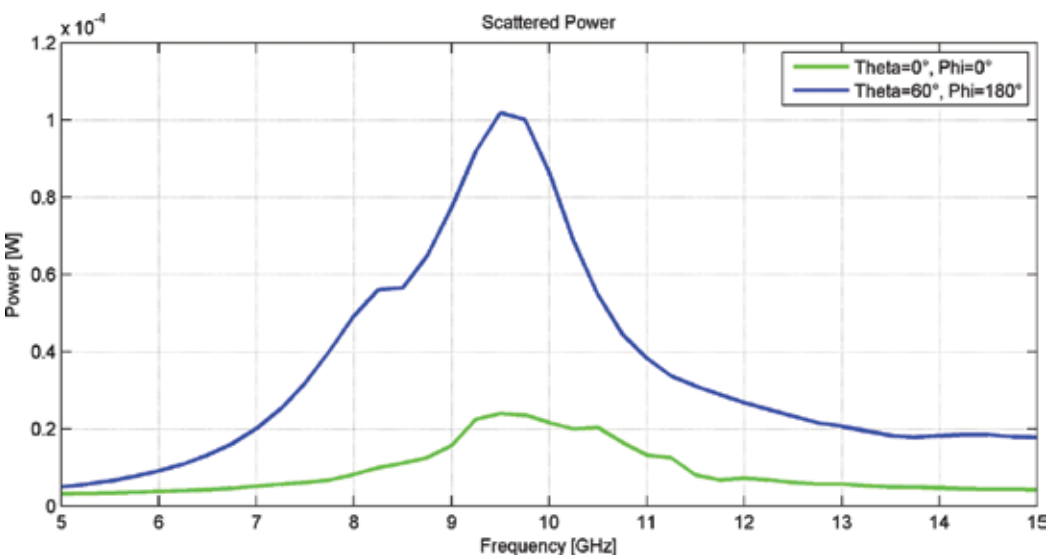

Figure 12. The power scattered by a conical FSS made of straight strips, for various plane wave incidence: $\theta = 60°$, $\varphi = 180°$ (blue line), $\theta = 0°$, $\varphi = 0°$ (green line).

From **Figure 14**, a frequency selective behaviour can be appreciated, similar to the planar and cylindrical case of previous sections.

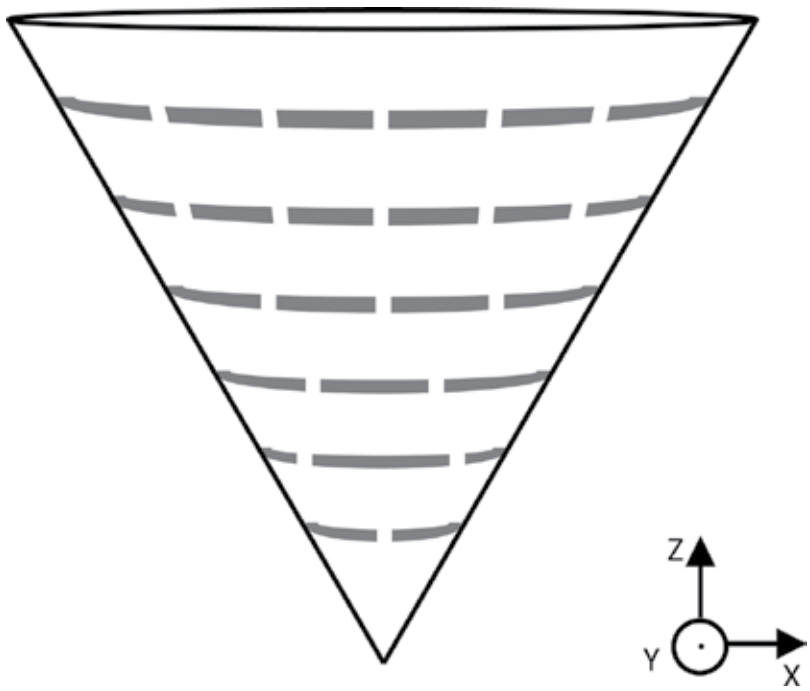

Figure 13. Geometry of a conformal conical FSS composed of curved metallic strips.

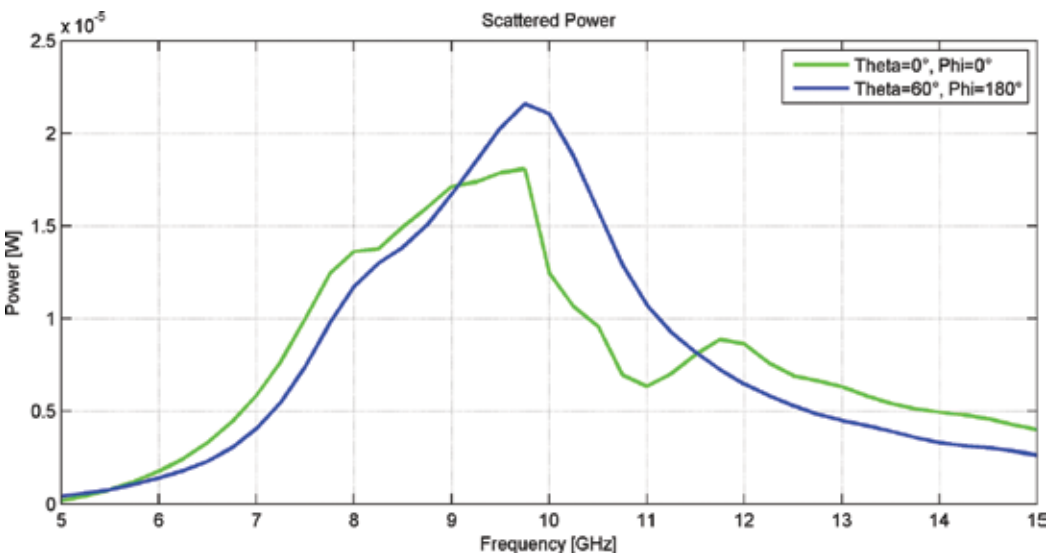

Figure 14. The power scattered by a conical FSS made of curved strips, for various plane wave incidence: $\theta = 60°$, $\varphi = 180°$ (blue line), $\theta = 0°$, $\varphi = 0°$ (green line).

http://dx.doi.org/10.5772/66661

3. Slot geometry

3.1. Planar slots

The scattering of plane waves by planar FSS made of slots cut in a PEC surface obeys the Babinet's principle and therefore can be predicted by the results of the complementary strip case. In fact, field transmitted by the slotted surface, and then the transmitted power, is minimum at those frequencies for which the total field scattered by the complementary strip surface achieves its maximum value. Accordingly, the analysis of one of the two structures allows to predict the frequency behaviour of the other one. For non-planar structures, unfortunately, the same investigation must be performed numerically, which can become resource demanding for electrically large structures. For an infinite cylindrical surface, however, application of periodic boundary conditions can reduce this burden.

3.2. Straight slots on a cylinder

In this scenario, slots are placed on a conformal cylindrical surface with a radius of 42 mm (**Figure 15**). We show the results obtained by changing the transverse spatial period, so implying different number of slots. Slots are 15 mm long and 1 mm wide to be complementary to the strips of previous section. The impinging plane wave is polarized along the *y*-axis and propagates along a direction normal to the cylinder.

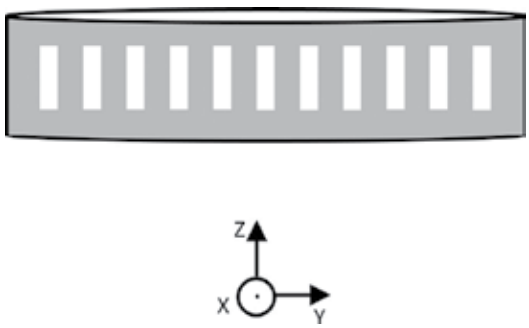

Figure 15. Relevant to the geometry of a conformal metallic cylindrical FSS composed of straight slots.

From **Figure 16**, a frequency-selective behaviour, complementary to the one of the structure of Section 2.4, can be still appreciated for the non-planar surface case mainly for the largest transverse spacing. Instead, the mutual coupling badly affects this behaviour in a similar way as observed for the planar structures, so making the minimum of the scattered power less pronounced.

3.3. Curved slots on a cylinder

In this scenario, we consider curved, 15 mm long and 1 mm wide slots arranged on a conformal cylindrical surface with a radius of 42 mm (**Figure 17**). In this way, two curvature effects are considered, that is, of both the single scattering element and the surface. An infinite structure along the *z*-axis is simulated by resorting to periodic boundary conditions. The incident plane wave is *z*-polarized and propagates normally to the cylinder.

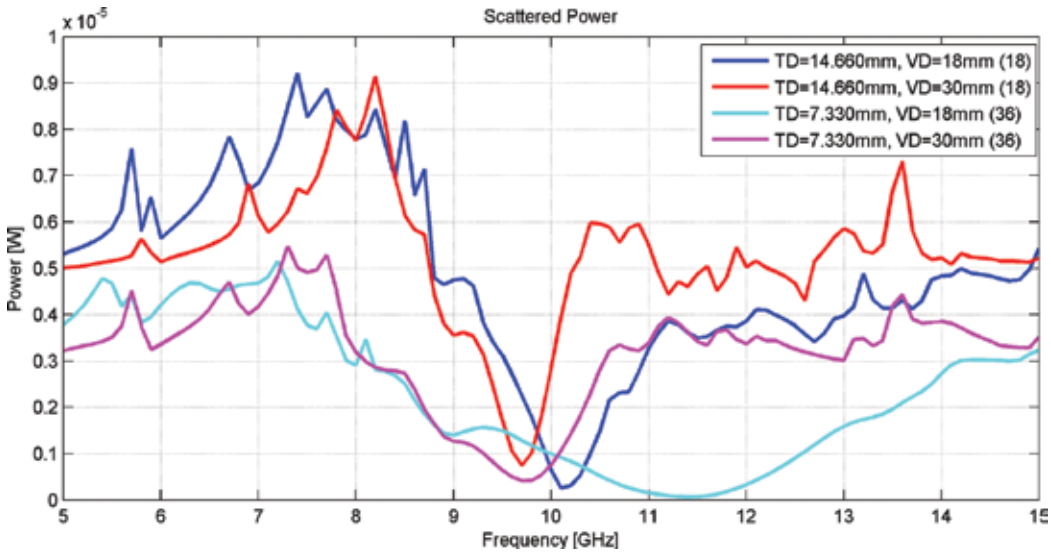

Figure 16. The power scattered by a cylindrical FSS made of straight slots, for various transverse (TD) and vertical (VD) spacings (in brackets, the number of slots is reported).

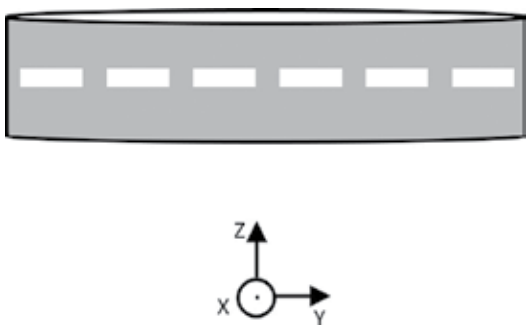

Figure 17. Relevant to the geometry of a conformal metallic cylindrical FSS composed of curved slots.

From **Figure 18**, a frequency-selective behaviour can be still appreciated for the non-planar surface case and curved loops mainly for the largest transverse spacing, along the same line as the case of strips of Section 3.3. Again, the mutual coupling badly affects this behaviour so that for slot closer along the transverse direction no significant frequency-selective behaviour can be appreciated.

3.4. Curved loop slots on a cylinder

Finally, we consider one circular crown, made of curved loop slots, varying the horizontal and vertical deltas at the same time (**Figure 19**). The slots circumference is 30 mm long and 1 mm wide. The incident plane wave is y-polarized and propagates normally to the cylinder.

From the results given in **Figure 20**, a frequency-selective behaviour of the scattered power is observed especially for the largest spacings. However, when the loops are approaching each other, the mutual coupling affects the selectiveness by slightly reducing it.

http://dx.doi.org/10.5772/66661

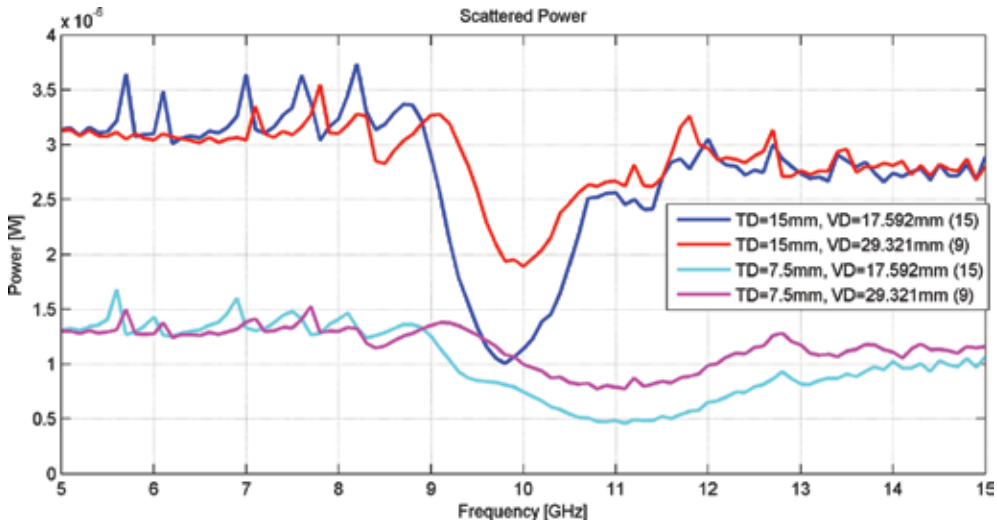

Figure 18. The power scattered by a cylindrical FSS made of curved slots, for various transverse (TD) and vertical (VD) spacings (in brackets, the number of slots is reported).

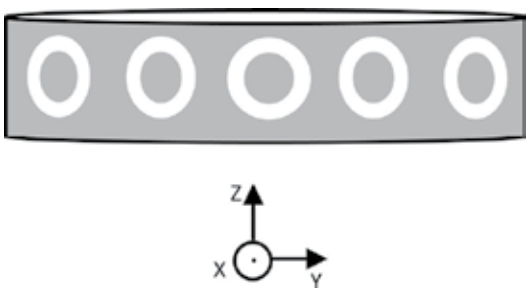

Figure 19. Relevant to the geometry of a conformal metallic cylindrical FSS composed of loop slots.

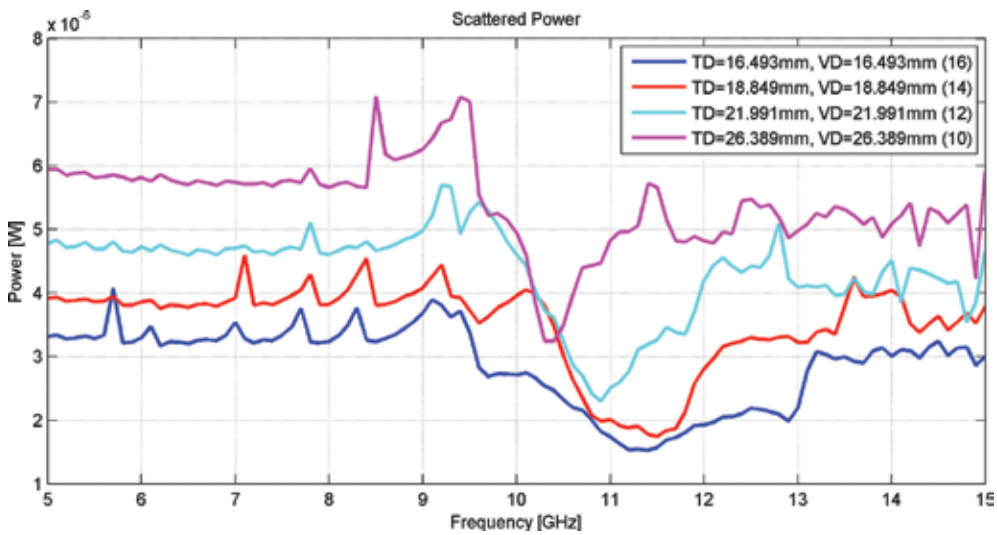

Figure 20. The power scattered by a cylindrical FSS made of loop slots, for various transverse (TD) and vertical (VD) spacings (in brackets, the number of loops is reported).

4. Conclusions

Scattering by conformal FSS cannot be easily investigated by standard techniques as planar periodicity is lost, thus requiring a purely numerical approach. Anyway, it is of interest to explore whether the main features of the planar surfaces behaviour still hold. With reference to a simple wire geometry over a conformal cylindrical surface the power scattered under plane-wave incidence has been evaluated under different scenarios. The main results confirm the possibility to achieve a peaked frequency-selective response under conditions similar to the planar case, that is, for the resonance (open wires) or anti-resonance (closed-loop wires) length. However, when the objects are approaching each other, mutual coupling effects change the induced current appreciably and reduce the frequency selectiveness of the surface. Similar conclusions can be drawn also when the strips are distributed along a conical surface and for FSS made of slots where a complementary stop band behaviour is observed, since the scattered power is reduced within a certain band.

This work has been funded by Campania Region under the **"MASTRI"** (Smart Materials and Structures) Excellence Network.

Author details

Giovanni Leone*, Francesco Mattiello and Rocco Pierri

*Address all correspondence to: giovanni.leone@unina2.it

Dipartimento di Ingegneria Industriale e dell'Informazione – Seconda Università degli Studi di Napoli, Aversa, CE, Italy

References

[1] B. A. Munk. Frequency Selective Surfaces: Theory and Design. John Wiley and Sons Inc. New Jersey (U.S.A.); 2000.

[2] T. K. Wu. Frequency Selective Surface and Grid Array. John Wiley and Sons Inc. New Jersey (U.S.A.); 1995.

[3] F. Mattiello, G. Leone, G. Ruvio. Analysis and Characterization of Finite-Size Curved Frequency Selective Surfaces. Studies in Engineering and Technology. 2015;**2**(1):9–21.

[4] G. Ruvio, G. Leone. State-of-the-art of Metamaterials: Characterization, Realization and Applications. Studies in Engineering and Technology. 2014;**1**(2):38–47.

[5] S. Narayan, R. M. Jha. Electromagnetic Techniques and Design Strategies for FSS Structure Applications. IEEE Antennas and Propagation Magazine. 2015; **57**:135–158.

[6] A. K. Rashid, B. Li, Z. Shen. An Overview of Three-Dimensional Frequency-Selective Structures. IEEE Antennas and Propagation Magazine. 2014; **56**:43–67.

http://dx.doi.org/10.5772/66661

[7] S. B. Savia, E. A. Parker, B. Philips. Finite Planar-and Curved-Ring-Element Frequency-Selective Surfaces. IEEE Proceedings Microwaves, Antennas Propagation. 1999; **146**: 401–406.

[8] C. Pelletti, G. Bianconi, R. Mittra, A. Monorchio. Analysis of Finite Conformal Frequency Selective Surfaces via the Characteristic Basis Function Method and Spectral Rotation Approaches. IEEE Antennas Wireless Propagation Letters. 2013; **12**:404–1407.

[9] A. Uzer, T. Ege. Scattering from Periodically Spaced Longitudinal Slots on a Conducting Cylinder. Electrical Engineering October 2005. **87**(6):291–293.

[10] E. Di Salvo, F. Frezza, E. Stoja, N. Tedeschi. Single Layer Cylindrical Frequency Selective Structures for Radome. Progress in Electromagnetics Research Symposium Proceedings, Stockholm, Sweden, Aug. 12–15. 2013

Chapter 8

A Rain Estimation System Based on Electromagnetic Propagation Models and DVB-S Opportunistic Sensors

Daniele Caviglia, Matteo Pastorino,
Andrea Randazzo and Andrea Caridi

Additional information is available at the end of the chapter

http://dx.doi.org/10.5772/66726

Abstract

Weather conditions have in general huge impact on the global economy, in particular on agriculture, industry, transport, and so forth. In recent years, also the occurrences of rapid and localized heavy rainfall in complex topographic areas became more frequent, possibly due to global warming. These facts cause injuries and deaths, and an accurate and early alert system is required to warn people and operators. In this chapter, we describe a real-time and low-cost system for precipitation detection, aimed at collecting additional data with respect to those obtainable from traditional sensors. Such a system is based on the opportunistic usage of satellite digital video broadcasting (DVB-S) microwave signals and estimates the rain intensity from the detected attenuation. Our system proved to accurately obtain results comparable with rain gauges located in the experimentation area, with much tighter spatial and temporal scales than traditional schemes.

Keywords: rainfall estimation, nowcasting, antennas, electromagnetic propagation, electronic circuits

1. Introduction

In several countries around the world, the occurrence of flash flood events is notably increasing with more extensive damages. Usually, flash flooding is a result of heavy localized rainfall, such as that from slow moving intense thunderstorms. Consequently, in the last few years, there has been an increasing interest in developing techniques aimed at regularly monitoring the amount of rainfall [1–7].

Besides the well-known weather prediction networks aimed at providing information on the expected precipitation, the monitoring of rainfalls during the events is now considered of

paramount importance for the civil protection. The most used apparatuses for rainfall measurement are based on rain gauges, wheatear radars, radiometers, and global positioning system (GPS) systems. Rain gauges measure the quantity of rain fallen into a small bucket in a predefined time interval, usually in the range of 10–15 minutes. Therefore, they are not generally suitable for real-time monitoring of the atmospheric phenomenon, especially when dealing with thunderstorms that may occur over small basins, with a size of a few square kilometres, and consequently a lag time in the order of half an hour, or even less.

Weather surveillance radars (WSR) [8] exploit the reflection of the electromagnetic waves when impinging on hydrometeors in order to create maps of inspected regions, which are generally quite large (over 100 km in radius). In this case, too, the data are usually acquired every 10–15 minutes. The main problem of WSR is the high installation and maintenance cost, which does not allow to deploy a large number of measurement stations. X-band radars have also been proposed for weather monitoring [9, 10]. In this case, however, the useful range is limited (usually less than 60 km), requiring to create networks of interconnected systems in order to monitor a large area. GPS-based systems employ the microwave signal transmitted for positioning and navigation purposes in order to estimate the rainfall [11]. In fact, the time delay of the signal received by the receivers at earth (tropospheric delay) depends upon the dielectric properties of the atmosphere, and consequently, upon its water content [12]. However, it is worth noting that the quantity that can be extracted from the analysis of the tropospheric delay is just the precipitable water and not the actual rain at earth.

Recently, the rapid growth of mobile communications resulted in a global spread of wireless networks operating in the microwave band. Such networks can be used in an opportunistic way for environmental characterization [13]. In particular, the attenuation level of the measured signal can be used to estimate the intensity of the rain. This attenuation is caused by the phenomena of absorption and "scattering" of the electromagnetic field due to the water droplets in air, which are most significant for frequencies above 10 GHz (i.e., when the wavelength of the electromagnetic waves assumes the values of the same order of magnitude of the diameter of the drops). In this framework, the use of terrestrial links between mobile communication base stations, usually working at frequencies in the K or Ka bands, has been proposed in the literature for estimating the rainfall near the earth surface [14–17]. The main drawback of this method consists in the fact that such microwave links are mainly deployed in urban areas, while the hills and mountains that collect waterfall and produce flood events are scarcely covered. A second problem deals with the ownership of the infrastructure and propagation data by telecom operators, which requires their involvement in the process.

Given this situation, the opportunistic usage of attenuation data of the microwave links from geostationary satellites has been proposed recently [1–4]. In this chapter, we will describe a rain monitoring system based on the measurement of the electromagnetic radiation received by standard antennas used by commercial satellite digital video broadcasting (DVB-S) decoders. The developed apparatus employs a logarithmic amplifier/detector to convert the antenna received power into a voltage, which is then acquired by an analog-to-digital converter and transmitted to a central node via a wired or wireless link. The data are stored in a database and processed in order to estimate the rain rate over the area of interest. A mathematical model

http://dx.doi.org/10.5772/66726

based on antennas and propagation concepts is used to describe the relationship between the rain intensity and the measured values. In particular, the well-assessed ITU model described in [18] is employed for relating the specific attenuation along the path to the rain rate.

The chapter is organized as follows: in Section 2, the electromagnetic waves propagation and attenuation model is briefly reviewed. In Section 3, the developed rainfall estimation system is described. In Section 4, some experimental results are provided and discussed. Finally, conclusions are outlined in Section 5.

2. Mathematical formulation

From an electromagnetic point of view, the formulation of the approach is based on the propagation and attenuation of the electromagnetic waves transmitted by a commercial satellite for broadcasting services. In the far field of the transmitting antenna, the field is locally a plane wave, i.e.,

$$\mathbf{E}(\mathbf{r}) = E_p(\mathbf{r}) e^{-jk\hat{\mathbf{k}}\cdot\mathbf{r}} \hat{\mathbf{p}} \tag{1}$$

$$\mathbf{H}(\mathbf{r}) = \frac{1}{\eta} E_p(\mathbf{r}) e^{-jk\hat{\mathbf{k}}\cdot\mathbf{r}} \hat{\mathbf{k}} \times \hat{\mathbf{p}} \tag{2}$$

where $\mathbf{r}$ is the position vector, $\hat{\mathbf{p}}$ and $\hat{\mathbf{k}}$ are unit vectors denoting the polarization and direction of propagation, $k = \beta - j\alpha$ is the complex propagation constant (its real part is the phase constant and the imaginary part is the attenuation constant, whose unit is m^{-1}), E_p is the field amplitude, and η is the intrinsic impedance of the propagation medium. The power density of the wave is given by the Pointing vector, i.e.,

$$\mathbf{S}(\mathbf{r}) = \frac{1}{2} \mathbf{E}(\mathbf{r}) \times \mathbf{H}^*(\mathbf{r}) = \frac{1}{2\eta} \left| E_p \right|^2 e^{-2\alpha\hat{\mathbf{k}}\cdot\mathbf{r}} \hat{\mathbf{k}} = S_k(\mathbf{r}) \hat{\mathbf{k}} \tag{3}$$

When the attenuation due to atmospheric gases, multipath, and other effects can be neglected, the available power at the receiving antenna (located at position $\mathbf{r}_{RX}$) can be expressed as

$$P_L = A_{\text{eff}} S_k(\mathbf{r}_{RX}) \tag{4}$$

where A_{eff} denotes the effective area of the receiving antenna. Since

$$A_{\text{eff}} = e_{\text{pol}} e_{\text{load}} \frac{\lambda^2}{4\pi} G_{RX} \tag{5}$$

where G_{RX} is the gain of the receiving antenna and e_{pol} and e_{load} are the polarization and the load matching efficiencies, it results

$$P_L = \frac{\lambda^2}{4\pi} G_{RX} e_{\text{pol}} e_{\text{load}} S_d(\mathbf{r}_{RX}) \tag{6}$$

There are two conditions to be compared. In the first case, we assume that no rain is present. In this case, we denote the received power as P_L^0. When rainfall is present, there is an extra

attenuation that contributes to the imaginary part of the propagation constant. Therefore, we can write the attenuation due to rain as

$$L_{\text{rain}} = \frac{P_L^0}{P_L} = e^{2\alpha_{\text{rain}} l_{\text{rain}}} \tag{7}$$

where l_{rain} is the length of the path traveled by the plane wave interested by the rain. Since the rain originates at a height h_{rain} above the sea (as schematically shown in **Figure 1**), the length of the path interested by the rain is given by

$$l_{\text{rain}} = \frac{h_{\text{rain}} - h_{RX}}{\sin \theta_{\text{el}}} \tag{8}$$

where h_{RX} is the altitude of the receiving antenna and θ_{el} is its elevation angle. The rain height mainly depends upon the geographical location of the receiving antenna and can be obtained from weather services or by using the mean values provided in the ITU recommendation P.839 [19].

By expressing the attenuation L_{rain} in dB (L_{rain}^{dB}) and l_{rain} in kilometers ($l_{\text{rain}}^{\text{km}}$), we obtain

$$L_{\text{rain}}^{\text{dB}} = P_L^{0\ \text{dBm}} - P_L^{\text{dBm}} = 10 \log e^{2\alpha_{\text{rain}} l_{\text{rain}}} = 20\, \alpha_{\text{rain}}\, l_{\text{rain}} \log e = \alpha_{\text{rain}}^{dB/\text{km}}\, l_{\text{rain}}^{\text{km}} \tag{9}$$

where $\alpha_{\text{rain}}^{\text{dB/km}} = 0.02\, \alpha_{\text{rain}} \log e$ is the specific attenuation and the superscript dBm indicates that the quantities are expressed in decibel (referred to 1 mW).

According to ITU recommendation P.838 [18], which assumes that the specific attenuation is constant over the whole length interested by the rainfall, the attenuation per unit length, $\alpha_{\text{rain}}^{\text{Km}}$ [dB/km], is related to the rain rate r (mm/h) by the following equation

$$\alpha_{\text{rain}}^{\text{dB/Km}} = B\, r^A \tag{10}$$

where B and A are two coefficients that depends upon the frequency and the polarization of the electromagnetic wave. Normally, by using the ITU model, it is only possible to retrieve a global information about the overall rain rate along such path.

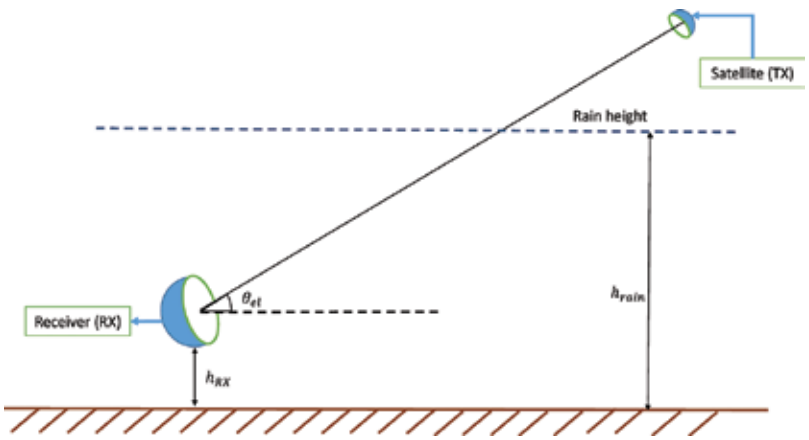

Figure 1. Schematic representation of the considered configuration.

http://dx.doi.org/10.5772/66726

By combining the model (10) and the link budget (9), the following equation is obtained

$$P_L^{\mathrm{dBm}} = P_L^{0\ \mathrm{dBm}} - B\, l_{\mathrm{rain}}^{\mathrm{km}}\, r^A = P_L^{0\ \mathrm{dBm}} - B\, l_{\mathrm{rain}}^{\mathrm{km}} \left(\frac{h_{\mathrm{rain}} - h_{RX}}{\sin\theta_{el}}\right)^A \tag{11}$$

which must be inverted in order to find the rain rate r starting from the received power. The superscript km in Eq. (11) indicates that the heights are expressed in kilometers. Consequently, it results that the rain rate can be estimated as

$$r = \left[\frac{P_L^{0\ \mathrm{dBm}} - P_L^{\mathrm{dBm}}}{B\left(h_{\mathrm{rain}}^{\mathrm{km}} - h_{RX}^{\mathrm{km}}\right)} \sin\theta_{el}\right]^{\frac{1}{A}} \tag{12}$$

It is worth noting that, in order to solve Eq. (12), the knowledge of the reference power P_L^0 (i.e., the received power in absence of rainfalls) is required. Such quantity can be estimated from historical data.

3. System description

The considered system exploits the information contained in the signal at the output of a low noise block (LNB), commonly used in the receiving chain of a consumer DVB-S set. In particular, the power level is measured by an ad-hoc designed sensor and the output of such sensor is then "inverted" in order to estimate the rainfall. The block diagram of the proposed measurement system is shown in **Figure 2**. Its main parts consist in a sensing board, a microcontroller unit, and a network interface.

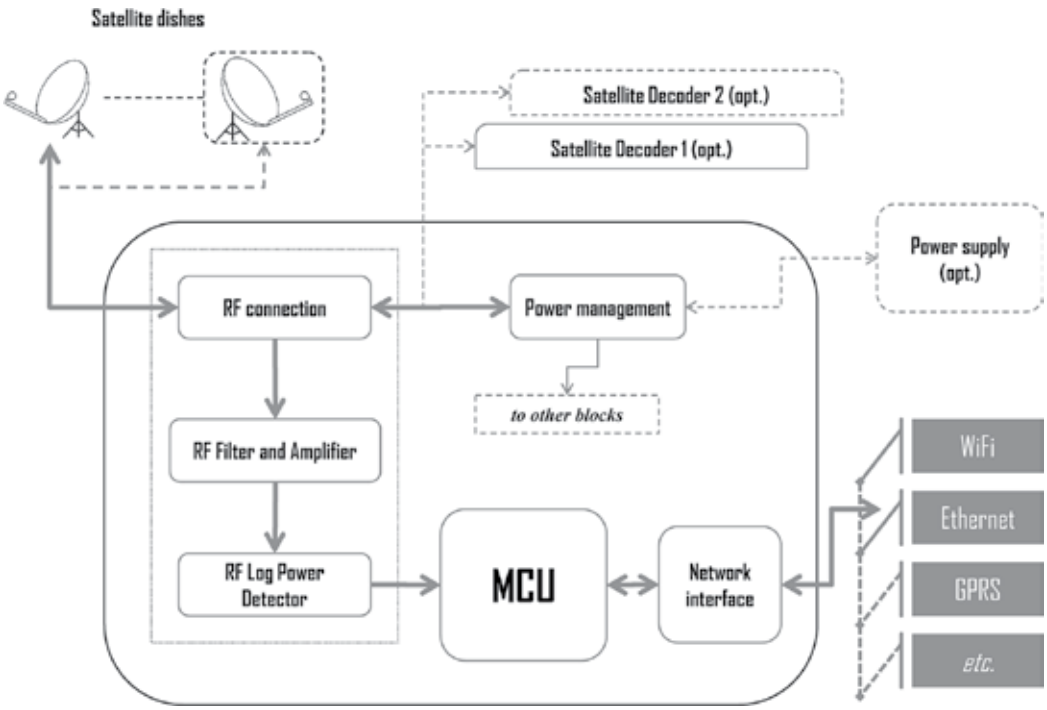

Figure 2. DVB-S power detector module.

The data acquisition module is connected to one or more receiving antennas for standard DVB-S television equipped with universal LNBs. Such devices, whose general block diagram is schematically shown in **Figure 3**, perform a first amplification and a down conversion of the signals received by the antennas. In particular, the electromagnetic waves propagating from the satellite to the user antenna have frequencies in the range of 10.7–12.75 GHz. In the LNB, such frequency band is divided into two subbands of approximately 1 GHz width each (low and high), which are downconverted in the range of 950–2150 MHz by mixing the received signal with a local reference signal having the suitable frequency (9.75 and 10.6 GHz for the low and high bands, respectively). The selection of the band forwarded to the decoder is performed by superimposing to the supply voltage a 22 kHz tone with amplitude of 0.5 V (if the tone is present, the high band is selected, otherwise the low one is used). In this way, it is possible to connect the LNB to the decoder (which in practical installation could be located at a distance of several tens of meters) with a low-cost cable and a reasonable attenuation (usage of the original frequencies would have required a much more expensive guiding structure). In order to increase the link capacity, two polarizations, horizontal and vertical, are also used (in our implementation we do not consider circularly polarized systems). The polarization selection is carried out by a control circuit in the LNB on the basis of the DC supply voltage (13 and 18 V for vertical and horizontal polarizations, respectively). It is worth noting that such a kind of LNB does not perform any automatic gain control (AGC) and thus preserves proportionality between the amplitudes of the received signal and the one forwarded to the decoder. Consequently, the power at the output of the LNB module can be modeled as $P_D = G_{conv} P_L$, where P_L is power received by the antenna and G_{conv} is the conversion gain of the downconverter, including all the possible gains of the eventually present amplifiers and the cable losses.

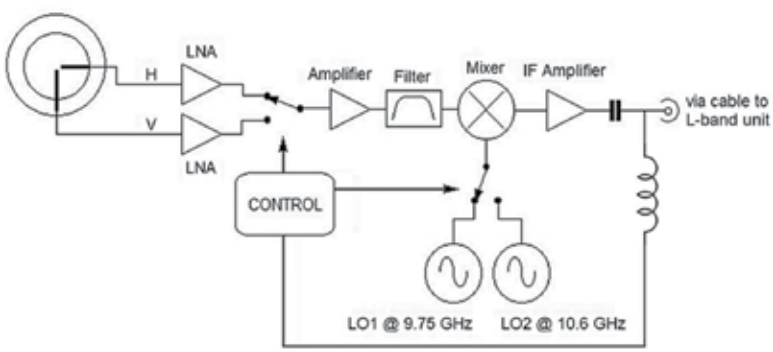

Figure 3. Universal low noise block (LNB) diagram.

The signal coming from the LNB is applied to the logarithmic power detector module via a directional coupler ("RF connection"), a filter and an amplifier (see **Figure 2**). The directional coupler performs two operations. First, it conveys the signal to a possible decoder without a significant attenuation, allowing the use of the antennas employed for usual TV operations with no inconvenience for the user. On the other direction, the power supply 13/18 V and the possible 22 kHz tone are transferred from the decoder to the LNB. The system can be operated

http://dx.doi.org/10.5772/66726

also without any decoder: in such a case, a dedicated power supply module is needed. At the same time, the directional coupler also directs part of the signal to the measurement electronics. The extracted signal, properly amplified and filtered, is processed by a logarithmic power detector, which integrates the signal power over the entire band 950–2050 MHz. In particular, the voltage at the output of the RF detector is related to the input power over a wide range by means of the following linear relationship

$$P_D^{\mathrm{dBm}} = c_1 V_{\mathrm{out}}^{\mu\mathrm{V}} + c_2 \tag{13}$$

where c_1 and c_2 are two parameters depending on the frequency range and on the used converter. The subscripts dBm and μV denote the measurement units. In the developed prototype, an analog device AD8314 detector [20] has been used, for which at the frequencies of interest, it results $c_1 = 50\ \mu\mathrm{V/dBm}$ and $c_2 = -53\ \mathrm{dBm}$.

The voltage signal is finally converted in digital format by using an analog-digital converter available in the microcontroller unit (MCU). The possible presence of the 22 kHz tone as well as the value of the supply voltage is detected, too. Such data, indicating band and polarization of the received signal, can be used to adapt the inversion algorithm parameters to best estimate the intensity of the precipitation.

The firmware in the MCU also performs the following functions:

- sample the signals at predefined intervals;
- carry out a preprocessing of the acquired data (e.g., average the measurements over a predefined number of acquisitions);
- package the data in a suitably defined format;
- send the data to the central server via the "network interface."

In the present implementation, the measurement hardware samples the detected power level each second, averages the readings and delivers the data packet with an interval of 1 minute. It is worth noting that we decided to take advantage of the whole L-band signal supplied by the LNB, with the aim at averaging over the set of all available transponders the variation of transmitted power. This operation has also the advantage to avoid the adoption of a receiver, thus resulting in a cost reduction, which is particularly useful in the case of realization of a network of sensors arranged densely on a vast territory. A further consequence is to take advantage of the signals coming from the three satellites of the constellation, which exhibit different oscillations around their nominal position: in this way, the obtained reference level appears to be quite stable, and consequently the rain-no-rain detection algorithm is facilitated. A different choice has been reported in Ref. [2], where channels at specific frequencies have been used.

The required power supply for the sensor module is derived opportunistically from the DC supply voltage (13/18 V) present on the cable, in the same way according to which the LNB is powered. This is achieved via an appropriate "power management" unit equipped with a buck converter, able to provide the voltage needed to power both the signal detection

module and the network interface. In addition, proper low-dropout regulators are employed, to improve the quality of the supply voltage, both in terms of stability and of noise content. Finally, it is worth noting that the "network interface" can be connected to different modules (such as LAN or Wi-Fi network, and also GPRS or LPWAN), depending on the connection possibilities available in the various sites.

A picture of the developed RF sensing board is shown in **Figure 4** [the two F connectors provide connectivity toward the decoder (left) and to the LNB (right)].

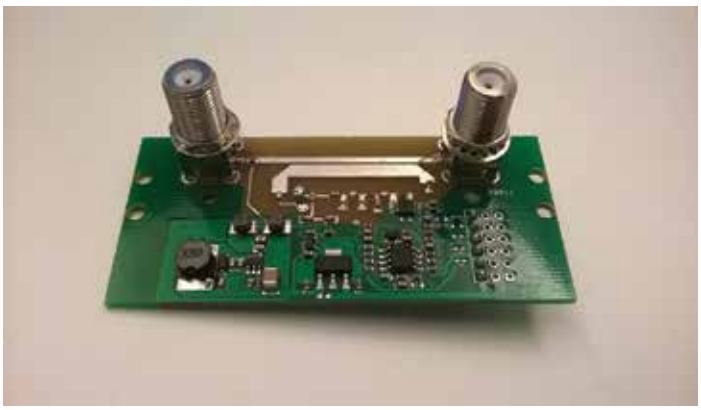

Figure 4. RF power detection board.

4. Experimental results

The developed system has been validated by using a test site located at the Department of Electrical, Electronic, and Telecommunication Engineering, and Naval Architecture (DITEN) of the University of Genoa. The antenna, which is installed at coordinates (44.4033° N, 8.959° E) and at a height $h_{\text{dish}} = 60$ m above the sea level, is pointed toward the Eutelsat "Hot Bird" commercial broadcasting satellite constellation at 13.0°E. The low-band, vertical polarization combination was chosen. An example of the output of the RF detector, related to a period of 36 hours, is shown in **Figure 5**. In the same figure, the corresponding received power is also reported, obtained by applying the transformation in Eq. (13). As it can be seen, the received power is almost constant and equal to about −18.5 dBm (in the considered period) when there is no rain (the left part of the graph, for an approximately 5 hours long interval). The occurrence of rainfall yields an attenuation in the range of 2–5 dB (depending on the rain intensity).

The data in **Figure 5** have been used to test the rain rate estimation approach described in Section 2. The parameters a and b have been chosen according to the ITU recommendation P.838-3 [18]. In particular, the following values have been used: $A = 1.16$; $B = 0.017$. The elevation angle of the dish antenna, for the considered satellite, is equal to $\theta_{\text{el}} = 38.7°$. The rain heigth $h_{\text{rain}_{\text{sea}}}$ has been computed by using the empirical model defined in the ITU recommendation P.839-4 [19], i.e.,

http://dx.doi.org/10.5772/66726

$$h_{\text{rain}_{\text{km}}} = h_{0_{\text{km}}} + 0.36 = 3.27 \text{ km} \quad (14)$$

where h_0 is the zero isotherm height, which depends upon the geographical position of the test site and can be estimated by using the mean tabulated values provided by ITU. The length of the part of the slant path interested by the rain, computed by using Eq. **(8)**, is equal to $l_{\text{rain}} = 5.23$ km. The reference power level $P_L^{0\ \text{dBm}}$ has been estimated from the historical data set. In particular, it has been found by searching the "flat" parts of the time series (after a noise filtering) and by averaging the corresponding measured power values. The obtained values, for the considered test case, is $P_L^{0\ \text{dBm}} = -18.66$ dBm. The rainfall intensity is shown in **Figure 6**. In particular, such graph reports the quantity, $R = r\delta t$, where r is the rain rate estimated by using Eq. (12).

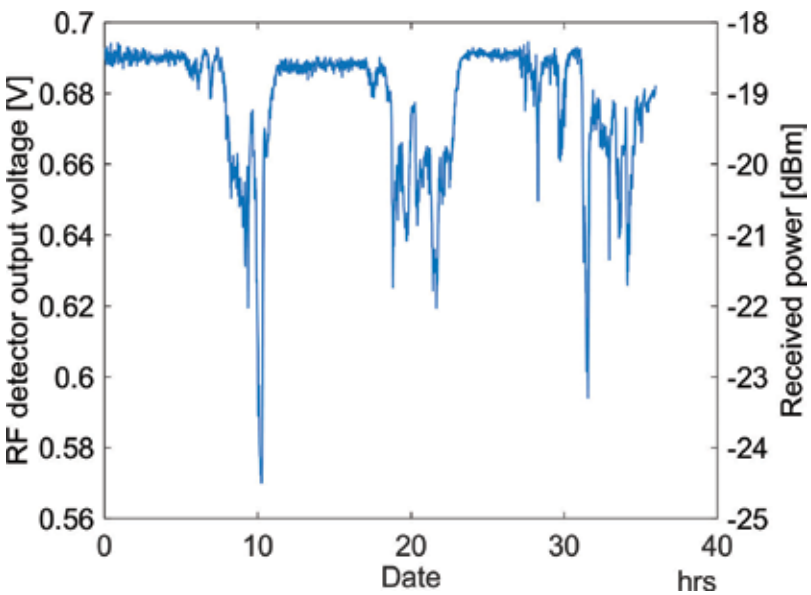

Figure 5. Output voltage of the RF detector and corresponding measured power.

In order to evaluate the correctness of the obtained results, they have been compared with the measurements of a standard rain gauge, made available by the Department of Civil, Chemical and Environmental Engineering (DICCA) of the University of Genoa [21]. Such instrument is located near the test site and provides the rainfall over periods of 30 minutes. Consequently, the estimated rain quantity has been integrated over the same period in order to obtain comparable values (denoted as R_{30}). The obtained results are shown in **Figure 7**. As it can be seen, there is a quite good agreement between the measured and the reference values. The small differences can be motivated by two facts. First, the rain gauge is not exactly below the path antenna-satellite. Moreover, it provides information about the rain in a single point, whereas the proposed estimation system gives an integral measure of the overall rain along the propagation path.

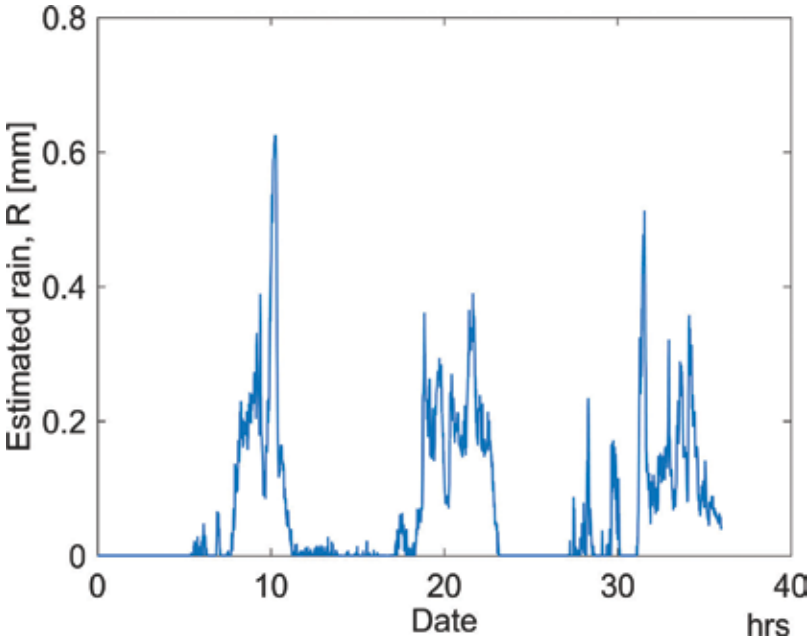

Figure 6. Estimated rainfall.

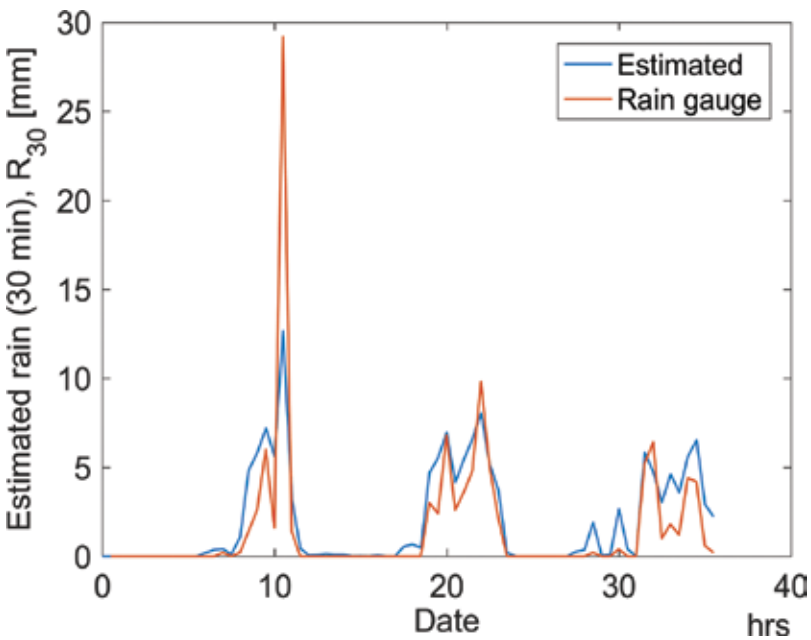

Figure 7. Estimation of accumulated rainfall in 30-minute intervals, and comparison with the measurements provided by a rain gauge.

http://dx.doi.org/10.5772/66726

5. Conclusions

In this chapter, a novel rain monitoring system has been proposed. The approach is based on the measurement of the electromagnetic radiation by using standard antennas adopted by commercial DVB-S decoders. It is based mathematically on the receiving properties of the antenna and the inversion of the ITU model for rain precipitations. In the chapter, both hardware and software have been described.

Experimental results have also been reported. They concerned comparison with data obtained by standard rain gauge. Although, preliminary, these results confirm the possibility of calculating with good accuracy the rainfall over the electromagnetic path, allowing the potential of a very largely distributed low-cost measurement network. Further developments will be devoted at exploring the possibility of combining multiple data collected by several separate rain monitoring apparatuses of this kind.

Author details

Daniele Caviglia[1,2], Matteo Pastorino[1*], Andrea Randazzo[1,2] and Andrea Caridi[2]

*Address all correspondence to: pastorino@dibe.unige.it

1 Department of Electrical, Electronic, Telecommunications Engineering and Naval Architecture (DITEN), University of Genoa, Genova, Italy

2 Artys Srl, Piazza della Vittoria, Genova, Italy

References

[1] B. Federici, G. L. Gragnani, G. parodi, A. Randazzo, D. Caviglia, M. Pastorino, D. Sguerso, A. Caridi, and C. Montecucco. System and method for monitoring a territory. EU Patent EP2688223A1. 22-01-2014.

[2] L. Barthès and C. Mallet. Rainfall measurement from the opportunistic use of an Earth–space link in the Ku band. Atmospheric Measurement Techniques. 2013;**6**(8):2181–2193.

[3] K. S. Choi, J. H. Kim, and D. S. Ahn. System and method for integrally collecting rainfall attenuation and rainfall intensity data in satellite system. US Patent US20130130618A1. 23-05-2013.

[4] L. Brocca, C. Massari, L. Ciabatta, W. Wagner, and A. Stoffelen. Remote sensing of terrestrial rainfall from Ku-band scatterometers. IEEE Journal of Selected Topics in Applied Earth Observations and Remote Sensing. 2016;**9**(1):533–539.

[5] H. Chen and V. Chandrasekar. Estimation of light rainfall using Ku-band dual-polarization radar. IEEE Transactions on Geoscience and Remote Sensing. 2015;**53**(9):5197–5208.

[6] J. Shi, C. Xu, J. Guo, and Y. Gao. Real-time GPS precise point positioning-based precipitable water vapor estimation for rainfall monitoring and forecasting. IEEE Transactions on Geoscience and Remote Sensing. 2015;**53**(6):3452–3459.

[7] V. Pastoriza, F. Machado, P. Marino, and F. P. Fontan. Nowcasting of the spatiotemporal rain field evolution for radio propagation studies. IEEE Transactions on Antennas and Propagation. 2013;**61**(6):3312–3320.

[8] M. I. Skolnik. Radar Handbook. 3rd edition. New York: McGraw-Hill; 2008.

[9] M. Gabella, R. Notarpietro, S. Turso, and G. Perona. Simulated and measured X-band radar reflectivity of land in mountainous terrain using a fan-beam antenna. International Journal of Remote Sensing. 2008;**29**(10):2869–2878.

[10] S. Turso, S. Paolella, M. Gabella, and G. Perona. MicroRadarNet: A network of weather micro radars for the identification of local high resolution precipitation patterns. Atmospheric Research. 2013;**119**:81–96.

[11] M. Bevis, S. Businger, T. A. Herring, C. Rocken, R. A. Anthes, and R. H. Ware. GPS meteorology: Remote sensing of atmospheric water vapor using the global positioning system. Journal of Geophysical Research. 1992;**97**(D14):15787.

[12] E. D. Kaplan and C. Hegarty, Eds. Understanding GPS: Principles and Applications. 2nd ed. Boston: Artech House; 2006.

[13] H. Messer. Environmental monitoring by wireless communication networks. Science. 2006;**312**(5774):713–713.

[14] H. Leijnse, R. Uijlenhoet, and J. N. M. Stricker. Rainfall measurement using radio links from cellular communication networks. Water Resources Research. 2007;**43**(3):1-6.

[15] H. Messer, A. Zinevich, and P. Alpert. Environmental sensor networks using existing wireless communication systems for rainfall and wind velocity measurements. IEEE Instrumentation & Measurement Magazine. 2012;**15**(2):32–38.

[16] O. Goldshtein, H. Messer, and A. Zinevich. Rain rate estimation using measurements from commercial telecommunications links. IEEE Transactions on Signal Processing. 2009;**57**(4):1616–1625.

[17] A. Zinevich, P. Alpert, and H. Messer. Estimation of rainfall fields using commercial microwave communication networks of variable density. Advances in Water Resources. 2008;**31**(11):1470–1480.

[18] Recommendation ITU-R P.838-3, "Specific attenuation model for rain for use in prediction methods", International Telecommunication Union, 2005

[19] Recommendation ITU-R P.839-4, "Rain height model for prediction methods", International Telecommunication Union. 2013.

[20] Analog Devices. 100 MHz to 2.7 GHz, 45 dB RF Detector/Controller. AD8314 Datasheet. 2006.

[21] DICCA Weather Station. [Online]. Available: http://www.dicca.unige.it/meteo/.

Chapter 9

Real-Time Electromagnetic Signal Processing: Principles and Illustrations

Shulabh Gupta and Christophe Caloz

Additional information is available at the end of the chapter

http://dx.doi.org/10.5772/67356

Abstract

Real-time electromagnetic signal processing has recently appeared as a novel signal-processing paradigm to manipulate and control electromagnetic signals in real time directly in the analog domain. This has led to attractive alternatives to conventional digital techniques, which typically suffer from poor performances and high cost at microwave and millimeter wave frequencies. This novel paradigm is based on dispersion-engineered electromagnetic structures, and in this review chapter, two types of structures are presented and discussed in details: phasers and metasurfaces. While phasers are typically group delay engineered to manipulate and rearrange spectral components in the time domain, metasurfaces enhances these functionalities by providing spatial processing in addition to temporal processing. Two kinds of phasers are presented here: static and dynamic all-pass C-section phasers, and all-dielectric metasurface-based spatial phasers. Finally, two applications illustrating real-time signal processing are discussed: 2D beam scanning leaky-wave antenna for high-resolution spectrum analysis and a dispersion code multiple access (DCMA) system.

Keywords: analog signal processing, dispersion engineering, real-time systems, metamaterials, metasurfaces, all-pass systems, phasers, leaky-wave antennas, spectrum analyzers, dispersion modulation systems

1. Introduction

Recent decade developments in wireless communications may be described in terms of the evolution of the fundamental nature of corresponding services, which are referred to as mobile generations, not compatible with the previous cellular standards. The first mobile generation (1G) was based on analog transmission. Its evolution in 1992 into the second mobile generation (2G), introducing digital transmission, represented a major technological advance. The third

mobile generation (3G) appeared in 2001 and brought multimedia support, spread spectrum access, and peak bit rate exceeding 200 kbit/s. Since 2011/2012, the prevailing technology has been the fourth mobile generation (4G), which covers Internet protocol (IP) packet-switched networks and thus provides ultrabroadband (Gbit/s speed) mobile access. 4G systems use the LTE (Long Term Evolution) standard, which embodies an OFDMA (Orthogonal Frequency Division Multiple Access) scheme for base station and a hybrid SCOFDM (Single Carrier OFDM) for multiple access. Thus, each mobile generation has evolved into a new generation about every 10 years to keep up with the ever-rising demands by end-consumers. The fifth mobile generation (5G) standards are expected to be established around 2019/2020 and 5G networks should be deployed between 2020 and 2030 [1, 2].

Extrapolating from current market trends of rising consumer demand and financial growth in the mobile technology, it is predicted that 5G networks will be required to support a 1000-fold increase in data capacity to handle over 100 billion devices featuring peak rates of 10 Gb/s and low data transmission latency [3]. The bandwidth of current microwave cellular systems is around 600 MHz, and it is divided among different communication operators. While efforts have been made to increase the operation bandwidth for higher data throughput, the best attempts have led to an increase of only 80 MHz. Moreover, this increase comes at a high cost in terms of modification requirements of existing infrastructures. Due to these issues, some amendments have been operated in current IEEE 802.11 networks, in particular, advancement toward 5G with the introduction of IEEE 802.11ad for exploiting the 60 GHz millimeter-wave spectrum. However, current 802.11ad is still based on single carrier OFDM and is limited in terms of the achievable peak data rate. Therefore, it clearly appears that a mere evolution of current mobile technologies will be largely insufficient to meet the anticipated demands of 5G networks. There is a most pressing need for disruptive technological solutions [4, 5].

In order to address the aforementioned challenges of 5G networks, two potential disruptive directions have been suggested, both related to the physical layers [4]: (1) transition to millimeter-wave frequency bands to leverage their huge available spectrum and hence achieve drastic channel capacity enhancement and (2) deployment of massive MIMO systems with advanced beam-forming techniques providing various cognitive features, such as for instance smart channel detection. While millimeter-wave frequencies transition aims at wider spectrum usage, cognition and multiple access techniques are targeted for more efficient spectral efficiency [4]. Smart cognitive functions involve the automated identification of free channels in mobiles and base stations for better exploitation of the channels' potential. For instance, beam-division multiple access (BDMA) maximizes the spectrum efficiency by dividing antenna beams according to the available angular sectors of mobile stations. BDMA offers an attractive multiple access approach but suffers from excessive high-speed signal processing requirements, and hence with potentially prohibitive cost and complexity for 5G [6].

Realizing the considerable potential of millimeter-wave technologies, the WiFi alliance recently introduced the WiGig standard (802.11ad), which targets several applications in the 60 GHz range [7]. Among these applications is small-cell mobile backhaul, which consists of fixed interconnections of mobile service base stations to the backbone network. WiGig backhaul will enhance mobile speed access by using point-to-point microwave and millimeter-wave radio

http://dx.doi.org/10.5772/67356

links [8]. Another application, already in use currently, is that of data center interconnects, where point-to-point wireless links replace cumbersome cables and introduce real-time network configurability [8, 9]. These interconnects have been shown to exhibit superior cost and atmospheric loss performance [4] than free-space optics (FSO) systems [10]. While IEEE 802.11ad uses the licensed band around 60 GHz, other frequency bands with comparable signal propagation characteristics through the atmosphere are available, in particular, the 71–76, 81–86, and 92–95 GHz bands. Overall, millimeter-wave frequency operation enables directive transmission, reduced signal interference, and enhanced signal-to-noise ratio in a wide spectrum range [11].

While transition to millimeter-wave may simplify system architectures, it also requires major technological progress in terms of hardware constraints. Current systems heavily rely on digital techniques, whose high-power consuming mixed signal subsystems, which require ultrafast analog-to-digital (ADC) and digital-to-analog converters (DAC), become prohibitive in such high-frequency and large-bandwidth regimes [4]. In particular, conventional microwave architectures, where each antenna is connected to an ADC/DAC, are inapplicable to millimeter-wave systems unless a spectacular technological breakthrough occurs in electronics technology. As of today, millimeter-wave systems must resort to hybrid architectures, where a significant part of the signal processing is performed at baseband, implying high system complexity and cost. More importantly, this approach is highly restricted in operation bandwidth, which defeats the original purpose of accessing wider spectrum resources at millimeter-waves.

Considering the exploding demand increase of 5G in data capacity and the inability of current technology to meet the related challenges, a paradigm-shifting breakthrough is clearly needed for millimeter-wave communication systems. While the conventional wisdom points toward baseband and RF architectures, with the aim of realizing computationally efficient interfaces and higher density integrated designs, this chapter presents a fundamentally different and a potentially disruptive signal processing technology, which does not depend on digital techniques and hence without suffering from their technological bottlenecks. This signal processing paradigm is called radio-analog signal processing or R-ASP in short.

2. Radio analog signal processing (R-ASP)

R-ASP might be defined as the manipulation of signals in their pristine analog form and in real time to realize specific operations enabling microwave or mm-wave and terahertz applications [12]. The concept of R-ASP can be best understood by considering the two basic effects illustrated in **Figure 1**, chirping with time spreading and frequency discrimination in the time domain. Both effects involve a linear device with transfer function $H(\omega) = e^{j\varphi(\omega)}$, assumed to be of unity transmission magnitude and whose phase, $\varphi(\omega)$, is a nonlinear frequency function, or whose group delay, $\tau(\omega) = \partial\varphi(\omega)/\partial\omega$, is a function of frequency. Such an element, with *frequency-dependent group delay,* is called *temporally dispersive*. The bandwidth of $H(\omega)$ is assumed to cover the entire spectrum of the input signal.

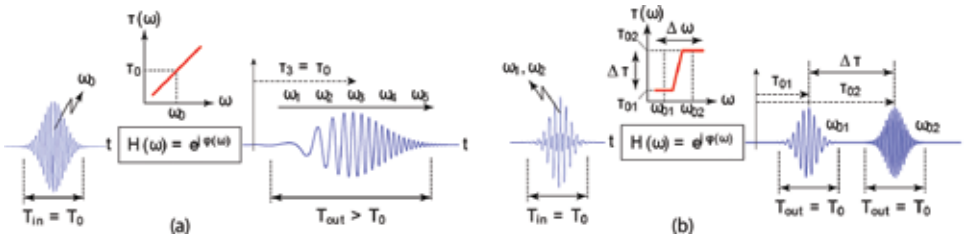

Figure 1. Basic effects in R-ASP. (a) Chirping with time spreading and (b) frequency discrimination in the time domain. ©IEEE; reprinted with permission.

In the first case, shown in **Figure 1(a)**, a pulse modulated at a frequency ω_0 is injected into a dispersive element, which exhibits a positive linear group delay slope over a frequency band centered at the ω_0, corresponding to a group delay τ_0. Due to the dispersion of this element, the different frequency components of the pulse experience different phase-shifts and therefore appear at different times. Here, the lower-frequency components are delayed less than the higher-frequency components and therefore appear earlier, while the center-frequency component appears at the time $\tau_3 = \tau_0$. This results in an output pulse whose instantaneous frequency is progressively increasing, a phenomenon called "chirping," and which has experienced time spreading ($T_{out} > T_0$), accompanied with reduced amplitude due to energy conservation.

In the second case, depicted in **Figure 1(b)**, the input pulse is modulated by a two-tone signal, with frequencies ω_{01} and ω_{02}, and passed through a dispersive element $H(\omega)$ exhibiting a positive stepped group delay, with two steps, centered at ω_{01} and ω_{02}, respectively. Based on this dispersive characteristic, the part of the pulse modulated at the lower frequency, ω_{01}, is delayed less than the part modulated at the higher frequency, ω_{02}, and hence emerges earlier in time. As a result, the two pulses are *resolved* (or separated) in the time domain, and their respective modulation frequencies may be deduced from their respective group delays from the dispersive transfer function, $H(\omega)$. Note that with the flat-step group delay considered here the pulses are *not* time-spread ($T_{out} = T_0$), assuming that the pulse bandwidth fits in the flat bands of the steps.

The R-ASP technology is widely applicable in areas such as instrumentation, sensing, security, all-analog communication systems, and dynamic and cooperative data wireless networks. Consequently, R-ASP has already led to wealth of novel applications such as real-time Fourier transformers [13], spectrum sniffers, discriminators and frequency meters [14–16], radio-frequency identification (RFID) systems [17], spatial spectrum analyzers [18, 19], pulse-position modulators (PPM) [20], DCMA system [21], dispersion code modulation [22], signal-to-noise ratio enhancer [23], frequency-division-modulators (FDM) [24], etc.

3. Electromagnetic phasers

The heart of an R-ASP system is a phaser, which is a component exhibiting a specified frequency-dependent group-delay response within a given frequency range, as described above [12].

http://dx.doi.org/10.5772/67356

Phasers are either reflection type or transmission type. Reflection-type phasers are single-port structures, which are transformed into two-port structures using a broadband circulator or a hybrid coupler. They are mostly based on Bragg reflections and include microstrip-chirped delay lines [25] and reflection-type waveguide phasers [26]. While reflection-type phasers suffers from less constraints in the design parameters compared to transmission-type phasers, their requirement of an external one-port to two-port conversion component, resulting in additional loss along with undesired phase distortions, is a major drawback. Transmission-type phasers, on the other hand, are inherently two-port components. Surface acoustic wave (SAW) devices [27], and magnetostatic devices [28] are good for designing high dispersion phasers; however, they are suitable only for very low frequencies and narrow-bandwidth applications. While some recently proposed transmission-type phasers, based on coupled-matrix analysis, features great design flexibility for advanced group delay engineering, they are typically restricted to narrow-band designs [29, 30]. For broader-band applications, coupled-line all-pass phasers are more suitable, offering also greater design simplicity and benefiting from efficient synthesis procedures [31, 32].

The coupled-line all-pass phasers reported to date are based on cascaded C-sections (CCS) and/or D-sections synthesizing prescribed group delay responses [33]. On the other hand, a longitudinal cascade of commensurate coupled transmission-lines, or cascaded coupled-line (CCL) phaser, was first demonstrated in Ref. [31]. A hybrid configuration based on the combination of a CCS and a CCL configuration, known as hybrid cascade (HC) coupled-line phaser was recently proposed in Ref. [34]. This set of three cascading configurations, CCL, CCS, and HC, represent the fundamental cascading schemes upon which more complex phasers can be constructed, leading to vast variety of coupled-line all-pass phasers with rich and exotic dispersion characteristics.

3.1. Passive coupled-line all-pass phasers

3.1.1. Basic transfer functions

Transmission all-pass transfer functions are constructed using two building-block transfer functions: the C-section and the D-section transfer functions [31]. A C-section transfer function can be realized by a two-port transmission-line device, consisting of a contra-directional coupled-line coupler, whose through and isolated ports are interconnected by an ideal transmission-line section, as shown in **Figure 2(a)**. Its transfer function can be obtained by applying the connecting boundary condition between the ingoing and outgoing waves at the two isolated and coupled ports of the coupler. The C-section transfer function is given by:

$$S_{21}(\theta) = \left(\frac{\rho - j\tan\theta}{\rho + j\tan\theta}\right), \quad \text{with} \quad \rho = \sqrt{\frac{1+k}{1-k}} \tag{1}$$

where k is the coupling coefficient between the coupled lines forming the structure. Its all-pass nature, $|S21| = 1$, $\forall\theta$, can be verified by observing that the magnitudes of the numerator and denominator in Eq. (1) are equal, and that the function provides a frequency-dependent group delay response with a maxima at $\theta = (2m - 1)\pi/2$, where m is an integer. This condition corresponds to frequencies where the length of the coupled-line section is an odd multiple of

a quarter wavelength. Upon the high-pass to low-pass transformation $s = j \tan \theta$, the C-section is seen to be a first-order phaser, with one real pole and one real zero, placed symmetrically about the imaginary axis in the s-plane.

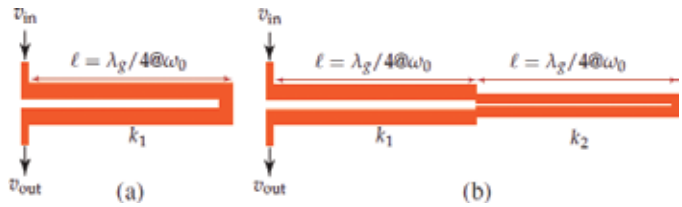

Figure 2. Transmission-type all-pass phaser topologies. (a) C-section and (b) D-section, with ω_0 being the quarter-wavelength frequency of a transmission line [34]. ©IEEE; reprinted with permission.

The derivation of a generalized transfer function corresponding to a coupled-line coupler terminated with an arbitrary all-pass load with transfer function $S0$ is provided in reference [34], and reads

$$S_{21}(\theta) = b + \frac{a^2 S_0}{1 - bS_0} \tag{2}$$

where in Eq. (2) a and b are the through and coupled transfer functions of the isolated coupler. The C-section transfer function is a particular case of this network with $S_0 = 1$.

The second-order all-pass phaser is the D-section, which consists of a contra-directional coupled-line coupler terminated with a C-section, as shown in **Figure 2(b)**. Using the transfer function from Eq. (2) with S_0 corresponding to a C-section, i.e., Eq. (1), the transfer function of a D-section is found as

$$S_{21}(\theta) = \left(\frac{1 - \rho_a \tan\theta^2 - j\rho_b \tan\theta}{1 - \rho_a \tan\theta^2 + j\rho_b \tan\theta}\right), \rho_a = \sqrt{\frac{1 - k_1}{1 + k_2}}\sqrt{\frac{1 + k_1}{1 - k_2}},\ \rho_b = \sqrt{\frac{1 - k_1}{1 + k_1}}\sqrt{\frac{1 - k_1}{1 + k_2}}, \tag{3}$$

where $k_{1,2}$ are the coupling coefficients of the two sections. Upon the transformation $s = j \tan \theta$, the D-section is seen to be a second-order phaser, with two pairs of complex para-conjugate zeros and poles in the s-plane.

3.1.2. Phaser topologies

The C-section and a D-section group delay profiles have a specific and restricted shape that depends on the specific length and coupling coefficients of the sections. However, exploiting several coupled-line sections in a flexible fashion allows synthesizing virtually arbitrary prescribed group delay responses between the input and the output ports for a given bandwidth. Such phasers can be categorized based on how the different coupled-line sections are connected together. The three possible basic configurations shown in **Figure 3** are next described.

http://dx.doi.org/10.5772/67356

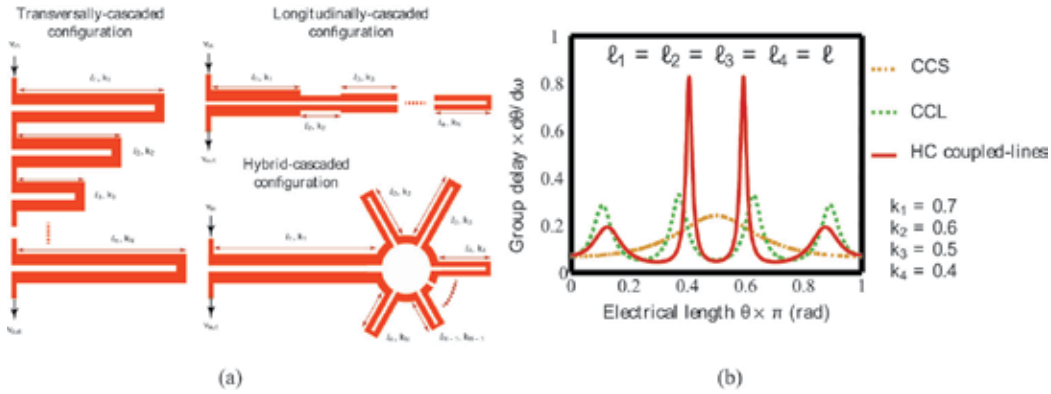

Figure 3. Cascaded coupled-line all-pass phasers [34]. (a) Generic topologies for a cascaded C-sections (CCS), cascaded coupled-lines (CCL) and hybrid-cascaded (HC) coupled-line phasers. (b) Typical group delay response of the three phaser topologies in (a) over the lowest coupled-line section harmonic frequency band with $N = 4$ coupled-line sections of identical length $l_i = l$. ©IEEE; reprinted with permission.

1. *Cascaded C-section (CCS) phaser*. When several C-sections are cascaded in the direction that is transverse to the axis of the transmission lines forming the C-sections, as shown in **Figure 3(a)**, a CCS configuration is formed. The resulting transfer function is then simply the product of the individual C-section transfer functions and is given by

$$S_{21}^{CCS}(\theta) = \prod_{i=2}^{N}\left(\frac{\rho_i - j\tan\theta}{\rho_i + j\tan\theta}\right), \tag{4}$$

where $\rho_i = (1 + k_i)/(1 - k_i)$, k_i being the coupling coefficient of the ith section.

2. *Cascaded coupled-lines (CCL) phaser*. In this configuration, several coupled-line sections are cascaded in the direction of the transmission lines forming the coupled-lines, as shown in **Figure 3(a)**, with the last section being a C-section Cristal [31]. The corresponding transfer function can be derived by iteratively constructing the load transfer functions starting from the last coupled-line section toward the input port, as derived by Gupta et al. [34]. The result is

$$S_{21}^{CCL}(\theta) = b_1 + \frac{a_1^2 S_2(\theta)}{1 - b_1 S_2(\theta)}, \tag{5}$$

where $S_2(\theta)$ is the overall transfer function of the structure starting from the 2nd to the Nth coupled-line section. It is to be noted that a D-section is the particular case of a CCL coupled-line phaser with $N = 2$.

3. *Hybrid-cascaded (HC) coupled-line phaser*. This configuration is based on a combination of CCS and CCL sections, as illustrated in **Figure 3(c)**. This configuration can be seen as a coupled-line coupler terminated with a CCS phaser. The corresponding transfer function can be derived by substituting the CCS transfer function as S_0 in Eq. (2), resulting in

$$S_{21}^{HC}(\theta) = b_1 + \frac{a_1^2 S_0(\theta)}{1 - b_1 S_0(\theta)},\ S_0(\theta) = \prod_{i=2}^{N}\left(\frac{\rho_i - j\tan\theta}{\rho_i + j\tan\theta}\right), \tag{6}$$

The diversity of possible delay functions provided by the CCS, CCL, and HC coupled-line phasers is too great to be tractable in such a chapter. Therefore, for the sake of simplicity, we shall restrict our analysis to the case of commensurate coupled-line sections having all the same lengths. However, it should be kept in mind that the above transfer functions are general and that the phasers exhibit much richer synthesis possibilities than those presented next.

3.1.3. Group delay response

The three configurations in **Figure 3(a)** exhibit very different group delay responses, as shown in **Figure 3(b)** for the case of $N = 4$ and $l_1 = l_2 = l_3 = l_4 = l$. For the second condition, the CCS phaser has a delay shape similar to that of a regular C-section, with a single delay maximum in $\theta \in [0, \pi]$. In contrast, the CCL configuration exhibits four delay peaks. These peaks are quasi-uniformly spaced and quasi-equal in magnitude, with group delay swings, $\Delta\tau = \tau_{max} - \tau_{min}$, that are larger than those obtained in the CCS case. Similar to the CCL case, the HC coupled-line phaser exhibits four delay peaks, but with significantly different characteristics. While the outermost delay peaks are lower, the middle ones have a steep slope within a narrow bandwidth and thus exhibit a very large delay swing $\Delta\tau$. Thus, for a given maximum achievable coupling k, for the three configurations, the HC coupled-line phaser provides the largest group delay swing $\Delta\tau$.

3.2. Active and reconfigurable C-section all-pass phasers

The above phasers are fixed in group delay profiles. However, there are some occasions requiring reconfigurability in group delay response when the radio systems need to be adaptive in a dynamic environment. One example is the recently proposed DCMA system [21], where the communication between any two users requires the real-time establishment of a pair of complementary dispersion codes at the transmitter and receiver ends, respectively. In a time-variant environment, dynamically increasing the group delay swing may mitigate the interference and hence improve the signal-to-noise ratio.

To address such requirements, the group delay and amplitude response of a C-section phaser can be tuned by varying the amplitude of the transfer function of the loading network S_0. This leads to a reconfigurable all-pass phaser, where all-pass amplitude is obtained by cascading a pair of gain and loss loaded C-sections [35, 36].

3.2.1. Single loaded C-section

Figure 4(a) shows a single loaded C-section, consisting of a coupled-line coupler and a loading network connected at one end of the coupler.

http://dx.doi.org/10.5772/67356

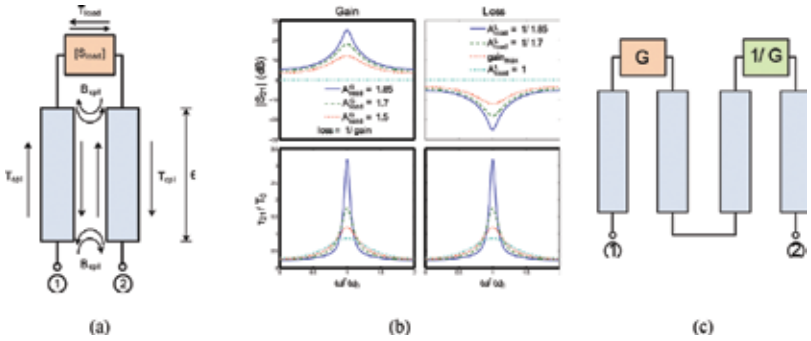

Figure 4. Proposed active reconfigurable all-pass phaser by cascading a gain-loss pair. (a) Loaded C-section [35] and (b) amplitude |S21| and normalized group delay τ/T_0 of the gain/loss loaded C-section, where the coupling factor $k = 0.5$ at ω_0. (c) Loss-gain all-pass C-section pair. ©IEEE; reprinted with permission.

The loading network, assuming perfect matching, is represented by the two-port S-parameters,

$$[S_{\text{load}}]_{2\times 2} = \begin{bmatrix} 0 & T_{\text{load}} \\ T_{\text{load}} & 0 \end{bmatrix}, \text{ with } T_{\text{load}} = A_{\text{load}}(\omega)e^{j\varphi_{\text{load}}(\omega)}, \text{ with} \tag{7}$$

For simplicity, let $\varphi_{\text{load}}(\omega) = 0$ and $A_{\text{load}}(\omega) = A_{\text{load}}$, where A_{load} is a real constant. The coupled-line coupler is characterized by the four-port S-parameters

$$[S_{cpl}]_{4\times 4} = \begin{bmatrix} 0 & T_{cpl} & 0 & B_{cpl} \\ T_{cpl} & 0 & B_{cpl} & 0 \\ 0 & B_{cpl} & 0 & T_{cpl} \\ Bs_{cpl} & 0 & T_{cpl} & 0 \end{bmatrix}, \text{ where} \tag{8a}$$

$$B_{cpl}(\omega) = \frac{jk\ \sin\theta}{\sqrt{1-k^2}\cos\theta + j\sin\theta},\ T_{cpl}(\omega) = \frac{\sqrt{1-k^2}}{\sqrt{1-\ k^2}\cos\theta + j\sin\theta}\ , \tag{8b}$$

are the backward coupling and through responses respectively, with the parameters, k and $\theta = \pi\omega/2\omega_0$, being the nominal coupling factor at the center frequency ω_0 and the electrical length of the coupler, respectively.

Connecting the loading network and the coupler as shown in **Figure 4(a)** yields the two-port S-parameters of the loaded C-section, which read: $S_{11}(\omega) = S_{22}(\omega) = 0$,

$$S_{21}(\omega,\ A_{\text{load}} = G) = G\frac{\sqrt{1}-\ k^2\cot\theta - j\ (1-k/G)}{\sqrt{1}-\ k^2\cot\theta + j\ (1-kG)} \tag{9}$$

3.2.2. Parametric study and all-pass paired gain-loss C-section unit

We can easily verify that Eq. (9) exhibits the following properties:

$$|S_{21}(\omega,\ G)| = \frac{1}{|S_{21}\left(\omega,\ \frac{1}{G}\right)|},\ \text{ and } \tau_{21}(\omega,\ G) = \frac{1}{\tau_{21}\left(\omega,\ \frac{1}{G}\right)} \tag{10}$$

respectively, with $G > 1$ as gain. Eq. (10) states that two loaded C-sections with opposite amplitudes, G and $1/G$, exhibit identical group delay responses and reciprocal amplitude responses. **Figure 4(c)** shows the responses, Eq. (**10**), with fixed coupling factor $k = 0.5$ and varying gain and loss, G and $1/G$, of the loading networks.

Therefore, cascading the paired gain and loss loaded C-sections leads to an all-pass C-section unit, as shown in **Figure 4(b)**. The amplitude and group delay responses of the resulting all-pass paired gain-loss C-section unit are respectively.

$$|S_{21}^{AP}(\omega)| = |S_{21}(\omega,\ G)| \times |S_{21}\left(\omega, \frac{1}{G}\right)| = 1 \tag{11}$$

$$\tau_{21}^{AP}(\omega) = \ \tau_{21}(\omega,\ G) + \ \tau_{21}(\omega,\ G) = 2\tau_{21}(\omega,\ G), \tag{12}$$

3.2.3. Reconfigurable phaser using gain-loss C-sections and numerical demonstration

We can now cascade N gain-loss C-section units, as shown in **Figure 5**, to synthesize arbitrary group delay responses. The ith constituent unit is tuned at center frequency $\omega_{0i} = 2\pi f_{0i}$ and assigned to the loading networks a gain-loss pair, G_i and $1/G_i$, respectively. The coupling factor, denoted as k, is the same for all units.

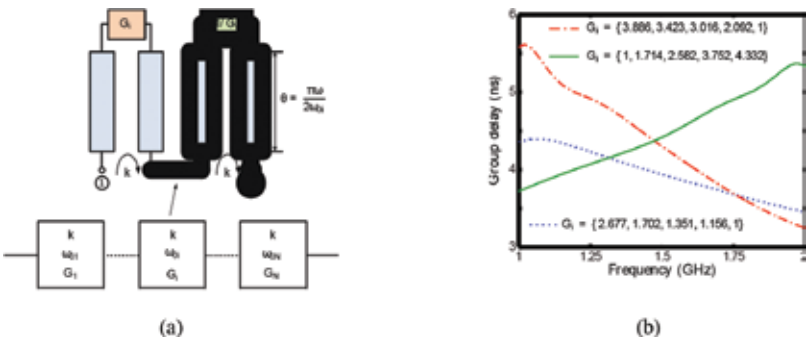

Figure 5. N-unit all-pass reconfigurable phaser based on the paired gain-loss C-section unit shown in **Figure 4(c)** [35]. ©IEEE; reprinted with permission.

An $N = 5$ unit numerical example, where $k = 0.2$ and center frequency $f_{0i} = \{1, 1.25, 1.5, 1.75, 2\}$ GHz, is given. **Figure 5** shows three different group delay profiles along with the corresponding three different sets of controlling gain. Enhancement of the group delay swing and the reversed slope of the group delay curve is achieved [35, 36].

3.3. Spatial phasers

Phasers so far considered are all guided-wave in nature such as the ones based on coupled-line couplers as recalled in **Figure 6(a)**. The phaser converts an input pulse, $v_{\text{in}}(t)$, according to its specified group delay profile, $\tau(\omega)$, into a dispersed signal, $v_{\text{out}}(t)$. The same operation can also

http://dx.doi.org/10.5772/67356

be performed in the space-domain using a spatial component with an incident pulsed wavefront, $v_{in}(x,y,t)$, as shown in **Figure 6(b)**. Such a device is called a *spatial phaser*. For the sake of simplicity, the input wave is assumed to be a plane-wave polarized along the x-axis. The ideal response of a spatial phaser is an all-pass response, i.e., $|T_{xx}(\omega)| = 1$, with a specified dispersion $\tau_{xx} = \tau_{xx}(\omega) = -d\{\angle T_{xx}(\omega)\}/d\omega$. Such a spatial phaser can also be realized using metasurfaces.

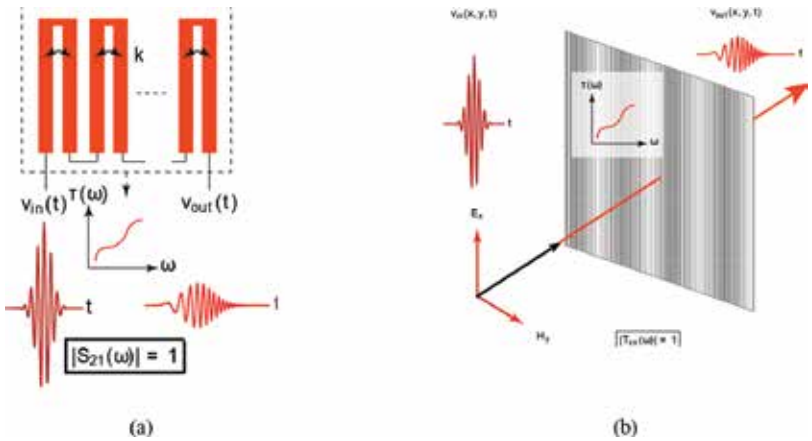

Figure 6. Phasers [12]. (a) Conventional guided-wave phasers and (b) proposed spatial phasers. ©IEEE; reprinted with permission.

A conventional phaser, shown in **Figure 6(a)**, is typically a series connection of C or D sections used in the hybrid configuration of **Figure 3** [34]. For example, a microwave C-section is a dispersive basic building block, where cascading C-sections of different frequency and delay characteristics, provides a specified group delay response. In a similar way, a spatial phaser, represented in **Figure 6(b)**, can be implemented by spatially cascading of all-pass spatial building blocks featuring different transmission delay characteristics [37]. These spatial all-pass units will be described next.

3.3.1. Conventional all-dielectric metasurface

Metasurfaces are spatial arrays made of subwavelengthly spaced scattering particles providing unprecedented flexibility in controlling electromagnetic wavefronts in space, time, or both space and time [38–42]. Recently, there has been a great interest in all-dielectric metasurfaces due to their low-loss characteristics and fabrication simplicity, as compared to their plasmonic implementations. All-dielectric metasurface structures are commonly based on coupled dielectric resonator unit cells, which simultaneously provide broadband full-transmission and 2π phase coverage, as a result of constructive interference between their electric and magnetic dipole responses [43, 44].

Figure 7(a) shows a conventional all-dielectric metasurface structure, consisting of a 2D array of coupled dielectric resonators of permittivity ε_r: (1) in a host dielectric layer of permittivity ε_r and (2) when a plane wave, $v_{in}(x,y,t)$ is incident on the unit cell, the electric and magnetic

dipole responses of the dielectric resonators are excited. If the resonators are designed such that the induced electric dipoles p and magnetic dipoles m are excited at the same frequency and have the same quality factor, then zero backscattering and thereby full transmission in the forward direction is achieved. While the host dielectric is not a fundamental component of the metasurface, it is just needed to provide mechanical support to the resonator array. Due the corresponding dielectric layered structure, spurious Fabry-Perot resonances may appear within the host substrate, contaminating the desired transmission response [43].

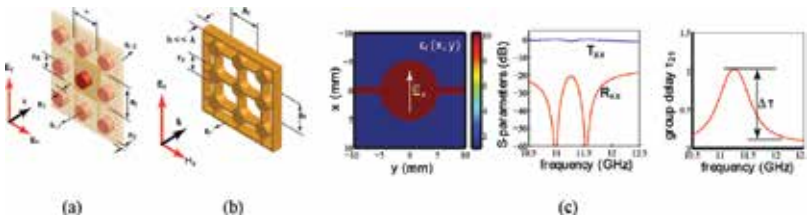

Figure 7. All-dielectric metasurfaces. (a) Conventional all-pass dielectric metasurface and (b) proposed all-pass and all-dielectric metasurface based on 2D array of inter-connected coupled disks [37]. (c) Typical transmission and reflection characteristics of the proposed all-dielectric metasurface with horizontal interconnections. ε_r = 10.2, h = 5.08 mm and interconnection thickness = 2.54 mm [37]. ©IEEE; reprinted with permission.

3.3.2. Proposed phaser based on all-dielectric metasurface

Taking inspiration from the coupled-dielectric metasurfaces of **Figure 7(a)**, **Figure 7(b)** shows an all-dielectric metasurface structure, particularly suitable for microwave and mm-wave frequencies. It consists of a periodic 2D array of dielectric resonators, however, instead of being supported by a host substrate of different permittivity, the resonators are connected to each other via thin dielectric interconnections. The overall structure may be seen as a perforated dielectric substrate, where dielectric material is removed in undesired areas using standard laser hole drilling processes [37].

The dielectric interconnections therefore provide the required mechanical support to hold the dielectric unit cells together. Since there is no host substrate, the proposed structure does not exhibit spurious Fabry-Perot type resonances, unlike in their optical counterparts, while maintaining its inherent all-pass response.

3.3.3. Results

To compute the transmission and reflection characteristics of the proposed structure, shown in **Figure 7(b)**, we used the rigorous coupled-wave analysis (RCWA) [45]. RCWA is a semi-analytical method usually applied to compute scattering parameters in periodic dielectric structures, where the scattered fields are represented as series of spatial harmonics. In this method, the unit cell is represented by a permittivity function ε_r (x, y) in **Figure 7(c)**, which is periodic in the x- and y-directions to form the full metasurface. The two dielectric interconnections are also shown along the x- and y-directions, respectively. The unit cell is incident with a linearly polarized plane-wave E_x, and the corresponding transmission $T_{xx}(\omega)$ and reflection $R_{xx}(\omega)$ response are then obtained using the RCWA method. To be noted is that the unit cell

http://dx.doi.org/10.5772/67356

size is assumed to be subwavelength (i.e., $a_x = a_y << \lambda$) so that only the fundamental spatial harmonic exists in the structure.

Figure 7(c) shows the typical transmission and reflection characteristics of the proposed lossless unit cell where only y-oriented interconnections are present. A good matching is achieved with an almost ideally flat transmission response. In addition, a strong dispersion response is observed as desired, as it can be seen from the nonzero group delay swing $\Delta\tau$.

4. Applications

The phasers described in the previous section represent the fundamental units for performing real-time signal processing operations on broadband signals. In this section, two applications are presented in the area of instrumentation and wireless communication, to illustrate the versatility of these phasers.

4.1. Antenna beam scanning in 2D

A common technique to achieve ultrafast signal processing of broadband signals in microwaves and optics is real-time spectrum analysis based on frequency-to-space mapping. While optical diffraction gratings [46] and virtual image phased arrays [47] have been extensively used in optics for spectral decomposition of an optical signal in space, leaky-wave antennas (LWAs) have been used for the same purpose at microwaves with a simpler test signal injection mechanism [18].

Most of these systems are restricted to 1-D decomposition and thus suffer from restricted frequency resolution. An optical system combining two orthogonally placed dispersive components to achieve spectral decomposition in two dimensions of space has recently been proposed [48]. However, the first microwave implementation of a 2D spatial disperser to achieve high-resolution spectrum analysis of broadband microwave signals was presented in Ref. [19].

4.1.1. Spectral decomposition principle

The general objective of a 2D spectral decomposition system is illustrated in **Figure 8(a)**. The temporal frequencies (f_m) of an input signal to analyze ($v_{\text{in}}(t)$) are mapped, in real-time, onto different spatial frequencies ($\mathbf{k}_m = (\varphi_m, \theta_m)$) over a two-dimensional plane in space.

A conventional 1D LWA separates the test signal into its frequency components in space following the beam-scanning law of the antenna, where each frequency component is radiated along a specific direction of space according to $\theta_{\text{MB}}(\omega) = \sin^{-1}[\beta(\omega)/c]$ [49]. The dispersion relation $\beta(\omega)$ of the radiating structure dictates the mapping between temporal and spatial frequencies, and thus a 1D leaky-wave antenna acts as an analog real-time spectrum analyzer along one dimension of space [18].

To order to extend the functioning of spatial-spectral decomposition from 1D to 2D, in order to increase the frequency resolution in spectrum analysis, we proposed the technique shown in

Figure 8(b). Consider an array of M LWAs excited by phasers [12], as shown in **Figure 8(a)**. Let us assume that each of the LWAs is a composite right/left-handed (CRLH) antenna, covering the signal bandwidth [ω_{start}, ω_{stop}] [49]. Such antennas naturally provide spectral decomposition along the y-axis from forward to backward region including broadside, according to $\beta(\omega) = \omega/\omega_R - \omega_L/\omega$ [18, 49].

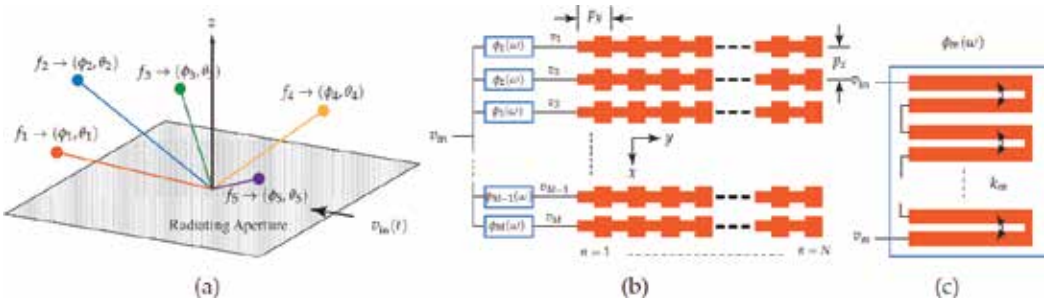

Figure 8. Proposed structure for 2D spectral decomposition, consisting of an array of LWAs fed by phasers [19]. (a) Antenna array layout and (b) one of the phasers, which is here a cascaded C-section phaser. ©IEEE; reprinted with permission.

The frequency discrimination along the x-axis is achieved using a dispersive feeding network wherein the mth antenna in the array is connected with a phaser, providing a phase shift $\varphi_m(\omega)$. First assume, for simplicity, that the LWAs only radiate along broadside ($\theta = 0°$) in the $\varphi = 90°$ plane. Consider the radiation at a certain frequency $\omega 0$ in the $\varphi = 0°$ plane for the following three cases:

1. The LWAs are excited in phase, i.e., $|\varphi_{m+1}(\omega_0) - \varphi_m(\omega_0)| = 2k\pi$, where k is an integer: In this case, frequency $\omega 0$ points to broadside, i.e., $\theta = 0°$.
2. $\varphi_{m+1}(\omega_0) - \varphi_m(\omega_0) > 0$: In this case, $\omega 0$ points in the forward direction, i.e., $90° > \theta_{MB} > 0$.
3. $\varphi_{m+1}(\omega_0) - \varphi_m(\omega_0) < 0$: In this situation, the frequency $\omega 0$ radiates in the backward direction, i.e., $-90° < \theta_{MB} < 0$.

Therefore, an appropriate feeding phasers allows for a full-space frequency scanning along the x-axis. Moreover, if the above three phase conditions are satisfied at several frequency points within the given bandwidth, the backward to forward frequency scan will repeat periodically for each frequency subband. Finally, integrating the x-axis scanning with the conventional y-axis scanning of the antenna results in 2D frequency scanning in space.

4.1.2. Results

Let us assume the cascaded C-section phaser as the dispersive feed element to the array, as shown in **Figure 8(c)**. This phaser consists of several C-sections, which are formed using a coupled-line coupler with a coupling coefficient k. The corresponding transmission phase is given by $\varphi_i(\omega) = -2q_0\tan^{-1}(1+k_i)/(1-k_i)\tan((\pi\omega)/(2\omega_\lambda))$, where q_0 is the number of C-sections in the phaser and ω_λ is the quarter-wavelength frequency of the coupler. The radiation properties

http://dx.doi.org/10.5772/67356

of the overall LWA array of **Figure 8(b)** can then be determined based on the above dispersive network and CRLH LWA dispersion relation.

Figure 9 shows the computed array factor results of several different dispersion characteristics of the feeding section. First, a nondispersive network is assumed (with $k = 0$), as shown in the first row of **Figure 9**. In this case, the LWA array shows conventional 1D scanning along the y-axis, since all the antennas are fed in-phase. Next, a small dispersion in $\varphi(\omega)$ is introduced using $k \neq 0$, as shown in the second row of **Figure 9**. As a result, the frequency scanning plane is rotated to about $\varphi = 45°$ plane. In this case, the frequency point ωA where $|\varphi_{m+1}(\omega_A) - \varphi_m(\omega_A)| = 0$,

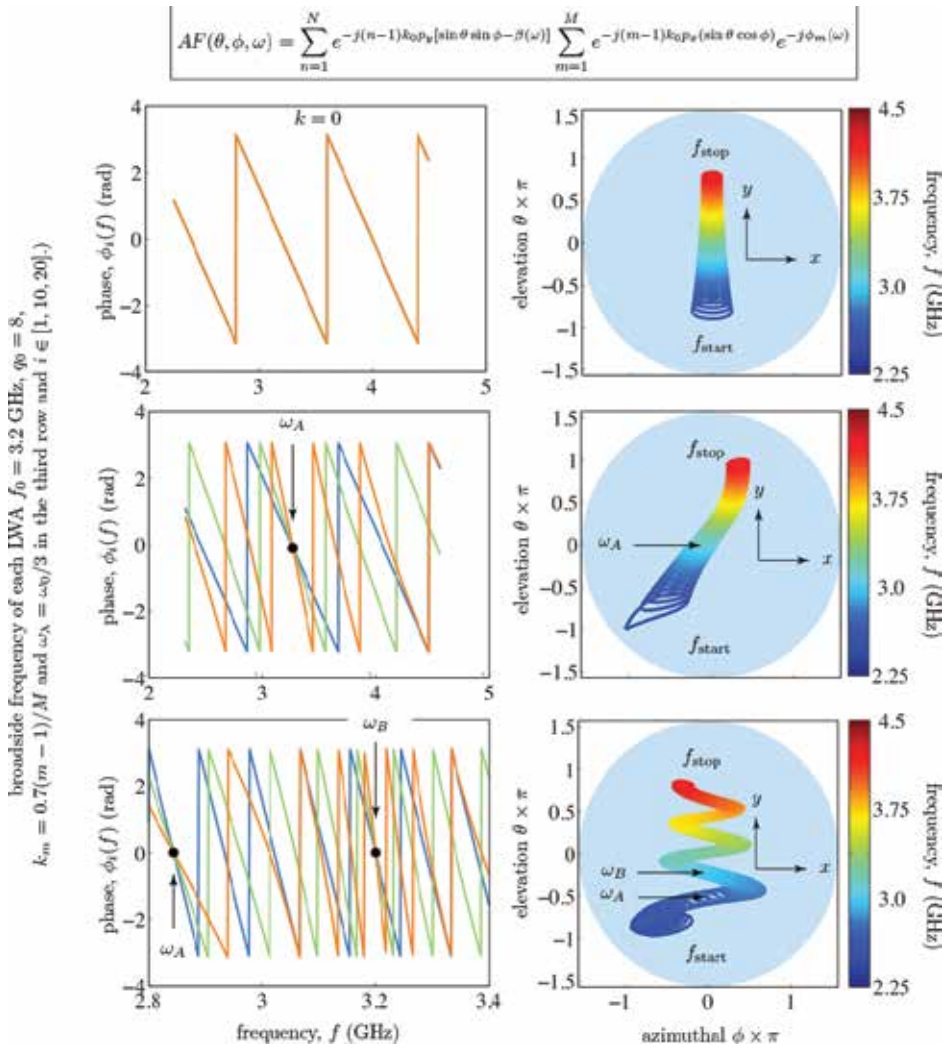

Figure 9. Array factor computed results corresponding to the structure in **Figure 8** with $M \times N = 20 \times 30$ showing the dispersion profile of the phaser feeding elements at the input of each leaky-wave antenna and the 3-dB contour plots of the 2D radiation patterns in the (θ, φ) plane [19]. ©IEEE; reprinted with permission.

corresponds to the broadside frequency in the $\varphi = 0°$ plane. The interesting case is when the dispersion characteristics of the phaser is periodic in frequency due to its commensurate nature, within the radiating band of the LWA, as shown in the third row of **Figure 9**. In this case, a periodic frequency scanning is achieved between the left and right half of the $(\theta - \varphi)$ plane, thereby distributing the same frequency band in a larger area in space leading to a higher frequency resolution.

4.2. Dispersion code multiple access (DCMA) system

The second application of R-ASP presented here is in wireless communication applications. One important concept in wireless communication is *multiple access*. A multiple access technology plays a crucial role in sharing common resources between multiple users in dense wireless communication environments. Typical techniques include frequency domain multiplexing (FDM), time-domain multiplexing (TDM), code division multiple access (CDMA), and space division multiple access (SDMA) [50].

All these techniques are dominantly based on digital technologies, and thus suffer from poor performances at high frequencies and in broadband regimes. Considering their limitations in meeting the future throughput and reliability demands for the next-generation wireless networks, a dispersion code multiple access (DCMA) scheme has been recently introduced in Ref. [51]. Due to its analog and real-time operation, DCMA is naturally scalable to high-frequencies and can accommodate ultra-wideband signals, using efficient phasers [12, 46]. The first rigorous investigation on the bit-error-rate (BER) performance of a DCMA system was recently presented in Ref. [21].

4.2.1. Principle

Consider a three user communication system, as shown in **Figure 10(a)**, where sender A wishes to communicate with receiver B only. Each user is associated with a phaser with a specific group delay versus frequency profile [12]. A linear group delay profile is chosen here for simplicity. Sender A first prechirps and expands a broadband input pulse using a positively sloped delay phaser. It then transmits it to both receivers B and C. While the intended receiver is B, it is able to recompress the pulse using a negatively sloped delay phaser. However, receiver C is unable to retrieve the original signal since the received signal is further expanded due to its positively sloped delay phaser. Therefore, A and B form a secure wireless channel between them, owing to their complementary phaser profiles, since $\tau_A(\omega) + \tau_B(\omega) = \text{const.}, \forall\omega$. In situations where there are more users, each user pair with two complementary phasers forms a wireless channel. Therefore, exploiting several dispersion code pairs, multiple channels can exist in the same frequency band, thereby sharing the available communication resources at the same time. This is the basic concept of DCMA.

4.2.2. Signal propagation modeling

Consider the $N \times N$ DCMA system shown in **Figure 10(b)**. The transfer function of the kth transmitting phaser is assumed to have the all-pass from $H_k^{Tx}(\omega) = \exp(j\varphi_k^{Tx})$, with

http://dx.doi.org/10.5772/67356

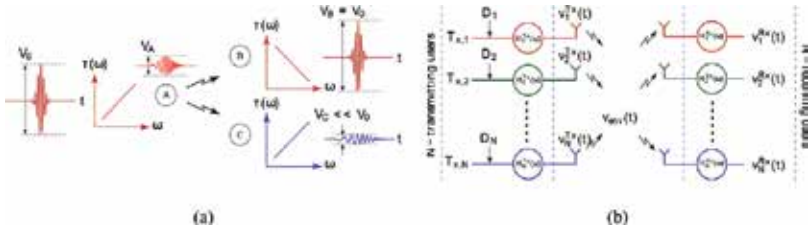

Figure 10. Dispersion code multiple access (DCMA) [21]. (a) Principle. (b) $N \times N$ DCMA system. For each transmitter, the intended receiver is indicated with the same color code [21]. ©IEEE; reprinted with permission.

$\varphi_k^{Tx}(\omega) = -\int_{\omega 1}^{\omega 2} \tau_k^{Tx}(\omega)d\omega = -\varphi_0 - \int_{\omega 1}^{\omega 2} \tau_k^{Tx}(\omega)d\omega$, where $\tau_k(\omega)$ is the group delay versus frequency profile of the phaser, $\varphi_0 = -\tau_0(\omega_2 - \omega_1)$, with τ_0 being the average group delay of the phaser. Similarly, the transfer function of the lth receiving phaser is $H_k^{Rx}(\omega) = \exp(j\varphi_l^{Rx})$, where $\varphi_l^{Rx}(\omega) = -\int_{\omega 1}^{\omega 2} \tau_l^{Rx}(\omega)d\omega = -\varphi_0 + \int_{\omega 1}^{\omega 2} \tau_l^{Rx}(\omega)d\omega$. In this example, the kth transmitting and the kth receiving phaser are dispersion matched with complimentary delay responses and thus form the kth wireless channel.

The digital information of user k can be specified by a vector D_k. This information is impressed on a periodically pulsed signal, following an on-off-keying (OOK) modulation format. Following this, the input to the kth transmitting phaser is given by $v_k^{in}(t) = \sum_{m=1} M\, D_k(m)a_0(t - mT_0)\sin(\omega_0 t)$, where $a_0(t)$ is a baseband pulse, T_0 is the bit-period and ω_0 is the carrier frequency. The output signal from the kth transmitting phaser is $v_k^{Tx}(t) = F^{-1}[F\{v_k^{in}(t)\}H_k^{Tx}(\omega)]$, where F represents the Fourier transform. When all the users are transmitting together, the total signal in the environment is the sum of all the signals present, and thus is given by $v_{env(t)} = \sum N\, v_k^{Tx}(t)$. This signal is then received at the lth receiver as $v_l^{Rx}(t) = F^{-1}[F\{v_{env}(t)\}H_{env}(\omega)H_l^{Rx}(\omega)]$, where $H_{env}(\omega)$ is the transfer function of the wireless environment.

The received signal is then demodulated to extract the information using a simple thresholding mechanism. Finally, it is compared with the information D_k, which was originally sent, with $l = k$ at the intended transmitter to determine the bit-error rate in each wireless channel.

4.2.3. Results

An appropriate selection of phaser code profiles, $\tau_k(\omega)$, is important to achieve optimal channel discrimination between the different wireless channels in the DCMA system of **Figure 10**. One attractive choice is based on a set of Chebyshev polynomials, exhibiting a fixed min-max amplitude range in a given region, ensuring that the dispersed pulses are always contained within one-bit period [51]. The corresponding delay response of the kth transmitting phaser can be written $\tau_k(\omega) = \Delta\tau[\tau_k(\omega')] + \tau_0$, with $\omega' = 2(\omega - \omega_0)/(\omega_2 - \omega_1)$, where $\tau_k(\omega')$ is the kth Chebyshev polynomial of the first kind, $\Delta\tau$ is the delay swing, and $(\omega_2 - \omega_1)$ is the bandwidth of $a_0(t)$. Some typical Chebyshev delay codes are plotted in **Figure 11(a)** along with their complementary responses.

Next, to estimate the bit-error rate (BER) of an *ideal DCMA system*, these assumptions were made: (1) direct line-of-sight transmission with no multiple reflections, (2) nondispersive channels, i.e., $H_{env}(\omega)$ = const. = 1, and (3) noiseless environment. **Figure 11(b)** shows the numerically computed BERs for different Chebyshev codes and delay swing $\Delta\tau$'s. A 20-bit data stream is specified at each transmitting location, and the corresponding BER is computed as an average of multiple simulation data. When only odd Chebyshev polynomials are used (third column), the BER of all channels progressively drops to zero as $\Delta\tau$ is increased. This simulation suggests that odd Chebyshev codes are excellent candidates for DCMA.

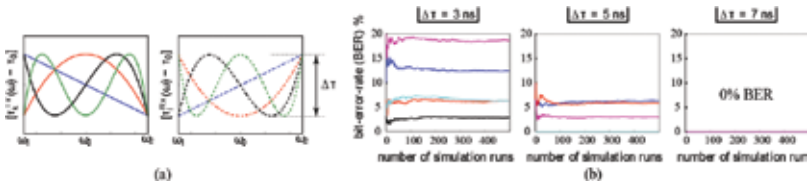

Figure 11. DCMA system results [21]. (a) Typical Chebyshev delay codes and (b) the computed BERs for a 5 × 5 DCMA system with different odd-order only Chebyshev delay profiles and delay swings $\Delta\tau$'s for the following parameters: T_0 = 20 ns, $a_0(t)$ is Gaussian pulse with full-width half maximum (FWHM) of 0.25 ns, $\omega_0 = (\omega_2 - \omega_1) = 2\pi$ (5 GHz). Each color corresponds to a wireless channel between two intended transmitters and receivers. ©IEEE; reprinted with permission.

While the DCMA technology is presented here for multiple-access, it is ideally suited for enhancing the data throughput of a single wireless channel. Consider the DCMA system of **Figure 10(b)**, and assume that the serial data stream of a signal transmitter is converted into N parallel streams, which are then modulated through unique phaser dispersions across each of the N channels. Using the DCMA principle described above, each of these parallel data streams can be retrieved on the receiver side of the system, and combined back to produce the final output data stream. By increasing N, larger amount of data can be simultaneously transmitted within the same bandwidth. Such a system has been recently described as a dispersion code modulation (DCM) system [22].

5. Conclusions

In the context of the exploding demands for future wireless networks, R-ASP has been presented as a novel signal processing paradigm. Due to its analog and real-time nature, it represents a fundamentally different technology to manipulate and control radio signals, in contrast to conventional DSP techniques, particularly suited for microwave and mm-wave systems. In this chapter, recent developments in R-ASP technology have been presented in detail. Several novel passive and active phasers, based on coupled-line couplers have been discussed along with their spatial counterparts using all-dielectric metasurface structures. Finally, two applications have been presented: a 2D real-time spectrum analyzer and a DCMA system, to illustrate the applicability of such phasers in instrumentation and communication systems, respectively.

http://dx.doi.org/10.5772/67356

Author details

Shulabh Gupta[1]* and Christophe Caloz[2]

*Address all correspondence to: shulabh.gupta@carleton.ca

1 Department of Electronics, Carleton University, Ottawa, Ontario, Canada

2 Department of Electrical Engineering, Polytechnique Montréal, Montréal, Québec, Canada

References

[1] Huawei, "5g: A technology vision," White Paper, 2013.

[2] Ericsson, "The real-time cloud," White Paper, 2013.

[3] A. Osseiran, "The foundation of the mobile and wireless communications systems for 2020 and beyond: Challenges, enablers and technology solutions", Proc. IEEE 77th Veh. Tech. Conf., 2013-June.

[4] F. Boccardia, B. L. Alcatel-Lucent, R. W. H. J. T. U. of Texas at Austin, A. L. U. P. Fabra, A. L. Thomas L. Marzetta (Bell Labs, and P. A. University), "Five disruptive technology directions for 5g."

[5] W. Chin, Z. Fan, and T. R. Haines, "Emerging technologies and research challenges for 5g wireless networks," Toshiba Research Europe Limited, Bristol, UK.

[6] S. Gupta, "Automatic analog beamforming transceiver for 60 ghz radios," University of California, Los Angeles.

[7] "Defining the future of multi-gigabit wireless communications," WiGig white paper, 2010.

[8] "The 60 ghz band cuts 4g backhaul costs," Electronic Design Article, 2013.

[9] D. Halperin, S. Kandula, J. Padhye, and D. Wetherall, "Augmenting data center networks with multi-gigabit wireless links," Microsoft Research and University of Washington, 2011.

[10] N. Hamedazimi, H. Gupta, V. Sekar, and S. R. Das, "Patch panels in the sky: A case for free-space optics in data centers," Department of Computer Science, Stony Brook University, Stony Brook, NY, USA.

[11] "Millimeter waves: Emerging markets brochure," A Thintri Market Study, 2012.

[12] C. Caloz, S. Gupta, Q. Zhang, and B. Nikfal, "Analog signal processing: a possible alternative or complement to dominantly digital radio schemes," IEEE Microw. Mag., vol. 14, no. 6, pp. 87–103, Sep. 2013.

[13] J. D. Schwartz, I. Arnedo, M. A. G. Laso, T. Lopetegi, J. Azaña, and D. Plant, "An electronic UWB continuously tunable time-delay system with nanosecond delays," IEEE Microw. Wireless Compon. Lett., vol. 18, no. 2, pp. 103–105, Jan. 2008.

[14] B. Nikfal, S. Gupta, and C. Caloz, "Increased group delay slope loop system for enhanced-resolution analog signal processing," IEEE Trans. Microw. Theory Tech., vol. 59, no. 6, pp. 1622–1628, Jun. 2011.

[15] B. Nikfal, D. Badiere, M. Repeta, B. Deforge, S. Gupta, and C. Caloz, "Distortion-less real-time spectrum sniffing based on a stepped group-delay phaser," IEEE Microw. Wireless Compon. Lett., vol. 22, no. 11, pp. 601–603, Oct. 2012.

[16] S. Abielmona, S. Gupta, and C. Caloz, "Compressive receiver using a CRLH-based dispersive delay line for analog signal processing," IEEE Trans. Microw. Theory Tech., vol. 57, no. 11, pp. 2617–2626, Nov. 2009.

[17] S. Gupta, B. Nikfal, and C. Caloz, "Chipless RFID system based on group delay engineered dispersive delay structures," IEEE Antennas Wirel. Propagat. Lett., vol. 10, pp. 1366–1368, Dec. 2011.

[18] S. Gupta, S. Abielmona, and C. Caloz, "Microwave analog real-time spectrum analyzer (RTSA) based on the spatial-spectral decomposition property of leaky-wave structures," IEEE Trans. Microw. Theory Tech., vol. 59, no. 12, pp. 2989–2999, Dec. 2009.

[19] S. Gupta and C. Caloz, "Real-time 2-d spectral-decomposition using a leaky-wave antenna array with dispersive feeding network," in 2015 IEEE International Symposium on Antennas and Propagation USNC/URSI National Radio Science Meeting, July 2015, pp. 29–30.

[20] H. V. Nguyen and C. Caloz, "Composite right/left-handed delay line pulse position modulation transmitter," IEEE Microw. Wireless Compon. Lett., vol. 18, no. 5, pp. 527–529, Aug. 2008.

[21] S. Gupta, L. Zou, M. A. Salem, and C. Caloz, "Bit-error-rate (ber) performance in dispersion code multiple access (dcma)," in 2015 IEEE International Symposium on Antennas and Propagation USNC/URSI National Radio Science Meeting, July 2015, pp. 1015–1016.

[22] L. Zou, S. Gupta, and C. Caloz, "Dispersion code modulation concept for spectral efficiency enhancement in wireless communications," in IEEE International Symposium on Antennas and Propagation, Jun. 2016.

[23] B. Nikfal, Q. Zhang, and C. Caloz, "Enhanced-snr impulse radio transceiver based on phasers," IEEE Microwave and Wireless Components Letters, vol. 24, no. 11, pp. 778–780, Nov. 2014.

[24] B. Nikfal and C. Caloz, "Low-complexity and frequency-scalable analog real-time fdm receiver based on a dispersive delay structure," in Microwave Conference (EuMC), 2011 41st European, Oct 2011, pp. 397–400.

[25] M. A. G. Laso, T. Lopetegi, M. J. Erro, D. Benito, M. J. Garde, M. A. Muriel, M. Sorolla, and M. Guglielmi, "Chirped delay lines in microstrip technology," IEEE Microw. Wireless Compon. Lett., vol. 11, no. 12, pp. 486–488, Dec. 2001.

[26] Q. Zhang, S. Gupta, and C. Caloz, "Synthesis of narrow-band reflection-type phaser with arbitrary prescribed group delay," IEEE Trans. Microw. Theory Tech., vol. 60, no. 8, pp. 2394–2402, Aug. 2012.

[27] C. K. Campbell, Surface Acoustic Wave Devices and Their Signal Processing Applications. San Diego, USA: Academic Press, 1989.

[28] W. S. Ishak, "Magnetostatic wave technology: a review," Proc. IEEE, vol. 76, no. 2, pp. 171–187, Feb. 1988.

[29] Q. Zhang, D. L. Sounas, and C. Caloz, "Synthesis of cross-coupled reduced-order phasers with arbitrary group delay and controlled magnitude," IEEE Trans. Microw. Theory Tech., vol. 61, no. 3, pp. 1043–1052, Mar. 2013.

[30] H.-T. Hsu, H.-W. Yao, K. A. Zaki, and A. E. Atia, "Synthesis of coupled-resonators group-delay equalizers," IEEE Trans. Microw. Theory Tech., vol. 50, no. 8, pp. 1960–1968, Aug. 2002.

[31] E. G. Cristal, "Theory and design of transmission line all-pass equalizers," IEEE Trans. Microw. Theory Tech., vol. 17, no. 1, pp. 28–38, Jan. 1969.

[32] S. Gupta, A. Parsa, E. Perret, R. V. Snyder, R. J. Wenzel, and C. Caloz, "Group delay engineered non-commensurate transmission line all-pass network for analog signal processing," IEEE Trans. Microw. Theory Tech., vol. 58, no. 9, pp. 2392–2407, Sept. 2010.

[33] Q. Zhang, S. Gupta, and C. Caloz, "Synthesis of broadband phasers formed by commensurate C- and D-sections," Int. J. RF Microw. Comput. Aided Eng., Aug. 2013.

[34] S. Gupta, Q. Zhang, L. Zou, L. J. Jiang, and C. Caloz, "Generalized coupled-line all-pass phasers," IEEE Trans. Microw. Theory and Tech., vol. 63, no. 3, pp. 1007–1018, March 2015.

[35] L. Zou, S. Gupta, and C. Caloz, "Reconfigurable phaser using gain-loss c-sections for radio analog signal processing (r-asp)," in 2015 Asia-Pacific Microwave Conference (APMC), vol. 3, pp. 1–3, Dec. 2015.

[36] L. F. Zou, S. Gupta, and C. Caloz, "Loss-gain equalized reconfigurable C-section analog signal processor," in IEEE Transactions on Microwave Theory and Techniques, vol. PP, no. 99, pp. 1–10, Oct. 2016, in press. doi: 10.1109/TMTT.2016.2615920.

[37] S. Gupta, K. Achouri, and C. Caloz, "All-pass metasurfaces based on interconnected dielectric resonators as a spatial phaser for real-time analog signal processing," in 2015 IEEE Conference on Antenna Measurements Applications (CAMA), pp. 1–3, Nov. 2015.

[38] N. Yu and F. Capasso, "Flat optics with designer metasurfaces," Nat. Mater., vol. 13, pp. 139–150, April 2014.

[39] K. Achouri, M. A. Salem, and C. Caloz, "General metasurface synthesis based on susceptibility tensors," IEEE Trans. Antennas Propag., vol. 63, no. 7, pp. 2977–2991, Jul 2015.

[40] C. Pfeiffer and A. Grbic, "Controlling vector bessel beams with metasurfaces," Phys. Rev. Appl., vol. 2, p. 044012, Oct. 2014.

[41] A. Shaltout, A. Kildishev, and V. Shalaev, "Time-varying metasurfaces and lorentz nonreciprocity," Opt. Mater. Express, vol. 5, no. 11, pp. 2459–2467, Nov. 2015.

[42] Y. Hadad, D. L. Sounas, and A. Alu, "Space-time gradient metasurfaces," Phys. Rev. B, vol. 92, p. 100304, Sep. 2015.

[43] M. Decker, I. Staude, M. Falkner, J. Dominguez, D. N. Neshev, I. Brener, T. Pertsch, and Y. S. Kivshar, "High-efficiency light-wave control with all-dielectric optical huygens' metasurfaces," pp. 813–820, May 2014.

[44] A. Arbabi, Y. Horie, M. Bagheri, and A. Faraon, "Complete control of polarization and phase of light with high efficiency and sub-wavelength spatial resolution," arXiv:1411.1494, pp. 4308–4315, Nov. 2014.

[45] M. G. Moharam and T. K. Gaylord, "Rigorous coupled-wave analysis of planar-grating diffraction," J. Opt. Soc. Am., vol. 71, no. 7, pp. 811–818, Jul 1981.

[46] J. Goodman, Introduction to Fourier Optics. Englewood, CO: Roberts and Company Publishers; 3rd edition, 2004.

[47] M. Shirasaki, "Large angular dispersion by a virtually imaged phased array and its application to a wavelength demultiplexer," Opt. Lett., vol. 21, no. 5, pp. 366–368, Mar. 1996.

[48] C. Dragone and J. Ford, "Free-space/arrayed-waveguide router," US Patent 6,263,127, 2001.

[49] C. Caloz, D. R. Jackson, and T. Itoh, "Leaky-wave antennas (chap. 9)," in Frontiers in Antennas: Next Generation Design and Engineering, F. B. Gross, Ed. McGraw Hill, 2011.

[50] J. G. Proakis and M. Salehi, Digital Communications, 5th ed. McGraw-Hill Science/Engineering/Math, 2007.

[51] B. Nikfal, M. Salem, and C. Caloz, "A method and apparatus for encoding data using instantaneous frequency dispersion," US 62/ 002,978, Nov. 2013.

Chapter 10

Manipulating Electromagnetic Waves with Zero Index Materials

Shiyang Liu, Jialin Zhou, Ying Han, Xinning Yu,
Huajin Chen and Zhifang Lin

Additional information is available at the end of the chapter

http://dx.doi.org/10.5772/66663

Abstract

Zero-index material is a typical metamaterial with an effective zero refractive index, possessing a variety of exotic electromagnetic properties and particular functionalities. We have considered two kinds of zero-index materials with the first one a nearly matched zero index made of magnetic metamaterial and the second one a radially anisotropic zero index. The magnetic metamaterial-based systems are shown to be significant in wavefront engineering and flexibly tunable by an external magnetic field and a temperature field. The radially anisotropic zero-index-based systems can remarkably enhance the omnidirectional isotropic radiation by enclosing a line source and a dielectric particle within a shell configuration. The physical origin lies in that the dielectric particle effectively rescatters the trapped anisotropic higher order modes and converts them into the isotropic 0th order mode radiated outside the system. The case for the system with the loss is then examined and the energy compensation with a gain particle is also demonstrated.

Keywords: zero index materials, magnetic metamaterials, multiple scattering theory, omnidirectional isotropic radiation, Mie theory

1. Introduction

Metamaterials are a kind of composite electromagnetic (EM) materials consisting of subwavelength "meta-atoms" with either electric or magnetic response or even both, which possess nearly arbitrary profile of effective permittivity ε and permeability μ in principle [1–3]. A great deal of novel and unique EM properties, not occurring in natural materials, such as negative refraction [4, 5], cloaking [6, 7], illusion [8], and subwavelength propagation [9, 10] are theoretically predicted and experimentally implemented from the microwave region to the optical region. Zero-index material (ZIM) is a typical metamaterial with effective zero

refractive index, including ε-near-zero [11–13], μ-near-zero [14, 15], or both ε and μ near zero, a matched ZIM (MZIM) [16–18], and even more generally the ZIM with anisotropy [19–21].

Due to the extraordinary refractive index of the ZIMs, a great variety of bizarre EM behaviors and potential applications based on ZIM have been extensively investigated and reported. It has been demonstrated both theoretically and experimentally that the ZIM can be used to squeeze the electromagnetic wave and make it tunnel through a deep subwavelength channel with arbitrary shape, serving as a highly efficient coupler between incoming and outgoing waveguides [11, 13, 22]. Due to the zero phase delay in the ZIM, the phase pattern of an EM wave can be flexibly engineered, enabling the wavefront shaping [16, 23, 24]. The ZIM can also be used to modify and enhance the directive emission with high efficiency [20, 25, 26]. Compact omnidirectional metamaterial antennas can also be designed based on the anomalous transmittance of ε-near-zero ultranarrow radial channels [27]. Interestingly, by incorporating dielectric defects into the MZIM or ε-near-zero material the transmission and reflection can be switched by delicately controlling the defects [16, 28, 29]. Later on, Luo et al. [30] have implemented nearly perfect bending waveguides with anisotropic ZIM, while Cheng et al. [19] have used another kind of anisotropic ZIM, a radially anisotropic ZIM (RAZIM), to combine multiple sources and acquire omnidirectional radiation.

The ZIMs are usually composed of the building blocks made of metallic materials or dielectric materials, or sometimes are supposed to homogeneous media with the desired parameters in theoretical research. Here, we first present another kind of metamaterials composed of building blocks made of ferrite materials with intrinsic magnetic response, which are accordingly called magnetic metamaterials. The effective electric permittivity ε_{eff} and magnetic permeability μ_{eff} can be tuned by an external magnetic field (EMF) or temperature due to the dependence of ferrite materials on EMF and temperature, thus providing us with more degrees of tunability. In addition, the permeability of ferrite material is a second rank tensor with nonzero off-diagonal elements, indicating the time-reversal-symmetry breaking nature in magnetic metamaterials [31]. As a result, nonreciprocal behaviors can be observed in such system, even for the geometrically symmetric ZIM made of magnetic metamaterial. Then, we will consider a composite system constructed by a RAZIM shell enclosing a dielectric rod inside, which is used to implement a strongly enhanced two-dimensional (2D) isotropic radiation with relatively high efficiency. In addition, different from the configuration with the gain particles inserted inside the MZIM [32], our proposal does not alter the structure of the RAZIM shell and keep its homogeneity, which makes it experimentally feasible.

The research content of the present chapter consists of two main parts. In the first part, we present the design of ZIM with magnetic metamaterials by optimizing the parameters of configuration. Then, by calculating the photonic band diagrams and retrieving the effective constitutive parameters we can confirm the implementation of the ZIM. After that, the field patterns are simulated to demonstrate the zero-phase delay of the ZIM and wavefront modulation by sculpturing typical outgoing interfaces. Finally, the effective refractive index is shown to be thermally controlled due to the dependence of the saturation magnetization of ferrite materials on the ambient temperature. In the second part, we demonstrate a remarkable enhancement of omnidirectional radiation with the RAZIM shell by surrounding the line source together with a particular particle. A rigorous theoretical approach is presented to

analyze the phenomenon and optimize the related parameters. Then, the influence of the loss is examined, which can be compensated by introducing a gain particle. Finally, all the results are summarized in the conclusion part.

2. ZIM made of magnetic metamaterials

Magnetic metamaterials concerned in present work consist of an array of ferrite rods arranged periodically in air with either square or triangular lattice. Actually, configurations with some randomness introduced to the system are similar in the long wavelength limit, provided that the filling ratio of the ferrite materials is the same. Single-crystal yttrium-iron-garnet (YIG) is a good candidate for designing magnetic metamaterials due to its extremely low loss. In particular, the magnetic permeability of ferrite materials is dependent on an EMF, allowing for the realization of magnetically manipulable negative-index materials [33]. Combining the time-reversal symmetry breaking nature under an EMF, the one-way waveguiding tunable by an external magnetic field has been realized as well [34–36]. Bi and coworkers have shown that the thermally tunable negative index can also be realized with the magnetic metamaterials around the Curie temperature T_c based on the ferrimagnetic-paramagnetic transition of ferrite material. However, due to the narrow temperature range for the Mn-Zn ferrite material used in their work, the tunability is highly limited. Differently, for the single-crystal YIG employed in present design an even wider temperature range is permitted so that the effective refractive index can be adjusted from negative to zero and then to positive [37], signifying a great possibility to realize the gradient negative-zero-positive index material (NZPIM) [38, 39] when an appropriate gradient temperature field is applied to the system.

2.1. Photonic band diagrams and effective-medium theory

To examine the eigenmodes of the magnetic metamaterials, we employ the multiple-scattering theory to calculate the photonic band diagrams, which is proved to be powerful for the systems consisting of nonoverlap spheres or circular cylinders [40–45]. As for the effective electric permittivity ε_{eff} and magnetic permeability μ_{eff}, we will present simply a coherent potential approximation based effective-medium theory to retrieve these two constitutive parameters [46]. First thing first, for definiteness we should give the magnetic permeability of the single-crystal YIG ferrite rods fully magnetized along the z direction, parallel to the rod axes, which is a second rank tensor given by [47]

$$\widehat{\mu} = \begin{pmatrix} \mu_r & -i\mu_\kappa & 0 \\ i\mu_\kappa & \mu_r & 0 \\ 0 & 0 & 1 \end{pmatrix}, \qquad \widehat{\mu}^{-1} = \begin{pmatrix} \mu'_r & -i\mu'_\kappa & 0 \\ i\mu'_\kappa & \mu'_r & 0 \\ 0 & 0 & 1 \end{pmatrix}, \tag{1}$$

with $\mu_r = 1 + \frac{\omega_m(\omega_0 - i\alpha\omega)}{(\omega_0 - i\alpha\omega)^2 - \omega^2}$, $\mu_\kappa = \frac{\omega_m\omega}{(\omega_0 - i\alpha\omega)^2 - \omega^2}$, $\mu'_r = \frac{\mu_r}{\mu_r^2 - \mu_\kappa^2}$, and $\mu'_\kappa = \frac{-\mu_\kappa}{\mu_r^2 - \mu_\kappa^2}$, where $\omega_0 = \gamma H_0$ is the resonance frequency with $\gamma = 2.8$ MHz/Oe the gyromagnetic ratio, H_0 is the sum of the EMF applied in the z direction and the shape anisotropy field [47], $\omega_m = 4\pi\gamma M_s$ is the characteristic frequency with $4\pi M_s = 1750$ G the saturation magnetization, and $\alpha = 3\times10^{-4}$ is the damping

coefficient of the single-crystal YIG. The electric permittivity of the single-crystal YIG ferrite rods is $\varepsilon_s = 25 + i3\times10^{-3}$. In the calculation of photonic band diagram, we set $\alpha = 0$ [31] and $\varepsilon_s = 25$ to obtain the eigenmodes. For the 2D system, the transverse electric (TE) mode and the transverse magnetic (TM) mode are decoupled and we consider only the TM mode with the electric field polarized along the rod axis. In this case, the magnetic field of the incident wave is perpendicular to the EMF so that the magnetic field will interact with the precessing magnetic dipoles of the ferrite, thus leading to the control of an EMF on the magnetic permeability.

To calculate the eigenmodes and simulate the electric field patterns, we illustrate here how the multiple scattering theory is used to serve the purpose. For an incident TM wave, the electric field impinging to the ith ferrite rod can be expanded in terms of the vector cylindrical wave functions

$$\boldsymbol{E}_{\text{inc}} = E_0 \sum_m p_m J_m(k_0 r_i)\, e^{im\phi_i} \boldsymbol{e}_z, \tag{2}$$

where E_0 is the amplitude of the electric field, $J_m(k_0 r_i)$ is the mth order cylindrical Bessel function, k_0 is the wavenumber in the vacuum, $\boldsymbol{r}_i$ is the position vector of the polar angle ϕ_i in the coordinate system with the origin at the ith ferrite rod, $\boldsymbol{e}_z$ is the unit vector along rod axis, p_m is the expansion coefficient for the mth order partial wave of an incident field. The total scattering electric field can also be obtained by summarizing the scattering electric field from all the ferrite rods

$$\boldsymbol{E}_{sca} = -E_0 \sum_{i=1}^{N} \sum_{m=-m_c}^{m_c} b_m^{(i)} H_m^{(1)}(kr_i) e^{im\phi_i} \boldsymbol{e}_z, \tag{3}$$

where m_c is the critical angular momentum in the simulation to ensure the numerical convergence, N is the number of the ferrite rods, $H_m^{(1)}(kr_i)$ is the mth order Hankel function of the first kind, $b_m^{(i)}$ is the mth order scattering coefficient for the ith ferrite rod, which can be obtained according to

$$b_m^{(i)} = t_m^{(i)} \left[p_m^{(i)} - \sum_{j\neq i} \sum_n S_{mn}(i,j) b_n^{(j)} \right], \tag{4}$$

where $S_{mn}(i,j)$ is the structural factor that transforms the scattered wave from the jth ferrite rod into the incident wave on the ith ferrite rod and $t_m^{(i)}$ is the Mie-scattering coefficient of the ith ferrite rod, which was obtained exactly in literature [48].

$$t_m = \frac{\frac{\mu_s}{\mu_b} J'_m(x) - J_m(x)\left[\frac{m_s^2}{m'_s} D_m(m'_s x) + \frac{m\mu'_k}{x}\right]}{\frac{\mu_s}{\mu_b} H_m^{(1)'}(x) - H_m^{(1)}(x)\left[\frac{m_s^2}{m'_s} D_m(m'_s x) + \frac{m\mu'_k}{x}\right]}, \tag{5}$$

In Eq. (5), $J_m(x)$ and $H_m(x)$ are, respectively, the Bessel function and the Hankel function of the first kind, the superscript '" represents the derivative with respect to $x = k_b r_s$ with r_s the radius of the ferrite rod, $k_s^2 = \omega^2 \varepsilon_s \mu_s$, $m_s = k_s/k_b$, $m'_s = m_s/\sqrt{\mu'_r}$, and $D_n(m_s x) = J'_n(m_s x)/J_n(m_s x)$.

Actually, there exist $N\times(2m_c+1)$ scattering coefficients for the whole system, corresponding to $N\times(2m_c+1)$ linear equations, which is the kernel part of the multiple scattering theory. In matrix form, the linear equations can be cast into

$$(\mathcal{S}+t^{-1})b=p. \tag{6}$$

The magnetic field can be derived easily from Maxwell's equations. To calculate the photonic band diagram, we should set $p = 0$ to solve the stationary-state equations so that the eigenfrequencies corresponding to the wavevectors in reduced Brillouin zone can be obtained.

For convenience, we recapitulate the results for the effective-medium theory; more details are referred to the published literature [46]. The scenarios of the effective-medium theory are as follows: (1) transform the periodic lattice of the magnetic metamaterials into the effective medium with effective constitutive parameters ε_{eff} and μ_{eff}; (2) take the unit cell of the magnetic metamaterials as an equal-area coated rod with ferrite rod as the inner core and the background medium as the coated layer with radius r_0, which is evidently an approximation, applicable only for the lattice with high symmetry. For a square lattice the radius $r_0=\frac{a}{\sqrt{\pi}}$, while for a hexagonal lattice the corresponding radius of the coated layer is $r_0=\sqrt[4]{3}\frac{}{\sqrt{2\pi}}a$; (3) the effective constitutive parameters ε_{eff} and μ_{eff} are determined by the condition that the total scattering of this coated rod in the effective medium vanishes in the long wave limit, namely, $k_0r_0\ll1$ and $k_0\sqrt{\varepsilon_{\text{eff}}}\sqrt{\mu_{\text{eff}}}\ll1$. After some mathematical manipulations, we can obtain the simplified equations determining the effective electric permittivity ε_{eff} and the effective magnetic permeability μ_{eff}.

$$\varepsilon_{\text{eff}}=(1-f)\varepsilon_0+f\tilde{\varepsilon}_s,\qquad \frac{\mu_{\text{eff}}-\mu_0}{\mu_{\text{eff}}+\mu_0}=f\,\frac{\tilde{\mu}_s-\mu_0-\xi}{\tilde{\mu}_s+\mu_0+\xi}, \tag{7}$$

where f is the filling fraction with $f=r_s^2/r_0^2$, and

$$\begin{gathered}\tilde{\varepsilon}_s=2\varepsilon_sF_2(x_s),\quad \tilde{\mu}_s=\mu_sG_2(x_s),\quad \xi=-\frac{(1-f)\mu_0^2(\mu_\kappa/\mu_r)^2(\tilde{\mu}_s/\mu_s)^2}{(1-f)\mu_0+(1+f)\tilde{\mu}_s},\\ F_2(x_s)=J_1(x_s)/[x_sJ_0(x_s)],\quad G_2(x_s)=J_1(x_s)/[x_sJ'_1(x_s)],\end{gathered} \tag{8}$$

with $x_s=k_sr_s$. It is noted that for the isotropic dielectric rod μ_κ is equal to zero, then Eq. (7) can be recovered to that for the isotropic metamaterials [49].

2.2. Phase patterns and wavefront engineering

By use of multiple-scattering theory, we calculate the photonic band diagrams for the magnetic metamaterials composed of the single-crystal YIG ferrite rods of the radius $r_s = 3.3$ mm and arranged periodically with square lattice with the lattice separation $a = 10$ mm. The results are shown in **Figure 1(a)** and **(c)**, corresponding, respectively, to the magnetic metamaterials under the EMF $H_0 = 510$ Oe and $H_0 = 460$ Oe. It can be found that there appear no eigenmodes below the first band, suggesting the formation of the photonic band gap. The first band possesses the negative slope, namely, $\mathrm{d}\omega/\mathrm{d}k<0$, corresponding to the negative ε_{eff} and μ_{eff}

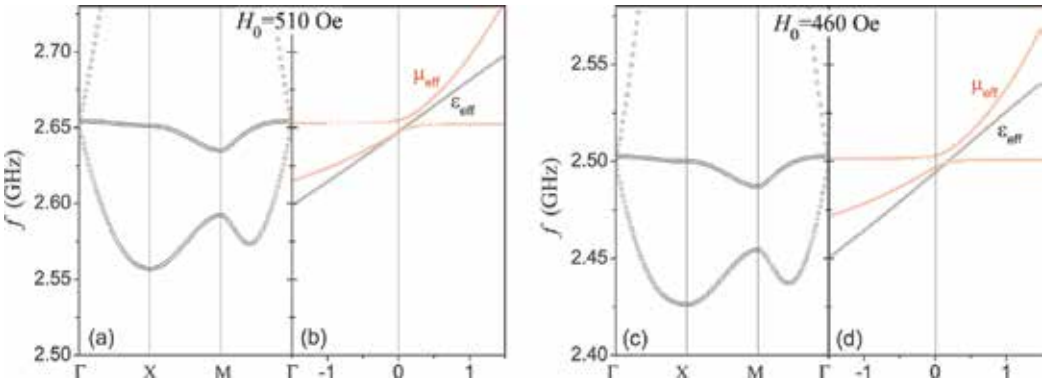

Figure 1. The photonic band diagrams for the magnetic metamaterials of square lattice under the EMF (a) $H_0 = 510$ Oe and (c) $H_0 = 460$ Oe, respectively. The corresponding effective electric permittivity ε_{eff} and magnetic permeability μ_{eff} are given in panels (b) and (d), respectively. The lattice separation is $a = 10$ mm and the radius of the ferrite rod is $r_s = 3.3$ mm.

as further corroborated by the effective constitutive parameters shown in **Figures 1(b)** and **(d)**. In particular, the first, second, and the third bands are degenerated at Γ point; meanwhile, the second band is nearly flat, signifying the characteristic of longitudinal mode. This accidental degeneracy can lead to the appearance of effective zero index with $\varepsilon_{\text{eff}} = \mu_{\text{eff}} = 0$ as confirmed by the effective-medium theory for the magnetic metamaterials under the EMF $H_0 = 510$ at the working frequency $f_w = 2.65$ GHz. Actually, the first and third bands form a Dirac cone at Γ point, which is consistent with that found by Huang et al. [16]. Interestingly, around the Dirac cone, the effective constitutive parameters ε_{eff} and μ_{eff} experience a nearly linear transition from negative to zero and then to positive except that a very narrow magnetic resonance appears, which is the difference of the magnetic metamaterials from the dielectric photonic crystals. This might be significant for investigating the EM features of NZPIM in frequency domain [50, 51]. More importantly, by decreasing the EMF from $H_0 = 510$ to 460 Oe both the photonic band diagram and the associated effective constitutive parameters are shifted downwards. As a result, the working frequency for the zero index is shifted from $f_w = 2.65$ to $f_w^{'} = 2.5$ GHz, suggesting the flexible tunability of the ZIM by an EMF. This offers us the opportunity to realize the NZPIM in space domain [38, 39] by applying a gradient EMF on magnetic metamaterials.

From the photonic band diagrams and the effective constitutive parameters ε_{eff} and μ_{eff}, we have obtained a good MZIM at the working frequency $f_w = 2.65$ GHz for the magnetic metamaterials under the EMF $H_0 = 510$ Oe. To examine the performance of the MZIM, the electric field pattern inside the MZIM can be simulated as shown in **Figure 2** for an MZIM slab illuminated by a Gaussian beam normally from the left-hand side. It can be found that although the thicknesses of three MZIM slabs are different, the phases of the outgoing beams are almost the same, showing nearly no change compared to that at the left interface. Inside the MZIM slab, the Gaussian beam experiences nearly no phase delay and electric field is nearly homogeneous, indicating the characteristic of the ZIM. In addition, the amplitude of the outgoing beam is comparable to that of the incident beam, indicating the impedance match of the MZIM with the air. Compared to the MZIM based on the dielectric photonic crystals the

http://dx.doi.org/10.5772/66663

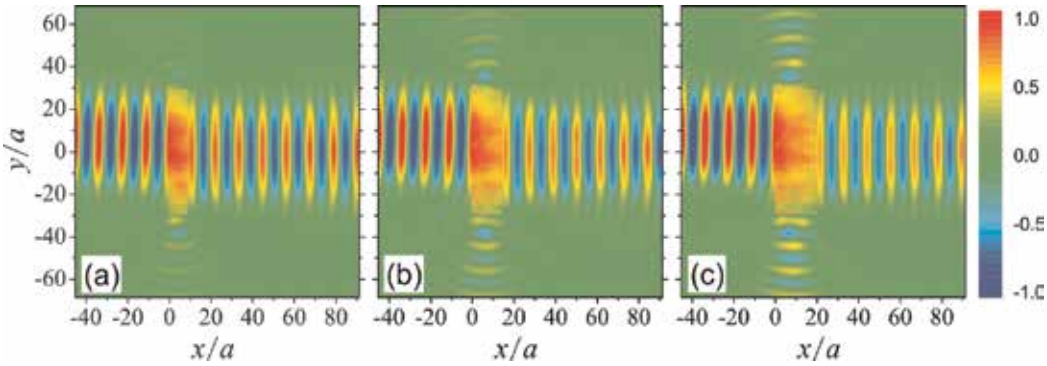

Figure 2. The electric field patterns of a Gaussian beam incident from the left-hand side of the ZIM slabs with the left interface fixed at $x = 0$ and the thickness of the slab $d_1 = 10a$ (a), $d_2 = 15a$ (b), and $d_3 = 20a$ (c), respectively. The height of the slab $D = 60a$, the working frequency is $f_w = 2.65$ GHz, and the other parameters are the same as those in Figure 1 (a) and (b).

coupling efficiency in present system is much higher, which originates from the anisotropy of the magnetic metamaterials as well as the subwavelength scale of the configuration. But for the dielectric photonic crystals the lattice separation is comparable to the working wavelength, implying a strong inhomogeneity. Anyhow, we can still observe some reflection due to the parallel momentum mismatch of the incident Gaussian beam at the interface. By calculating the reflectance and transmittance, we find that the reflectance becomes larger with the increase of the thickness, corresponding to 11.6, 18.9, and 24.1% for three different MZIM slabs. Differently, for a normal incident plane wave the reflectance is not larger than 1%, consistent with the above analysis. The transmittance for three different MZIM slabs are 84.3, 71.3, and 59.1%, less than 1 when adding to the reflectance, which comes from leaking of the EM energy from the upper and lower interface of the MZIM slabs as shown in **Figure 2**. Another interesting part is the upper shift of the reflection beam, corresponding to the nonreciprocal Goos-Hänchen shift, which deserves a further investigation in future work.

A particular functionality of the ZIM is to tailor the wavefront of the incident EM wave due to the zero phase delay inside the ZIM. We demonstrate such property by designing four typical outgoing interfaces sculptured from the MZIM, which are used to manipulate the wavefront of an incident Gaussian beam. The results are shown in **Figure 3**, where we can observe that the convex cylindrical face can transform the plane wavefront into the cylindrical one as shown in panel (a), different from the conventional convex lens that focuses the incident beam. It should be noted that the inhomogeneity of the outgoing beam arises from the anisotropy of the magnetic metamaterials. On the contrary, the concave cylindrical face can be used to focus the incident beam as shown in panel (b), behaving like a conventional convex lens but not a concave lens. The triangular prism can be used to split the incident beam into two separated ones propagating perpendicularly to the outgoing interfaces. More generally, we have shown in panel (d) an ordinary undulated interface that transforms the wavefront into the one identical to the interface. Actually, more imaginable configurations can be designed to engineer the wavefront in practice. In addition, the effective index of the magnetic metamaterials

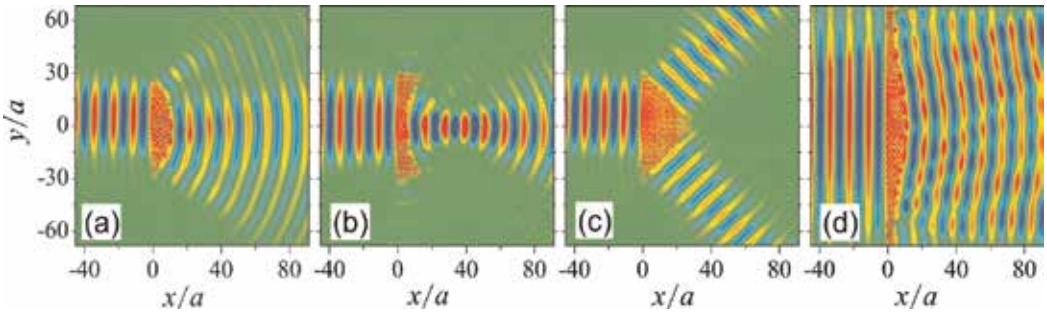

Figure 3. Wavefront engineering with different outgoing interfaces (a) convex cylindrical face, (b) concave cylindrical face, (c) triangular prism, and (d) ordinary undulated face. The radius of the curvature is 40a for panels (a) and (b), the waist radius of the incident Gaussian beam is 2λ for panels (a)–(c) and 6λ for (d). All the other parameters are the same as those in Figure 2.

can be controlled flexibly by an EMF, which can be used to transform the functionality of the above systems, for example, from focusing to defocusing or in an opposite manner.

2.3. Thermally controllable effective index

Another important property of ferrite materials is its saturation magnetization that is dependent on temperature, which can also be handled to control the EM properties of magnetic metamaterials. Single-crystal YIG bears a high Curie temperature $T_c = 523$ K, allowing a wide controlling temperature range and thus a better tunability on effective refractive index. The temperature field ranging from 0 (273.15 K) to 100°C (373.15 K) is considered for the magnetic metamaterials of triangular lattice with the lattice separation a = 10 mm and the rod radius $r_s = 3.4$ mm.

To examine the thermal effect on the magnetic metamaterials, we keep $H_0 = 485$ Oe unchanged, and tune the temperature T. The effective constitutive parameters ε_{eff} and μ_{eff} are presented in **Figure 4(a)–(c)**, respectively, under three different temperatures 306, 335, and 362

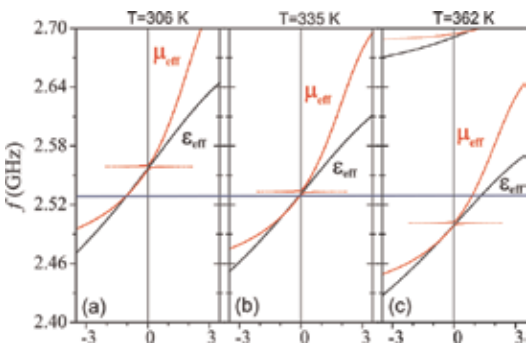

Figure 4. The real part of the retrieved effective electric permittivity ε_{eff} and magnetic permeability μ_{eff} for the magnetic metamaterials under three different temperatures (a) $T = 306$ K, (b) $T = 335$ K, and (c) $T = 362$ K, respectively. The lattice separation is a = 10 mm, the rod radius is $r_s = 3.4$ mm, and the EMF is $H_0 = 485$ Oe. The blue solid line marks the operating frequency $f_w = 2.53$ GHz.

K, corresponding to the saturation magnetization $4\pi M_s$ equal to 1740, 1650, and 1550 G. It should be noted that in our concerned frequency range $0.08 \leq \frac{a}{\lambda} \leq 0.09$, satisfying the long-wavelength approximation. As is shown in **Figure 4(a)**, under the temperature T = 306 K a nearly matched negative-index material with $\varepsilon_{\text{eff}} = \mu_{\text{eff}} = -1$ is obtained at the working frequency $f_w = 2.53$ GHz as marked by blue solid line. By improving the temperature, the curves of the effective constitutive parameters are shifted downwards as exhibited by comparing panels (a)–(c) due to the decrease of the saturation magnetization. Under the temperature $T = 362$ K, the effective electric permittivity $\varepsilon_{\text{eff}} = 1.36$ and the effective magnetic permeability $\mu_{\text{eff}} = 0.9$ are shown in **Figure 4(c)**, corresponding to a positive refractive index $n_{\text{eff}} = 1.1$. In particular, in between these two temperatures the effective electric permittivity $\varepsilon_{\text{eff}} = 0$ and the effective magnetic permeability $\mu_{\text{eff}} = -0.04$ close to zero under the temperature $T = 335$ K, resulting in the design of MZIM. As a result, a nearly continuous tuning of the effective constitutive parameters from negative to zero and then to positive is realized, suggesting that an NZPIM in space can be possibly implemented by the magnetic metamaterials under a gradient temperature field.

With the above knowledge, we can examine the performance of the magnetic metamaterials for molding EM wave propagation by simulating the field patterns of a TM Gaussian beam incident normally on a triangular prism with the apex angle $\theta = 90$. The results are shown in **Figure 5**, where we can observe that under the temperature $T = 306$ K the incident Gaussian beam is split into two separated beams propagating with the refractive angle $\theta_{\text{ref}} = 45$ as shown in panels (a) and (e), equal to the incident angle θ_{inc}, implying that the effective index of the triangular prism is $n_{\text{eff}} = -1$, consistent with the results from effective-medium theory given in **Figure 4(a)**. Under the temperature $T = 335$ K the effective constitutive parameters $\varepsilon_{\text{eff}} = 0$ and $\mu_{\text{eff}} = -0.04$, corresponding nearly to an MZIM, the electric field exhibits an invariant phase inside the prism, resulting in two perpendicularly outgoing beams with the same phase at two lateral interfaces as shown in panels (b) and (f). With further increasing the temperature to $T = 362$ K, we obtain the effective constitutive parameters $\varepsilon_{\text{eff}} = 1.36$ and $\mu_{\text{eff}} = 0.9$, corresponding to the effective index $n_{\text{eff}} = 1.1$, the Gaussian beam experiences a little bit focusing and collimation as shown in panels (c) and (g). When the temperature reaches $T = 367$ K, the effective constitutive parameters $\varepsilon_{\text{eff}} = 1.75$ and $\mu_{\text{eff}} = 1.11$, corresponding to the effective index $n_{\text{eff}} = 1.4$, a strong focusing with the outgoing beam waist radius shrunk nearly to λ can be observed as shown in panels (d) and (h).

3. Omnidirectional isotropic radiation via RAZIM

It has been shown that 2D RAZIM shell can be used to generate 2D isotropic radiation due to the fact that it can trap the anisotropic higher order modes, while it is transparent for the isotropic 0th order EM modes [19]. However, the efficiency is quite low since all the energy from the higher order modes are wasted, especially, when multiple sources are used since the energy of the higher order modes in that case occupies an even larger portion. We present an improved system with the 2D RAZIM shell enclosing a line source together with a conventional dielectric rod, which permits the generation of a perfect 2D EM mode; meanwhile, it is

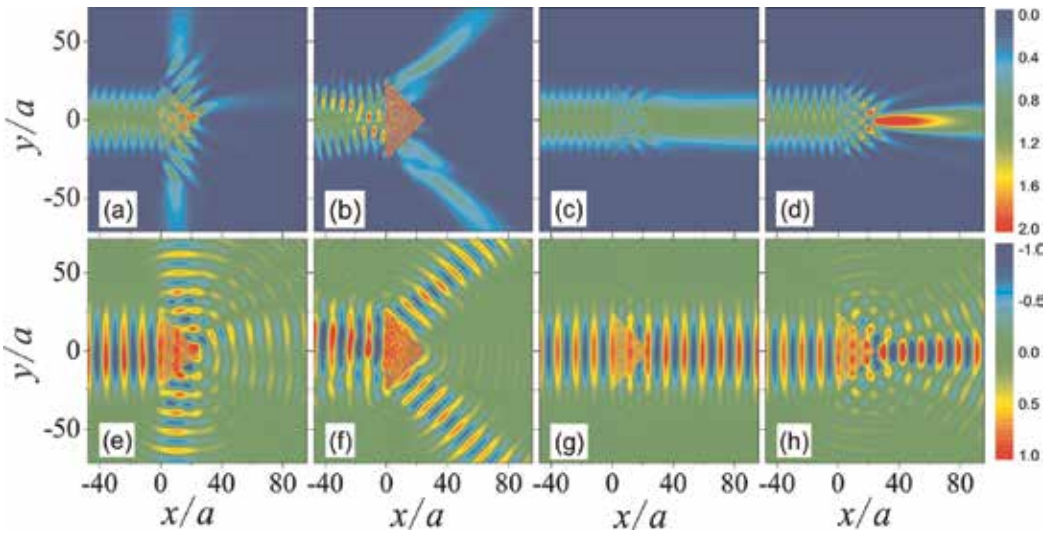

Figure 5. The electric field intensity $|E|^2$ (a)–(d) and electric field Re{E} (e)–(h) patterns for a Gaussian beam illuminating a triangular prism with the apex angle $\theta = 90°$ at the temperatures $T = 306$ K (a), (e); $T = 335$ K (b), (f); $T = 362$ K (c), (g); and $T = 367$ K (d), (h).

experimentally feasible. The dielectric rod can rescatter the anisotropic higher order EM modes and transform them into the isotropic 0th order modes. By positioning the dielectric rod at the strong field region of the anisotropic higher order modes, it can thus realize a great enhancement of omnidirectional radiation. The intrinsic loss of the RAZIM shell can also be examined and a gain-particle is used to compensate this dissipation.

3.1. Theoretical approach

The configuration of the system is schematically illustrated in **Figure 6**, where the shadowed green region is the RAZIM shell with a and b the inner and outer shell radii, and the dielectric rod and the line source are positioned inside the shell and denoted by D and S, respectively. In the cylindrical coordinate, the electric permittivity and magnetic permeability tensors of the RAZIM shell are characterized by [19, 52, 53]

$$\overline{\varepsilon} = \varepsilon_0(\hat{r}\hat{r}\varepsilon_r + \hat{\phi}\hat{\phi}\varepsilon_\phi + \hat{z}\hat{z}\varepsilon_z), \quad \overline{\mu} = \mu_0(\hat{r}\hat{r}\mu_r + \hat{\phi}\hat{\phi}\mu_\phi + \hat{z}\hat{z}\mu_z), \tag{9}$$

where $\mu_r \to 0$, corresponding to the radially anisotropic zero index. The origin of the cylindrical coordinate fixed at the center of the RAZIM shell. A line source of TM polarization is considered to interact with the RAZIM shell. For convenience, we first consider the simple system schematically illustrated in **Figure 6(a)** to depict the physical picture, based on which the system with further introducing a dielectric particle as shown in **Figure 6(b)** can be solved by further taking account of the mutual scattering between the dielectric particle and the RAZIM shell.

http://dx.doi.org/10.5772/66663

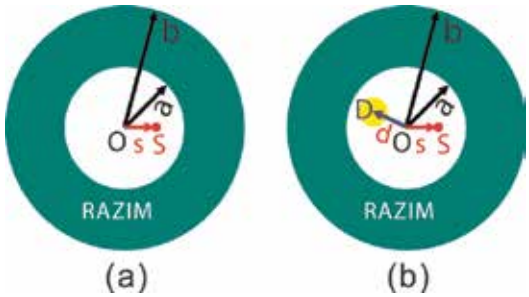

Figure 6. A schematic diagram illustrating the isotropic radiation system consisting of a RAZIM shell enclosing (a) a TM line source only and (b) both a TM line source and a dielectric rod of the radius r_d. The RAZIM shell center as well as the positions of the line source and the dielectric rod are denoted, respectively, by *O, S*, and *D* with $|OD| = d$ and $|OS| = s$. The background medium inside and outside the shell is vacuum. The inner and outer shell radii are *a* and *b*, respectively.

3.1.1. RAZIM shell enclosing only a single line source

In the framework of the generalized Lorenz-Mie theory, the EM field propagating in the RAZIM region can be expanded into the linear combination of the corresponding eigenmodes [19, 52]

$$E_z = \sum_m [B_m J_\nu(k_s r) + C_m H_\nu(k_s r)] e^{im\phi}, \quad a \le r \le b, \tag{10}$$

where $k_s^2 = k_0^2 \mu_\phi \varepsilon_z$ with k_0 the wavenumber in the vacuum, J_ν and H_ν are, respectively, the νth order Bessel functions and Hankel functions of first kind with the order $\nu = |m|\sqrt{\mu_\phi/\mu_r}$, and the summation m runs from $-\infty$ to ∞. The corresponding magnetic field in the transverse *xoy* plane can be obtained from Maxwell equations

$$H_r = \frac{1}{i\omega\mu_0\mu_r}\frac{1}{r}\frac{\partial E_z}{\partial \phi}, \quad H_\phi = -\frac{1}{i\omega\mu_0\mu_\phi}\frac{\partial E_z}{\partial r}, \tag{11}$$

for the TM waves. The electric field radiated by a TM line source positioned at $\boldsymbol{l}_s$ can also be expanded around the RAZIM shell center [54, 55]

$$\begin{aligned} E_z &= H_0(k|\boldsymbol{r}-\boldsymbol{l}_s|) = \sum_m J_m(ks) H_m(kr) e^{im\phi}, \quad r > s, \\ E_z &= H_0(k|\boldsymbol{r}-\boldsymbol{l}_s|) = \sum_m H_m(ks) J_m(kr) e^{im\phi}, \quad r < s, \end{aligned} \tag{12}$$

where $\boldsymbol{r}$ is the position vector and $s = |\boldsymbol{l}_s|$ is the separation between the line source and the RAZIM shell center. For convenience and without loss of generality, the line source is supposed to be located at (x_s, y_s) with $y_s = 0$, namely, the line source can be moved along the x axis. With these expansions, we can write the total electric field in different regions according to

$$\begin{aligned} E_z &= \sum_m [A_m J_m(kr) + J_m(ks) H_m(kr)] e^{im\phi}, \quad s < r \le a, \\ E_z &= \sum_m D_m H_m(kr) e^{im\phi}, \qquad\qquad\qquad\quad r \ge b, \end{aligned} \tag{13}$$

where the coefficients A_m characterize the reflection of mth order partial wave from the RAZIM shell, and D_m describes the transmission of the mth order partial wave radiating out of the shell.

By matching the boundary conditions, namely, the continuity of the tangential components of the EM field E_z and H_ϕ at the interface, we can work out the partial wave expansion coefficients for the EM fields in different regions,

$$B_m = q_m C_m, \qquad D_m = p_m C_m, \tag{14a}$$

$$A_m = q'_m J_m(ks), \qquad C_m = p'_m J_m(ks), \tag{14b}$$

where the generalized Mie coefficients are given by

$$p_m = \frac{k_s H_\nu(k_s b) J'_\nu(k_s b) - k_s H'_\nu(k_s b) J_\nu(k_s b)}{k_s H_m(kb) J'_\nu(k_s b) - k\mu_\phi H'_m(kb) J_\nu(k_s b)}, \tag{15a}$$

$$q_m = \frac{k\mu_\phi H_\nu(k_s b) H'_m(kb) - k_s H'_\nu(k_s b) H_m(kb)}{k_s H_m(kb) J'_\nu(k_s b) - k\mu_\phi H'_m(kb) J_\nu(k_s b)}, \tag{15b}$$

$$p'_m = \frac{k\mu_\phi H_m(ka) J'_m(ka) - k\mu_\phi H'_m(ka) J_m(ka)}{k\mu_\phi [H_\nu(k_s a) + q_m J_\nu(k_s a)] J'_m(ka) - k_s [H'_\nu(k_s a) + q_m J'_\nu(k_s a)] J_m(ka)}, \tag{15c}$$

$$q'_m = \frac{k_s H_m(ka) [H'_\nu(k_s a) + q_m J'_\nu(k_s a)] - k\mu_\phi H'_m(ka) [H_\nu(k_s a) + q_m J_\nu(k_s a)]}{k\mu_\phi [H_\nu(k_s a) + q_m J_\nu(k_s a)] J'_m(ka) - k_s [H'_\nu(k_s a) + q_m J'_\nu(k_s a)] J_m(ka)}. \tag{15d}$$

Regarding the RAZIM shell considered in our system, $\mu_r \to 0$, implying that the order ν of the cylindrical functions J_ν and H_ν in Eqs. (10), (13), and (15) tends to infinity for $m \neq 0$. As a result, $|H_\nu| \to \infty$ and $|J_\nu| \to 0$, leading to the vanishment of the Mie coefficient p'_m for $m \neq 0$. Therefore, it follows from Eq. (14) that $B_m \to 0$, $C_m \to 0$, and $D_m \to 0$ for $m \neq 0$. This indicates that the permitted propagating EM waves in the RAZIM shell are nearly independent of the azimuthal angle ϕ, as demonstrated by Eqs. (10) and (13). In addition, for the case when $\varepsilon_z = \mu_\phi = 1$, the Mie coefficients $p_0 = p'_0 = 1$, $q_0 = q'_0 = 0$, and $D_0 = J_0(kd)$. As a consequence, only the 0th order of the isotropic cylindrical EM wave can be radiated out of the RAZIM shell, ensuring its omnidirectionality, in agreement with the results obtained by Cheng et al. [19]. However, all the higher order modes of the cylindrical waves are confined within the RAZIM shell, hence, the RAZIM shell behaves like a cavity for these modes. Accordingly, the introduction of the RAZIM shell leads to the decrease of radiation power and reduces the radiation efficiency, although it can implement the spatial power combination for omnidirectional radiation.

http://dx.doi.org/10.5772/66663

Another important aspect for the RAZIM shell comes in the fact that it forms a cylindrical resonator for the higher order modes, which results in the creation of the standing wave with strong inhomogeneity inside the RAZIM shell. This particular feature arises from the anisotropy of the RAZIM shell, which is an essential aspect for the realization of isotropic radiation pattern. Besides, it is shown the RAZIM shell can be experimentally realizable both in microwave region [19] and in terahertz region [56], implying promising applications in future.

3.1.2. RAZIM shell enclosing a single line source together with a dielectric rod

To improve the radiating efficiency for the system shown in **Figure 6(a)**, we have to transform the higher order modes confined within the RAZIM shell into the isotropic lower order mode, and then radiating outside the RAZIM shell. To this end, a dielectric particle D can be introduced inside the RAZIM shell as illustrated in **Figure 6(b)**, which can rescatter the EM wave so that a part of the higher order modes can be converted into isotropic 0th order mode, thus enhancing the omnidirectional isotropic radiation from the RZAIM-shell-based system. Therefore, in this part we have to incorporate the contribution of the dielectric rod into theoretical framework. As is certain, the dielectric rod will change the scattering field inside central area surrounded by the shell and that propagating inside the shell. Therefore, the partial wave expansion coefficients A_m and C_m in Eq. (14b) should be altered

$$A_m = q'_m[J_m(ks) + E_m], \quad C_m = p'_m[J_m(ks) + E_m], \tag{16}$$

where E_m are the partial wave expansion coefficients of the scattered EM field from the dielectric rod D. As a result, the partial wave expansion coefficients B_m, and D_m are altered accordingly as indicated by Eq. (14a). It should be noted that the coefficients p_m, q_m, p'_m, and q'_m that characterize the scattering property of the RAZIM shell remain unchanged due to the fact that the RZAIM shell is intact when the dielectric rod D is introduced.

To consider the scattering behavior of the dielectric rod and obtain E_m, we should transform the expanding partial waves from the shell center to those from the dielectric rod D. The electric field inside the dielectric rod E_z^i and scattered by the rod E_z^s can be expanded easily into

$$E_z^i = \sum_m T_m J_m(k|\boldsymbol{r}-\boldsymbol{l}_d|)e^{im\phi}, \quad |\boldsymbol{r}-\boldsymbol{l}_d| < r_d, \tag{17a}$$

$$E_z^s = \sum_m S_m H_m(k|\boldsymbol{r}-\boldsymbol{l}_d|)e^{im\phi}, \quad |\boldsymbol{r}-\boldsymbol{l}_d| > r_d, \tag{17b}$$

where $\boldsymbol{l}_d$ is the position of the dielectric rod with $d = |\boldsymbol{l}_d|$ denoting the separation between the dielectric rod and the RAZIM shell center and r_d is the radius of the dielectric rod D. The partial wave expansion coefficients T_m and S_m are given by

$$T_m = b_m(R_m + I_m), \quad S_m = a_m(R_m + I_m), \tag{18}$$

where a_m and b_m are the Mie coefficients of the dielectric rod, I_m and R_m correspond to the contribution from the line source and that scattered inside by the RAZIM shell

$$I_m = H_m(kl)e^{in\phi'}, \quad R_m = \sum_n A_{m+n}J_n(kd)e^{in\phi_c}, \quad S_m = \sum_n E_{m+n}J_n(kd)e^{in\phi_c}. \tag{19}$$

The parameters in Eq. (19) are defined as $\phi_c = \angle DOS$, $\phi' = \angle DSO$, and $l^2 = d^2 + s^2 - 2d\,s\cos\phi_c$ is the distances from the dielectric rod to the line source S with $l/\sin\phi_c = d/\sin\phi'$. The Mie coefficients a_m and b_m of the dielectric rod can be easily obtained from the Mie theory [57]

$$b_m = \frac{k\mu_d J'_m(kr_d)H_m(kr_d) - k\mu_d J_m(kr_d)H'_m(kr_d)}{k_d J'_m(k_d r_d)H_m(kr_d) - k\mu_d H'_m(kr_d)J_m(k_d r_d)}, \tag{20a}$$

$$a_m = \frac{k\mu_d J'_m(kr_d)J_m(k_d r_d) - k_d J_m(kr_d)J'_m(k_d r_d)}{k_d J'_m(k_d r_d)H_m(kr_d) - k\mu_d H'_m(kr_d)J_m(k_d r_d)}, \tag{20b}$$

where $k_d^2 = k_0^2\varepsilon_d\mu_d$ with ε_d and μ_d being the permittivity and permeability of dielectric rod, respectively. For a particular case when the RAZIM shell is removed from the system, the corresponding scattering from the shell disappears, leading to R_m = 0. Combining Eqs. (16), (18), and (19) and after some mathematical manipulations, we can finally arrive at a set of linear equations

$$\sum_n (1 - a_m q'_n)J_{n-m}(kc)e^{i(n-m)\phi_c}E_n = \sum_n a_m q'_n J_n(kd)J_{n-m}(kc)e^{i(n-m)\phi_c} + a_m I_m, \tag{21}$$

which determine the coefficients E_n For now, we have solved the scattering problem for the RAZIM systems in both **Figure 6(a)** and **(b)**, based on which we can gain insight into the physical mechanism of the phenomenon as well as the role of the RAZIM shell and surrounded dielectric rod, meanwhile, optimize the configuration to achieve a better radiation efficiency.

3.2. Amplifying radiation with dielectric particle

In the simulations and calculations in this part except otherwise specified, the parameters for the RAZIM shell are a = 0.5, b = 1, $\mu_r = 0.01$, $\mu_\phi = 1$, $\varepsilon_z = 1$, and those for the dielectric rod are $r_d = 0.15$, $\varepsilon_d = 2$, and $\mu_d = 1$. The wavelength of the line source is set as unit $\lambda = 1$. To characterize the higher order modes trapped inside the RAZIM shell, we simulate the electric field amplitude $|E_z|$ pattern for the RAZIM shell enclosing only a line source, the result is shown in **Figure 7(a)**, where the line source is fixed at (0.1, 0) deviated from the shell center so that the higher order modes can be excited. A standing wave with strong inhomogeneity emerges, which is created by the higher order partial waves in Eq. (12) due to the nearly total reflection from the RAZIM shell. The EM wave-radiating outside the RAZIM shell can be calculated approximately by $E_z \approx D_0 H_0(kr) = [J_0(ks) + E_0]H_0(kr)$. Therefore, the performance of the dielectric rod can be evaluated approximately by calculating the amplitude of $|D_0|$. The simulating result is shown in **Figure 7(b)**, where the map of $|D_0|$ as the function of the dielectric rod position (x_d, y_d) is plotted, based on which we can find the optimal position of the dielectric rod is near to the area with the strongest electric field amplitude. In addition, $|D_0|$ has a much

http://dx.doi.org/10.5772/66663

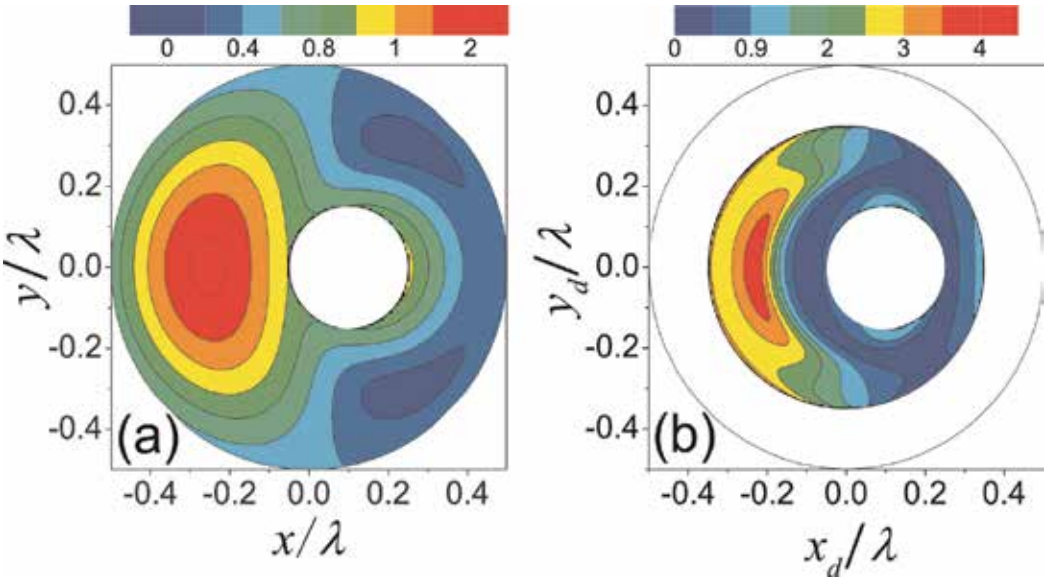

Figure 7. (a) The electric field amplitude pattern inside the RAZIM shell for the configuration in Figure 6(a). (b) The 0th order partial wave amplitude $|D_0|$ is plotted as the function of the dielectric rod position (x_d, y_d). The whiteout region in panel (b) denotes the area that the dielectric rod cannot reach. The line source is located at (0.1, 0), and the parameters of the RAZIM-based system are $a = 0.5$, $b = 1$, $r_d = 0.15$, $\mu_r = 0.01$, $\mu_\phi = 1$, $\varepsilon_z = 1$, $\varepsilon_d = 2$, and $\mu_d = 1$.

larger value than that of a free line source in a large area, indicating the crucial role of the dielectric rod for enhancing the isotropic radiation. Another merit of the present system lies in that the introduction of a dielectric rod inside the RAZIM shell does not destroy the homogeneity of the RAZIM shell, making it experimentally realizable.

To optimize the performance of the dielectric rod, we calculate the total power radiating out of the RAZIM shell, which is defined as

$$P_s = \oint_L \boldsymbol{S} \cdot \boldsymbol{e}_r \, \mathrm{d}l, \quad \text{with} \quad \boldsymbol{S} = \frac{1}{2}\mathrm{Re}[\boldsymbol{E} \times \boldsymbol{H}^*], \tag{22}$$

where $\boldsymbol{S}$ is the Pointing vector, the integral curve L is a circle around the shell center O with the radius larger than outer radius of the RAZIM shell b. Considering the fact that only the 0th order cylindrical wave is radiated out, the radiating power can be approximately evaluated according to $P_{wi} \approx \frac{2}{\omega\mu_0}|D_0|^2$. For the convenience of comparison, we also calculate the radiating power P_{wo} when the RAZIM shell is removed from the system $P_{wo} = \frac{2}{\omega\mu_0}\sum_m |a_m H_m(kl) + J_m(kl)|^2$. In **Figure 8**, we present the radiating power normalized by that of a line source in free space P_{s0} and the profile of the normalized irradiance by that of a line source in free space I_0. For the radiating power without the RAZIM shell P_{wo}/P_{s0}, its value exhibits nearly no change with respect to the dielectric rod position x_d as indicated by the blue dashed line in panels (a). Even when the dielectric rod is replaced by a gain particle, P_{wo}/P_{s0} remains close to 1, suggesting that without the RAZIM shell the insertion of either passive or active particle has nearly no obvious influence on the radiating power due to the nearly homogeneous distribution of a line

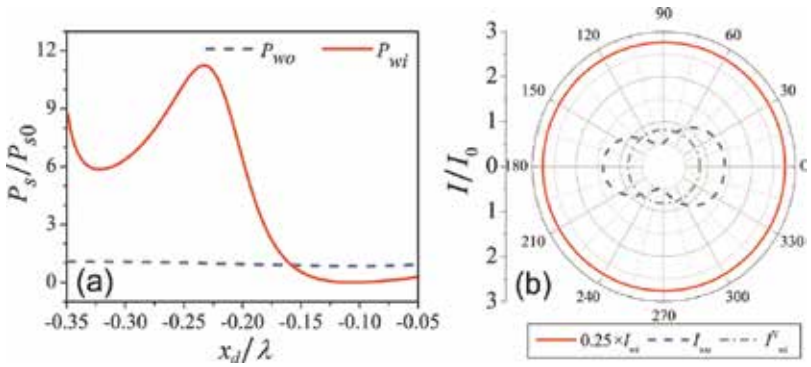

Figure 8. (a) The normalized radiating power P_s/P_{s0} is plotted as the function of the dielectric rod position x_d with the line source positioned at (0.1, 0), where the blue-dashed (red solid) line denotes the radiating power P_{wo} (P_{wi}) for the case without (with) the RAZIM shell. (b) The map of the normalized irradiance I/I_0, where the red solid line, the blue-dashed line, and the green dash-dotted line correspond to $I_{wi}/4$, I_{wo}, and I^N_{wi}, respectively, with $I_{wi}/4$ for the system with the RAZIM shell and the dielectric rod, I_{wo} for the system without the RAZIM shell, and I^N_{wi} for the system with RAZIM shell but without the dielectric rod D. The dielectric rod is placed at $(-0.24, 0)$ and all the other parameters are the same as those in Figure 7.

source in free space. Differently, for the radiating power with the RAZIM shell P_{wi}/P_{s0}, its value can be significantly improved as indicated by the red solid line shown in panels (a). The maximal enhancement is realized at the position close to the strongest electric field amplitude in **Figure 7(a)** with the value larger than 10. To illustrate the performance of the dielectric rod on the isotropic omnidirectional radiation, we present in **Figure 8(b)** the normalized irradiance by that of the line source in free space I_0 with the irradiance is defined as $I = \lim_{r\to\infty}(S \cdot r)$. From the irradiance profile for the system with the RAZIM shell I_{wi}, it can be found that the irradiance is reinforced by over 10 times as indicated by the red solid line, consistent with the result shown in **Figure 8(a)**. In addition, a highly isotropic feature is demonstrated as well by examining the irradiance map. For the convenience of comparison, we also present the irradiance I_{wo} for the system without the RAZIM shell as denoted by the blue dash line, which is not isotropic anymore and no evident enhancement is achieved with either the dielectric rod or the gain particle. The efficiency of the dielectric rod can be evaluated by comparing I_{wi} with the radiance I^N_{wi} for the case with the dielectric rod removed from the system. The profile of I^N_{wi} is denoted by the green dash-dot line, where we can find that only 80% EM energy of the line source is radiated out because of the trap of the high order modes by the RAZIM shell. This suggests that an insertion of a dielectric rod leads to a nearly 15 times amplification of the radiation power.

3.3. Amplifying radiation with gain particle

In practice, the loss should be an inevitable issue due to the finite size of the RAZIM shell and its resonant nature. To illustrate the effect of the loss on the radiation enhancement, we present in **Figure 9** the results for the system with the loss taken into account, where we can find that the output radiating power is reduced seriously compared to the results shown in **Figure 8**. To compensate the energy loss, the active coated nanoparticles might be a good choice. By

http://dx.doi.org/10.5772/66663

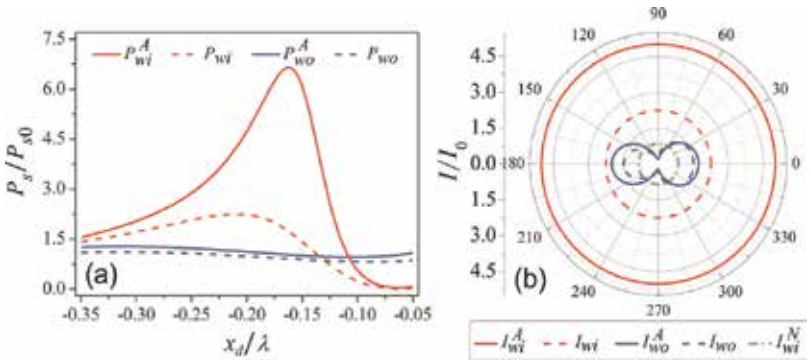

Figure 9. (a) The normalized radiating power P_s/P_{s0} is plotted as the function of the position x_d of the gain particle with $\varepsilon_d = 2.5–0.5i$ (solid lines) and the lossless dielectric particle with $\varepsilon_d = 2.5$ (dashed lines) for the system with (red lines) and without (blue lines) the RAZIM shell, respectively. The map of the normalized irradiance I/I_0 is shown in panel (b), where the red (blue) solid line corresponds to the result I^A_{wi} (I^A_{wo}) for the system with the gain particle modeled by $\varepsilon_d = 2.5–0.5i$ and with (without) the RAZIM shell, the red (blue) dashed line corresponds to the result I_{wi} (I_{wo}) for the system with the lossless dielectric particle of $\varepsilon_d = 2.5$ and with (without) the RAZIM shell, and the green dash-dotted line is for the system with the RAZIM shell but without the particle inside. The particle with the radius $r_d = 0.15$ is placed at $(-0.2, 0)$, the line source is positioned at (0.1, 0), $\mu_r = 0.01 + 0.005i$, $\mu_\phi = 1 + 0.005i$, and $\varepsilon_z = 2 + 0.005i$. All the other parameters are the same as those in Figure 6.

enclosing a gain particle with $\varepsilon_d = 2.5–0.5i$, we can compensate the energy loss from the RAZIM shell, yielding an enhancement of the output radiating power by a factor of about 7 as indicated by the red solid line in **Figure 9**. For comparison, the case for the system without the RAZIM shell but with a gain particle is also simulated as indicated by the blue solid line. Neither significant increase nor isotropy in the output radiation is achieved, suggesting once again the crucial role of the RAZIM shell.

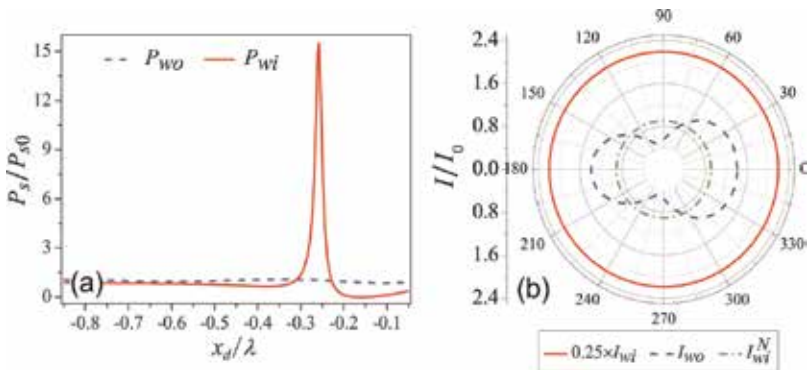

Figure 10. (a) The normalized radiating power P_s/P_{s0} is plotted as a function of the position x_d of the particle with $\varepsilon_d = 2$ for the system with (red solid line) and without (blue dashed line) the RAZIM shell, respectively. The map of the normalized irradiance I/I_0 is shown in panel (b), where the red solid (blue dashed) line corresponds to the result $0.25\times I_{wi}$ (I_{wo}) for the system with a lossless dielectric particle of $\varepsilon_d = 2.5$ and with (without) the RAZIM shell and the green dash-dotted line is for the system with the RAZIM shell but without the particle inside. The particle with the radius $r_d = 0.15$ is placed at $(-0.25, 0)$, the line source is fixed at (0.1, 0), $a = 1$, $b = 2$, $\lambda = 1$, $\mu_r = 0.001$, $\mu_\phi = 1$, and $\varepsilon_z = 1$.

The size of the RAZIM shell also has effect on the enhancement of the output radiation, which is illustrated in **Figure 10** for the RAZIM shell with $a = 1$ and $b = 2$. It can be found that the enhancement of the omnidirectional radiation becomes difficult in that only in a quite narrow range of the enhancement can be achieved as shown in **Figure 10(a)**. The underlying physics is as follows. Since the field due to the anisotropic higher order modes is trapped inside the RAZIM shell, the field is highly confined and anisotropic when the shell is small so that there appears the region with strong field easily. Then, a dielectric rod located near the position with strong field can rescatter the anisotropic modes into the isotropic mode, inducing a remarkable increase of the output radiating power. Differently, for large RAZIM shell, the anisotropic higher order modes are usually much less confined. As a result, the introduction of a dielectric rod cannot yield a strong rescattering of the trapped anisotropic modes into the isotropic field, resulting in a smaller enhancement of radiation power. Roughly speaking, the design works when the RAZIM shell is small. Nevertheless, the size of RAZIM shell is not necessarily limited to subwavelength scale. As shown in **Figure 10(b)** by the red solid line, a strong enhancement can still be achieved by a proper arrangement of the dielectric particle.

4. Conclusion

In summary, we have designed a kind of zero-index materials (ZIMs) with magnetic metamaterials based on the multiple scattering theory and effective-medium theory. The zero phase delay inside the ZIMs and the wavefront engineering are demonstrated. It is also shown that the effective index can be flexibly tuned by an external magnetic field and temperature, enabling the manipulation on the functionalities. In addition, the anisotropy of the ZIMs and the nonreciprocal feature of the magnetic metamaterials might induce nonreciprocal Goos-Hänchen and other physical consequences. Then, in the second part we have considered a radially anisotropic ZIM (RAZIM) based system with a RAZIM shell enclosing both a line source and a dielectric rod, which can implement a remarkably enhanced omnidirectional radiation. An exact theoretical approach is developed to solve the system, based on which we can optimize the configuration to achieve the high efficiency, more importantly, discover the underlying physics. Actually, the RAZIM shell allows only the 0-th order isotropic mode to radiate outside the system, ensuring the isotropy of the radiation. Differently, the anisotropic higher order modes are trapped, thus creating a strongly inhomogeneous standing wave. The dielectric rod can rescatter the anisotropic modes into isotropic one, enhancing the omnidirectional radiation remarkably. Besides, the present design is experimentally feasible, and meanwhile provides a highly efficient omnidirectional radiation by spatial power combination.

Acknowledgements

This work was supported by the China 973 Projects (No. 2013CB632701), the National Natural Science Foundation of China (Nos. 11274277, 11574055, and 11574275), MOE of China (B06011), the Zhejiang Provincial Natural Science Foundation of China (LR16A040001), and the open project of SKLSP (KF2016_3) in Fudan University.

http://dx.doi.org/10.5772/66663

Author details

Shiyang Liu[1]*, Jialin Zhou[1], Ying Han[1], Xinning Yu[2], Huajin Chen[2,3] and Zhifang Lin[2]

*Address all correspondence to: syliu@fudan.edu.cn

1 Institute of Information Optics, Zhejiang Normal University, Zhejiang, China

2 Surface Physics Laboratory, Department of Physics, Fudan University, Shangai, China

3 School of Electrical and Information Engineering, Guangxi University of Science and Technology, China

References

[1] Pendry JB. Negative refraction makes a perfect lens. Phys. Rev. Lett. 2000; **85**: 3966–3969.

[2] Shelby RA, Smith DR, Schultz S. Experimental verification of a negative index of reflection. Science. 2001; **292**: 77–79.

[3] Caiazzo M, Maci S, Engheta N. A metamaterial surface for compact cavity resonators. IEEE Antenn. Wireless Propag. Lett. 2004; **3**: 261–264.

[4] Shalaev VM. Optical negative-index metamaterials. Nat. Photon. 2007; **1**: 41–48.

[5] Valentine J, Zhang S, Zentgraf T, Ulin-Avila E, Genov DA, Bartal G, Zhang X. Three-dimensional optical metamaterial with a negative refractive index. Nature. 2008; **455**: 376–379.

[6] Leonhardt U. Optical conformal mapping. Science. 2006; **312**: 1777–1780.

[7] Pendry JB, Schurig D, Smith DR. Controlling electromagnetic fields. Science. 2006; **312**: 1780–1782.

[8] Lai Y, Ng J, Chen HY, Han DZ, Xiao JJ, Zhang ZQ, Chan CT. Illusion optics: the optical transformation of an object into another object. Phys. Rev. Lett. 2009; **102**: 253902.

[9] Maier SA, Kik PG, Atwater HA. Observation of coupled plasmon-polariton modes in Au nanoparticle chain waveguides of different lengths: estimation of waveguide loss. Appl. Phys. Lett. 2002; **81**: 1714–1716.

[10] Maier SA, Kik PG, Atwater HA, Meltzer S, Harel E, Koel BE, Requicha AAG. Local detection of electromagnetic energy transport below the diffraction limit in metal nanoparticle plasmon waveguides. Nat. Mater. 2003; **2**: 229–232.

[11] Edwards B, Alù A, Young M, Silveirinha M, Engheta N. Experimental verification of epsilon- near-zero metamaterial coupling and energy squeezing using a microwave waveguide. Phys. Rev. Lett. 2008; **100**: 033903.

[12] Garcia N, Ponizovskaya EV, Xiao JQ. Zero permittivity materials: band gaps at the visible. Appl. Phys. Lett. 2002; **80**: 1120–1122.

[13] Silveirinha MG, Engheta N. Tunneling of electromagnetic energy through subwavelength channels and bends using ε-near-zero materials. Phys. Rev. Lett. 2006; **97**: 157403.

[14] Jin Y, Zhang P, He SL. Squeezing electromagnetic energy with a dielectric split ring inside a permeability-near-zero metamaterial. Phys. Rev. B. 2010; **81**: 085117.

[15] Silveirinha MG, Belov PA. Spatial dispersion in lattices of split ring resonators with permeability near zero. Phys. Rev. B. 2008; **77**: 233104.

[16] Huang XQ, Lai Y, Hang ZH, Zheng HH, Chan CT. Dirac cones induced by accidental degeneracy in photonic crystals and zero-refractive-index materials. Nat. Mater. 2011; **10**: 582–586.

[17] Silveirinha MG, Engheta N. Design of matched zero-index metamaterials using nonmagnetic inclusions in epsilon-near-zero media. Phys. Rev. B. 2007; **75**: 075119.

[18] Ziolkowski RW. Propagation in and scattering from a matched metamaterial having a zero index of refraction. Phys. Rev. E. 2014; **70**: 046608.

[19] Cheng Q, Jiang WX, Cui TJ. Spatial power combination for omnidirectional radiation via anisotropic metamaterials. Phys. Rev. Lett. 2012; **108**: 213903.

[20] Yuan Y, Shen LF, Ran LX, Jiang T, Huangfu JT, Kong JA. Directive emission based on anisotropic metamaterials. Phys. Rev. A. 2008; **77**: 053821.

[21] Zhu WR, Rukhlenko ID, Premaratne M. Application of zero-index metamaterials for surface plasmon guiding. Appl. Phys. Lett. 2013; **102**: 011910.

[22] Liu RP, Cheng Q, Hand T, Mock JJ, Cui TJ, Cummer SA, Smith DR. Experimental demonstration of electromagnetic tunneling through an epsilon-near-zero metamaterial at microwave frequencies. Phys. Rev. Lett. 2008; **100**: 023903.

[23] Alù A, Silveirinha MG, Salandrino A, Engheta N. Epsilon-near-zero metamaterials and electromagnetic sources: tailoring the radiation phase pattern. Phys. Rev. B. 2007; **75**: 155410.

[24] Feng SM. Loss-induced omnidirectional bending to the normal in ε-near-zero metamaterials. Phys. Rev. Lett. 2012; **108**: 193904.

[25] Enoch S, Tayeb G, Sabouroux P, Guerin N, Vincent P. A metamaterial for directive emission. Phys. Rev. Lett. 2002; **89**: 213902.

[26] Ma YG, Wang P, Chen X, Ong CK. Near-field plane-wave-like beam emitting antenna fabricated by anisotropic metamaterial. Appl. Phys. Lett. 2009; **94**: 044107.

[27] Soric JC, Engheta N, Maci S, Alù A. Omnidirectional metamaterial antennas based on ε-near-zero channel matching. IEEE Trans. Antennas Propag. 2013; **61**: 33–44.

[28] Hao JM, Yan W, Qiu M. Super-reflection and cloaking based on zero index metamaterial. Appl. Phys. Lett. 2012; **96**: 101109.

[29] Nguyen VC, Chen L, Halterman K. Total transmission and total reflection by zero index metamaterials with defects. Phys. Rev. Lett. 2010; **105**: 233908.

[30] Luo J, Xu P, Chen HY, Hou B, Gao L, Lai Y. Realizing almost perfect bending waveguides with anisotropic epsilon-near-zero metamaterials. Appl. Phys. Lett. 2012; **100**: 221903.

[31] Wang Z, Chong YD, Joannopoulos JD, Soljačić M. Reflection-free one-way edge modes in a gyromagnetic photonic crystal. Phys. Rev. Lett. 2008; **100**: 013905.

[32] Zhu WR, Rukhlenko ID, Premaratne M. Light amplification in zero-index metamaterial with gain inserts. Appl. Phys. Lett. 2012; **101**: 031907.

[33] Liu SY, Chen WK, Du JJ, Lin ZF, Chui ST, Chan CT. Manipulating negative-refractive behavior with a magnetic field. Phys. Rev. Lett. 2008; **101**: 157407.

[34] Liu SY, Lu WL, Lin ZF, Chui ST. Magnetically controllable unidirectional electromagnetic waveguiding devices designed with metamaterials. Appl. Rev. Lett. 2010; **97**: 201113.

[35] Liu SY, Lu WL, Lin ZF, Chui ST. Molding reflection from metamaterials based on magnetic surface plasmons. Phys. Rev. B. 2011; **84**: 045425.

[36] Poo Y, Wu RX, Liu SY, Yang Y, Lin ZF, Chui ST. Experimental demonstration of surface morphology independent electromagnetic chiral edge states originated from magnetic plasmon resonance. Appl. Phys. Lett. 2012; **101**: 081912.

[37] Yu XN, Chen HJ, Lin HX, Zhou JL, Yu JJ, Qian CX, Liu SY. Continuously tuning effective refractive index based on thermally controllable magnetic metamaterials. Opt. Lett. 2014; **39**: 4643–4646.

[38] Ding YS, Chan CT, Wang RP. Optical waves in a gradient negative-index lens of a half-infinite length. Sci. Rep. 2013; **3**: 2954.

[39] Litchinitser NM, Maimistov AI, Gabitov IR, Sagdeev RZ, Shalaev VM. Metamaterials: electromagnetic enhancement at zero-index transition. Opt. Lett. 2008; **33**: 2350–2352.

[40] Li LM, Zhang ZQ. Multiple-scattering approach to finite-sized photonic band-gap materials. Phys. Rev. B. 1998; **58**: 9587–9590.

[41] Lin ZF, Chui ST. Electromagnetic scattering by optically anisotropic magnetic particle. Phys. Rev. E. 2004; **69**: 056614.

[42] Lin ZF, Chui ST. Manipulating electromagnetic radiation with magnetic photonic crystals. Opt. Lett. 2007; **32**: 2288–2290.

[43] Liu SY, Lin ZF. Opening up complete photonic bandgaps in three-dimensional photonic crystals consisting of biaxial dielectric spheres. Phys. Rev. E. 2006; **73**: 066609.

[44] Moroz A. Metallo-dielectric diamond and zinc-blende photonic crystals. Phys. Rev. B. 2002; **66**: 115109.

[45] Stefanou N, Yannopapas V, Modinos A. Heterostructures of photonic crystals: frequency bands and transmission coefficients. Comput. Phys. Commun. 1998; **113**: 49–77.

[46] Jin JJ, Liu SY, Lin ZF, Chui ST. Effective-medium theory for anisotropic magnetic metamaterials. Phys. Rev. B. 2009; **80**: 115101.

[47] Pozar DM. Microwave Engineering. New York: Wiley; 2004.

[48] Eggimann WH. Scattering of a plane wave on a ferrite cylinder at normal incidence. IRE Trans. Microwave Theory Tech. 1960; **8**: 440.

[49] Wu Y, Li J, Zhang ZQ, Chan CT. Effective medium theory for magnetodielectric composites: beyond the long-wavelength limit. Phys. Rev. B. 2006; **74**: 085111.

[50] Shen M, Ruan LX, Wang XL, Shi JL, Wang Q. Tunable band gap near the Dirac point in nonlinear negative-zero-positive index metamaterial waveguide. Phys. Rev. A. 2011; **83**: 045804.

[51] Yannopapas V, Vanakaras A. Dirac point in the photon dispersion relation of a negative/zero/positive-index plasmonic metamaterial. Phys. Rev. B. 2011; **84**: 045128.

[52] Ni YX, Gao L, Qiu CW. Achieving invisibility of homegeneous cylindrically anisotropic cylinders. Plamonics. 2010; **5**: 251-258.

[53] Wang N, Chen HJ, Lu WL, Liu SY, Lin ZF. Giant omnidirectional radiation enhancement via radially anisotropic zero-index metamaterial. Opt. Express. 2013; **21**: 23712.

[54] Abramowitz M, Stegun IA. Handbook of Mathematical Functions with Formulas, Graph, and Mathematical Tables. Dover; New York: 1964.

[55] Chew WC. Waves and Fields in Inhomogeneous Media. New York: IEEE Press; 1995.

[56] Chen ZC, Mohsen R, Gong YD, Chong TW, Hong MH. Realization of variable three-dimensional terahertz metamaterial tubes for passive resonance tunability. Adv. Mater. 2002; **24**: 143–147.

[57] Bohren CF, Huffman DR. Absorption and Scattering of Light by Small Particles. New York: John Wiley & Sons; 1983.

Edited by Sandra Costanzo

Wave Propagation Concepts for Near-Future Telecommunication Systems is an edited book discussing recent researches for the development of innovative telecommunication systems, with particular focus on the propagation aspects and radiating systems design. It is divided into two sections: Section 1, devoted to the illustration of advanced results in terms of microwave propagation at high operating frequencies, and Section 2, illustrating new electromagnetic concepts and applications.

ISBN 978-953-51-4855-5

Photo by sakkmesterke / iStock

IntechOpen